

Noise-activated dynamics of DNA through nanoporous gel

*a thesis submitted
in partial fulfillment of the requirements*

for the degree of
Doctor of Philosophy

by

**Mr. Aniruddha Deb
(Roll No. 176107009)**



**Department of Chemical Engineering
Indian Institute of Technology Guwahati**

March 2023



भारतीय प्रौद्योगिकी संस्थान गुवाहाटी
केमिकल इंजीनियरिंग विभाग
गुवाहाटी 781039, असम, भारत



Indian Institute of Technology Guwahati
Department of Chemical Engineering
Guwahati 781039, Assam, INDIA

CERTIFICATE

It is certified that the research work contained in this thesis entitled “**Noise-activated dynamics of DNA through nanoporous gel**”, done by Mr. Aniruddha Deb, was carried out under my supervision and have not been submitted as a thesis elsewhere for a PhD degree.

Thesis Supervisor

Dr. Partho S.G. Pattader

Associate Professor

Department of Chemical Engineering

IIT Guwahati, Assam-781039

भारतीय प्रौद्योगिकी संस्थान गुवाहाटी
केमिकल इंजीनियरिंग विभाग
गुवाहाटी 781039, असम, भारत



Indian Institute of Technology Guwahati
Department of Chemical Engineering
Guwahati 781039, Assam, INDIA

DECLARATION

I hereby declare that the matter embodied in this thesis is the result of investigations carried out by me in the Department of Chemical Engineering, Indian Institute of Technology Guwahati, Assam, India under the supervision of **Dr. Partho S.G. Pattader**, Department of Chemical Engineering and is submitted to the Indian Institute of Technology Guwahati, Guwahati-781039, Assam, India for the award of degree of Doctor of Philosophy. This work has not been submitted elsewhere for any degree or diploma of any institute or university to the best of my knowledge and belief.

In keeping with the general practice of reporting scientific observations, due acknowledgements have been made wherever the work of other investigators are referred, and copyright licenses have been taken from respective publishers.

IIT Guwahati

Aniruddha Deb

March 2023

Roll No. 176107009



ACKNOWLEDGEMENT

A Doctorate is considerably more than merely an academic degree. This adventure has changed me in many ways, both personally and scientifically. I want to use this opportunity to thank everyone who made this journey possible.

The road taken to complete this thesis has been one of the most incredible experiences of my life, which would not have been possible without the help of these people. First and probably most important, I would like to thank **Dr. Partho Sarathi Gooh Pattader**, my thesis supervisor, for allowing me to engage in a highly intriguing field of study. I am thankful for his constant assistance, valuable counsel, and engaging chats. Despite his hectic schedule, he was always willing to devote time to study problems and provide appropriate ideas to improve my work. I am confident that working under his direction will profoundly impact my life. His dedication to his profession, unwavering pursuit of perfection, and patience in training new scholars will always inspire me. It has been a delight to be guided by him. I would like to thank the members of my doctorate committee, Prof. Dipankar Bandyopadhyay and Prof. Mahua De from the Department of Chemical Engineering, and Prof. Lal Mohan Kundu from the Department of Chemistry, for their valuable recommendations and efforts throughout my thesis study. Also I would like to thank my thesis examiners **Prof. Sunando Dasgupta, IIT Kharagpur** and **Prof. Daniel Roxbury, University of Rhode Island** for their careful observation of the thesis and invaluable comments. My heartfelt gratitude goes to Dr. Pritam Roy, Dr. Ankur Pandey, Dr. Sunil Kumar Singh, and Dr. Kaniska Murmu, my senior lab mates, for their unwavering support and encouragement during my PhD duration. I would additionally like to thank Dr. Prerona Gogoi, one of my labmates, for her cooperation with experiments and thesis preparation.

I acknowledge my gratitude to my acquaintances and colleagues Dr. Awadh Kishor Kumar, Mr. Ponnala Rambabu, Mr. Niladri Samanta, and last but not least Mrs. Anushikha Roy for their contributions to making my time at IIT Guwahati unforgettable.

My sincerest gratitude goes to all of the faculty and staff members of IIT Guwahati's Department of Chemical Engineering, Centre for Nanotechnology, and Central Instruments Facility for their help and cooperation during this process. I would also like to thank the Analytical Laboratory in Chemical Engineering, the Centre for Nanotechnology, and the Central Instruments Facility at IIT Guwahati for their assistance with characterization facilities.

I would like to express my gratitude to all of my high school and college instructors and my friends and well-wishers for their support and encouragement throughout my life. Above all, I want to thank my parents, Mr. Suvendu Sekhar Deb and Mrs. Purnima Deb, and my brother, Mr. Arnab Deb, for their unending love and support.

Aniruddha Deb

ANIRUDDHA DEB

The logo of the Indian Institute of Technology Guwahati is a circular emblem. It features a central stylized figure of a person with arms raised, surrounded by three smaller circles. The text "Indian Institute of Technology Guwahati" is written in English around the bottom half of the circle, and "भारतीय प्रौद्योगिकी संस्थान गुवाहाटी" is written in Hindi around the top half.

**Dedicate the thesis to My
*Family.***



SYNOPSIS

Noise-activated dynamics of DNA through nanoporous gel

1. Introduction

The prime theme of this dissertation is to study the barrier crossing of a charged macromolecule through nanoporous gels for faster translocation in a noisy environment^{1,2}. The work aims to understand seemingly mundane but profoundly interesting rich phenomena like separating a particle from an adhered surface, steering a particle in a specific direction, flowing cereals from a packet to the milk bowl, trickling down of raindrops on window pane etc. These macroscopic phenomena and the microscopic realm of colloidal particles or molecular transport within cells have enough ingredients to kindle this work³.

The fast development of microfluidic devices and MEMS, find their application in various fields such as medical science, reaction engineering, computational and information technology, robotic engineering, etc. Study of the interaction at the interface of the two bodies becomes essential in controlling micro-droplet's motion in a microfluidic device⁴. This sort of interaction is defined as friction which is the prime cause of energy loss for a thermodynamically open system. Hence, an external noise was used to overcome friction. In this research work, we have focused on two important points-

1. How does an external noise affect a charged macromolecule's dynamics through nanoporous gel?
2. Role of coulombic/solid friction over linear kinematic friction on the translocation of DNA in presence of noise through nanoporous gels.

Although there exists a plethora of experimental studies in the literature of non-equilibrium dynamics, some uncovered areas call for more exploration like the athermal stochastic systems

where the source of random noise and the origin of the energy dissipation mechanism are decoupled.

The present thesis explores the usage of non-linear dynamics and friction specifically to study the faster translocation of DNA in a gel electrophoretic environment with the aid of gaussian white noise. The objectives of the present work are as follows:

- To investigate the effect of noise activated faster locomotion of DNA through the frictional landscape of nanoporous gels.
- To study the role of solid friction over linear kinematic friction in nanoporous gels and splitting of noise-bias in orthogonal direction for faster translocation of DNA.
- Asymmetric wave-induced translocation of DNA in a gel electrophoretic environment.
- To assess external noise induced kinetics of Aptamer-AuNP (apt-AuNP) assay within gel electrophoretic setup and to design an inexpensive non-invasive point-of-care (POC) aptasensor for rapid disease diagnosis.

Concisely, in the present thesis, objectives are distributed into following four chapters. The technical chapters in the thesis are preceded by an introductory chapter while at the end of the thesis a chapter containing the summary and future scopes have been included. A detailed list of publications and conferences attended are provided at the end of this synopsis section.

Chapter 2. Mechanism of fast locomotion of DNA using external noise through frictional landscape of nanoporous gel

In this Chapter, our experiments demonstrate that the mobility of DNA molecules in gel electrophoretic settings can be significantly faster ($\sim 100\%$ or more) than the conventional gel electrophoresis with the aid of external Gaussian noise^{1,5}. A modified Langevin simulation successfully predicts the drift velocity for an applied bias and noise, along with the consideration of space-dependent nonlinear solid friction, originating from the wide distribution of the gel pore size. In contrast to the conventional notion, this study reveals that an enormous amount of solid friction is operative at the interface of the DNA-gel matrix^{6,7}.

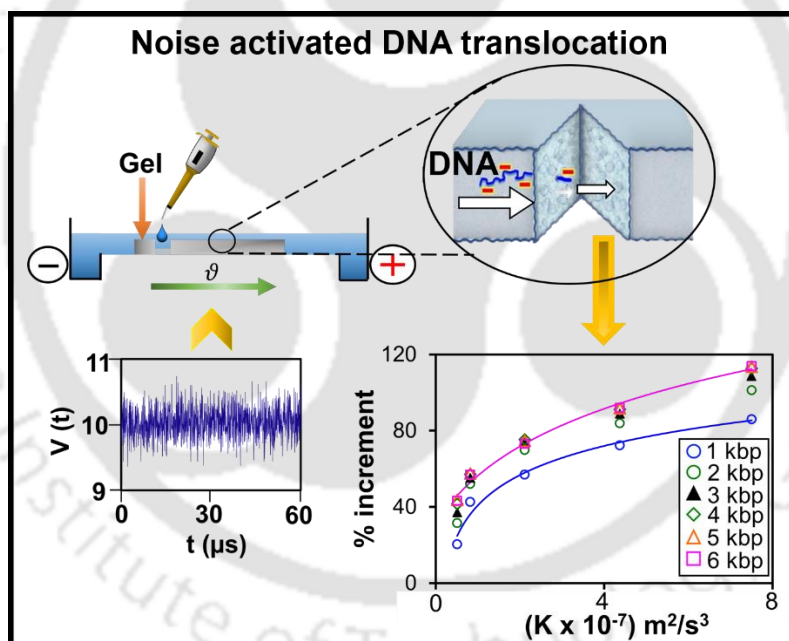


Figure 1. Schematic representation of the experimental setup. The function waveform generator is connected with a signal amplifier. The output from the amplifier is connected in series with a constant DC voltage source and the resultant output is applied across the agarose gel in the electrophoretic chamber.

This work suggests noise-activated faster DNA fingerprinting strategies and set up the platform for advanced research on resonance-induced super mobility to isolate a specific protein fragment from a crowd.

Chapter 3. Investigation on the effect of Gaussian White noise orthogonal to the drift of DNA in gel electrophoresis

The important outcome of this research problem is that an external noise in one direction can impart sufficient energy to a stuck biomolecule that can become mobile and can be steered in any preferred direction by applying a subcritical biased force. The biomolecule may choose the minimum energy path in the energy landscape when noise is applied orthogonal to that of the bias direction. Instead of overcoming the apex of the barrier directly, it may explore the lowest barrier height in the neighborhood and take the minimum energy path to bypass the energy loss associated with the apex-crossing^{8,9}.

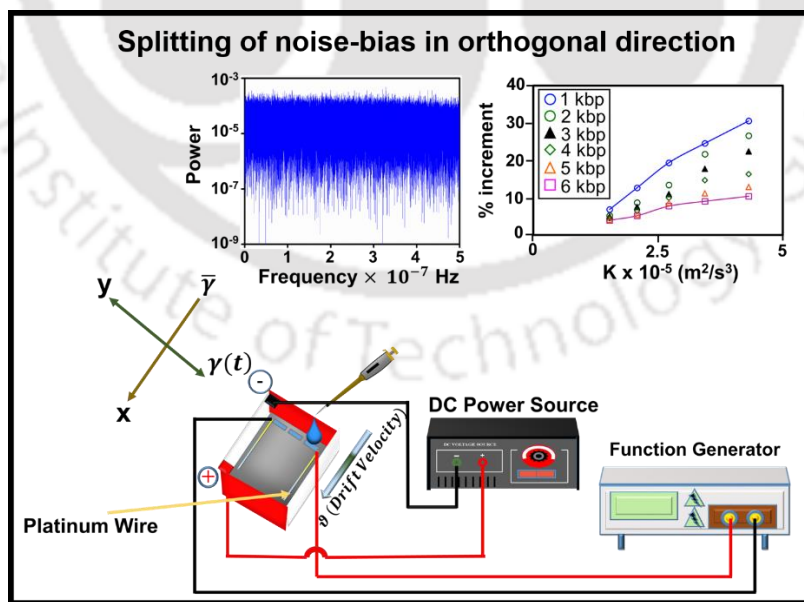


Figure 2. Schematic of the experimental setup involving the splitting of noise-bias along orthogonal direction.

The application of random noise in the form of fluctuating voltage pulses in the direction orthogonal to the applied electric field makes the separation process fast and can be used in chromatographic separation. The noise makes the DNA molecules overcome friction and traverse faster. Hence separation by gel electrophoresis should be quicker and at a low biased voltage if an orthogonal fluctuating voltage of zero mean is used.

Chapter 4. Asymmetric ramp wave driven dynamics of DNA for faster segregation

In this chapter, asymmetric ramp wave fluctuations were added in addition to biased voltage in a gel electrophoretic setting to showcase the effect of vibration influencing the DNA drift velocity through a nanoporous gel¹⁰. The main outcome of this chapter is that vibration makes the DNA molecule traversing “fluidized” in some sense enabling to move faster. Due to additional excitation generated by vibration, the depinning of the DNA molecule (like the peeling of a soft adhesive) enables faster DNA kinetics.

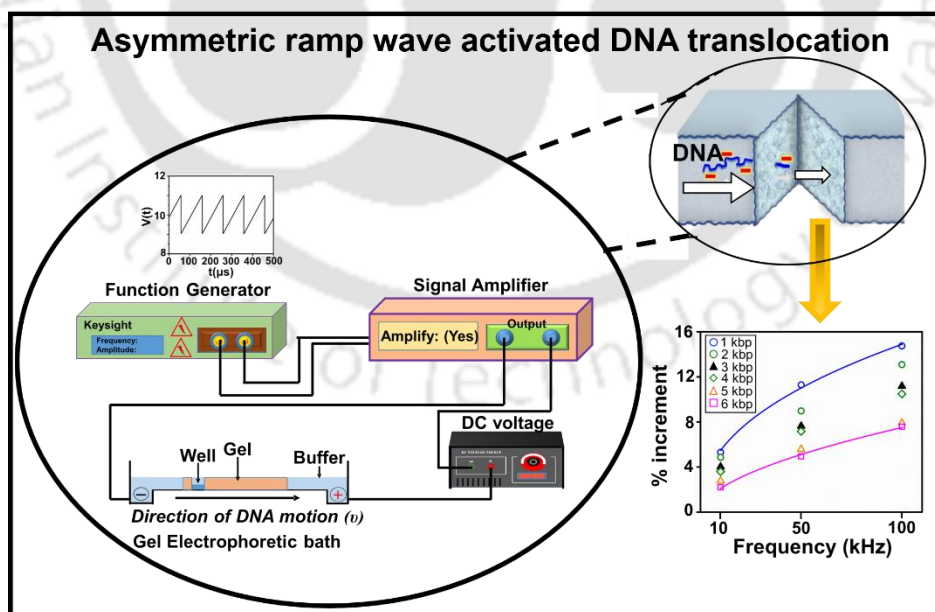


Figure 3. Representation of the ramp wave generated and applied along with biased voltage across the gel. The arrow with the symbol denotes the direction of the DNA band motion.

The initial slow dynamics phase vanishes and a picture of steadily enhanced velocity emerges during the vibration-assisted motion of DNA in addition to electric-biased voltage. The behavior of this subcritical dynamics is similar to that of a designed experiment where the drops are impelled to cross over a physical barrier in presence of external noise¹¹.

Chapter 5. Detection of *K.pneumoniae* for UTI diagnosis using gold nanoparticle conjugated aptasensor in gel electrophoretic setting

In this chapter, we have demonstrated how external vibration induced gel electrophoretic system can be utilised for diagnosis of a specific bacteria. Alongside, a point-of-care (POC) aptasensor prototype is also developed during the course of this investigation which supports our findings through gel electrophoretic detection of a specific bacteria (*K.pneumoniae*) responsible for UTI¹² and other health issues such as meningitis, lung infection¹³ etc.

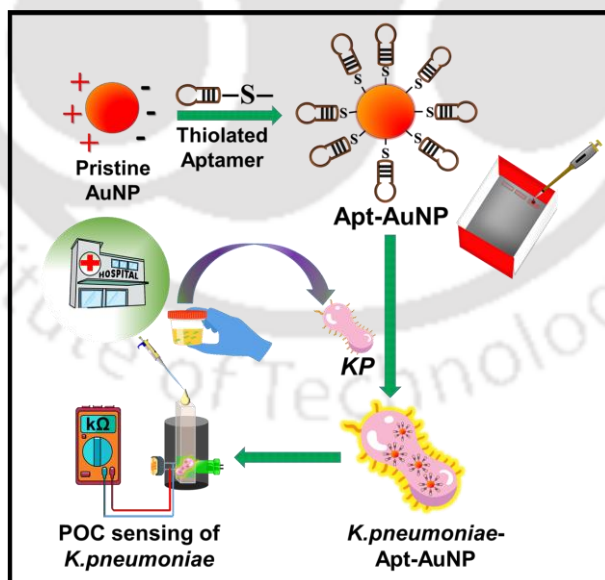


Figure 4. Schematic representation of specific uropathogen detection based on Apt-AuNP assay.

Based on the Localized Surface Plasmon Resonance (LSPR) phenomena of AuNP^{14,15}, a point-of-care aptasensor was designed that shows specific changes in the absorbance in the visible spectra in the presence of a target pathogen for robust and fast screening of UTI samples¹⁶. We have demonstrated the specific detection of *Klebsiella pneumoniae* bacteria with LoD as low as 3.4×10^3 CFU/mL.

We have demonstrated a generic methodology to determine the specific detection of uropathogen which can aid the doctor to treat the patient with antibiotics as early as possible.

Chapter 6. Conclusions and Future Scope

Chapter 6 concludes with the thesis summary and a brief discussion on the future prospects of noise/vibration activated macromolecule transport through nanoporous matrix.

Summary

The thesis explores the macromolecule (DNA) motion through gel pores by using external noise/ramp vibration to enhance DNA mobility through nanoporous gels. The nonlinear nature of the friction was identified by interrogating the system with random white noise, without engaging any sophisticated apparatus to measure the friction force directly. We have shown that the mobility of charged DNA molecules is independent of thermal noise but in the presence of Coulombic friction, it depends on the strength of external applied noise power K (m^2/s^3). The above study resonates with the application of external noise overcoming the entropic barrier of the pores present within the gel network, thus making a charged DNA molecule move faster.

References

1. Deb, A., Gogoi, P., Singh, S. K. & Gooh Pattader, P. S. Noise-Activated Fast Locomotion of DNA through the Frictional Landscape of Nanoporous Gels. *Langmuir* **38**, 11764–11769 (2022).
2. Shi, N. & Ugaz, V. M. Noise-enhanced gel electrophoresis. *Electrophoresis* **35**, 1758–1765 (2014).
3. Selmeczi, D. *et al.* Cell motility as random motion: A review. *Eur. Phys. J. Spec. Top.* **157**, 1–15 (2008).
4. Daniel, S., Chaudhury, M. K. & De Gennes, P. G. Vibration-actuated drop motion on surfaces for batch microfluidic processes. *Langmuir* **21**, 4240–4248 (2005).
5. Chaudhury, M. K. & Goohpattader, P. S. Noise-activated dissociation of soft elastic contacts. *Eur. Phys. J. E* **35**, 131 (2012).
6. Burlatsky, S. F. & Deutch, J. M. Solid friction in gel electrophoresis. *J. Chem. Phys.* **103**, 8216–8227 (1995).
7. Burlatsky, S. & Deutch, J. Influence of solid friction on polymer relaxation in gel electrophoresis. *Science (80)*. **260**, 1782–1784 (1993).
8. Semenov, A. N. & Subbotin, A. V. Orientation effects in DNA during gel-electrophoresis. *Polym. Sci. U.S.S.R.* **32**, 1208–1214 (1990).
9. Muthukumar, M. Mechanism of DNA Transport Through Pores. *Annu. Rev. Biophys. Biomol. Struct.* **36**, 435–450 (2007).
10. Baule, A., Touchette, H. & Cohen, E. G. D. Stick-slip motion of solids with dry friction subject to random vibrations and an external field. *Nonlinearity* **24**, 351–372 (2011).
11. Goohpattader, P. S., Mettu, S. & Chaudhury, M. K. Experimental investigation of the drift

- and diffusion of small objects on a surface subjected to a bias and an external white noise: Roles of coulombic friction and hysteresis. *Langmuir* **25**, 9969–9979 (2009).
12. Foxman, B., Barlow, R., D’Arcy, H., Gillespie, B. & Sobel, J. D. Urinary tract infection: Self-reported incidence and associated costs. *Ann. Epidemiol.* **10**, 509–515 (2000).
 13. Vieira, A. T. *et al.* Control of *Klebsiella pneumoniae* pulmonary infection and immunomodulation by oral treatment with the commensal probiotic *Bifidobacterium longum* 51A. *Microbes Infect.* **18**, 180–189 (2016).
 14. Zhao, W. *et al.* DNA aptamer folding on gold nanoparticles: From colloid chemistry to biosensors. *J. Am. Chem. Soc.* **130**, 3610–3618 (2008).
 15. Ahmadi, S., Kamaladini, H., Haddadi, F. & Sharifmoghadam, M. R. Thiol-Capped Gold Nanoparticle Biosensors for Rapid and Sensitive Visual Colorimetric Detection of *Klebsiella pneumoniae*. *J. Fluoresc.* **28**, 987–998 (2018).
 16. Cristea, O. M. *et al.* Urinary tract infection with *Klebsiella pneumoniae* in Patients with Chronic Kidney Disease. *Curr. Heal. Sci. J.* **43**, 137–148 (2017).

List of Journal Publications

From Thesis

1. Noise-Activated Fast Locomotion of DNA through the Frictional Landscape of Nanoporous Gels, **Aniruddha Deb**, Prerona Gogoi, Sunil K. Singh, and Partho Sarathi Gooh Pattader*, *Langmuir* 2022, **38, 38, 11764–11769**. [Selected as a Cover Image September 27, 2022 Volume38, Issue38, 11503-11810]. DOI: <https://doi.org/10.1021/acs.langmuir.2c01897>

2. Specific instantaneous detection of *K.pneumoniae* for UTI diagnosis using plasmonic gold nanoparticle conjugated aptasensor, **Aniruddha Deb**, Mousumi Gogoi, Tapas Kumar Mandal, Swapnil Sinha* and Partho Sarathi Gooh Pattader*. (Under review).

3. Splitting of noise-bias in orthogonal direction for faster DNA kinetics through nanoporous gels, **Aniruddha Deb** and Partho Sarathi Gooh Pattader*. (Manuscript under preparation).

4. Effect of asymmetric ramp wave activated translocation of DNA through nanoporous substrates, **Aniruddha Deb** and Partho Sarathi Gooh Pattader* (Manuscript under preparation).

Outside thesis

1. Chiral Resolution of Racemic Amines in μ -Reactor-Crystallizer. Singh, S.K.; Gogoi, P.; **Deb, A.**; Pattader, P. S. G, Chemical Engineering Science <https://doi.org/10.1016/j.ces.2022.117686>.

2. Janus micro-thread to micro-nanodroplets using dynamic contact line lithography, Kaniska Murmu, Ankur Pandey, Pritam Roy, **Aniruddha Deb**, Partho Sarathi Gooh Pattader*, Journal of Applied Polymer science, <https://doi.org/10.1002/app.52490>.

Conferences Attended

1. Effect of vibration on spontaneous dewetting morphology, kinetics and self-assembly of thin polymer films, **Aniruddha Deb** and Partho S.G. Pattader, **ACS Spring 2021**, Virtual mode, **DOI: 10.1021/scimeetings.1c00849**.
2. How to drive a DNA faster, **ACS Fall 2022, CHICAGO IL**, **Aniruddha Deb** and Partho S.G. Pattader **DOI: https://doi.org/10.1021/scimeetings.2c00389**.
3. Effect of vibration on dewetting morphology and kinetics, **Aniruddha Deb** and Partho S.G. Pattader, Jan 06-08, 2020, **ICFM-2020, IIT Kharagpur**.
4. Effect of labile underlayer on phase separation of PS-PMMA blend, **ACS Spring 2021**, Ankur Pandey, **Aniruddha Deb** and Partho S.G. Pattader.
5. “Noise induced enhanced DNA mobility through agarose gels”, **Aniruddha Deb**, Research & Industrial Conclave, Oral Presentation, 20-23rd January 2022, IIT Guwahati.



List of Figures

Figure No.	Description	Page No.
1.1.	Schematic representation of the experimental setup. (a) The function waveform generator is connected with a signal amplifier. The output from the amplifier is connected in series with a constant DC voltage source and the resultant output is applied across the agarose gel in the electrophoretic chamber. The arrow with the symbol denotes the direction of the DNA band motion. (b) The schematic of the enlarged gel cross-section depicts negatively charged DNA experiencing friction while traversing through the pores of the gel matrix.	15
1.2.	A physical representation of the PFGE versus Conventional gel electrophoresis. The gel (grey rectangle) is placed in a buffer in an electrophoretic chamber with anodes (+) and cathodes (-) (top diagrams). As represented in the bottom graphs, unlike conventional electrophoresis, where the biased voltage is unidirectional, PFGE cycles between several directions, allowing for more significant separation of DNA.	17
2.1.	Schematic representation of the experimental setup. (a) The function waveform generator is connected with a signal amplifier. The output from the amplifier is connected in series with a constant DC voltage source and the resultant output is applied across the agarose gel in the electrophoretic chamber. The arrow with the symbol denotes the direction of the DNA	50

	band motion. (b) The schematic of the enlarged gel cross-section depicts negatively charged DNA experiencing friction while traversing through the pores of the gel matrix.	
2.2.	<p>Effect of Gaussian noise on electrophoretic separation of DNA. (a) Agarose gel electrophoresis of DNA ladder (1-10 kbp) at 10 V bias for 4 h without any noise (i) and with the noise of different powers (K) depicted on the images (ii-vi). The DNA fragments in the image start from the well (dark rectangle at the top) and then move forward (downward in the image) to the positive electrode during electrophoresis. The band for 10 kbp is the closest to the well and the band for 5 kbp has maximum brightness. (b) A typical example of a time series of noise as voltage input at a low power of the noise. (c) Semi log plot of the input noise depicting Gaussian distribution with mean $\langle V(t) \rangle = 0$. The symbols indicate the noise input corresponding to the power shown in Figure 2.2.d: cyan triangle (Δ) - without noise, red diamond (\diamond) - $K= 5.2 \times 10^6 \text{ m}^2/\text{s}^3$, black circle ($\circ$) - $K= 8.2 \times 10^6 \text{ m}^2/\text{s}^3$, pink square ($\square$) - $K= 2.1 \times 10^7 \text{ m}^2/\text{s}^3$, blue diamond ($\diamond$) - $K= 4.4 \times 10^7 \text{ m}^2/\text{s}^3$, and green square ($\square$) - $K= 7.5 \times 10^7 \text{ m}^2/\text{s}^3$, (d) Displacement of the 1 kbp to 6 kbp after 4 h of gel electrophoresis without noise and with noise having different powers shown in the inset. To minimize the error, only estimation of the displacement up to 6 kbp was considered. The error bar represents the standard deviation from the results obtained from 9 sets of experiments. (e) % Increment of the displacement was estimated for 1 – 6 kbp (black circle (\circ), green circle</p>	51

	<p>(○), filled black triangle (▲), green diamond (◇), orange triangle (△), pink square (◻) represent 1 to 6 kbp respectively) at different power of the noise input. The percentage increment in displacement was estimated as %</p> $\text{Increment} = \frac{(x_n - x_c) \times 100}{x_c}$ <p>here x_n represents displacement for a particular DNA fragment (n) at a particular noise, and x_c is the displacement of the corresponding DNA fragment from the conventional gel electrophoresis without any noise. A typical displacement vs MW of DNA at various power of the noise but at a bias of 50 V is presented in Appendix section (Figure A.1.).</p>	
2.3.	<p>Displacement of the 1 kbp to 6 kbp after 90 min of gel electrophoresis without noise and with noise having different powers shown in the inset. Here, the symbols represent the noise powers as follows: cyan triangle (▲) - without noise, red diamond (◇) - $K = 5.2 \times 10^6 \text{ m}^2/\text{s}^3$, black circle (○) - $K = 8.2 \times 10^6 \text{ m}^2/\text{s}^3$, pink square (◻) - $K = 2.1 \times 10^7 \text{ m}^2/\text{s}^3$, blue diamond (◇) - $K = 4.4 \times 10^7 \text{ m}^2/\text{s}^3$, and green square (◻) - $K = 7.5 \times 10^7 \text{ m}^2/\text{s}^3$.</p>	53
2.4.	<p>(a) A typical power spectrum of the time-dependent voltage $V(t)$ as the noise input. The spectrum shows that the spectrum is reasonably flat up to the frequency $f_c = 2.5 \times 10^7 \text{ Hz}$. As this estimation is limited by the sampling time $dt = 40 \text{ ns}$ one can expect the noise is white over a larger frequency domain than $2.5 \times 10^7 \text{ Hz}$. (b) The autocorrelation function</p>	55

	(ACF) of the input noise suggests the noise is uncorrelated except at a very small time scale of the order of ns.	
2.5.	Agarose gel pore size and solid friction. (a) SEM image of the 0.8% agarose gel. The gel was initially frozen at $-20\text{ }^{\circ}\text{C}$ for overnight and then vacuum dried at 20 mTorr and $-103\text{ }^{\circ}\text{C}$ in a Lyophilizer for 24 h before the SEM analysis (b) Open-source ImageJ software was used to estimate the pore size (inset image showing the thresholding of the image). The probability distribution function $[P(\alpha)]$ of the pore size (α) (open blue circle) is fitted with the allometric regression of the form $[P(\alpha)] \sim \alpha^{-2.2}$. (c) Extreme value distribution of solid friction Δ used for the numerical simulation of the Langevin Eq. (1).	58
2.6.	FESEM images of agarose gel before (a) and after (b) electrophoresis experiment with noise having power $K=7.5 \times 10^7\text{ m}^2/\text{s}^3$. The identical procedure (as mentioned in the main text) of the freeze-drying technique was used before performing the FESEM. The pore size distributions show a negligible difference before and after electrophoresis (c).	59
2.7.	(a) Typical simulated trajectories of the DNA fragments (color code is shown in the inset) in gel electrophoretic setting at a particular noise $K = 2.1 \times 10^7\text{ m}^2/\text{s}^3$. (b) Simulated trajectories of 6 kbp DNA fragment at different powers of the noise shown in the figure. Inset shows 4 different trajectories of 6 kbp DNA fragments at low power ($K = 3.0 \times 10^4\text{ m}^2/\text{s}^3$)	61

	of the noise depicting the randomness and fluctuations during translocation.	
2.8.	The PDF of the displacement fluctuation in semi-log plot at different time windows (0.001, 0.01, and 0.05 ns) for 1 kbp (A) and 10 kbp (B) with space-dependent Δ . The peak position of the distribution is shifted to zero by $\tilde{x} = (x - x_p)$. The tails of these distributions are asymmetric and exponential. (C) The PDF of the displacement fluctuation for 1 kbp DNA with $\Delta = 0$ shows the Gaussian distribution.	62
2.9.	(a) Comparison of the drift velocity obtained from the 30 simulations for each case (curves) and the experiments (solid symbols). The error bar for the experimental data depicts the standard deviation of the results obtained from 9 sets of experiments in each case. (b) Arrhenius/Non-Arrhenius-like behavior. The velocity data for all the fragments (1 – 6 kbp) are plotted following Eq. (3) having $\Delta \sim n^{0.1}$ and $\tau_L \sim n^{-0.4}$. The blue shaded (high K) region shows noise-activated Arrhenius-like behavior and is represented with a black dash-dot line. Whereas, the yellow shaded (low K) region depicts Super-Arrhenius behavior, the velocity obtained is much higher (shown with a pink dash line) than that expected from Arrhenius prediction (black dash-dot line).	64
3.1.	Schematic of the experimental setup involving the splitting of noise bias in orthogonal direction. The noise is generated as voltage pulses from the function generator which is fed in such a way that the bias direction ($\bar{\gamma}$ is the term for bias force along X-direction) and the noise fluctuations	79

	<p>$(\gamma(t))$ is the term for external noise fluctuations along Y- direction) are completely orthogonal across the gel interface. The role played by $\bar{\gamma}$ and $\gamma(t)$ are discussed in the subsequent sections and adopted using the modified Langevin equation described in section 3.3.1. The resulting potential is generated due to the presence of TAE buffer and subsequently applied across the two electrodes of the electrophoretic chamber.</p>	
3.2.	<p>(A) Typical simulated trajectories of the DNA fragments (color code is shown in the inset) in gel electrophoretic setting tracked at a particular noise power $K = 4.32 \times 10^5 \text{ m}^2/\text{s}^3$ along X direction. (B) Noise fluctuations along the Y direction in gel electrophoretic setting for $n= 1$ kbp at different noise powers K (shown in inset).</p>	83
3.3.	<p>Role of solid friction on DNA mobility. (A) Plot of Velocity vs power of noise for $n=1, 3$ and 6 kbp with finite τ and Δ (implying presence of solid friction). The symbols represent the experimental drift velocity whereas the solid lines represent the simulation velocity obtained from 30 simulations in each case for different DNA fragments. (B) Plot of Velocity vs power of noise for $n=1, 3$ and 6 kbp with finite τ and $\Delta=0$. The error bars for the experimental data depicts the standard deviation of the results obtained from 9 sets of experiments in each case.</p>	86
3.4.	<p>Splitting of noise-bias in orthogonal direction. (A) Agarose gel electrophoresis of DNA ladder (1-10 kbp) at 10 V bias for 4 h without any noise (i) and with the splitting of noise-bias in orthogonal direction (ii-vi) with different powers (K) depicted on the image. The DNA fragments in</p>	88

the image start from the well (dark rectangle) and then move downward during electrophoresis. (B) % increment of the displacement was estimated for 1 – 6 kbp at different power of the noise input. The percentage increment in displacement was estimated as % increment = $\frac{(x_n - x_c) \times 100}{x_c}$, here x_n represents displacement for a particular DNA fragment at a particular noise, and x_c is the displacement of the corresponding DNA fragment from the conventional gel electrophoresis without any noise. To minimize the error while computing, only estimation up to 6 kbp was considered. The noise powers used for calculating are depicted along with the gel doc images mentioned in 3.4.A.

Unidirectional noise-bias induced gel electrophoresis. (C) Agarose gel electrophoresis of DNA ladder (1-10 kbp) at 10 V bias for 4 h without any noise (i) and with the unidirectional noise-bias (ii-vi) with different powers (K) depicted on the image. The DNA fragments in the image start from the well (dark rectangle) and then move downward during electrophoresis. (D) % Increment of the displacement was estimated for 1 – 6 kbp at different power of the noise input. The percentage increment in displacement was estimated as % increment = $\frac{(x_n - x_c) \times 100}{x_c}$, here x_n represents displacement for a particular DNA fragment at a particular noise, and x_c is the displacement of the corresponding DNA fragment from the conventional gel electrophoresis without any noise. Similar range of noise power was used in this case as in the case of orthogonal noise-

	<p>bias scenario. (E) A typical power spectrum of the time dependent voltage $V(t)$ as the noise input. The spectrum states that it is reasonably flat up to the frequency $f_c = 5 \times 10^7$ Hz. As, this estimation is bounded by the sampling time distribution constraint $dt = 20$ ns, so actually we can consider the noise to be white over a larger frequency domain than 5×10^7 Hz.</p>	
3.5.	<p>Drift velocity of the DNA fragments (splitting of external noise-bias in orthogonal direction). Comparison between the experimental drift velocity (symbols) and the velocity predicted by the equation (3) (line) obtained from 30 simulations in each case for different DNA fragments. The error bar for the experimental data depicts the standard deviation of the results obtained from 9 sets of experiments in each case.</p>	91
3.6.	<p>PDF of displacement fluctuations in X and Y direction. The PDF of the displacement fluctuation in semi-log plot at different time windows (0.001, 0.01, 0.05 ns and 0.1 ns) for 1 kbp (A & B) with and without space-dependent Δ. Plot (C) & (D) demonstrates the PDF of the displacement fluctuation along Y- direction for 1 kbp DNA considering finite Δ and with $\Delta = 0$ shows Gaussian distribution and no asymmetric tail distribution. The displacement distributions are generated using the simulation based on modified Langevin equation. The trajectories are traced and plotted at power of noise $K = 4.32 \times 10^5$ m²/s³.</p>	92
3.7.	<p>The PDF of the displacement distribution in semi-log plot at different time windows (0.001, 0.01, 0.05 ns and 0.1 ns) for 1 kbp (A) and 6 kbp (B)</p>	94

	<p>with space-dependent Δ. The peak position of the distribution is shifted to zero by $\tilde{x} = (x - x_p)$. The tails of these distributions are asymmetric and exponential. Plot (C) represent the PDF of the displacement distributions for 1 kbp DNA with $\Delta = 0$ which shows the Gaussian distribution.</p>	
4.1.	<p>Schematic representation of the experimental set-up. The function waveform generator (generating periodic ramp vibrations) is connected with a signal amplifier. The output of the amplifier is linked in series with a source of continuous DC voltage, and the resulting output is applied across the agarose gel in the electrophoretic chamber. The arrow with the symbol denotes the direction of the DNA band motion.</p>	110
4.2.	<p>(A) A typical example of a time series of noise as voltage input at a particular power of the noise. The corresponding gel doc images represent (i) without noise (conventional gel electrophoresis) and (ii) with noise (external noise-bias induced gel electrophoresis) scenarios. (B) A typical example of a time series of periodic ramp vibrations as voltage input. Here, external ramp vibrations was used along with bias voltage to demonstrate the electrophoretic separation of DNA. The corresponding gel doc images represent (i) without vibration (conventional gel electrophoresis) and (ii) with ramp vibration (ramp vibration induced gel electrophoresis) scenarios. The yellow arrows on the gel doc image (ii) represents the faster mobility of bands. Using ramp vibration of frequency 100 kHz, separation of 1 kbp DNA band was faster by $\sim 8\%$ than one with power of noise $K = 2.99 \times 10^5 \text{m}^2/\text{s}^3$. A comparison is made based on</p>	112

	the voltage amplitude of noise and the ramp vibrations that were generated using the waveform generator separately.	
4.3.	<p>Effect of asymmetric ramp vibration on the electrophoretic separation of DNA fragments. (A) Agarose gel electrophoresis of DNA ladder (1-10 kbp) at 10 V bias for 4 h without any ramp vibration (i) and with ramp vibrations of different frequencies depicted on the images (ii-iv). The DNA fragments in the image start from the well (dark rectangle at the top) and then move forward (downward in the image) to the positive electrode during electrophoresis. (B) Displacement of the 1 kbp to 6 kbp after 4 h of gel electrophoresis without ramp vibrations and with ramp vibrations having different frequencies shown in the inset. To reduce the error while calculating, only estimation of the displacement up to 6 kbp was considered. The error bar represents the standard deviation from the results obtained from 9 sets of experiments. (C) % Increment of the displacement was estimated for 1 – 6 kbp. The percentage increment in displacement was estimated as $\% \text{ Increment} = \frac{(x_n - x_c) \times 100}{x_c}$, here x_n represents displacement for a particular DNA fragment (n) at a particular ramp wave frequency, and x_c is the displacement of the corresponding DNA fragment from the conventional gel electrophoresis without any frequency.</p>	115
5.1.	<p>Schematics of the Cell-SELEX work flow carried out for DNA Aptamer development for target <i>K.pneumoniae</i>. (A) Outline various steps followed in the Cell-SELEX procedure. (B) Depicts the sequence of three Negative</p>	139

	Rounds (NR); 1, 2 and 3 during the SELEX. (C) Depicts the ssDNA library construction used in the present SELEX process. PBS is the Primer Binding Site at both 3' and 5' ends which were 17 bases long flanking the randomized sequence of 36 bases.	
5.1.1	Specificity of selected Aptamers for target <i>K.pneumoniae</i> bacteria. KPBA1 sequence shows the maximum specificity. [The inset shows A- Control, B- <i>K.pneumoniae</i> , C- <i>E.coli</i> , D- <i>S.aureus</i> , E- <i>E.faecalis</i>]. The error bars in the diagram indicate the standard deviation of the readings obtained from 3 measurements.	140
5.2.	UV-Vis spectra demonstrating the optimization concentration of Apt-AuNP conjugation which shows a bathochromic shift of ~ 3 nm using 0.05 μ M Apt- 0.0024 nM AuNP.	141
5.3.	Gel doc image depicting the free aptamer (Lane-1), DNA aptamer-gold nanoparticle conjugate (Lane 2) and external noise exposed DNA Aptamer-AuNP conjugate band (Lane 3). Using noise power $K = 3.44 \times 10^5 \text{ m}^2/\text{s}^3$ on the aptamer-AuNP band during electrophoresis, the mobility of the band increases (Lane 3).	145
5.4.	A schematic representation of the detection procedure in the developed point-of-care (POC) aptasensor prototype.	147
5.5.	(A) TEM image of pristine gold nanoparticles and (B) TEM image of Apt-AuNP conjugate. Plot (C) demonstrates the UV spectra of the pristine AuNP and the Apt-AuNP matrix. The aptamer peak at $\lambda \sim 260 \text{ nm}$ (inset) also confirms the aptamer binding to the nanoparticle surface. Plot (D)	148

	<p>shows the average particle size of the synthesized AuNPs and the Apt-AuNP conjugate. Plot (E) shows the zeta potential of the pristine AuNPs and Apt-AuNPs. The error bars in plots (D) and (E) indicate the standard deviation of the particle sizes obtained from 4 separate experimental studies.</p>	
5.6.	<p>(A) TEM image of the Apt-AuNP conjugate attached on the surface of <i>K.pneumoniae</i>. (B) TEM image of Apt-AuNP not adhered to the non-target analyte (<i>E.coli</i>). Plot (C) shows the UV spectra of <i>K.pneumoniae</i> (range: 10^2-10^8 CFU/mL). With increasing concentration, the absorbance is also increasing as depicted in the figure. (D) and (E) shows the optical images taken at bright light and UV light (365 nm) respectively. D1, D2 and E1, E2 denote AuNP and Apt-AuNP matrix respectively. D3-D9 and E3-E9 denote the optical images of <i>K.pneumoniae</i> solution with increasing concentration ranging from 10^2-10^8 CFU/mL in Apt-AuNP matrix. UV-Vis spectra of <i>K.pneumoniae</i> (range: 10^2-10^8 CFU/mL) spiked into non-specific aptamer-AuNP conjugate along with the corresponding optical images are shown in the Figure 5.7. Very light pale red as appears in D2 and E2 are illusive, this is due to the reflection from dark red AuNPs in nearby cuvette D1 and E1. (Please refer Figure 5.7.)</p>	149
5.7.	<p>Plot (A) shows the UV spectra of <i>K.pneumoniae</i> (range: 10^2-10^8 CFU/mL) spiked into a non-specific Apt-AuNP. With increasing <i>K.pneumoniae</i> concentration, the absorbance change is null as depicted in figure (A). (B) and (C) show the optical images taken at a bright light and UV light (365</p>	151

	<p>nm) respectively. B1, C1 denote AuNP, and B2, C2 show non-specific Apt-AuNP matrix respectively. B3-B9 and C3-C9 denote the optical images of the non-specific Apt-AuNP matrix spiked with <i>K.pneumoniae</i> solution of increasing concentration ranging from 10^2-10^8 CFU/mL. Lower panels of figure (B) and (C) represent the same cuvettes except the cuvette containing AuNP (B1 and C1). Thus, the B2 (Apt-AuNP) in the lower panel appears almost colorless as the reflection from the nearby B1 cuvette (red in color) is missing. The photograph is illusive (due to vicinity of the dark red AuNP solution), thus UV-Vis spectroscopy is shown in figure (A).</p>	
5.8.	<p>Plot (A) shows the Raman spectra of pristine AuNPs and Apt-AuNP conjugation. Since, the particles are stabilized by citrate molecules, the peaks corresponding to the presence of citrate are mentioned in the plot. The presence of trisodium citrate is depicted by a peak at 830 cm^{-1} signifying $\nu(C - C)$, peak at 943 cm^{-1} signifying $\nu(C - COO)$, peak at 1257-1282 cm^{-1} signifying $\delta(COO)$ and peak at 1406 cm^{-1} demonstrating $\nu_s(COO)$. Plot (B) denotes the Raman spectra when Apt-AuNP attaches to <i>K.pneumoniae</i> (orange). The peaks at 898 cm^{-1} and 1078 cm^{-1} (highlighted in the plot) conform attachment to the target analyte (orange line). The pink line depicts Raman spectra when a non-target analyte (<i>E.coli</i>) was dispensed into the Apt-AuNP matrix conforming to no such specific signatures.</p>	152

5.9.	<p>Plot (A) shows the UV Vis spectra when a cocktail of non-target analytes (<i>E.coli</i>, <i>S.aureus</i>, and <i>E.faecalis</i>) was mixed and dispensed into the Apt-AuNP matrix denoted by A1. The bacterial concentration of <i>E.coli</i>, <i>S.aureus</i>, and <i>E.faecalis</i> was fixed at 1×10^5 CFU/mL in each case. Plot (B) shows the UV spectra when mixed analytes comprising <i>K.pneumoniae</i>, <i>E.coli</i>, <i>S.aureus</i>, and <i>E.faecalis</i> was dispensed into the Apt-AuNP matrix denoted by B1. The bacterial concentration of <i>K.pneumoniae</i>, <i>E.coli</i>, <i>S.aureus</i>, and <i>E.faecalis</i> was fixed at 1×10^5 CFU/mL in each case. Due to the attachment of <i>K.pneumoniae</i>, a response with an increase in UV absorbance occurs.</p>	154
5.10.	<p>Plot (A) shows the response of the device for different types of LEDs, green LED (green inverted triangle), blue LED (blue diamond), white LED (hollow white square), red LED (red polygon), and yellow LED (yellow inverted triangle). Green LED shows the best response for aptasensor detection having wavelength (510-555 nm). Plot (B) shows the specific response of the aptasensor towards target analyte <i>K.pneumoniae</i> detection using green LED. The aptasensor shows negligible response towards <i>E.coli</i>, <i>S.aureus</i>, and <i>E.faecalis</i>.</p>	156
5.11.	<p>Plot (A) shows the aptasensor response when healthy fresh urine is spiked with increasing concentrations of <i>K.pneumoniae</i> (10^2-10^8 CFU/mL) using identical volume. Plot (B) shows the aptasensor response when <i>K.pneumoniae</i>, <i>E.coli</i>, <i>S.aureus</i>, and <i>E.faecalis</i> were spiked into fresh healthy urine. The readings were taken within laboratory premises. [A-</p>	157

	Blank, B- <i>K.pneumoniae</i> , C- <i>E.coli</i> , D- <i>S.aureus</i> , E- <i>E.faecalis</i> , F- <i>E.coli</i> , <i>S.aureus</i> & <i>E.faecalis</i> mixed together]. The concentration of the respective bacteria was 1×10^5 CFU/mL in each case. The error bars in the diagram indicate the standard deviation of the readings obtained from 4 measurements with the aptasensor.	
5.12.	Plot shows the POC aptasensor response using a non-specific aptamer sequence SABA11 (5'-/5ThioMC6-D/GGC TGG ATG GGG CGT GTT GAT TCG AGT CGG AGA CGG CAT CCT GCA CAA ATG CCA ACG GTG CGG ACA GCG-3'). The aptamer used is non-specific for <i>K.pneumoniae</i> but specific to <i>S.aureus</i> . <i>K.pneumoniae</i> , <i>E.coli</i> , <i>S.aureus</i> , and <i>E.faecalis</i> were spiked into fresh healthy urine. The readings were taken within laboratory premises. [A-Blank, B- <i>K.pneumoniae</i> , C- <i>K.pneumoniae</i> and <i>E.coli</i> mixed, D- <i>K.pneumoniae</i> , <i>E.coli</i> , and <i>E.faecalis</i> mixed, E- <i>S.aureus</i>]. The concentration of the respective bacteria was 1×10^5 CFU/mL in each case. The error bars in the diagram indicate the standard deviation of the readings obtained from 4 measurements with the developed aptasensor prototype.	159
5.13.	Plot (A) shows the calibration curve for the <i>K.pneumoniae</i> concentration ($(1-11) \times 10^5$ CFU/mL as a function of normalized resistance. The inset shows the calibration curve for the <i>K.pneumoniae</i> concentration ($(1-11) \times 10^4$ CFU/mL as a function of normalized resistance. Plot (B) shows the comparison of clinical results (obtained from a GNRC hospital) from UTI patients with the results obtained from the optical device developed	163

	<p>in this work using the calibration curve. Plot (C) shows the aptasensor results taken from the clinical UTI patient samples (OPD) within GNRC hospital premises. The signal change was found only in the case of a positive <i>K.pneumoniae</i> infected urine sample which was also confirmed by the hospital reports. [A- Blank, B- <i>K.pneumoniae</i>, C- Sterile, D- <i>E.coli</i>, E- <i>S.aureus</i>, F- <i>P.aeruginosa</i>, G- <i>C.freundii</i>, H- <i>C.koseri</i>, I- <i>P.vulgaris</i>, J- <i>Enterococcus species</i>, K- <i>Candila species</i>]. The error bars in the diagram indicate the standard deviation of the readings obtained from 4 measurements with the help of the aptasensor.</p>	
5.14.	<p>Demographic data corresponding to validation of aptasensor prototype. Table (A) and (B) shows the statistical variations (age, sex, symptoms) of the suspected UTI patients from which the urine samples were collected. Table (C) and (D) shows the statistical confidence level analysis from the collected UTI patient samples from GNRC hospital.</p>	164
5.15.	<p>Absolute resistance ($k\Omega$) as a function of <i>K.pneumoniae</i> concentration (CFU/mL).</p>	166
5.16.	<p>Stability of the aptamer-AuNP matrix response of the device for a particular concentration of <i>K.pneumoniae</i> (1×10^5) CFU/mL over the period of 8 weeks. The error bars in the figure indicate the standard deviation of readings obtained during the measurement of the same sample three times with our aptasensor.</p>	167
5.17.	<p>Streaked CLED agar plates of different pathogenic bacteria causing UTI. The streaking was done within GNRC hospital laboratory premises.</p>	167

5.18.	Schematic representation of the detection procedure of the target analyte (<i>K. pneumoniae</i>) using the developed Apt-AuNP assay. (A), (B), (C) and (D) represents the AuNPs, Apt-AuNP assay, <i>K. pneumoniae</i> (10^3 CFU/mL) binding with Apt-AuNP and high concentration of <i>K. pneumoniae</i> (10^8 CFU/mL) binding with Apt-AuNP respectively. Inset shows the respective sequence of TEM images. A1, B1, C1 and D1 demonstrates the bright field and UV light (~ 365 nm) exposed images of AuNP, Apt-AuNP assay, <i>K.pneumoniae</i> (10^3 CFU/mL) bound Apt-AuNP assay and <i>K.pneumoniae</i> (10^8 CFU/mL) bound Apt-AuNP assay respectively. A2, B2, C2 and D2 demonstrates the respective UV-Vis spectroscopy of the above-mentioned sequence.	168
A.1.	A typical Model of Brownian motion.	190
A.2.	Schematic representing the skewness of a distribution	192
A.3.	Semi-Log plot of input noise in the form of voltage pulses.	193
A.4.	Power spectrum of input white noise.	194

List of Tables

Section No.	Description	Page No.
5.3.8	Estimated Cost of the point-of-care Aptasensor	159
5.3.8	Description of components used for device fabrication	160



Contents

Topic	Page No.
<u>CHAPTER 1</u>	1
1.1. Motivation for current research	2
1.2. Literature review	4
1.2.1. Noise induced motion in nature	4
1.2.2. Noise driven polymer dynamics	8
1.2.3. Overview on gel electrophoresis.....	13
1.2.4. Polymer translocation through nanopore	17
1.2.5. Thesis overview & Objectives	21
References.....	23
<u>CHAPTER 2</u>	43
ABSTRACT.....	45
2.1. Introduction.....	46
2.2. Materials and Methods.....	47
2.2.1. Materials.....	47
2.2.2. Preparation of Gel.....	47
2.2.3. Estimation of Pore Size.....	48
2.2.4. Instrument.....	48
2.2.5. Experimental Procedure.....	49
2.3. Results and Discussion.....	50
2.3.1 Noise activated DNA translocation.....	50
2.3.2 Noise Characterization.....	54
2.3.3 Details of the numerical simulation.....	56
2.3.4. Modified Langevin Model.....	57
2.3.5. Escape rate of the DNA molecule.....	65
2.4. Conclusions.....	66
References.....	67
<u>CHAPTER 3</u>	72
ABSTRACT.....	74
3.1. Introduction.....	75

3.2. Materials and Methods.....	77
3.2.1. Materials.....	77
3.2.2. Preparation of Gel.....	78
3.2.3. Experimental Methodology.....	78
3.2.4. Instruments used	80
3.3. Results and Discussion.....	80
3.3.1. Simulation model.....	80
3.3.2. Role of solid friction.....	83
3.3.3. Noise assisted DNA translocation through nanoporous matrix.....	86
3.3.4. Modified Langevin equation for predicting DNA mobility.....	89
3.3.5. Displacement trajectories tracked using simulation model.....	91
3.4. Conclusions.....	94
References.....	96
<u>CHAPTER 4</u>	101
ABSTRACT.....	103
4.1. Introduction.....	104
4.2. Materials and Methods.....	107
4.2.1. Materials.....	107
4.2.2. Preparation of gel.....	107
4.2.3. Instruments used	108
4.2.4. Experimental Procedure.....	109
4.3. Results and Discussion	109
4.4. Conclusions and Final remarks	117
References.....	118
<u>CHAPTER 5</u>	128
ABSTRACT.....	131
5.1. Introduction	132
5.2. Materials & Methods.....	135
5.2.1. Reagents.....	135
5.2.2. Instruments used	135
5.2.3. Phosphate saline buffer.....	136
5.2.4. Gold nanoparticle synthesis	136
5.2.5. Bacterial Culture	136

5.2.6. Aptamer development by Cell-SELEX	137
5.2.7. Preparation of aptamer modified AuNPs.....	140
5.2.8. Optimization of the Apt-AuNP parameters.....	141
5.2.9 Transmission Electron Microscopy study.....	142
5.2.10. Preparation of samples for Raman analysis	142
5.2.11. Specificity assay for target analyte detection.....	143
5.2.12. Development of aptasensor.....	143
5.2.13. Detection of <i>K.pneumoniae</i> in clinical urine samples.....	143
5.2.14. Agarose gel preparation & Experimental Procedure.....	144
5.3. Results & Discussion.....	144
5.3.1. Detection mechanism using gel electrophoretic study.....	144
5.3.2. Detection mechanism.....	146
5.3.3. Characterization.....	152
5.3.4. Specificity study	153
5.3.5. Aptasensor Prototype Fabrication	154
5.3.6. Selection of the LED	155
5.3.7. Specificity of the aptasensor	157
5.3.8. Cost estimation & Description of components.....	159
5.3.9. Calibration & Clinical Trial.....	162
5.3.10. Limit of detection & Stability analysis of aptasensor.....	165
5.3.11. CLED Agar culture of uropathogens.....	167
5.3.12. Summary of the detection mechanism.....	168
5.4. Conclusions.....	169
References.....	170
<u>CHAPTER 6</u>	180
6.1. Summary.....	182
6.2. Future Scope.....	185
<u>Appendix-A</u> : Definitions regarding stochastic dynamics regime	189
<u>Appendix-B</u> : Curriculum Vitae of Dr. Aniruddha Deb	197



CHAPTER 1

Introduction

Contents

1.1. Motivation for current research	2
1.2. Literature Review	
1.2.1 Noise induced motion in nature	4
1.2.2 Noise driven polymer dynamics.....	8
1.2.3 Overview on gel electrophoresis.....	13
1.2.4 Polymer translocation through nanopore.....	17
1.2.5 Thesis overview & Objectives.....	21
References.....	23

1.1. Motivation for current research

“As our cause is new, so must we think anew and act anew”—Abraham Lincoln

Natural systems are frequently perturbed by chance (noise). For a realistic representation of natural system, it is critical to explore the impact of noise on the system's dynamic behavior. Noise may cause a variety of intriguing consequences. Many biological processes involve the translocation of biomolecules through nanosized pores, such as the movement of proteins across membrane channels and DNA and RNA over nuclear pores^{1,2}. An external driving force is necessary to get past a significant entropic barrier during transit through nanopores and to guarantee rapid translocation. For the separation and purification of synthetic as well as biological macromolecules, electrophoresis and the forced motion of polymer molecules are essential. Food, medicine and most of other industries are associated with separation process that involves motion of an entity through some medium and exhibits resistance. For example, chromatographic separation process³ also involves motion of mobile phases through a stationary phase and the different retention time for different components determines the separation efficacy. Scientists have become very interested in polymer translocation, studying its underlying physics through experiments⁴⁻⁹, hypotheses¹⁰⁻¹⁸, and numerical simulations¹⁸⁻²⁵. The impact of noise on cell biology has attracted a surge of research during the past two decades. Rapid improvements in experimental techniques, including high-resolution imaging and molecular-level probes, have driven this. Random perturbations can enhance detection and support the emergence of noise prowess in weak non-linear systems. But since noise is so commonplace and pervasive, some fundamental issues are posed. Some examples relating can be described as:

- ❖ How does noise affect the behaviors of an entity at the molecular and cellular levels?

- ❖ How have single or multiple clusters of organisms evolved to respond to noise to enhance their productivity/performance?

In light of these growing questions, mathematical biologists need to use statistical physics and stochastic dynamics to solve these problems within the context of cell biology. In the present thesis, we seek to model our experiments by imposing external noise to macromolecules and embracing the question:

- ❖ How does an external noise affect a biomolecule's dynamics when friction occurs at the moving body's interface?
- ❖ What will happen whether or not the underlying friction is linear?

So, to address these questions, we have developed our experiments to address the translocation of macromolecular chains through nanoporous gel using external Gaussian noise to inhibit the effect underneath solid frictional forces. This frictional study may help explain various biological transport mechanisms that take place inside the cell. A relevant experiment also shows that while a colloid particle diffuses quickly along a microtubule made of a linear phospholipid bilayer, the displacement distribution is exponential rather than gaussian²⁶ which readily suggests the presence of non-linear friction in the system. According to the authors, this type of transport procedure resembles the activated diffusion seen in glassy systems. In this dissertation, we attempted to explore the cause of the frequent occurrence of such exponential displacement distributions in dynamic processes.

1.2. Literature Review

Numerous examples of non-equilibrium stochastic dynamics can be found in natural phenomena²⁷. According to a survey of the literature, such processes may be fully characterised by employing transition probabilities that fulfil the Fokker-Planck equation. The factors involved in this study of non-linear stochastic systems pave the way for a particular macromolecule (DNA) translocation method through nanoporous gels. A few examples of noise-induced mobility in nature is covered in Section 1.2.1. Section 1.2.2 discusses the physics behind noise-assisted polymer dynamics and concurrent entropic barrier crossing. Section 1.2.3 discusses the principles of Agarose Gel electrophoresis, pore size, and related biological applications. The physics behind the translocation of a polymer chain through a nanopore and its applications are covered in Section 1.2.4. The overall thesis outline and goals of our current research are elaborated in Section 1.2.5.

1.2.1. Noise induced motion of macroscopic objects in nature

This dissertation's primary focus is the investigation of noise-induced motion of macromolecules within an electrophoretic gel framework. Our study was inspired by natural phenomena such as rainwater pouring down on a window pane and cereal flowing from a package to a bowl. The macroscopic examples from nature are dominant, but our investigations are also greatly inspired by the dynamics of colloidal particles and molecules through cells²⁸.

The phenomenon known as stochastic resonance (SR) describes the circumstance where an increase in input noise enhances a system's awareness to distinguish between weak²⁹ and strong signals. Accordingly, it belongs to the more significant phenomena category where random fluctuation's positive effects can be observed. Over the past three decades, intense study on stochastic resonance has mostly been conducted in physics, but more recently, in biology. At least

as early as 1991^{30,31}, the idea that SR may have an impact on biological systems was considered. The most important research that appeals to the reader is the intriguing and challenging paper by Chialvo and Apkarian³². Because of their typically high noise levels, sensory neurons can sometimes function as threshold devices or excitable systems. This naturally raises the question of whether or not SR may explain certain animal's extraordinary sensitivity to detect faint coherent signals contained in a noisy environment. Results generated from studies on the mechanoreceptor hair cells of the crayfish *Procambarus clarkii* were published in 1993 by Douglass et al³³. These cells are utilized to identify coherent water movements, such as those brought on by a predator's approach. In their studies, an electromechanical transducer was driven by both coherent and random signals from signal and noise generators, causing the hair cell mobility through the saline environment. Electrophysiological recordings were seized from a single cell activated with a weak stimulus. Most cells had unmistakable signs of SR. A basic theoretical model of a neuron and numerical data from an electrical analogue simulation of the Fitzhugh-Nagumo equations demonstrate SR's distinctive hallmark. In studies using cutaneous mechanoreceptors from mammals, Collins et al.³⁴ showed SR. They employed a small-area tip to deliver mechanical stimulation to an in-vitro preparation of isolated rat skin. A regular (albeit aperiodic) component and a noisy part made up this input stimulus. Cross-correlation revealed a positive relationship in 11 of the 12 examined neurons peak in relation to the intensity of the input noise. The cercal system of the domestic cricket *Acheta domestica* has been the subject of experiments by Levin and Miller³⁵, and these studies have likewise revealed SR. This invented mechanosensory system can detect modest, low-frequency air disturbances.

Research in the rapidly expanding subject of microfluidic device development, or MEMs (Micro Electromechanical Systems), finds application in a wide range of disciplines, including medicine,

computational & robotic engineering, and so forth. Controlling the mobility of tiny droplets in a microfluidic device or manipulating particles on a surface requires a thorough understanding of the interaction between the two substances at their interface. In essence, this contact caused friction (or hysteresis in the case of liquid-solid interactions), which causes energy loss in thermodynamically open systems while also being a crucial part of an object's motion. To move liquid drops that are stuck on solid surfaces, researchers have focused on several routes³⁶⁻⁴⁰. Several methods were developed, and external vibration-aided motion succeeded in this aspect. Researchers have successfully demonstrated that the drop motion vibration minimizes the hysteresis effect. The ability of external vibration to move water drops stuck to a temperature gradient surface has been established by Mettu et al.⁴¹. When exposed to periodic vibration, a liquid drop attached to a thermal gradient surface due to contact angle hysteresis moves quickly. The physics behind this event has been described in terms of the contact angle created by the drop and the accompanying equilibrium statistics. When an external force deforms a drop, the drop enters a non-equilibrium condition⁴². A liquid drop becomes caught in one of the metastable phases as a result of the non-ideality of a solid surface. When a drop is exposed to vibration energy^{38-40,43,44}, it can break free of its metastable condition and achieve a state of global equilibrium. The macroscopic features of an equilibrium system are the focus of classical thermodynamics, and an assembly of several tiny particles governs them. A new method of investigating the nature of these minuscule particles is required to advance the molecular theory of matter. The oscillations of the molecule's dynamic characteristics become crucial at this tiny scale to explain various macroscopic features⁴⁵. The theory that may be used to examine the behavior of spontaneous and natural fluctuations is statistical mechanics⁴⁶. Fluctuations of the molecules encrypt the energy states of the system, and the study of statistical mechanics provides the key to unlocking the code.

This approach was used to study the dynamic behavior of a macroscopic molecule in this thesis. A stochastic process is how a system reacts to random input variables. The output is defined by either a stochastic velocity or displacement. Whether the dynamic system is linear or non-linear, the variation in displacement and velocity encodes the dissipative character of the system. A system in thermal equilibrium with its surroundings is the focus of well-researched and well-established equilibrium thermodynamics. Certain properties of equilibrium systems apply to them but not to non-equilibrium ones. The most stable and preferable state of an equilibrium system is determined by the global reduction of free energy. Regardless of the system's original condition, this state will ultimately be reached. This sort of straightforward energy minimization approach is unable to describe a system that is pushed out of equilibrium by an external force field. In recent years, there has been a lot of interest in understanding non-equilibrium systems, however this interest is not yet completely realised. Morris, Cohen, and Evan⁴⁷ provided significant work in this line, identified the apparent violation of the prevalent second law of thermodynamics in non-equilibrium steady-state systems and developed the fluctuation theorem, a relationship between the likelihood of entropy creation and consumption. The resonance frequency of the drop is another crucial factor in drop motion on a solid surface when it is susceptible to external vibration since it greatly influences velocity. According to studies by Kelvin⁴⁸, Rayleigh⁴⁹, Lamb⁵⁰, and Chandrasekhar⁵¹, a drop can display a variety of resonance modes depending on the mass and surface tension of the liquid. Due to this Stochastic Resonance⁵² (SR) composition, there has recently been conjecture that it may have some biological purpose⁵³. Henceforth a polymer chain undergoing activated crossing over a barrier helps explain why double well illustration within Kramer's framework is physically possible^{54,55}, which seems like a strange occurrence at first. The

particle is trapped in one well indefinitely in the absence of noise. It can occasionally hop over the barrier due to the noise^{56,57}.

1.2.2. Noise-driven polymer dynamics (Barrier Hopping and Role of activation energy)

Biological applications⁵⁸, including the transport of macromolecules through bio-membranes and DNA gel electrophoresis rely on the dynamics of polymers overcoming barriers, which is not just a fundamental topic in soft matter physics. Since the original publication by Kramer's^{58,59}, there has been a growing interest in the escape from metastable situations⁶¹. It may be observed in various natural systems, including chemical systems, spin systems, quantum liquids, polymers, and transport problems in intricate systems like glasses and proteins. The dynamics of complex non-equilibrium systems, such as molecular dissociation in strongly coupled chemical systems, electron transport in a quantum double-well structure, microstructures, lasers, Josephson junction devices, ratchet model development, ligand migration in proteins, and biological systems, are best described by the noise-triggered escape in systems with metastable states and fluctuating barriers^{60,62-64}. Each system is an open system with inherent non-linear dynamics that interacts with noisy circumstances⁶⁴, which causes noise-induced events.

In contrast to stochastic resonance, which is governed by deterministic barrier modulations, the continuous time translation symmetry is violated in these complicated non-stationary non-equilibrium systems⁶⁵. The use of noise to leave a metastable state with oscillating or fluctuating barriers has grown in favor recently^{57,66-68}. Researchers including Lacks et al.⁶⁹, Evans and Ritchie⁷⁰, Schallamach⁷¹, and Garg⁷² demonstrated the dissociation kinetics of polymer chains within the Kramer's framework. Garg⁷² was the first scientist to demonstrate that the pre-exponential frequency factor also changes with the applied load in addition to the barrier height.

The force-modulated frequency and barrier energy factors in the Kramers equation were then employed in a number of studies⁷³⁻⁷⁵ to model the linear loading rate dissociation kinetics of polymer chains in the manner of Evans and Ritchie⁷⁰ and Schallamach⁷¹. Inspired by their studies, the average overall frequency of a soft sphere breaking off from a rigid surface (assuming the presence of linear friction) is defined as follows:

$$v = \left[\frac{\tau_L}{2\pi} \omega_1(P) \omega_2(P) \right] \exp\left[\frac{2\Delta U(P)}{mK\tau_L} \right] \dots \dots \dots (1)$$

Equation (1) depicts the celebrated Kramer's equation within a strong friction regime⁷⁶ where τ_L demonstrates the Langevin relaxation time, $\Delta U(P)$ is the barrier height and m is the mass of the sphere. The strength of the Gaussian white noise K is represented using (m^2/s^3). $\omega_1(P)$ and $\omega_2(P)$ are defined as frequencies close to the energy potential's highest and lowest values and follow its curve. In macroscopic systems, the random noise may be ambient or thermal in nature.

In many instances, an extra periodic driving force or some external random perturbations pull the system away from thermal equilibrium⁷⁷. While theoretically and statistically significant, analytical progress towards the theory of oscillating barrier crossing is challenging⁷⁸. The increase of stability by thermal noise in systems with a metastable state and a sporadically driven potential is an intriguing phenomenon that appears in the weak noise domain^{79,80}. This noise enhancement stability (NES) characteristic has been found experimentally and statistically in various physical systems⁸¹⁻⁸⁵. According to research, increasing the magnitude of the thermal noise strength causes a reduction in the mean lifespan of the metastable phase of a physical system. The improved stability shows that the system stays in the metastable state for longer than it would be without noise. According to Kramer's formula⁵⁹, the mean initial passage time of a Brownian particle

propagating in potential fields comprising a reduction in metastable and unstable states with increasing noise power :

$$\tau_k = A \times e^{\Delta U/q} \dots\dots\dots (2)$$

A is a pre-factor in eq. (2) that depends on the curvature of the potential at the metastable state and height of the potential barrier of ΔU , and $2q$ is the noise intensity. However, the reliance of the mean first passage time (MFPT) on noise intensity was shown to exhibit resonance character with non-monotonic behavior for unstable or oscillating metastable states. This is the so-called NES phenomenon: noise can affect the system's stability. In contrast to the deterministic situation, a system remains in an unstable or oscillating metastable state for longer when noise is present. The escape time as a function of noise strength approaches a maximum. Dayan et al. theoretically examined an overdamped Brownian particle's transient dynamics in a time-dependent cubic potential with a metastable state. A wide variety of control parameter values enhance system stability, as demonstrated numerically⁸⁰. The author's primary hypothesis was that increasing the magnitude of the noise would reduce the mean escape time because noise drives the particle to explore more of the accessible area than if there was no noise. The particle is forced to sample a larger portion of the accessible area as a result of noise than would be the case in a system without noise; therefore, one's initial instinctive reaction about such a system is that an increase in the noise amplitude should reduce the mean escape time. However, their simulation investigations revealed that when the frequency of the periodic driving force is suitably adjusted, the escape time increases as the noise intensity increases. This showcased that noise can alter the system's stability unexpectedly. Mantegna and Spagnolo^{79,86-90} dubbed this phenomenon as Noise Enhancing Stability (NES), and it results in a non-monotonic behavior of the average escape time as a function of the noise level. The NES phenomenon was seen experimentally by measuring the escape time

from a time-modulated physical apparatus known as the tunnel diode^{87,88}. The NES effect appears when there is a significant driving force in potential profiles with metastable states. The absence of the potential barrier for a limited period characterizes the dynamical domain; hence, the system is generally deterministically unstable. Due to the interplay between the noise and the time-dependent driving force after this period, the Brownian particle may return to the potential well⁷⁹. In contrast to the dynamic lifetime, the mean lifetime of the metastable state rises with noise intensity. Studies have shown that the average escape time does not behave in a monotonic manner as a function of noise intensity. They have also demonstrated a unique and fascinating dynamical regime that is characterized by the average escape time diverging into an exponential Kramers-like behaviour⁷⁹. In particular, Wackerbauer⁸³ examined how switching processes in one-dimensional discontinuous mappings, such as the piecewise linear map, the Lorenz map, and the piecewise linear Lorenz map, were affected by dynamical noise. The main finding is that all Lorenz-type map's switching dynamics are significantly reduced by dynamical noise. This loss is mainly caused by the noise-induced escape of a typical route into an attractor zone that isn't as regularly visited. This results in noise-induced stabilization or an increase in mean passage time. As a result, there is an increase in mean passage time or noise-induced stabilisation⁸¹. Discoveries in the transient dynamics of a modulated metastable system, which displays the NES phenomenon, are associated to several noisy Lorenz system properties. Yoshimoto⁹¹ showed in recent studies that when noise lengthens the laminar zone, one type of noise-induced order manifests itself as intermittent chaos. Xie and Mei⁹² investigated the transient features of a bistable kinetic system driven by two correlated noises: an additive noise and a multiplicative colored noise. A bistable kinetic system driven by two correlated noises, an additive noise and a multiplicative colored noise, was the subject of Xie and Mei's⁹² investigation. They found a one-peak pattern in the mean

first passage time (MFPT) as a function of noise level for strongly correlated sounds, suggesting that increasing noise intensity lengthens the average escape time.

The investigation of the noise-induced effects on the dynamics of a chain molecule traversing a potential barrier in the presence of a metastable state was provided by N.Pizzolato et al.⁹³. To simulate molecular dynamics and account for interactions between nearby monomers, a two-dimensional stochastic version of the Rouse model for a flexible polymer was used. With increasing noise intensity, researchers found a non-monotonic behavior of the mean first passage time, its standard deviation, and the polymer center of inertia. The research on barrier crossing in arrays of components (molecules) has received fresh attention within the biological setting due to noise⁹⁴, and it appears that performance may be increased overall by adjusting the noise level.

Nan Shi et al.⁹⁵ depicted that accelerated mobility and decreased diffusion can be combined in a resonance state by changing the applied electric field at a frequency suited to the typical activation timeframe in practical settings (e.g. electrophoretic separation of DNA). By accurately regulating the strength and duration of the driving electric field, it is possible to improve separation performance and enable the bi-directional transport of different-sized biomolecules. The fact that these phenomena are easily accessible in regular hydrogels as opposed to idealized nanomachined topologies suggests a wide range of possible applications.

1.2.3. Overview on Gel electrophoresis techniques

Physics in the 21st century is a broad approach to comprehending the material universe rather than a specific collection of regimens and methodologies. The purpose of physics is to unravel the description of the basic building blocks of the material universe and their interactions. When biological sciences are applied, the establishment of empirical analysis and mathematical modelling enhances. D'Arcy Wentworth Thompson⁹⁶ studied a geometric model for the animal form, and Hermann Walther Nernst⁹⁷ provided the framework for present research of membrane potentials and ion channels. Watson and Crick⁹⁷ used x-ray crystallography, a physics and chemistry method, to discover the structure of deoxyribonucleic acid (DNA). In recent decades, many biophysicists are now fascinated by investigating the physical basis of specific molecule's biological function⁹⁸⁻¹⁰⁰, molecule motion¹⁰¹⁻¹⁰³, the mechanisms of cellular micro organelles¹⁰⁴, and refining traditional approaches to investigate these frameworks in greater detail¹⁰⁵⁻¹⁰⁷. The focus of this dissertation was on improving current procedures by including variations in the physical system. The ability to do molecular separation has been a significant tool in biophysics. The separation process is critical in biotechnology, genetics, and medicines. Reuss¹⁰⁸ originally summarized electrophoresis in a study published in 1809, where he observed clay particle electrophoresis across a layer of quartz. Almost all surfaces were found to charge when they came into contact with an aqueous solution during electrophoresis. In 1937, Tiselius¹⁰⁹ created the first advanced electrophoretic device. Electrophoresis was extensively applied and adapted to molecules, from proteins to amino acids, during the 1940's and 1950's. During the 1970's, there was a boom of interest in deoxyribonucleic acid (DNA) electrophoresis. Researcher Joseph Sambrook headed a Spring Harbor Laboratory team that improved DNA electrophoresis with agarose gels in 1973¹¹⁰. This has led to several new ideas and findings on DNA mobility^{111,112}.

The utilization of electrophoresis in randomly cross-linked hydrogels such as polyacrylamide or agarose is commonly used to separate molecules. Biologists and biochemists use agarose gel medium for the electrophoretic separation of DNA.

Furthermore, because of the consistency of the developed matrix created in an agarose gel, the position of DNA inside the gel may be detected immediately. Agarose gels were utilized in all of the experiments mentioned in our thesis. To assess the effective pore size of agarose gels, Ferguson plots¹⁰¹ (log mobility vs. gel concentration) of DNA macromolecules of various sizes can be employed. A 1% agarose gel was found to have a median pore radius of about 100 nm¹¹³, which is comparable to the pore diameters discovered by prior electrophoretic experiments^{114–116}. However, the method employed to calculate it has some bearing on the projected gel pore radius. Agarose gel pore radii predicted by DNA gel electrophoresis lattice models are typically 2-fold lower than those anticipated by Ferguson plot techniques^{116,117}.

Noolandi et al.^{118,119} identified a non-monotonic reliance on "band-inversion" in lengthy monomer segments separated at higher gel concentrations and electric fields. The precise transport mechanism, and hence the shape of the mobility dependency on length, is a complex function of the electric field strength and the gel pore size in relation to the appropriate DNA size. Researcher's proposed mechanisms for DNA electrophoresis in gels including elementary Ogston sieving^{120–122} (for small DNA molecules), entropic trapping^{98,100,123,124}, prevalent biased reptation^{125–127}, reptation with random fluctuations^{128–130}, reptation with chain stretching^{125,131,132}, and the well-established reptation model¹³³. According to the postulated processes for DNA electrophoresis, electrophoretic mobility varies with length. Lumpkin and Zimm et al.¹³⁴ devised an adaption of the well-established reptation model (first presented by de Gennes¹²⁷) that electrophoretic mobility was inversely proportional to length. Rodbard and Chrambach¹²¹ extended the Ogston model¹²⁰ by

linking a molecule's elementary Ogston sieving motion in a porous network to DNA electrophoresis. Gel electrophoresis for molecule separation creates a sequence of hurdles or impediments in the form of friction when moving through gel pores.

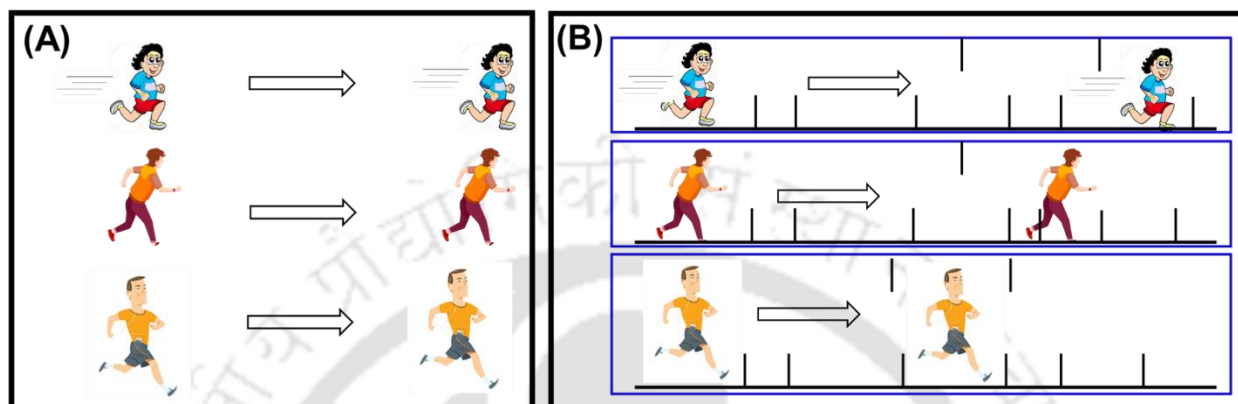


Figure 1.1. The left schematic (A) depicts the physical picture analogous to free solution electrophoresis. Here, the molecule translocation is size-independent. The schematic on the right (B) is analogous to gel electrophoresis. The obstacles in the path of motion (black solid lines) show the porous gel matrix picture. Smaller M.W. molecules traverse faster, whereas the larger M.W. molecules travels slower.

The Pulsed Field Gel Electrophoresis (PFGE) approach, developed by Schwartz and Cantor¹³⁵ in 1984, allows for the separation of DNA molecules bigger than 20 kbp and up to 5 Mbp in agarose gels, closing the gap between resolution (0.1- 30 kbp) and cytogenetic procedures (> 5 Mbp). PFGE uses giant DNA molecule's elongated and directed shape in agarose gels at limited field strengths. The simplicity with which the genome size is measured is a significant component of this technology, which can be prone to incorrect measurement using other techniques. PFGE has proved to be particularly effective in analyzing giant DNA molecules from a range of sources, including precisely fragmented genomic bacteria¹³⁶, mammals & reptiles¹³⁷, parasitic protozoans¹³⁸⁻¹⁴⁰, and entire chromosomal DNA's from fungus¹⁴¹⁻¹⁴³. The development of PFGE

methods for separating giant DNA molecules has energized research into the chromosomal DNA molecules, genomic structure, and electrophoretic theory. The switching interval duration and the direction of electric field orientation are two of the key drawbacks of PFGE. One such issue that has arisen as a result of the aforementioned PFGE elements is resolution loss. The demand for an innovative methodology that provide more detailed findings in molecular epidemiology investigations employing inexpensive and easy technologies that can screen more samples is urgent. The miniaturization of market-available procedures gives much-needed respite for biochemists screening DNA/Protein samples.

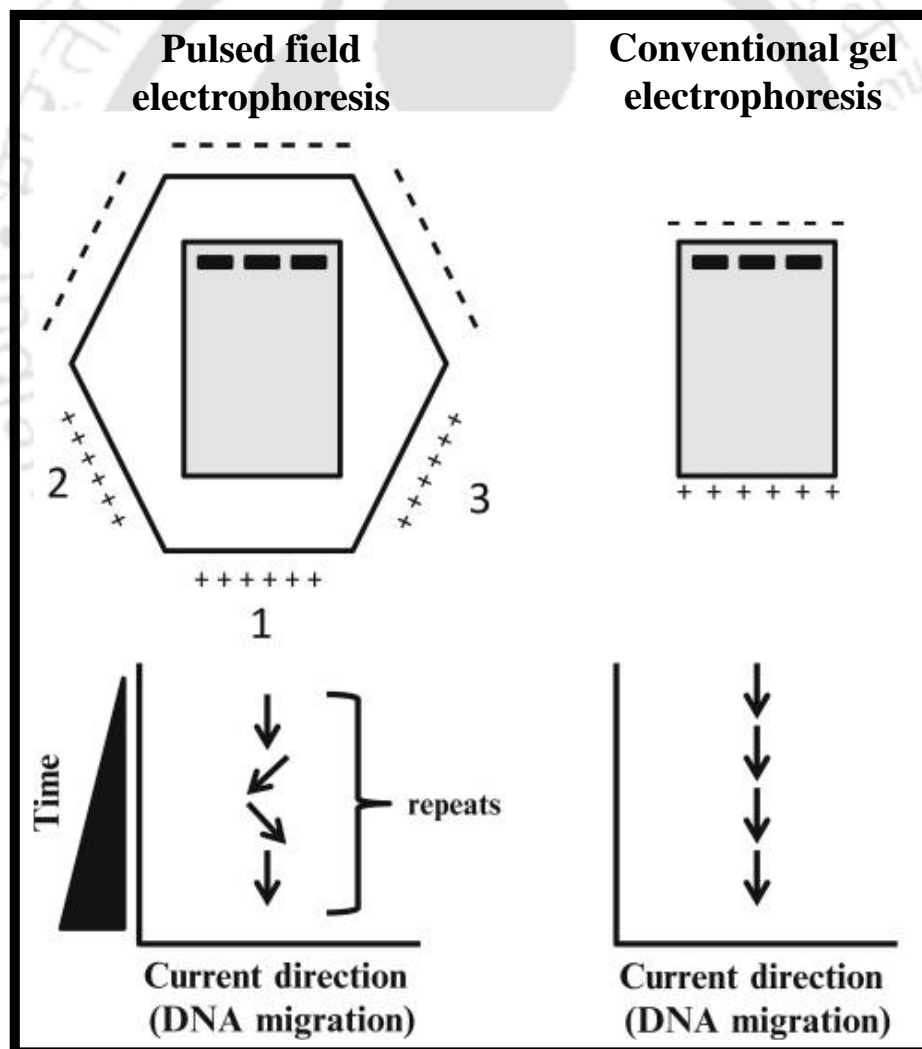


Figure 1.2. A physical representation of the PFGE versus Conventional gel electrophoresis^{144,145}. The gel (grey rectangle) is placed in a buffer in an electrophoretic chamber with anodes (+) and cathodes (-) (top diagrams). As represented in the bottom graphs, unlike conventional electrophoresis, where the biased voltage is unidirectional, PFGE cycles between several directions, allowing for more significant separation of DNA^{144,146}.

1.2.4. Polymer translocation through the nanoporous matrix

Soft condensed matter is the environment in which DNA and nanopores are situated. This field is situated at the scientific landscape's intersection of biology, chemistry, and physics. Two forms of force are primarily applied to DNA when it moves through nanopores: electroosmosis¹⁴⁷ and electrophoresis force¹⁴⁸. The mobility of the DNA molecule can be controlled by electrophoresis force or electroosmosis flow (EOF), depending on the geometry of the pore, the relative size, and the overall charge of the DNA molecule (for small pores). Here, we present a few examples of typical soft matter systems:

- ❖ Colloids are microscopic items or droplets suspended in a liquid. Depending on how effectively they interact with one another, they may operate as a transition between solid, liquid, and gas phases. These phase transitions are occasionally investigated in other systems as models for phase transitions.
- ❖ Polymers are long-chain compounds, and their behavior is primarily governed by configurational entropy.
- ❖ Gels are cross-linked networks of polymers that absorb a large amount of liquid. In a suitable solvent they can swell to several times their initial size.

Polymer translocation is fundamental in a wide range of biological activities, including mRNA transport via nuclear pore and micro-organism-based viral injection into a cell. This prevalent notion has been employed in nanopore sensing for the past two decades to detect, characterize, verify, qualify, or sequence biomolecules such as DNA/RNA, proteins, and other polyelectrolytes^{149–155}. Nanopores have been providing scientists with fascinating insights into the realm of single biomolecules for over 20 years. A nanopore is just an extremely small hole in a thin membrane with a diameter of a few nanometers. Researchers have investigated two key problems in DNA transport through nanopores. First, researchers have researched the pace at which molecules enter a nanopore and what physical factors limit their transit. Second, they investigated the electric conduction of a nanopore and how it is affected by the presence of a macromolecule.

Voltage-driven translocation was first used to measure and quantify viruses, nanoparticles, and blood cells¹⁵⁶. The notion of sequencing a single-stranded DNA molecule (ssDNA) using a nanopore originally surfaced in the 1980s¹⁵⁷. A series of studies were then carried out in the 1990s to verify the proof-of-concept idea^{4,6,7}. The intense translocation survey was sparked by the success in estimating the length and differentiating RNA from ssDNA using biological pores. To obtain the first nucleobase-level resolution, the ssDNA had to be held stationary in a α -HL nanopore¹⁵⁸. Due to the translocation rate being too high due to electric forces, nucleobase resolution detection cannot be performed. While this happened, sophisticated nanopore manufacturing methods were quickly developing, enabling the use of artificial solid-state nanopores. Solid-state nanopores may be made in various sizes and have more consistent mechanical, chemical, and thermal characteristics than biological pores¹⁵⁹. The use of translocation for sensing applications other than sequencing, including biological screening, medical diagnostics, and protein profiling, is

constantly being suggested^{153,155,160–162}. Another prominent area at the moment is the detection and analysis of tiny molecules like ions, biomarkers, aptamers, RNA, virus, or protein fragments¹⁵⁰. The fundamental idea is that stress propagates throughout the chain's conformation from the trapped end to the open end during a polymer chain's translocation. As a result, the initial conformation and friction in the nanopore affect the translocation time.

Further, it is challenging to investigate the capture process directly from experiments since it is not visible until the polymer penetrates the nanopore¹⁶³. By simulating the capture of DNA molecules by a cylindrical pore using Monte Carlo simulations, Nakane et al.¹⁶⁴ discovered that the capture rate is exponentially dependent on the applied electric potential at low fields but linearly dependent at high fields. Later, Chen et al.¹⁶⁵ used experimental data from the translocation of λ DNA through a solid-state nanopore under a micro-volt bias to confirm the linear dependency of the capture rate on voltage. The issue was later explored by Wong et al.¹⁶⁶ using analytical calculations, and they offered a different explanation for the decrease in long polymers near the nanopore that Chen et al. had seen. In the presence of external electric potential and salt gradients, Chou¹⁶⁷ analytically computed the steady-state electrokinetic equations to capture charged particles by nanopores. Experimental research on the relationship between capture rates and polymer chain length was conducted by Wanunu et al.¹⁶⁸ to capture a dsDNA into a solid-state nanopore. By combining the barrier regime and the drift regime into a single statement, Muthukumar¹⁶⁹ created a broad theory to explain the capture rate. In the barrier-limited domain, his approach was able to reproduce the experimentally reported electric field and chain length-dependent capture rates. At the same time, in the field-dominated drift regime, it was able to reproduce the chain length-independent yet electric field-dependent capture rates. In his estimate, he included the energy barrier gain that results from the polymer chain end discovering the

nanopore from a coiled state, which was omitted in earlier computations. Grosberg et al.¹⁷⁰ concentrated on comprehending the functions of electrophoresis and diffusion in the capture process for the translocation of DNA or other polyelectrolytes. By taking into account various experimental circumstances, further research on the capture mechanism has concentrated on revising earlier hypotheses to reflect experimental findings. For instances like, electro hydrodynamic coupling for rod- or coil-shaped DNA near the nanopore¹⁷¹, electrostatic interactions between polyelectrolyte and nanopore^{172,173}, entropic barrier to enter the pore¹⁷⁰, salt concentration¹⁷⁴, osmotic pressure¹⁷⁵, EOF^{176,177}, and dielectrophoresis¹⁷⁸. The study and characterization of this process is crucial for the ideal designing and progressive development of next-generation nanopore DNA sequencing and analysis technologies, and literature has provided further insight into how DNA passes through a nanopore.

Various technical applications employ solid state nanopores, including separation processes¹⁷⁹, water desalination¹⁸⁰, ion-selective screening¹⁸¹, and power production¹⁸². When compared to biological nanopores, the accuracy of solid state nanopores is their greatest obstacle. Due to their rapid translocation speed^{183,184} and large ionic current noise¹⁸⁵, solid state nanopores are still unable to directly read DNA bases like biological nanopores⁴. Additional obstacles, such as undesirable topologies (such as folds and knots)¹⁸⁶ and the requirement to perform genomic distance calibration on the DNA without previous knowledge of the distance, prevent solid state nanopores from becoming a potent biological sensor. It is acknowledged that the aforementioned issues represent significant obstacles in the way of the successful implementation of nanopore sequencing. However, other problems still need to be resolved (e.g., enhancing the mechanism of lipid bilayer stability in the case of sequencing using a protein pore, handling with DNA secondary structures etc.). The urge to develop fresh concepts and create a translocation system to fulfill a

specific need, such as faster macromolecule separation using external noise for human society, is the need of the hour. This crucial question forms the basis of the current dissertation, which is discussed elaborately in the subsequent chapters.

1.2.5. Thesis overview and objectives

This dissertation investigates the possibility of influencing basic noise-induced behavior in a large ensemble of globally networked excitable systems. Soft matter research addresses many issues, from particle suspensions to polymer solutions to cell networks. The enormous domain encompasses most of the structures seen in genuine biological systems, such as the human body. The goal of soft matter research is to put physical theories to the test, anticipate previously unknown behavior, and provide ideas for fresh, experimental procedures. Because of advances in research in molecular theory of matter, a new perspective is required to explore the nature of these minuscule particles detailed in earlier sections. The oscillations of the dynamic characteristics of molecules become critical at this microscopic level to explain many macroscopic aspects. Statistical mechanics is the guiding pathway for studying the behavior of natural and spontaneous fluctuations. Molecular fluctuations encode the energy states of the system, while statistical mechanics is a support tool. In this dissertation, we will utilise this method to investigate the dynamic behavior of a macromolecule and along the way, we will try to learn about the underlying solid friction. We have arranged our experiments so that the input is a bias voltage with random Gaussian noise and the output (drift velocity) is stochastic. The variation of velocity or displacement encodes whether the dynamic system is linear or non-linear. These concerns are addressed in our current thesis. This study investigates the effects of non-linear dynamics helped by external noise on the translocation of macromolecules across nanoporous gels. It focuses on

how external noise might cause a macromolecule to travel quicker in a nanoporous gel environment, as this is a unique and extensively covered subject throughout our thesis. This approach is essential in the field of molecular biology and biotechnology. Understanding the molecular mechanics of DNA molecular chain separation is of essential importance. We developed a basic phenomenological model to represent the key aspects of non-linear dynamics. The thesis chapters briefly overview numerous intriguing noise-induced events in non-linear dynamical systems.

- ✓ In Chapter 2 it is demonstrated that the mobility of DNA molecules in gel electrophoretic settings can be substantially faster (100% or more) than traditional gel electrophoresis with the use of Gaussian white noise. A modified Langevin equation correctly predicts drift velocity with bias and noise.
- ✓ Chapter 3 deals with the important outcome that an external noise in one direction can transmit sufficient energy to a stuck molecule that can become mobile and be steered in any particular direction by applying a subcritical biased force. The object may choose the minimum energy path in the energy landscape when external noise is applied orthogonal to that of the bias voltage direction. Instead of immediately crossing the barrier's apex, it may investigate the neighbourhood's lowest barrier height and choose the least energy-consuming route to avoid the energy loss caused by apex-crossing.
- ✓ Chapter 4 provided a novel route towards specific M.W. band (kbp) sorting wherein asymmetric ramp wave vibrations were added in addition to biased voltage in a gel electrophoretic setting to showcase the effect of vibrations influencing the DNA drift velocity through a nanoporous gel. The primary outcome of this chapter is that vibration makes the DNA molecule traversing “fluidized” in some sense, enabling to move faster. Due to additional excitation generated by

vibration, the depinning of the DNA molecule (like the peeling of a soft adhesive) enables faster DNA kinetics.

- ✓ Chapter 5 demonstrated how external vibration-induced gel electrophoretic system can be utilized for the diagnosis of a specific bacteria. Alongside, a POCT prototype was also developed during the course of this investigation which supports our findings through gel electrophoretic detection of a specific bacteria (*K.pneumoniae*) responsible for UTI and other health issues such as meningitis, lung infections etc.
- ✓ In Chapter 6, the summary of the technical chapter's and future research outlook has been elaborated on and discussed.

References

1. Roberts, K. *et al. Molecular Biology Of The Cell. Boltsupply.Com* (2002).
2. J. Darnell, H.Lodish, D. B. *Molecular Cell Biology 5th Ed. W.H. Freeman* (1995).
3. Zhao, L. *et al. Manipulation of pore structure during manufacture of agarose microspheres for bioseparation. Eng. Life Sci.* **20**, 504–513 (2020).
4. Kasianowicz, J. J., Brandin, E., Branton, D. & Deamer, D. W. Characterization of individual polynucleotide molecules using a membrane channel. *Proc. Natl. Acad. Sci. U. S. A.* **93**, 13770–13773 (1996).
5. Akeson, M., Branton, D., Kasianowicz, J. J., Brandin, E. & Deamer, D. W. Microsecond time-scale discrimination among polycytidylic acid, polyadenylic acid, and polyuridylic acid as homopolymers or as segments within single RNA molecules. *Biophys. J.* **77**, 3227–

- 3233 (1999).
6. Meller, A., Nivon, L., Brandin, E., Golovchenko, J. & Branton, D. Rapid nanopore discrimination between single polynucleotide molecules. *Proc. Natl. Acad. Sci. U. S. A.* **97**, 1079–1084 (2000).
 7. Meller, A., Nivon, L. & Branton, D. Voltage-driven DNA translocations through a nanopore. *Phys. Rev. Lett.* **86**, 3435–3438 (2001).
 8. Storm, A. J., Chen, J. H., Ling, X. S., Zandbergen, H. W. & Dekker, C. Fabrication of solid-state nanopores with single-nanometre precision. *Nat. Mater.* **2**, 537–540 (2003).
 9. Schneider, G. F. *et al.* DNA translocation through graphene nanopores. *Nano Lett.* **10**, 3163–3167 (2010).
 10. Sung, W. & Park, P. J. Polymer translocation through a pore in a membrane. *Phys. Rev. Lett.* **77**, 783–786 (1996).
 11. Di Marzio, E. A. & Mandell, A. J. Phase transition behavior of a linear macromolecule threading a membrane. *J. Chem. Phys.* **107**, 5510–5514 (1997).
 12. Park, P. J. & Sung, W. Polymer release out of a spherical vesicle through a pore. *Phys. Rev. E - Stat. Physics, Plasmas, Fluids, Relat. Interdiscip. Top.* **57**, 730–734 (1998).
 13. Lubensky, D. K. & Nelson, D. R. Driven polymer translocation through a narrow pore. *Biophys. J.* **77**, 1824–1838 (1999).
 14. Muthukumar, M. Translocation of a confined polymer through a hole. *Phys. Rev. Lett.* **86**, 3188–3191 (2001).
 15. Ambjörnsson, T., Apell, S. P., Konkoli, Z., Di Marzio, E. A. & Kasianowicz, J. J. Charged

- polymer membrane translocation. *J. Chem. Phys.* **117**, 4063–4073 (2002).
16. Matsuyama, A. Kinetics of polymer translocation through a pore. *J. Chem. Phys.* **121**, 8098–8103 (2004).
 17. Ambjörnsson, T., Lomholt, M. A. & Metzler, R. Directed motion emerging from two coupled random processes: Translocation of a chain through a membrane nanopore driven by binding proteins. *J. Phys. Condens. Matter* **17**, (2005).
 18. Huopaniemi, I., Luo, K., Ala-Nissila, T. & Ying, S. C. Langevin dynamics simulations of polymer translocation through nanopores. *J. Chem. Phys.* **125**, (2006).
 19. Chuang, J., Kantor, Y. & Kardar, M. Anomalous dynamics of translocation. *Phys. Rev. E - Stat. Physics, Plasmas, Fluids, Relat. Interdiscip. Top.* **65**, 1–8 (2002).
 20. Tian, P. & Smith, G. D. Translocation of a polymer chain across a nanopore: A Brownian dynamics simulation study. *J. Chem. Phys.* **119**, 11475–11483 (2003).
 21. Kantor, Y. & Kardar, M. Anomalous dynamics of forced translocation. *Phys. Rev. E - Stat. Non-linear, Soft Matter Phys.* **69**, 1–12 (2004).
 22. Ali, I. & Yeomans, J. M. Polymer translocation: The effect of backflow. *J. Chem. Phys.* **123**, (2005).
 23. Luo, K., Huopaniemi, I., Ala-Nissila, T. & Ying, S. C. Polymer translocation through a nanopore under an applied external field. *J. Chem. Phys.* **124**, (2006).
 24. Sun, L. Z. & Luo, M. B. Hard sphere diffusion behaviour of polymer translocating through interacting pores. *Chinese Phys. Lett.* **25**, 4050–4053 (2008).
 25. Luo, K. & Metzler, R. Polymer translocation into laterally unbounded confined

- environments. *J. Chem. Phys.* **133**, (2010).
26. Wang, B., Anthony, S. M., Bae, S. C. & Granick, S. Anomalous yet Brownian. *Proc. Natl. Acad. Sci. U. S. A.* **106**, 15160–4 (2009).
 27. Wio, H. S. *Noise Induced Phenomena: a Sampler.* (2003). doi:10.1063/1.1566651
 28. Tsekov, R. & Lensen, M. C. Brownian motion and the temperament of living cells. *Chinese Phys. Lett.* **30**, (2013).
 29. Asdi, A. S. & Tewfik, A. H. Detection of Weak Signals using Adaptive Stochastic Resonance. *Int. Conf. Acoust. Speech, Signal Process.* **2**, 1332–1335 (1995).
 30. Bulsara, A., Jacobs, E. W., Zhou, T., Moss, F. & Kiss, L. Stochastic resonance in a single neuron model: Theory and analog simulation. *J. Theor. Biol.* **152**, 531–555 (1991).
 31. Longtin, A., Bulsara, A. & Moss, F. Time-Interval Sequences in Bistable Systems and the Noise-Induced Transmission of Information by Sensory Neurons. **67**, 656–659 (1991).
 32. Ivey, C., Apkarian, A. V. & Chialvo, D. R. Noise-induced tuning curve changes in mechanoreceptors. *J. Neurophysiol.* **79**, 1879–1890 (1998).
 33. Douglass, J. K., Wilkens, L., Pantazelou, E. & Moss, F. Noise enhancement of information transfer in crayfish mechanoreceptors by stochastic resonance. *Nature* **365**, 337–340 (1993).
 34. Collins, J. J., Imhoff, T. T. & Grigg, P. Noise-enhanced information transmission in rat SA1 cutaneous mechanoreceptors via aperiodic stochastic resonance. *J. Neurophysiol.* **76**, 642–645 (1996).
 35. Levin, J. E. & Miller, J. P. Broadband neural encoding in the cricket cercal sensory system

- enhanced by stochastic resonance. *Nature* **380**, 165–168 (1996).
36. Smith, T. & Lindberg, G. Effect of acoustic energy on contact angle measurements. *J. Colloid Interface Sci.* **66**, 363–366 (1978).
 37. Andrieu, C., Sykes, C. & Brochard, F. Average Spreading Parameter on Heterogeneous Surfaces. *Langmuir* **10**, 2077–2080 (1994).
 38. Daniel, S., Chaudhury, M. K. & De Gennes, P. G. Vibration-actuated drop motion on surfaces for batch microfluidic processes. *Langmuir* **21**, 4240–4248 (2005).
 39. Dong, L., Chaudhury, A. & Chaudhury, M. K. Lateral vibration of a water drop and its motion on a vibrating surface. *Eur. Phys. J. E* **21**, 231–242 (2006).
 40. Brunet, P., Eggers, J. & Deegan, R. D. Vibration-induced climbing of drops. *Phys. Rev. Lett.* **99**, 3–6 (2007).
 41. Mettu, S. & Chaudhury, M. K. Motion of drops on a surface induced by thermal gradient and vibration. *Langmuir* **24**, 10833–10837 (2008).
 42. Hänggi, P., Bartussek, R., Talkner, P. & Łuczka, J. Noise-induced transport in symmetric periodic potentials: White shot noise versus deterministic noise. *Europhys. Lett.* **35**, 315–317 (1996).
 43. Basaran, O. A. & DePaoli, D. W. Non-linear oscillations of pendant drops. *Phys. Fluids* **6**, 2923–2943 (1994).
 44. Colosqui, C. E., Teng, T. & Rahmani, A. M. Wetting Driven by Thermal Fluctuations on Terraced Nanostructures. *Phys. Rev. Lett.* **115**, (2015).
 45. Kornek, U. *et al.* Oscillations of soap bubbles. *New J. Phys.* **12**, (2010).

46. Chandler, D. *Introduction to Modern Statistical Mechanics (David Chandler)*. SIAM Review **30**, (1988).
47. Evans, D. J., Cohen, E. G. D. & Morriss, G. P. Probability of second law violations in shearing steady states. *Phys. Rev. Lett.* **71**, 2401–2404 (1993).
48. Kelvin, Lord. *Mathematical and Physical Papers*. **I**, (1882).
49. Baron Rayleigh, J. W. S. *The Theory of Sound*. Oxford University **I**, (1895).
50. LAMB, H. *HYDRODYNAMICS*. CAMBRIDGE UNIVERSITY PRESS (1916).
51. Chandrasekhar, S. & Gillis, J. *Hydrodynamic and Hydromagnetic Stability*. *Physics Today* **15**, (1962).
52. Wiesenfeld, K. & Moss, F. Stochastic resonance and the benefits of noise: From ice ages to crayfish and SQUIDS. *Nature* **373**, 33–36 (1995).
53. Fulinski, A. Active transport in biological membranes and stochastic resonances. *Phys. Rev. Lett.* **79**, 4926–4929 (1997).
54. Sebastian, K. L. & Paul, A. K. R. Kramers problem for a polymer in a double well. *Phys. Rev. E - Stat. Physics, Plasmas, Fluids, Relat. Interdiscip. Top.* **62**, 927–939 (2000).
55. Madureira, A. J. R. & Hanggi, P. Escape from a fluctuating double well. *Phys. Rev. E* **51**, 3849–3861 (1995).
56. J.LUCZKA, P. H. White Noise induced transport in Periodic structures. *Europhys. Lett.* **31**, 431–436 (1995).
57. Maier, R. S. & Stein, D. L. Noise-activated escape from a sloshing potential well. *Phys.*

- Rev. Lett.* **86**, 3942–3945 (2001).
58. Chichigina, O., Valenti, D. & Spagnolo, B. A simple noise model with memory for biological systems. *Fluct. Noise Lett.* **5**, (2005).
59. Kramers, H. A. Brownian motion in a field of force and the diffusion model. *Phys.* **7** 284–304 (1940).
60. Hänggi, P., Talkner, P. & Borkovec, M. Reaction-rate theory: Fifty years after Kramers. *Rev. Mod. Phys.* **62**, 251–341 (1990).
61. Hales, J., Zhukov, A., Roy, R. & Dykman, M. I. Dynamics of activated escape and its observation in a semiconductor laser. *Phys. Rev. Lett.* **85**, 78–81 (2000).
62. Reimann, P. Brownian motors: Noisy transport far from equilibrium. *Phys. Rep.* **361**, 57–265 (2002).
63. Mel'nikov, V. I. The Kramers problem: Fifty years of development. *Phys. Rep.* **209**, 1–71 (1991).
64. Malakhov, A. N. & Pankratov, A. L. Influence of thermal fluctuations on time characteristics of a single josephson element with high damping exact solution. *Phys. C Supercond. its Appl.* **269**, 46–54 (1996).
65. Valenti, D., Fiasconaro, A. & Spagnolo, B. Stochastic resonance and noise delayed extinction in a model of two competing species. *Phys. A Stat. Mech. its Appl.* **331**, 477–486 (2004).
66. Lehmann, J., Reimann, P. & Hänggi, P. Surmounting oscillating barriers. *Phys. Rev. Lett.* **84**, 1639–1642 (2000).

67. Smelyanskiy, V. N., Dykman, M. I. & Golding, B. Time oscillations of escape rates in periodically driven systems. *Phys. Rev. Lett.* **82**, 3193–3197 (1999).
68. Dykman, M. I., R.Mannella, McClintock, P. & Stocks, N. Phase shifts in Stochastic resonance. *Phys. Rev. Lett.* **68**, 2985–2988 (1992).
69. Lacks, D. J., Willis, J. & Robinson, M. P. Fold catastrophes and the dependence of free-energy barriers to conformational transitions on applied force. *J. Phys. Chem. B* **114**, 10821–10825 (2010).
70. Evans, E. & Ritchie, K. Dynamic strength of molecular adhesion bonds. *Biophys. J.* **72**, 1541–1555 (1997).
71. Schallamach, A. A Theory of Dynamic Rubber Friction. *Rubber Chem. Technol.* **39**, 320–327 (1966).
72. Garg, A. Escape-field distribution for escape from a metastable potential well subject to a steadily increasing bias field. *Phys. Rev. B* **51**, 15592–15595 (1995).
73. Ghatak, A., Vorvolakos, K., She, H., Malotky, D. L. & Chaudhury, M. K. Interfacial Rate Processes in Adhesion and Friction. *J. Phys. Chem. B* **104**, 4018–4030 (2000).
74. Dudko, O. K., Filippov, A. E., Klafter, J. & Urbakh, M. Beyond the conventional description of dynamic force spectroscopy of adhesion bonds. *Proc. Natl. Acad. Sci. U. S. A.* **100**, 11378–11381 (2003).
75. Dudko, O. K., Hummer, G. & Szabo, A. Theory, analysis, and interpretation of single-molecule force spectroscopy experiments. *Proc. Natl. Acad. Sci. U. S. A.* **105**, 15755–15760 (2008).

76. Van Den Brink, A. M. & Dekker, H. Reaction rate theory: Weak-to strong-friction turnover in Kramers' Fokker-Planck model. *Phys. A Stat. Mech. its Appl.* **237**, 515–553 (1997).
77. Matsumoto, K. & Tsuda, I. Noise-Induced Order. *J. Stat. Phys.* **31**, 87–106 (1983).
78. Bier, M. & Astumian, R. D. Matching a Diffusive and a Kinetic Approach for escape over a fluctuating barrier. *Phys. Rev. Lett.* **71**, 1649–1652 (1993).
79. Mantegna, R. N. & Spagnolo, B. Noise enhanced stability in an unstable system. *Phys. Rev. Lett.* **76**, 563–566 (1996).
80. Dayan, I., Gitterman, M. & H. Weiss, G. Stochastic resonance in transient dynamics. *Phys. Rev. A* **46**, 757–761 (1992).
81. Spagnolo, B., Agudov, N. V. & Dubkov, A. A. Noise enhanced stability. *Acta Phys. Pol. B* **35**, 1419–1436 (2004).
82. Agudov, N. V. & Spagnolo, B. Noise-enhanced stability of periodically driven metastable states. *Phys. Rev. E - Stat. Physics, Plasmas, Fluids, Relat. Interdiscip. Top.* **64**, 4 (2001).
83. Wackerbauer, R. When noise decreases deterministic diffusion. *Phys. Rev. E - Stat. Physics, Plasmas, Fluids, Relat. Interdiscip. Top.* **59**, 2872–2879 (1999).
84. Mielke, A. Noise induced stability in fluctuating, bistable potentials. *Phys. Rev. Lett.* **84**, 818–821 (2000).
85. Yoshimoto, M., Kurosawa, S. & Nagashima, H. Effect of noise on chaos in a One-dimensional Map. *J. Phys. Soc. Japan* **67**, 1924–1929 (1998).
86. Mantegna, R. N. & Spagnolo, B. Numerical simulation of resonant activation in a fluctuating metastable model system. *J. Phys. IV JP* **8**, 1–5 (1998).

87. Spagnolo, B., Cirone, M., La Barbera, A. & De Pasquale, F. Noise-induced effects in population dynamics. *J. Phys. Condens. Matter* **14**, 2247–2255 (2002).
88. SPAGNOLO, B., FIASCONARO, A. & VALENTI, D. Noise Induced Phenomena in Lotka-Volterra Systems. *Fluct. Noise Lett.* **03**, L177–L185 (2003).
89. Lanzara, E., Mantegna, R. N., Spagnolo, B. & Zangara, R. Experimental study of a non-linear system in the presence of noise: The stochastic resonance. *Am. J. Phys.* **65**, 341–349 (1997).
90. Mantegna, R. N., Spagnolo, B. & Trapanese, M. Linear and non-linear experimental regimes of stochastic resonance. *Phys. Rev. E - Stat. Physics, Plasmas, Fluids, Relat. Interdiscip. Top.* **63**, 1–8 (2001).
91. Yoshimoto, M. Noise effects on the one-dimensional return map of the high flow rate chaos of the Belousov-Zhabotinsky reaction. *Phys. Lett. Sect. A Gen. At. Solid State Phys.* **312**, 59–64 (2003).
92. Xie, C. W. & Mei, D. C. Mean first-passage time of a bistable kinetic model driven by multiplicative coloured noise and additive white noise. *Chinese Phys. Lett.* **20**, 813–816 (2003).
93. Pizzolato, N., Fiasconaro, A. & Spagnolo, B. Noise effects in polymer dynamics. *Int. J. Bifurc. Chaos* **18**, 2871–2876 (2008).
94. Doering, C. R. & Gadoua, J. C. Resonant activation over a fluctuating barrier. *Phys. Rev. Lett.* **69**, 2318–2321 (1992).
95. Shi, N. & Ugaz, V. M. Noise-enhanced gel electrophoresis. *Electrophoresis* **35**, 1758–1765

- (2014).
96. Alan, W. D'arcy thompson's 'On growth and form' and the rediscovery of geometry within the geographic tradition. *Scottish Geogr. J.* **126**, 231–257 (2010).
 97. Nernst, W. The electromotive effectiveness of the ions. *J. Phys. Chem.* **4U**, 129–181 (1889).
 98. Baumgärtner, A. & Muthukumar, M. A trapped polymer chain in random porous media. *J. Chem. Phys.* **87**, 3082–3088 (1987).
 99. Djabourov, M., Clark, A. H., Rowlands, D. W. & Ross-Murphy, S. B. Small-Angle X-ray Scattering Characterization of Agarose Sols and Gels. *Macromolecules* **22**, 180–188 (1989).
 100. Muthukumar, M. & Baumgärtner, A. Effects of Entropic Barriers on Polymer Dynamics. *Macromolecules* **22**, 1937–1941 (1989).
 101. Ferguson, K. A. Starch-gel electrophoresis—Application to the classification of pituitary proteins and polypeptides. *Metabolism.* **13**, 985–1002 (1964).
 102. Viovy, J. L. Electrophoresis of DNA and other polyelectrolytes: Physical mechanisms. *Rev. Mod. Phys.* **72**, 813–872 (2000).
 103. Nancy C. Stellwagen. Electrophoresis of DNA in agarose gels, polyacrylamide gels and in free solution. *Electrophoresis* **30**, 1–7 (2009).
 104. MATHEWS, HOLDE, V. & AHERN. *BIOCHEMISTRY 3rd Edition.* (1999).
 105. Barkema, G. T., Caron, C. & Marko, J. F. Scaling properties of gel electrophoresis of DNA. *Biopolymers* **38**, 665–667 (1996).
 106. Slater, G. W. A theoretical study of an empirical function for the mobility of DNA fragments

- in sieving matrices. *Electrophoresis* **23**, 1410–1416 (2002).
107. Winkle, D. H. V., Beheshti, A. & Randolph L. Rill. DNA electrophoresis in agarose gels: A simple relation describing the length dependence of mobility. *Electrophoresis* **23**, 15–19 (2002).
108. Reuss, F. *Memoirs of the Imperial Society of Moscow Naturalists*. (1809).
109. Tiselius, A. A new apparatus for electrophoretic analysis of colloidal mixtures. *Trans. Faraday Soc.* **33**, 524–531 (1937).
110. Green, M. R. & Joseph Sambrook. *Molecular Cloning: A LABORATORY MANUAL*. **1**, (2012).
111. Heller, C. Separation of double-stranded and single-stranded DNA in polymer solutions: I. Mobility and separation mechanism. *Electrophoresis* **20**, 1962–1976 (1999).
112. Louis Viovy, J., Duke, T. & Caron, F. The physics of DNA electrophoresis. *Contemp. Phys.* **33**, 25–40 (1992).
113. Stellwagen, N. C. & Holmes, D. L. Resolution of a paradox in the electrophoresis of DNA in agarose gels. *Electrophoresis* **11**, 649–652 (1990).
114. Stellwagen, N. C. Agarose gel pore radii are not dependent on the casting buffer. *Electrophoresis* **13**, 601–603 (1992).
115. Serwer, P. & Hayes, S. J. Exclusion of spheres by agarose gels during agarose gel electrophoresis: Dependence on the sphere's radius and the gel's concentration. *Anal. Biochem.* **158**, 72–78 (1986).
116. Chui, M. M., Phillips, R. J. & McCarthy, M. J. Measurement of the porous microstructure

- of hydrogels by nuclear magnetic resonance. *Journal of Colloid And Interface Science* **174**, 336–344 (1995).
117. Slater, G. W., Rousseau, J., Noolandi, J., Turmel, C. & Lalande, M. Quantitative analysis of the three regimes of DNA electrophoresis in agarose gels. *Biopolymers* **27**, 509–524 (1988).
118. Doi, M. *et al.* Band Inversion in Gel Electrophoresis of DNA. *Phys. Rev. Lett.* **61**, (1988).
119. Noolandi, J., Rousseau, J., Slater, G. W., Turmel, C. & Lalande, M. Self-Trapping and Anomalous Dispersion of DNA in Electrophoresis. *Phys Rev Lett* **58**, 2428–2432 (1987).
120. A.G. OGSTON. The SPACES IN A UNIFORM RANDOM SUSPENSION OF FIBRES. *Trans. Faraday Soc.* **54**, 1754–1757 (1958).
121. Rodbard, D. & Chrmbach, A. Unified theory for gel electrophoresis and gel filtration. *Proc. Natl. Acad. Sci. U. S. A.* **65**, 970–977 (1970).
122. Rodbard, D. & Chrmbach, A. Estimation of molecular radius, free mobility, and valence using polyacrylamide gel electrophoresis. *Anal. Biochem.* **40**, 95–134 (1971).
123. Rousseau, J., Drouin, G. & Slater, G. W. Entropic trapping of dna during gel electrophoresis: Effect of field intensity and gel concentration. *Phys. Rev. Lett.* **79**, 1945–1948 (1997).
124. Turner, S. W. P., Cabodi, M. & Craighead, H. G. Confinement-Induced Entropic Recoil of Single DNA Molecules in a Nanofluidic Structure. *Phys. Rev. Lett.* **88**, 4 (2002).
125. Gary W. Slater and Jaan Noolandi. New Biased-Reptation Model For Charged Polymers. *Phys. Rev. Lett.* **55**, 1579–1582 (1985).

126. Slater, G. W. & Noolandi, J. Reptating charged polymer chains in electric fields. *Europhys. Lett.* **1**, 347–353 (1986).
127. De Gennes, P. G. Reptation of a polymer chain in the presence of fixed obstacles. *J. Chem. Phys.* **55**, 35–42 (1971).
128. T.A.J.Duke, Semenov, A. N. & J.L.Viovy. Mobility of a Reptating Polymer. *Phys. Rev. Lett.* **69**, 3260–3263 (1992).
129. Heller, C., Duke, T. & Viovy, J. L. Electrophoretic mobility of DNA in gels. II. Systematic experimental study in agarose gels. *Biopolymers* **34**, 249–259 (1994).
130. Semenov, A. N., Duke, T. A. J. & Viovy, J. L. Gel electrophoresis of DNA in moderate fields: The effect of fluctuations. *Phys. Rev. E* **51**, 1520–1537 (1995).
131. Slater, G. W. & Noolandi, J. Reptating charged polymer chains in electric fields. *Europhys. Lett.* **1**, 347–353 (1986).
132. Slater, G., Rousseau, J. & Noolandi, J. On the Stretching of DNA in the Reptation Theories of Gel Electrophoresis. *Biopolymers* **26**, 863–872 (1987).
133. Widom, M. & Lehyani, I. A.-. Repton model of gel electrophoresis in the long chain limit. *Physica A* **244**, 510–521 (1997).
134. Zimm, B. H. & Lumpkin, O. Reptation of a Polymer Chain in an Irregular Matrix: Diffusion and Electrophoresis. *Macromolecules* **26**, 226–234 (1993).
135. Schwartz, D. C. *et al.* New techniques for purifying large DNAs and studying their properties and packaging. *Cold Spring Harb. Symp. Quant. Biol.* **47**, 189–195 (1982).
136. Smith, C. L., Econome, J. G., Schutt, A., Klco, S. & Cantor, C. R. A physical map of the

- Escherichia coli K12 genome. *Science* (80). **236**, 1448–1453 (1987).
137. Dudek, B. *et al.* Comparison of the phylogenetic analysis of PFGE profiles and the characteristic of virulence genes in clinical and reptile associated Salmonella strains. *BMC Vet. Res.* **15**, 1–12 (2019).
 138. Van der Ploeg, L. H. T., Schwartz, D. C., Cantor, C. R. & Borst, P. Antigenic variation in trypanosoma brucei analyzed by electrophoretic separation of chromosome-sized DNA molecules. *Cell* **37**, 77–84 (1984).
 139. Vollrath, D. & Davis, R. W. Resolution of DNA molecules greater than 5 megabases by contour-clamped homogeneous electric fields. *Nucleic Acids Res.* **15**, 7865–7876 (1987).
 140. Orbach, M. J., Vollrath, D., Davis, R. W. & Yanofsky, C. An electrophoretic karyotype of Neurospora crassa. *Mol. Cell. Biol.* **8**, 1469–1473 (1988).
 141. Carle, G. F. & Olson, M. V. Separation of chromosomal DNA molecules from yeast by orthogonal-field-alternation gel electrophoresis. *Nucleic Acids Res.* **12**, 5647–5664 (1984).
 142. Carle, G. F. & Olson, M. V. An electrophoretic karyotype for yeast. *Proc. Natl. Acad. Sci. U. S. A.* **82**, 3756–3760 (1985).
 143. C.Schwartz, D. & R.Cantor, C. Separation of Yeast Chromosome-Sized DNAs by Pulsed Field Gradient Gel Electrophoresis. *Cell* **37**, 67–75 (184AD).
 144. Finney, M. Pulsed-Field Gel Electrophoresis. in *Current Protocols in Molecular Biology* 1–9 (2000).
 145. Sharma-Kuinkel, B. K., Rude, T. H. & Jr, V. G. F. Pulse Field Gel Electrophoresis. *Methods Mol. Biol.* **1373**, 117–130 (2016).

146. Birren, B. W., Lai, E., M.Clark, S., Hood, L. & Simon, M. I. Optimized conditions for pulsed field gel electrophoretic separations of DNA. *Nucleic Acids Res.* **16**, 7563–7582 (1988).
147. Squires, A. & Meller, A. DNA capture and translocation through nanoscale pores - A fine balance of electrophoresis and electroosmosis. *Biophys. J.* **105**, 543–544 (2013).
148. Van Dorp, S., Keyser, U. F., Dekker, N. H., Dekker, C. & Lemay, S. G. Origin of the electrophoretic force on DNA in solid-state nanopores. *Nat. Phys.* **5**, 347–351 (2009).
149. Wen, C. & Zhang, S. L. On current blockade upon analyte translocation in nanopores. *J. Appl. Phys.* **129**, (2021).
150. Reynaud, L., Bouchet-Spinelli, A., Raillon, C. & Buhot, A. Sensing with nanopores and aptamers: A way forward. *Sensors (Switzerland)* **20**, 1–29 (2020).
151. Xue, L. *et al.* Solid-state nanopore sensors. *Nat. Rev. Mater.* **5**, 931–951 (2020).
152. Hasnain, M. J. U., Bakhtawar Afzal & Hussain, T. A review on nanopore sequencing technology, its applications and challenges. *Pure Appl. Biol.* **9**, 154–161 (2020).
153. Nehra, A., Ahlawat, S. & Singh, K. P. A biosensing expedition of nanopore: A review. *Sensors Actuators, B Chem.* **284**, 595–622 (2019).
154. Waduge, P. *et al.* Nanopore-Based Measurements of Protein Size, Fluctuations, and Conformational Changes. *ACS Nano* **11**, 5706–5716 (2017).
155. Varongchayakul, N., Song, J., Meller, A. & Grinstaff, M. W. Single-molecule protein sensing in a nanopore: a tutorial. *Chem. Soc. Rev.* **47**, 8512–8524 (2018).
156. Wanunu, M. Nanopores: A journey towards DNA sequencing. *Phys. Life Rev.* **9**, 125–158

- (2012).
157. Deamer, D., Akeson, M. & Branton, D. Three decades of nanopore sequencing. *Nat. Biotechnol.* **34**, 518–524 (2016).
 158. Ashkenazy, N., Sanchez-Quesada, J. & Ghadiri, M. R. Recognizing a single base in an individual DNA strand: A step toward nanopore DNA sequencing. *Angew. Chemie Int. Ed. English.* **44**, 1401–1404 (2007).
 159. Goto, Y., Akahori, R., Yanagi, I. & Takeda, K. ichi. Solid-state nanopores towards single-molecule DNA sequencing. *J. Hum. Genet.* **65**, 69–77 (2020).
 160. Yuan, Z., Liu, Y., Dai, M., Yi, X. & Wang, C. Controlling DNA Translocation Through Solid-state nanopores. *Nanoscale Res. Lett.* **15**, 1–9 (2020).
 161. Haque, F., Li, J., Wu, H. C., Liang, X. J. & Guo, P. Solid-state and biological nanopore for real-time sensing of single chemical and sequencing of DNA. *Nano Today* **8**, 56–74 (2013).
 162. Miles, B. N. *et al.* Single molecule sensing with solid-state nanopores: Novel materials, methods, and applications. *Chem. Soc. Rev.* **42**, 15–28 (2013).
 163. Gershow, M. & Golovchenko, J. A. Recapturing and trapping single molecules with a solid-state nanopore. *Nat. Nanotechnol.* **2**, 775–779 (2007).
 164. Nakane, J., Akeson, M. & Marziali, A. Evaluation of nanopores as candidates for electronic analyte detection. *Electrophoresis* **23**, 2592–2601 (2002).
 165. Chen, P. *et al.* Probing Single Dna Molecule Transport Using. *Nano Lett.* **4**, 2293–2298 (2004).
 166. Wong, C. T. A. & Muthukumar, M. Polymer capture by electro-osmotic flow of oppositely

- charged nanopores. *J. Chem. Phys.* **126**, (2007).
167. Chou, T. Enhancement of charged macromolecule capture by nanopores in a salt gradient. *J. Chem. Phys.* **131**, 1–9 (2009).
168. Wanunu, M., Morrison, W., Rabin, Y. & Meller, A. Electrostatic Focusing of Unlabeled DNA into Nanoscale Pores using a Salt Gradient. *Nat. Nanotechnol.* **5**, 160–165 (2010).
169. Muthukumar, M. Theory of capture rate in polymer translocation. *J. Chem. Phys.* **132**, (2010).
170. Rowghanian, P. & Grosberg, A. Y. Electrophoretic capture of a DNA chain into a nanopore. *Phys. Rev. E - Stat. Non-linear, Soft Matter Phys.* **87**, 1–8 (2013).
171. Rowghanian, P. & Grosberg, A. Y. Electrophoresis of a DNA coil near a nanopore. *Phys. Rev. E - Stat. Non-linear, Soft Matter Phys.* **87**, 1–9 (2013).
172. Jeon, B. J. & Muthukumar, M. Electrostatic Control of Polymer Translocation Speed through α -Hemolysin Protein Pore. *Macromolecules* **49**, 9132–9138 (2016).
173. Buyukdagli, S. & Ala-Nissila, T. Controlling polymer capture and translocation by electrostatic polymer-pore interactions. *J. Chem. Phys.* **147**, (2017).
174. Jeon, B. J. & Muthukumar, M. Polymer capture by α -hemolysin pore upon salt concentration gradient. *J. Chem. Phys.* **140**, 1–7 (2014).
175. Hatlo, M. M., Panja, D. & Van Roij, R. Translocation of DNA molecules through nanopores with salt gradients: The role of osmotic flow. *Phys. Rev. Lett.* **107**, 1–5 (2011).
176. Buyukdagli, S. Facilitated polymer capture by charge inverted electroosmotic flow in voltage-driven polymer translocation. *Soft Matter* **14**, 3541–3549 (2018).

177. Zhang, Y. *et al.* Electroosmotic Facilitated Protein Capture and Transport through Solid-State Nanopores with Diameter Larger than Length. *Small Methods* **4**, 1–8 (2020).
178. Chinappi, M., Yamaji, M., Kawano, R. & Cecconi, F. Analytical model for particle capture in nanopores elucidates competition among electrophoresis, electroosmosis, and dielectrophoresis. *ACS Nano* **14**, 15816–15828 (2020).
179. Dong, G. *et al.* Enhanced CO₂/N₂ separation by porous reduced graphene oxide/Pebax mixed matrix membranes. *J. Memb. Sci.* **520**, 860–868 (2016).
180. O’Hern, S. C. *et al.* Nanofiltration across defect-sealed nanoporous monolayer graphene. *Nano Lett.* **15**, 3254–3260 (2015).
181. Walker, M. I. *et al.* Extrinsic Cation Selectivity of 2D Membranes. *ACS Nano* **11**, 1340–1346 (2017).
182. Zhang, Y., He, Y., Tsutsui, M., Miao, X. S. & Taniguchi, M. Short channel effects on electrokinetic energy conversion in solid-state nanopores. *Sci. Rep.* **7**, 1–14 (2017).
183. Storm, A. J. *et al.* Fast DNA translocation through a solid-state nanopore. *Nano Lett.* **5**, 1193–1197 (2005).
184. Plesa, C. *et al.* Fast translocation of proteins through solid state nanopores. *Nano Lett.* **13**, 658–663 (2013).
185. Smeets, R. M. M., Dekker, N. H. & Dekker, C. Low-frequency noise in solid-state nanopores. *Nanotechnology* **20**, (2009).
186. Chen, K. *et al.* Ionic Current-Based Mapping of Short Sequence Motifs in Single DNA Molecules Using Solid-State Nanopores. *Nano Lett.* **17**, 5199–5205 (2017).



CHAPTER 2

Noise activated fast locomotion of DNA through frictional landscape of nanoporous gel

Contents

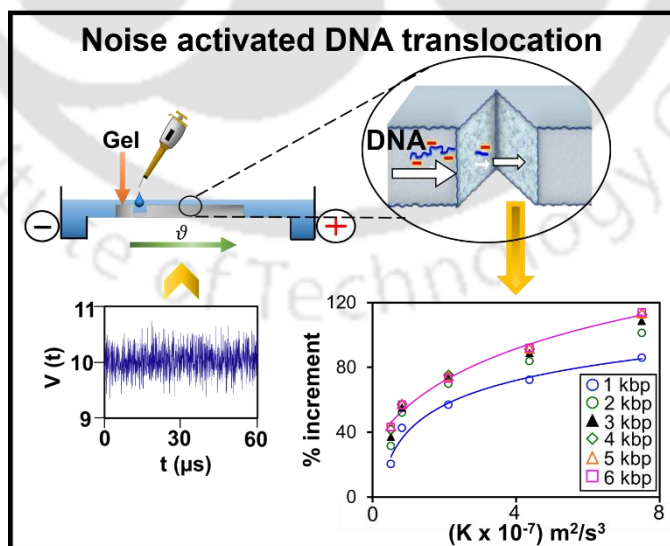
ABSTRACT.....	45
2.1. Introduction.....	46
2.2. Materials and Methods.....	47
2.2.1. Materials.....	47
2.2.2. Preparation of Gel.....	47
2.2.3. Estimation of Pore Size.....	48
2.2.4. Instrument.....	48
2.2.5. Experimental Procedure.....	49
2.3. Results and Discussion	50
2.3.1 Noise activated DNA translocation	50
2.3.2 Noise Characterization	54
2.3.3 Details of the numerical simulation.....	56
2.3.4. Modified Langevin Model.....	57
2.3.5. Escape rate of the DNA molecule.....	65
2.4. Conclusions.....	66
References.....	67



ABSTRACT

It is hypothesized that nonlinear solid friction between the gel matrix and DNA molecules inhibits the motion of DNA through the nanopores of the gel during electrophoresis. In this article, it is demonstrated that external noise can alleviate the effect of solid friction, thus enhancing the mobility of DNA in an electrophoretic setting. In the presence of noise, the mobility of DNA increases by more than ~113 % compared to conventional electrophoresis. Although at a high power of noise, DNA exhibits Arrhenius kinetics, at a low power of noise, super Arrhenius kinetics suggest the collective behavior of the activated motion of DNA molecules. Stochastic simulation following modified Langevin dynamics with the asymmetric pore size distribution of the agarose gel successfully predicts the mobility of DNA molecules and reveals the salient features of the overall dynamics. This “noise lubricity” may have broader applicability from molecular to macroscopic locomotion.

Graphical Abstract



Keywords: Noise activated process, Langevin dynamics, Solid friction, Non- Arrhenius kinetics.

2.1. Introduction

Children learn how to use noise to release a stuck (due to some tiny obstacles) toy car on an inclined plank by tapping it, from their experience. One can also tap on a horizontal platform having a pile of sand to allow free spreading of the sand from the ‘jammed’ state. The tapping acts as an external perturbation or noise that provides sufficient energy to the system to overcome the surface defects on the plank or the jamming potential barrier in the case of a sand pile. Similar scenarios are encountered almost every day such as the motion of a stuck tiny water droplet either on a windshield of a car on a rainy day or on a shower curtain during a bath. Noise is generated from the random blow of the wind in the former case, whereas, for the later, it is the self-excited oscillations due to the condensation of steam and/or coalescence of multiple droplets¹. The potential barriers in such cases originate from the solid friction or its surrogate, contact angle hysteresis, at the solid-solid or solid-liquid interface, respectively. The solid friction restricts the diffusive as well as biased motion of the nano-micro² to the large-scale macroscopic objects³⁻⁵. The friction also affects the dynamics of the charged particles or long-chain molecules like DNA or proteins through a narrow pore^{6,7}. Burlatsky and Deutch pointed out that the electrophoretic motion of DNA is hindered by solid friction that originates from the DNA-gel matrix interactions along with the viscous dissipation between DNA and the buffer-solvent that is present inside the pores⁸⁻¹⁰. [also see the responses of Burlatsky and Deutch to the technical comments by Viovy and Duke¹¹]. This solid friction is engendered from the adhesive interactions between the pore-wall of the gel matrix and the flexible DNA molecules, rubbing between them, distortion of the gel fibers, and other forms of local kinetic energy dissipation.

To detach from the wall of the gel matrix, an electric field-driven DNA molecule has to overcome these energy dissipative interactions, characterized by critical forces. Constrictions, defined by the

dimensions of the pores, govern the solid frictional forces. As the distribution of the pore size spans over a wide range, one can expect a wide distribution of critical forces. These critical forces can be overcome when enough energy is supplied to the DNA molecules. Here we report a novel approach for faster transportation of DNA molecules that ensues from the noise-activated subcritical detachment of DNA from the gel matrix in an electrophoretic setting. The experimental configuration promotes rapid sorting for DNA or protein fingerprinting.

2.2. Materials and Methods

2.2.1. Materials

Agarose powder and Ethidium bromide were procured from Loba Chemie. Tris Acetate-EDTA (TAE) buffer was purchased from Himedia, and the DNA 1 kbp to 10 kbp molecular weight (MW) ladder was obtained from Takara Bio Inc. Miniphor UVT System (Serial No. 106888 GB) was used for the horizontal gel electrophoresis and as a DC power supply unit (GeNei Electrophoresis Power Supply, 0-500V, 0-500 mA) was used. For the noise generation and amplification of the signal, an arbitrary waveform generator (SIGLENT SDG- 1062X) and an amplifier (Q44 Keysight 33502A 2-Channel Isolated Power Amplifier) were used.

2.2.2. Preparation of gel

0.8% (w/v) agarose was prepared by dissolving 0.8 g of agarose powder in 100 ml of 1X Tris Acetate-EDTA (TAE) buffer. A homogenous solution was prepared by first mixing thoroughly and then kept in a microwave oven (Make: Samsung Model No: MC28H5023AKTL) at a power of 900 W for a period of 1 min. The solution temperature was ~ 100 °C. The solution thus prepared

was cool down to $\sim 30\text{ }^{\circ}\text{C}$ and subsequently, $3\text{ }\mu\text{L}$ of 0.5 mg/ml aqueous Ethidium bromide (EtBr) was added to the solution. The EtBr facilitates the detection of DNA bands under UV illumination. TAE buffer was used to maintain the pH of the solution at ~ 8 . The gel was cast onto a gel electrophoretic platform by pouring the agarose solution into the gel chamber wherein a comb was placed at one end of the gel platform to form the wells into which the DNA would be loading before electrophoresis. The agarose solution was allowed to be set at room temperature for 2 h.

2.2.3. Estimation of pore size

The gel was initially frozen at $-20\text{ }^{\circ}\text{C}$ for overnight and then vacuum dried at 20 mTorr and $-103\text{ }^{\circ}\text{C}$ in a Lyophilizer for 24 h before the FESEM analysis. Although sufficient care was taken while measuring the pore size distribution, it is undeniable that the freezing and drying may distort the pores marginally than in the wet state. However, we are interested in the nature of the pore size distribution rather than the absolute pore size. Thus, the freeze-drying technique adopted here is sufficient to provide adequate information about the distribution. From the FESEM image, the pore area was identified using an open source software, ImageJ. Local contrast-based thresholding was performed to get the area and the distribution of the pore size (area) was obtained from the statistical analysis of the same using Origin Pro 9.0 64 Bit software.

2.2.4. Instrument

Waveform generator (Model: SIGLENT SDG 1062X) was used for generating Gaussian white noise in the form of voltage pulses $V(t)$.

Oscilloscope (Model: RIGOL DS1052E) was used to observe and collect the voltage data ($V(t)$), generated by the waveform generator for further analysis.

Amplifier (Model: Q44 Keysight 33502A 2-Channel Isolated Amplifier) was used to amplify the Gaussian noise signal generated from the waveform generator.

Electrophoretic chamber (Model: Miniphor UVT System 106888GB) was used for performing the agarose gel electrophoresis for the separation of the DNA bands.

UV illumination/gel documentation chamber (Model: Chemidoc XRS+ System with Image Lab Software #1708265) was used for visualization of the DNA bands.

Lyophilizer (Model: LABCONCO Freezone 4.5L Benchtop Freeze Dryer, #720401000) was used for freeze drying the agarose gel for FESEM analysis.

FESEM (Model: JSM 7610F, JEOL, JAPAN) was used for imaging the freeze-dried agarose gel section to determine the pore size distribution.

2.2.5. Experimental procedure

The DNA (1 kbp to 10 kbp) molecular weight ladder was loaded into the wells of the gel. Any bubble formation during the loading of the DNA was avoided carefully. The gel was run at 10 V DC at a constant current of ~ 1 mA across a separation distance of $d = 13$ cm between two Pt electrodes. The duration of the electrophoresis was 4 h. The temperature of the gel and the TAE buffer was maintained at 23 ± 1 °C. Visualization of the DNA fragments was done using a Gel Doc (Chemidoc XRS+) instrument. The system software captures the images at various modes of magnification. Gaussian white noise was generated and amplified using a function waveform generator and a noise amplifier, respectively. The waveform generator and the amplifier were connected in series with a DC voltage source as schematically shown in Figure 2.1. To characterize the noise, the output from the waveform generator as voltage signal via an amplifier and an

oscilloscope was collected. The stored data was then extracted for further analysis. The minimum interval for the sampling data was 40 ns. The images of the DNA bands after electrophoretic separation were analyzed using the open-source ImageJ software.

2.3. Results and Discussion

2.3.1. Noise activated DNA translocation

The experimental setup was similar to the conventional agarose gel electrophoresis under the influence of a constant bias voltage with a provision for introducing Gaussian noise as time-dependent voltage input. A function generator, along with an amplifier, was attached with a bias DC voltage source in a series connection, and the resultant potential was applied across a gel in an electrophoretic set-up through a pair of Pt electrodes and Tris Acetate-EDTA (TAE) buffer (Figure 2.1).

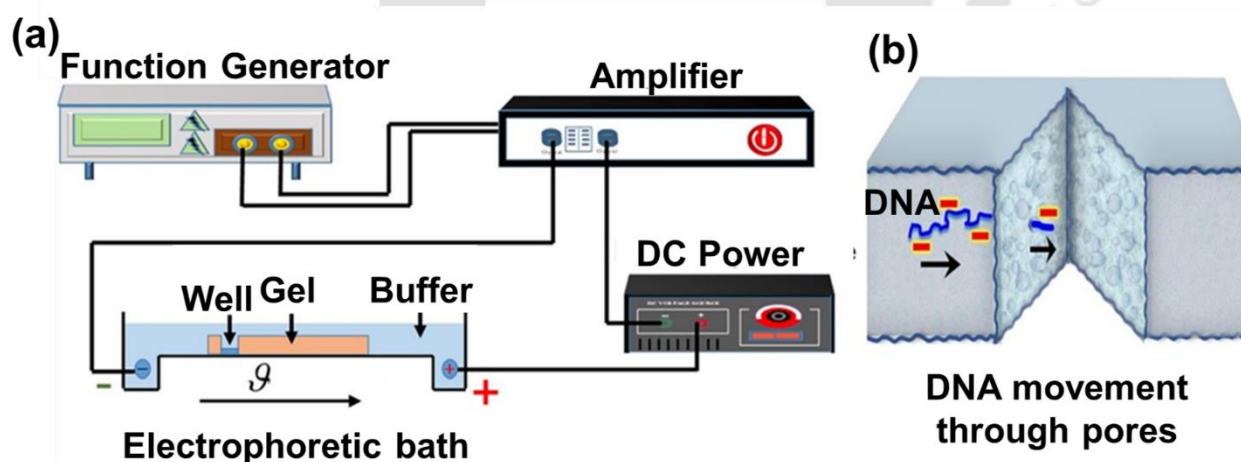


Figure 2.1. Schematic representation of the experimental setup. (a) The function waveform generator is connected with a signal amplifier. The output from the amplifier is connected in series

with a constant DC voltage source and the resultant output is applied across the agarose gel in the electrophoretic chamber. The arrow with the symbol denotes the direction of the DNA band motion. (b) The schematic of the enlarged gel cross-section depicts negatively charged DNA experiencing friction while traversing through the pores of the gel matrix.

Under the influence of a bias voltage, the negatively charged DNA fragments slither through the gel having the network of porous tortuous micro/nanotubes, the birth of which itself is engendered by the longitudinal transport of DNA through the gel matrix, similar to the mechanism proposed for entangled polymers^{10,12}. Keeping the bias voltage fixed at 10 V, the intensity of the Gaussian noise was controlled by amplifying the voltage amplitude of the noise. In presence of the noise and with the increase of the noise amplitude, the mobility of the DNA increases and at a given noise, the mobility decreases with the increase of the MW of DNA (Figure 2.2.a, 2.2.d).

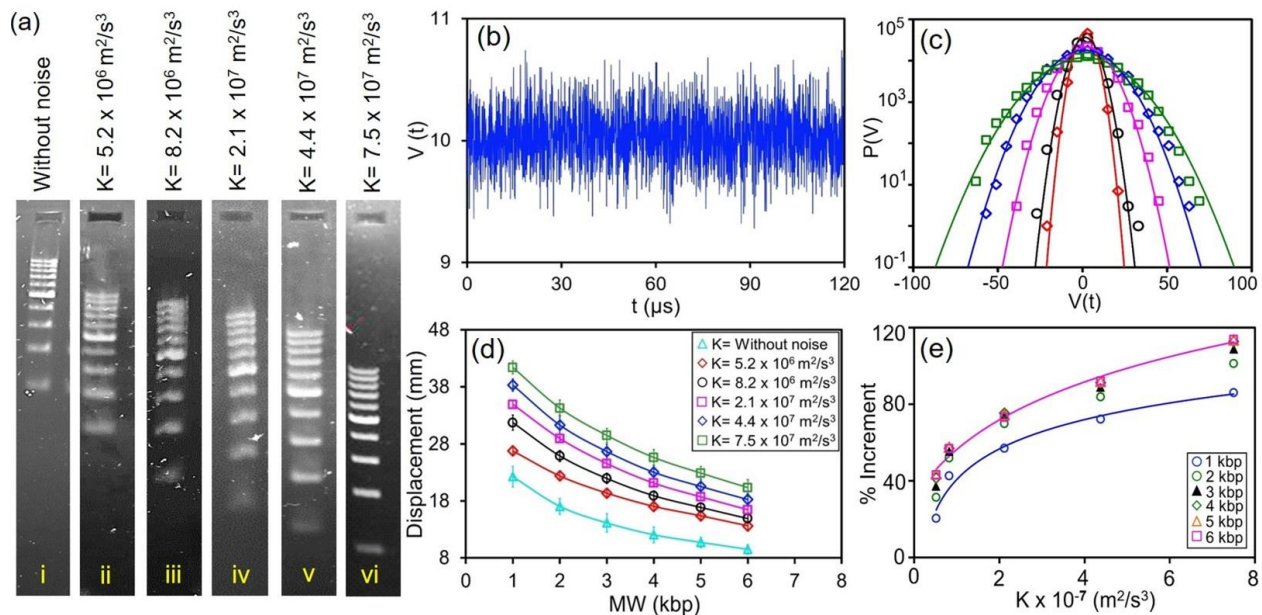


Figure 2.2. Effect of Gaussian noise on electrophoretic separation of DNA. (a) Agarose gel electrophoresis of DNA ladder (1-10 kbp) at 10 V bias for 4 h without any noise (i) and with the noise of different powers (K) depicted on the images (ii-vi). The DNA fragments in the image start

from the well (dark rectangle at the top) and then move forward (downward in the image) to the positive electrode during electrophoresis. The band for 10 kbp is the closest to the well and the band for 5 kbp has maximum brightness. (b) A typical example of a time series of noise as voltage input at a low power of the noise. (c) Semi log plot of the input noise depicting Gaussian distribution with mean $\langle V(t) \rangle = 0$. The symbols indicate the noise input corresponding to the power shown in Figure 2.2.d: cyan triangle (Δ) - without noise, red diamond (\diamond) - $K = 5.2 \times 10^6 \text{ m}^2/\text{s}^3$, black circle (\circ) - $K = 8.2 \times 10^6 \text{ m}^2/\text{s}^3$, pink square (\square) - $K = 2.1 \times 10^7 \text{ m}^2/\text{s}^3$, blue diamond (\diamond) - $K = 4.4 \times 10^7 \text{ m}^2/\text{s}^3$, and green square (\square) - $K = 7.5 \times 10^7 \text{ m}^2/\text{s}^3$, (d) Displacement of the 1 kbp to 6 kbp after 4 h of gel electrophoresis without noise and with noise having different powers shown in the inset. To minimize the error, only estimation of the displacement up to 6 kbp was considered. The error bar represents the standard deviation from the results obtained from 9 sets of experiments. (e) % Increment of the displacement was estimated for 1 – 6 kbp (black circle (\circ), green circle (\circ), filled black triangle (\blacktriangle), green diamond (\diamond), orange triangle (Δ), pink square (\square) represent 1 to 6 kbp respectively) at different power of the noise input. The percentage increment in displacement was estimated as $\% \text{ Increment} = \frac{(x_n - x_c) \times 100}{x_c}$, here x_n represents displacement for a particular DNA fragment (n) at a particular noise, and x_c is the displacement of the corresponding DNA fragment from the conventional gel electrophoresis without any noise. A typical displacement vs MW of DNA at various power of the noise but at a bias of 50 V is presented below.

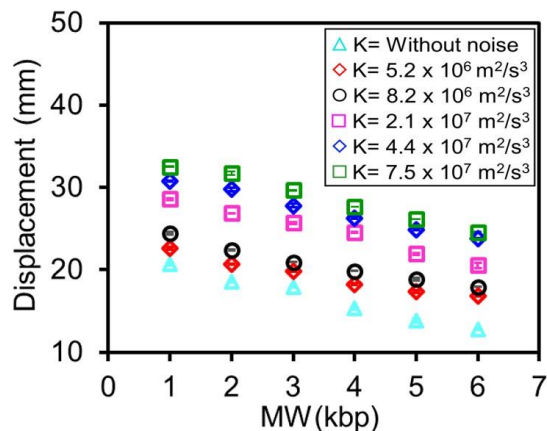


Figure 2.3. Displacement of the 1 kbp to 6 kbp after 90 min of gel electrophoresis without noise and with noise having different powers shown in the inset. Here, the symbols represent the noise powers as follows: cyan triangle (Δ) - without noise, red diamond (\diamond) - $K = 5.2 \times 10^6 \text{ m}^2/\text{s}^3$, black circle (\circ) - $K = 8.2 \times 10^6 \text{ m}^2/\text{s}^3$, pink square (\square) - $K = 2.1 \times 10^7 \text{ m}^2/\text{s}^3$, blue diamond (\diamond) - $K = 4.4 \times 10^7 \text{ m}^2/\text{s}^3$, and green square (\square) - $K = 7.5 \times 10^7 \text{ m}^2/\text{s}^3$.

Under the influence of the noise having power, $K = 5.15 \times 10^6 \text{ m}^2/\text{s}^3$ (see section 2.3.2.1 for power calculation), almost 20 % enhancement in the mobility of 1kbp DNA over the conventional gel electrophoresis was achieved. The mobility of 1 kbp DNA increased further up to 86 % with the amplified noise having the power of $K = 7.5 \times 10^7 \text{ m}^2/\text{s}^3$. The increment of mobility was found to be more than 113 % for 6 kbp DNA at the same power of the noise (Figure 2.2.e).

As reported by Burlatsky et al. sorting of the negatively charged DNA fragments based on the molecular weight is only possible in an electrophoretic setting because of the solid friction offered by the gel^{8,13}. Otherwise, free electrophoresis only in a buffer, without the gel, shows similar mobility towards a positive electrode for the large DNA molecules (having base pairs larger than $\sim 400 \text{ bp}$)^{14,15}. This suggests that the linear kinematic friction is not sufficient to resolve the large

DNA fragments. The resolution effect due to the presence of non-linear solid friction endures even in the presence of noise with increased mobility.

It is the general notion that displacement fluctuation of a free Brownian particle in a thermal bath exhibits Gaussian distribution. This is true when the particle experiences linear kinematic friction where the cause of friction is coupled with the source of the noise, - the heat bath. However, the non-Gaussian asymmetric tail of the displacement distribution, especially at the larger fluctuations, is observed when a particle/object interacts with a surface through Coulombic solid friction⁵. A similar observation is also reported in the case of a colloidal particle diffusing along a lipid bilayer tube or diffusing through the entangled F-actin network¹⁶. The use of external Gaussian noise alleviates the effect of the nonlinear solid friction (“Noise-lubricity”) and enhances the mobility retaining the resolution characteristics of the gel (Figure 2.2.a). An earlier report suggests a similar subcritical detachment of a soft elastic body from a rigid contactor in presence of mechanical noise that promotes diffusive exploration of different states in an energy landscape and selects the least action pathway¹⁷.

2.3.2. Noise Characterization

2.3.2.1. Power of the noise

The power of the noise is calculated per base pair of the nucleotide as follows:

Time-dependent random acceleration experienced per base-pair $\gamma(t) = \frac{2CV(t)}{md}$ where

C = Charge of an electron,

d = Distance between two electrodes of the electrophoretic chamber,

m = mass of a base pair,

V(t) = time-dependent voltage generated by function waveform generator,

The mean of the noise input, $\langle \gamma \rangle = 0$,

The power of the noise then calculated as $K = \langle \gamma^2 \rangle dt$,

The $\langle \gamma^2 \rangle$ denotes the mean square acceleration and dt is the noise pulse duration (40 ns).

The noise correlation time scale τ_c can be obtained from the corner frequency of the power spectra of the Gaussian white noise as described in the section 2.3.2.2. The correlation time obtained by this method is ~ 6 ns. The autocorrelation function of the noise, as shown in the figure 2.4.b, also suggest that the noise is not fully uncorrelated at very small time scale of the order of ns. Thus, the power of the noise is nominally defined as the product of the mean square acceleration and the pulse width of $dt \sim 40$ ns which is larger than 6 ns.

2.3.2.2. The power spectrum of the experimental input noise

The power spectrum of the input noise is shown in Figure 2.4.a. The power spectrum of the noise, having total bandwidth ($-f_{\max}$ to $+f_{\max}$, f_{\max} being the maximum frequency) of 50 MHz, is reasonably flat indicating the noise can be considered as white noise up to the maximum frequency f_{\max} . However, this is limited by the data sampling frequency with $dt = 40$ ns. The actual bandwidth of the input noise might be larger than this 50 MHz.

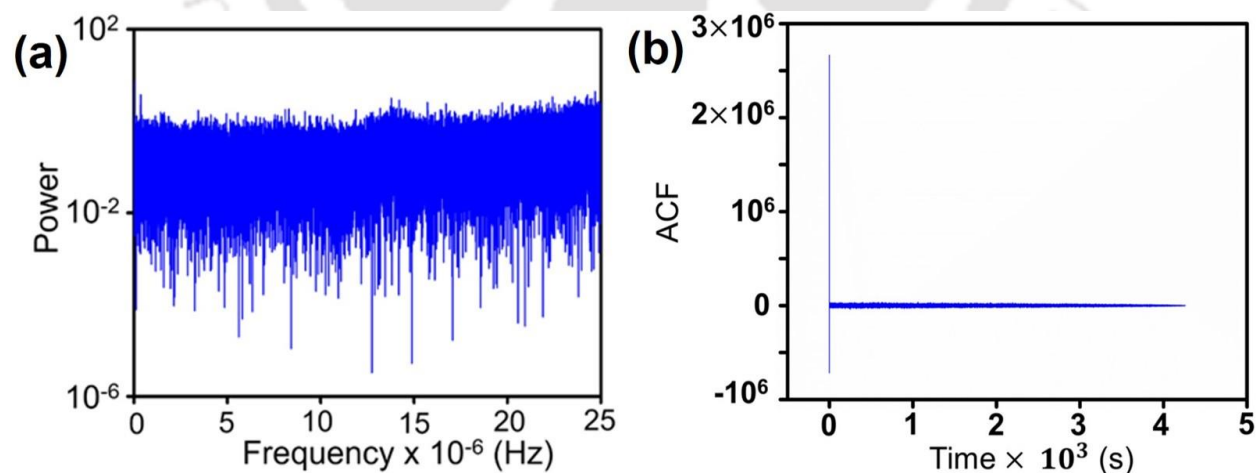


Figure 2.4. Power Spectra and autocorrelation of the input noise. (a) A typical power spectrum of the time-dependent voltage $V(t)$ as the noise input. The spectrum shows that the spectrum is

reasonably flat up to the frequency $f_c = 2.5 \times 10^7 \text{ Hz}$. As this estimation is limited by the sampling time $dt = 40 \text{ ns}$ one can expect the noise is white over a larger frequency domain than $2.5 \times 10^7 \text{ Hz}$.

(b) The autocorrelation function (ACF) of the input noise suggests the noise is uncorrelated except at a very small time scale of the order of ns.

2.3.3. Details of the Numerical Simulation

A numerical simulation of the modified Langevin Equation (Eq. 1 in the main text):

$$\frac{d\mathcal{G}}{dt} + \frac{\mathcal{G}(t)}{\tau_L} + \sigma(\mathcal{G})\Delta(x) = \bar{\gamma} + \gamma(t) \dots \dots \dots (1)$$

was carried out following the methodology of Gillespie¹⁸ using MATLAB. The DNA molecule is assumed as a point mass at the center of gravity of the molecule at any point in time. Random noise is generated as a voltage signal using an inbuilt random number generator having Gaussian distribution. The simulations were performed with an integration time step of $dt = 0.04 \text{ ps}$ so that the ratio of $\frac{\tau_L}{dt} \sim 10$.

Space dependent Δ

To introduce the space-dependent Δ , first, a set of random Δ values are generated that follows Extreme value distribution: $P(\Delta) = \frac{1}{s} \exp\left(\frac{\Delta - \Delta_m}{s}\right) \exp\left(-\exp\left(\frac{\Delta - \Delta_m}{s}\right)\right)$. Then each Δ value is assigned to the position, x , in such a manner so that over a random length (l) of space, the same Δ value will be experienced. This length (l) also follows a normal distribution.

Specific conditions for $|\Delta| > |\bar{\gamma} + \gamma(t)|$

At any instance, if the velocity of the DNA molecule is zero and the $|\Delta| > |\bar{\gamma} + \gamma(t)|$, the velocity will remain as zero unless, at a later time, one pulse of the noise $\gamma(t)$ will be sufficient enough so

that the total acceleration $|\bar{\gamma} + \gamma(t)|$ surpasses the magnitude of the Δ . If at any instance, while $|\Delta| > |\bar{\gamma} + \gamma(t)|$, the velocity is small and less than a critical value ϑ_0 , exponential decay of the velocity with the Langevin time scale τ_L is assumed. Otherwise, the full equation (A1) is integrated numerically.

2.3.4. Modified Langevin Model.

The noise used here is the time-dependent accelerations $\gamma(t) = \frac{qV(t)}{md}$, experienced by each base pair unit. Here m is the average mass of a unit base pair, q is the total charge of a base pair, d is the distance between the two electrodes, and $V(t)$ is the delta correlated time-dependent voltage (Figure 2.2.b). The distribution of the noise pulses is Gaussian (Figure 2.2. (c)). This noise-induced drifted motion of the DNA molecules can be approximated by a modified Langevin equation:

$$\frac{d\vartheta}{dt} + \frac{\vartheta(t)}{\tau_L} + \sigma(\vartheta)\Delta(x) = \bar{\gamma} + \gamma(t), \dots \dots \dots (1)$$

Here, $\bar{\gamma} = \frac{Eq}{m}$ is the bias driving force per unit base pair with $E = \frac{V}{d}$ being the electric field, pertinent to the applied constant bias voltage V . $\Delta(x)$ is the space-dependent nonlinear solid friction associated with a signum function, $\sigma(\vartheta) = \frac{\vartheta}{|\vartheta|}$, that defines the direction of the solid friction opposite to that of the instantaneous velocity, ϑ . τ_L being the Langevin relaxation time, $\frac{\vartheta}{\tau_L}$ accounts for the linear kinematic friction. This Langevin description enables us to capture the salient features of the external noise-activated dynamics of the center of mass of DNA.

Unlike the earlier reports,¹⁹ here we have considered the motion of the center of mass of a DNA molecule. Often, in gels having a high agarose concentration (corresponds to relatively small pore sizes, thus associated with higher average friction), DNA gets trapped inside the constricted pores

in loop-like conformations. In this scenario, due to size fluctuations, and the interplay between the relaxation time scale and the time period of the external forcing pulses, DNA exhibits anomalous mobility that results in band inversion^{20–22}. The location of the DNA at a given instant of time must be associated with a conformation that corresponds to a particular friction value. This friction value has to be conserved as far as the conformation is maintained and the associated location is occupied by the DNA.

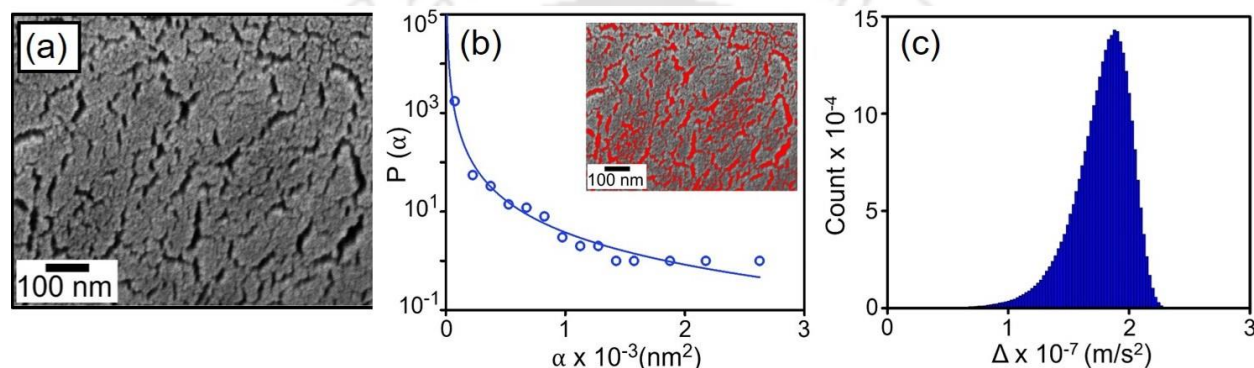


Figure 2.5. Agarose gel pore size and solid friction. (a) SEM image of the 0.8% agarose gel. The gel was initially frozen at $-20\text{ }^{\circ}\text{C}$ for overnight and then vacuum dried at 20 mTorr and $-103\text{ }^{\circ}\text{C}$ in a Lyophilizer for 24 h before the SEM analysis (b) Open-source ImageJ software was used to estimate the pore size (inset image showing the thresholding of the image). The probability distribution function $[P(\alpha)]$ of the pore size (α) (open blue circle) is fitted with the allometric regression of the form $[P(\alpha)] \sim \alpha^{-2.2}$. (c) Extreme value distribution of solid friction Δ used for the numerical simulation of the Langevin Eq. (1).

Apart from this, as evident from the FESEM image of the gel, the pore size (α) is distributed over space (Figure 2.5.a). As the solid friction is related to the constriction, defined by the pore walls, the variation of Δ , as a function of the space is thus justified. The allometric decay of the pore size (Figure 2.5.b) readily suggests that the frequency of encounters with the high solid friction sites

(small pore) by a DNA molecule is more than the number of encounters with the low solid friction sites (large pore). Thus, one can qualitatively assume an ‘Extreme value’ distribution of Δ : $P(\Delta) = \frac{1}{s} \exp\left(\frac{\Delta - \Delta_m}{s}\right) \exp\left[-\exp\left(\frac{\Delta - \Delta_m}{s}\right)\right]$, randomly dispersed over the space. Here, Δ_m is the magnitude of Δ with the maximum occurrence, and s is the scale parameter of the distribution. A typical Δ value distribution is depicted in Figure 2.5.c. While the DNA molecules slither through the pores, this random space-dependent Δ , implicitly takes into account the time-dependent molecular conformations. Granick’s group reported an interesting observation while imaging a single DNA molecule transporting through an agarose gel²³. They demonstrated that the trailing end and the leading end of a DNA molecule are stuck at the same position of an agarose matrix for quite some time before leaving the position. This observation straightaway suggests that there is a distribution of constrictions throughout the gel matrix, which encouraged us to consider the random distribution of Δ as a function of position. Also, FESEM analysis was done after the application of noise to show that there was no prominent change in the pore size distribution.

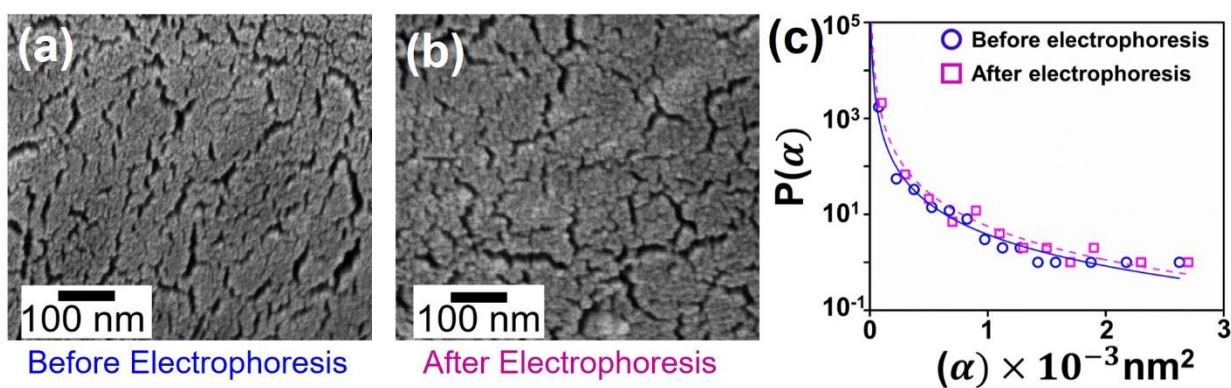


Figure 2.6. FESEM image of gel. FESEM images of agarose gel before (a) and after (b) electrophoresis experiment with noise having power $K=7.5 \times 10^7 \text{ m}^2/\text{s}^3$. The identical procedure (as mentioned in the main text) of the freeze-drying technique was used before performing the

FESEM. The pore size distributions show a negligible difference before and after electrophoresis (c).

Pore size estimation using ImageJ software

The following steps were followed to estimate the pore size:

1. Initially, the FESEM image was loaded in ImageJ software (Version 1.52s 64-bit).
2. Under the “Analyze” and under the drop-down menu, “Set Scale” was selected and from the known distance, the global scale was assigned.
3. From the “Image” option, under the drop-down menu the “Adjust” option was selected and thresholding was applied to the pores selecting “red color”.
4. Next, from the “Analyze” tab, “Analyze particles” was selected from the drop-down menu to get the pore areas.
5. The pore area values were exported in an excel sheet and then transferred to Origin Software (Version 9.0 64 Bit) to get the pore size distribution with proper fitting.
6. Next, from the “Analyze” tab, “Analyze particles” was selected from the drop-down menu to get the pore areas.
7. The pore area values were exported in an excel sheet and then transferred to Origin Software (Version 9.0 64 Bit) to get the pore size distribution with proper fitting.

Considering this space-dependent Δ , the numerical integration of Langevin Eq. 1, following Gillespie¹⁸, successfully simulates the trajectories of the DNA and captures the salient features of the dynamics. (See Figure 2.7).

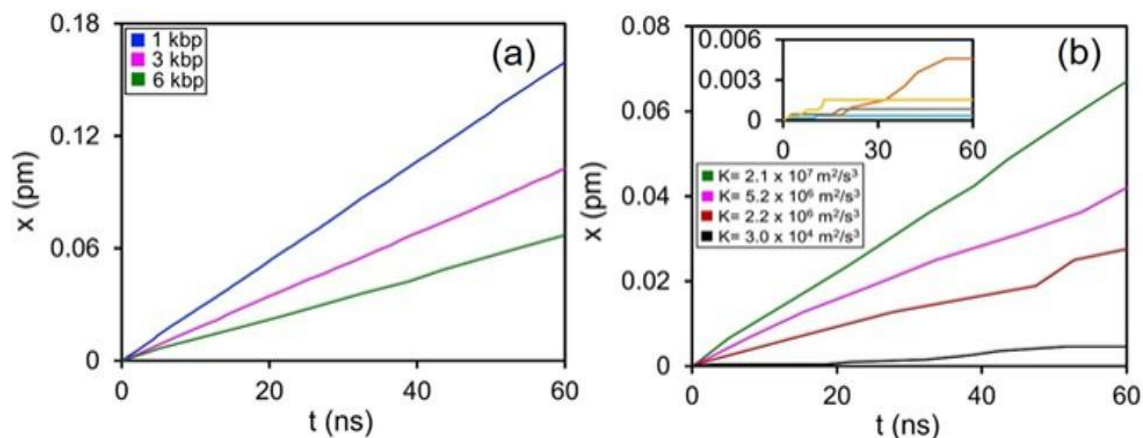


Figure 2.7. Simulation results from the Langevin Eq. (1). (a) Typical simulated trajectories of the DNA fragments (color code is shown in the inset) in gel electrophoretic setting at a particular noise $K = 2.1 \times 10^7 \text{ m}^2/\text{s}^3$. (b) Simulated trajectories of 6 kbp DNA fragment at different powers of the noise shown in the figure. Inset shows 4 different trajectories of 6 kbp DNA fragments at low power ($K = 3.0 \times 10^4 \text{ m}^2/\text{s}^3$) of the noise depicting the randomness and fluctuations during translocation.

Langevin simulation at a very low power of the noise shows considerable ‘stick’ states in the trajectories of DNA molecules at some high Δ value (i.e. at a small pore) (Figure 2.7.b inset).

Displacement distribution

From the trajectory, at different time steps, the displacement jumps were calculated. The probability density function (PDF) of the displacement \tilde{x} are depicted for 1 kbp and 10 kbp in Figure 2.8.A and 2.8.B with a peak shift of $\left(\tilde{x} = (x - x_p)\right)$. Here x_p denotes the displacement value having maximum count in the distribution of x . Due to the presence of non-linear friction, the distribution is asymmetric and having a non-Gaussian exponential tail. Assuming average solid

friction Δ , from the steady-state solution of the Klein-Kramers equation^{24,25} the PDF of the velocity distribution can be obtained as:

$$P(\vartheta) = P_o \exp\left(-\frac{\vartheta^2}{K\tau_L} - \frac{2|\vartheta|\Delta}{K} + \frac{2\vartheta E q}{K m}\right), \dots \dots \dots (A2)$$

The presence of the 2nd term within the argument of the exponential function imparts the asymmetric non-Gaussian tail in the velocity distribution that is evident from the displacement PDF. Simulation with $\Delta = 0$ must give rise to symmetric Gaussian distribution according to equation 1, and thus depicted in Figure 2.8.C for 1 kbp DNA. PDF. Simulation with $\Delta = 0$ must give rise to symmetric Gaussian distribution according to equation 1, and thus depicted in Figure 2.8.C for 1 kbp DNA.

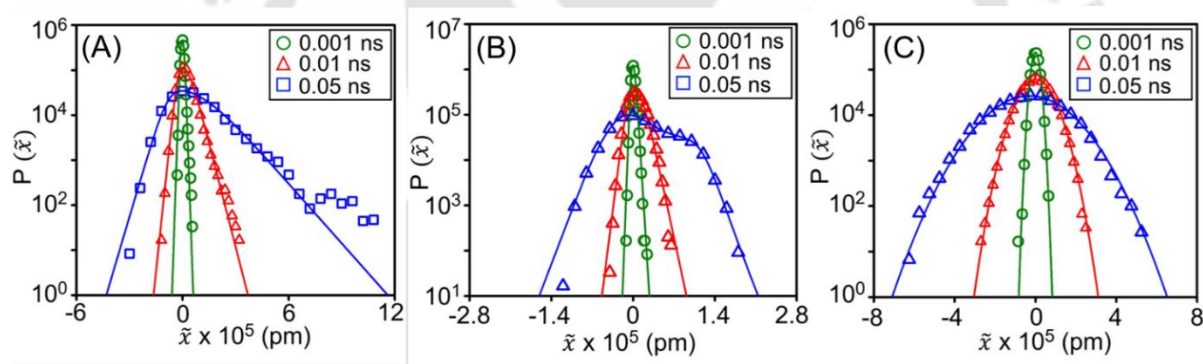


Figure 2.8. PDF of displacement fluctuation. The PDF of the displacement fluctuation in semi-log plot at different time windows (0.001, 0.01, and 0.05 ns) for 1 kbp (A) and 10 kbp (B) with space-dependent Δ . The peak position of the distribution is shifted to zero by $\tilde{x} = (x - x_p)$. The tails of these distributions are asymmetric and exponential. (C) The PDF of the displacement fluctuation for 1 kbp DNA with $\Delta = 0$ shows the Gaussian distribution.

Drift velocity calculated from the simulated trajectories are in reasonable agreement with the experimental results (Figure 2.9.a). For the longer duration of the electrophoresis with a large number of DNA molecules, one can still assume an approximate average Δ value for a particular

gel with a specific agarose concentration. Considering the linear approximation of Eq. (1) and from the Fokker-Planck solution in the velocity space, one can estimate the average drift velocity as^{3,26-28} :

$$\vartheta_d = \frac{\bar{\gamma}\tau_L}{1 + \frac{\Delta^2\tau_L}{K}}, \dots\dots\dots (2)$$

This approximate drift velocity (ϑ_d) agrees well with the experimental drift velocity of the DNA molecules with $\Delta \sim n^{0.1}$ and $\tau_L \sim n^{-0.4}$ (Figure 2.9.a). From the linearization of the Langevin equation, the approximate drift velocity can be obtained as:

$$\vartheta_d = \frac{\bar{\gamma}\tau_L}{1 + \frac{\Delta^2\tau_L}{K}}, \dots\dots\dots(2)$$

Here, $\bar{\gamma} = \frac{Eq}{m}$ is the bias driving force per unit base pair. τ_L is the Langevin relaxation time and Δ is the average solid friction force per unit base pair. The approximate drift velocity is estimated from the stationary solution of the Fokker Planck equation in velocity space^{3,26}. The drift velocity obtained from equation (2) is shown in Figure 2.9.a.

Although the approximate Eq. (2) describes the drift velocity reasonably well, its validity is somewhat dubious in the present scenario. From the fitting of the drift velocity using Eq. (2), the Langevin relaxation time τ_L is found to be of the order of $\sim 10^{-13}$ s, which is much smaller than the sampling time, dt , of the external noise input ($\frac{\tau_L}{dt} \sim 10^{-5}$). Ideally, for Eq. (2) to be applicable, the Langevin relaxation time, τ_L , should be longer than the noise correlation time scale, τ_c . However, the power spectra of the noise reveal that the noise is white till $f_c = 2.5 \times 10^7$ Hz (Figure 2.4.a). Considering this f_c as the corner frequency, the approximate correlation time constant, $\tau_c \sim 6$ ns, (from the equation, $\tau_c = \frac{1}{2\pi f_c}$). The estimation of f_c is however limited by the

experimental sampling rate of the noise data collection. Thus, one can expect that actual τ_c may be much smaller than the 6 ns as the $f_c > 2.5 \times 10^7$ Hz. In support of this smaller noise correlation, numerical simulation of the Langevin Eq. (1), satisfactorily agrees with the experimental drift velocity with $\frac{\tau_L}{dt} \sim 10$ (Figure 2.9.a).

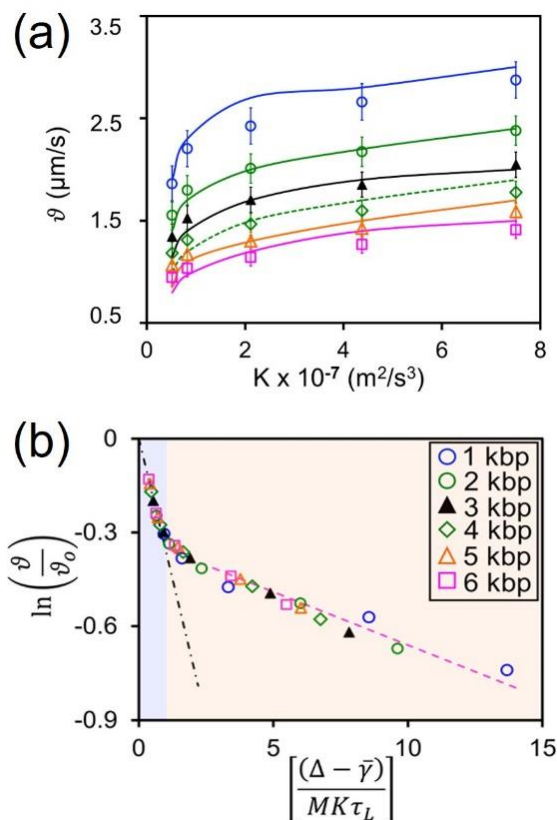


Figure 2.9. (a) Comparison of the drift velocity obtained from the 30 simulations for each case (curves) and the experiments (solid symbols). The error bar for the experimental data depicts the standard deviation of the results obtained from 9 sets of experiments in each case. (b) Arrhenius/Non-Arrhenius-like behavior. The velocity data for all the fragments (1 – 6 kbp) are plotted following Eq. (3) having $\Delta \sim n^{0.1}$ and $\tau_L \sim n^{-0.4}$. The blue shaded (high K) region shows noise-activated Arrhenius-like behavior and is represented with a black dash-dot line. Whereas, the yellow shaded (low K) region depicts Super-Arrhenius behavior, – the velocity obtained is

much higher (shown with a pink dash line) than that expected from Arrhenius prediction (black dash-dot line).

2.3.5. Escape rate of the DNA molecule

As discussed above, the energy barrier, E_a , originates from the nonlinear interactions of DNA molecules with the gel matrix. Solid friction, Δ , being the significant contributor to the nonlinear interactions, one can assume the scaling of the energy barrier $E_a \sim \Delta$ as the first approximation. The rate of the detachment of DNA molecules from the gel matrix manifests in the drift velocity of the molecules and can be represented as:

$$\vartheta = \vartheta_o \exp \left[-\frac{c(\Delta - \bar{\gamma})}{MK\tau_L} \right], \dots \dots \dots (3)$$

Here C is a constant and ϑ_o is the critical velocity while the biased force per unit mass, $\bar{\gamma}$, is sufficient to transcend the energy barrier, i.e. $\bar{\gamma} \approx \Delta$. The energy supplied through the external noise, $MK\tau_L$, represents the mechanical analog to thermal energy $k_B T$, where M is the molecular weight of DNA. While $\ln \left(\frac{\vartheta}{\vartheta_o} \right)$ is plotted against $\left[\frac{(\Delta - \bar{\gamma})}{MK\tau_L} \right]$ all the velocity data for different DNA fragments merge into a single master curve with the same average Δ values used for Eq. (2) (Figure 2.9.b). Although at the high power of the noise (K), the velocity follows the Arrhenius-Eyring^{26,29} like equation (black dash-dot line in Figure 2.9.b), it exhibits Super-Arrhenius-like behavior (pink dashed line in Figure 2.9.b) at a low power of the noise. Arrhenius expression for a kinetic process implicitly assumes a single and well-defined rate-limiting energy barrier to transcend. However, the free energy landscape of gel electrophoresis is populated with multiple metastable states separated by saddle points. Thus a process in which a particle or molecule maneuvers through these pathways overcoming the multiple saddle points, bypassing the pinnacles of the energy barriers, exhibits Non-Arrhenius kinetics.

The super Arrhenius behavior is often observed in thermally activated viscous slowing down of a weakly bonded glass-forming liquid in a super-cooled regime³⁰. At a temperature lower than a characteristic threshold temperature T^* for a liquid, its viscosity follows Super-Arrhenius behavior. This is attributed to the collective and cooperative nature of the thermally activated system at low temperature ($T < T^*$) for a weakly bonded system. At the low power of the noise (analogous to low temperature), super Arrhenius behavior of DNA translocation indicates that the dynamics are influenced by the cooperative motion of DNA, affected by prominent non-linear friction. The magnitude of this friction is distributed over a wide range and is the source of space-dependent energy barriers. DNA molecule translocates through the different pathways meandering downhill of the energy landscape towards the global equilibrium. In this quest, DNA may stick to a local energy pit until and unless a high-energy noise pulse rescues it. However, the overall motion of the DNA is collectively emerging as space averaged drift velocity. At a high power of the noise, the effect of the nonlinear friction is alleviated by frequent such rescue events. Thus, free-flowing yet noise-activated Arrhenius characteristics emerge at high athermal energy.

2.4. Conclusions

Our experiments demonstrate that the mobility of DNA molecules in gel electrophoretic settings can be significantly faster ($\sim 100\%$ or more) than the conventional gel electrophoresis³¹ with the aid of external Gaussian noise. The drift velocity of the DNA induced by activated “noise-lubricity” follows the Arrhenius-Eyring-like escape rate at the high energy of the external noise. Whereas, at low energy, the cooperative dynamics of the DNA molecules impart super Arrhenius-like behavior. A modified Langevin simulation successfully predicts the drift velocity for an applied bias and noise, along with the consideration of space-dependent nonlinear solid friction, originating from the wide distribution of the gel pore size. In contrast to the conventional notion,

this study reveals that an enormous amount of solid friction ($\sim 10^7$ m/s²) is operative at the interface of the DNA-gel matrix. Activated translocation can be observed from the sub molecular electronic level (due to thermal noise)³² to the macroscopic objects (due to mechanical noise)³³ as well. This work suggests strategies for noise-activated faster DNA fingerprinting and sets up the platform for advanced research on resonance-induced super mobility³⁴ for the isolation of a specific protein fragment from a crowd.

References

1. Daniel, S., Chaudhury, M. K. & Chen, J. C. Fast Drop Movements Resulting from the Phase Change on a Gradient Surface. *Science (80)*. **291**, 633–636 (2001).
2. Bormuth, V., Varga, V., Howard, J. & Schaffer, E. Protein Friction Limits Diffusive and Directed Movements of Kinesin Motors on Microtubules. *Science (80)*. **325**, 870–873 (2009).
3. De Gennes, P. G. Brownian motion with dry friction. *J. Stat. Phys.* **119**, 953–962 (2005).
4. Goohpattader, P. S. & Chaudhury, M. K. Diffusive motion with nonlinear friction: Apparently Brownian. *J. Chem. Phys.* **133**, (2010).
5. Goohpattader, P. S., Mettu, S. & Chaudhury, M. K. Experimental investigation of the drift and diffusion of small objects on a surface subjected to a bias and an external white noise: Roles of coulombic friction and hysteresis. *Langmuir* **25**, 9969–9979 (2009).
6. Muthukumar, M. Polymer translocation through a hole. *J. Chem. Phys.* **111**, 10371–10374 (1999).

7. Muthukumar, M. Theory of sequence effects on DNA translocation through proteins and nanopores. *Electrophoresis* **23**, 1417–1420 (2002).
8. Burlatsky, S. & Deutch, J. Influence of solid friction on polymer relaxation in gel electrophoresis. *Science* **260**, 1782–1784 (1993).
9. Burlatsky, S. F. & Deutch, J. M. Solid friction in gel electrophoresis. *J. Chem. Phys.* **103**, 8216–8227 (1995).
10. Viovy, J. L. Electrophoresis of DNA and other polyelectrolytes: Physical mechanisms. *Rev. Mod. Phys.* **72**, 813–872 (2000).
11. Viovy, J. L., Duke, T., Burlatsky, S. & Deutch, J. Solid friction and polymer relaxation in gel electrophoresis. *Science* (80). **264**, 112–113 (1994).
12. De Gennes, P. G. Reptation of a polymer chain in the presence of fixed obstacles. *P.G. Gennes' Impact Sci. Soft Matter Biophys.* **2**, 35–42 (2009).
13. Slater, G. W., Kenward, M., McCormick, L. C. & Gauthier, M. G. The theory of DNA separation by capillary electrophoresis. *Curr. Opin. Biotechnol.* **14**, 58–64 (2003).
14. Olivera, B. M., Baine, P. & Davidson, N. Electrophoresis of the Nucleic Acids. *Biopolymers* **2**, 245–257 (1964).
15. Stellwagen, N. C. Electrophoresis of DNA in agarose gels, polyacrylamide gels and in free solution. *Electrophoresis* **30**, 188–195 (2009).
16. Wang, B., Anthony, S. M., Sung, C. B. & Granick, S. Anomalous yet Brownian. *Proc. Natl. Acad. Sci. U. S. A.* **106**, 15160–15164 (2009).

17. Chaudhury, M. K. & Goohpattader, P. S. Noise-activated dissociation of soft elastic contacts. *Eur. Phys. J. E* **35**, 131 (2012).
18. Gillespie, D. T. The mathematics of Brownian motion and Johnson noise. *Am. J. Phys.* **64**, 225–240 (1996).
19. Duke, T. A. J. & Viovy, J. L. Simulation of megabase DNA undergoing gel electrophoresis. *Phys. Rev. Lett.* **68**, 542–545 (1992).
20. Noolandi, J., Rousseau, J., Slater, G. W., Turmel, C. & Lalande, M. Self-Trapping and Anomalous Dispersion of DNA in Electrophoresis. *Phys. Rev. Lett.* **58**, (1987).
21. Lalande, M., Noolandi, J., Turmel, C., Rousseau, J. & Slater, G. W. Pulsed-field electrophoresis: application of a computer model to the separation of large DNA molecules. *Proc. Natl. Acad. Sci. U. S. A.* **84**, 8011–8015 (1987).
22. Zimm, B. H. Size fluctuations can Explain Anomalous Mobility in Field-Inversion Electrophoresis of DNA. *Phys. Rev. Lett.* **61**, 2965–2968 (1988).
23. Guan, J., Wang, B., Bae, S. C. & Granick, S. Modular stitching to image single-molecule DNA transport. *J. Am. Chem. Soc.* **135**, 6006–6009 (2013).
24. Kramers, H. A. Brownian motion in a field of force and the diffusion model. *Phys.* **7** 284–304 (1940).
25. Risken, H. *The Fokker-Planck-Equation. Methods of Solution and Applications.* Springer-Verlag vol. 18 (1989).
26. Goohpattader, P. S. & Chaudhury, M. K. Random motion with interfacial contact: driven

- diffusion vis-à-vis mechanical activation. *Eur. Phys. J. E. Soft Matter* **35**, 67 (2012).
27. Caughey, T. K. & Dienes, J. K. Analysis of a nonlinear first-order system with a white noise input. *J. Appl. Phys.* **32**, 2476–2479 (1961).
 28. Kawarada, A. & Hayakawa, H. Non-Gaussian velocity distribution function in a vibrating granular bed. *J. Phys. Soc. Japan* **73**, 2037–2040 (2004).
 29. Eyring, H. Viscosity, Plasticity, and Diffusion as Examples of Absolute Reaction Rates. *J. Chem. Phys.* **283**, 283–291 (1936).
 30. Tarjus, G., Kivelson, D. & Viot, P. Viscous slowing down of supercooled liquids as a temperature-controlled super-Arrhenius activated process: A description in terms of frustration-limited domains. *J. Phys. Condens. Matter* **12**, 6497–6508 (2000).
 31. SMITHIES, O. Zone electrophoresis in starch gels: group variations in the serum proteins of normal human adults. *Biochem. J.* **61**, 629–641 (1955).
 32. Franca, L. G., Long, Y., Li, C., Danos, A. & Monkman, A. The Critical Role of $n\pi^*$ States in the Photophysics and Thermally Activated Delayed Fluorescence of Spiro Acridine-Anthracenone. *J. Phys. Chem. Lett.* **12**, 1490–1500 (2021).
 33. Chaudhury, M. K. & Goohpattader, P. S. Activated drops: Self-excited oscillation, critical speeding and noisy transport. *Eur. Phys. J. E* **36**, (2013).
 34. Socoliuc, A. *et al.* Atomic-Scale Control of Friction by Actuation of Nanometer-Sized Contacts. *Science (80)*. **313**, 207–210 (2006).



CHAPTER 3

Investigation on the effect of Gaussian White noise orthogonal to the drift of DNA in gel electrophoresis

Contents

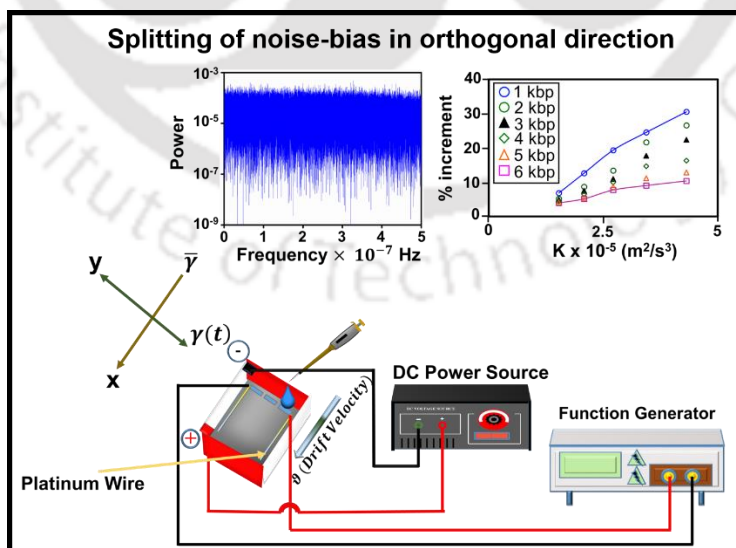
ABSTRACT.....	74
3.1. Introduction.....	75
3.2. Materials and Methods.....	77
3.2.1. Materials.....	77
3.2.2. Preparation of Gel.....	78
3.2.3. Experimental Methodology.....	78
3.2.4. Instruments used	80
3.3. Results and Discussion.....	80
3.3.1. Simulation model.....	80
3.3.2. Role of solid friction.....	83
3.3.3. Noise assisted DNA translocation through nanoporous matrix.....	86
3.3.4. Modified Langevin equation for predicting DNA mobility.....	89
3.3.5. Displacement trajectories tracked using simulation model.....	91
3.4. Conclusions.....	94
References.....	96



ABSTRACT

In this chapter, we have devised a novel strategy using the splitting of noise-bias in orthogonal direction to dislodge a DNA molecule traversing through a porous gel matrix such that the separation process is enhanced and the molecule takes the least energy pathway to reach the final destination. The devised experimental setup resembled like conventional agarose gel electrophoresis setup and we were able to get an enhanced drift velocity of 1 kbp DNA $\sim 30\%$ than conventional agarose gel electrophoresis. A comparison was made with unidirectional noise-bias assisted gel electrophoresis setup which showed $\sim 18\%$ increment when compared with conventional gel electrophoresis for 1 kbp DNA. This enhancement is justified on the basis of external noise alleviating the effect of solid friction and also providing the DNA enough energy to translocate through the minimal energy landscape. This developed model can be the backbone of many miniaturized macromolecule separation devices enabling rapid and easy solution to human society.

Graphical Abstract



Keywords: DNA translocation, orthogonal noise-bias, Langevin dynamics, solid friction.

3.1. Introduction

The translocation of polymers across membranes through nanopores is one of the crucial in biological processes at the cellular level¹ and in developing DNA analysis techniques. Applications such as nanopore-based sequencing technologies have led to numerous experimental, theoretical, and computational studies of polymer translocation²⁻⁴. Literatures have revealed that there happens to be a conundrum that it is difficult to separate different fragments of DNA in free solution. One possible way to overcome this barrier is to introduce a porous hydrogel matrix that will interact with the DNA, as it travels through under the influence of biased force. Longer DNA will experience more interactions as it traverses through the matrix. Literatures have uncovered two predominant transport regimes that can be accessed to separate DNA based on length by gel electrophoresis⁵. The first regime is that of Ogston sieving⁶, where the availability of free space within the matrix is much larger than the DNA size and DNA travels without any hindrance and in unperturbed form. The second well established regime is reptation regime⁷ which conveys the fact that the DNA size is larger than the free size formed by the matrix. Herein, the molecular transport of DNA through the gel pores occurs like a snake-like motion along its contour and mobility is inversely related to DNA length. The biased reptation⁸ with fluctuations model^{9,10} modified the biased reptation model (BRM) model accounting for the effective tube-length fluctuations¹⁰ which lead to qualitatively different answers for mobility as a function of polymer chain length. Adding noise to sliding dynamics problems creates a new domain of research. Simple examples of noise-induced motion can be found in nature which can be encountered in day-to-day life scenarios. A tiny water droplet on a glass surface may not move even when the glass surface is kept vertical^{11,12}. When the glass surface is vibrated the liquid drop gets enough energy to overcome the energy barrier and move on the surface. An intriguing recent finding also

shed light on the field of research wherein the presence of the self-generated noise can affect the flow behavior of non-linear systems. Researchers have depicted that in the wetting dynamics domain, the coalescence of condensing droplets leads to self-generated noise in which the coalescing droplets undergo a random motion on a surface due to the internal gradient of Laplace pressure^{13,14}. Suppose there is an external field, such as wettability gradient or temperature, the condensed drops drift towards a prescribed direction with its rate controlled by the difference between the temperatures of the steam and the substrate¹⁵. The basic notion behind all these examples is the direction of the drifted motion, which is dictated by the applied bias decoupled from the direction of random fluctuating noise pulses. Conventional gel electrophoresis provides an excellent fractionation of molecules within limited size ranges. For longer DNA molecules, the ability of gels to provide good fractionation has been attributed to how the mesh of cross-linked gel fibers obliges the DNA to wriggle end-on along a contorted path¹⁶. The description of this process by the reptation model can account for: the inverse dependence of mobility on molecular weight that is observed experimentally at low field strengths and the transition to length independent mobilities at high molecular weights, which is shown to be a consequence of the orientational effect of the field^{17,18}. The present research is aimed at displaying the driven mobility of the DNA macromolecule through the gel matrix network; in presence of external Gaussian white noise, which is sufficient to set free a stuck object/macromolecule in a noisy environment. A simple phenomenological model is developed that fits our data exceptionally well within the framework of a modified Langevin equation to showcase the enhancement of mobility and non-linear displacement statistics within the molecular domain using external Gaussian white noise and bias voltage.

We have introduced a simple methodology to incorporate the splitting of external applied noise and subcritical bias voltage in orthogonal direction to estimate the effect on DNA drift velocity using the conventional gel electrophoretic setup. The inclusion of noise was done in a simple way to emulate the stochastic dynamics of the macromolecule translocation which helps us to understand the detachment from the wall of the gel matrix, wherein an electric field driven DNA has to overcome these interactions¹⁹. The application of faster DNA translocation within porous matrix will certainly benefit the prevalent separation techniques. In electrophoresis, the emergence of new techniques is based on a general scheme: **miniaturization**. The basic premise is that conventional electrophoretic setup can be remodeled using the addition of external noise input which can be efficient and robust in healthcare and biomedical setting.

3.2. Materials and Methods

3.2.1. Materials

The basic raw materials for gel preparation, agarose powder and Ethidium bromide was purchased from (Loba Chemie). Tris Acetate-EDTA (TAE) buffer from Himedia, and the DNA (1 kbp to 10 kbp) molecular weight (MW) ladder was procured from Takara Bio Inc. Miniphor UVT System (Serial No. 106888 GB) was adopted for the horizontal gel electrophoresis and connected with a DC power supply unit (GeNei Electrophoresis Power Supply, 0-500V, 0-500 mA). For the purpose of noise generation and amplification of the generated signal, a function waveform generator (KEYSIGHT 33600A) with proper parameters was used. The noise generated was then characterized accordingly, the output was connected to an oscilloscope (GW INSTEK MDO-

2000A) and the noise data was stored using external USB drive. Platinum wire was procured from Alfa Aesar (Specifications: 0.127 mm (0.005 in) diameter, hard, 99.9% metal basis, Length 1m).

3.2.2. Preparation of Gel

Agarose gel (0.8% (w/v)) was made by dissolving 0.8 g of agarose powder in 100 ml of 1X Tris acetate-EDTA (TAE) buffer. The agarose was allowed to settle in the solution by mixing thoroughly and subsequently kept in a microwave oven for boiling (Make: Samsung, Model No. MC28H5023AKTL) at a power of 900 W for a duration of 1 min. The measured solution temperature was less than 100⁰ C. The solution was then allowed to cool down to ~30⁰ C and henceforth, 3 μ L of 0.5 mg/mL aqueous Ethidium bromide (EtBr) was added. EtBr was used because upon binding of the same to the DNA and illumination using UV light source, the visualization of DNA is possible. TAE buffer is used to maintain the pH of the solution ~8 because changes in pH can affect the net charge of the nucleic acids. The agarose gel was cast on a gel electrophoretic platform consisting of gel comb placed at one end for creating wells wherein DNA loading is done. The agarose solution was allowed to settle down in the chamber for 2 h to get the final desired agarose gel.

3.2.3. Experimental Methodology

The DNA molecular weight ladder (Takara Bio) was loaded into the wells of the gel. The loading of DNA ladder into the wells was done in a way such that positive pressure was maintained on the sample to prevent bubbles or buffer from entering the tip. The DNA ladder dissociates into ten fragments (1 kbp to 10 kbp) in the gel matrix. The gel was run at 10V DC voltage for a period of 4 h. The temperature of the gel and the TAE buffer was maintained at 23 \pm 1 $^{\circ}$ C. Visualization of the DNA fragments were done using Gel Doc (Chemidoc XRS+ system) instrument. The system software attached captures the images at various modes of magnification. White noise generated

and amplified subsequently using function waveform generator (KEYSIGHT 33600A) which influences the change in mobility over conventional gel electrophoresis by the combination of bias force (voltage) and the white noise. By modulating the applied external Gaussian white noise along with the bias, an accelerated mobility and reduced diffusion phenomenon happens. By controlling the amplification of the noise generated using the function generator, white noise of different powers was used while keeping the pulse width constant at (20 ns). In the case of orthogonal splitting of noise-bias, the electrophoretic separation involves two platinum wires spaced equally 0.5 cm apart on both sides of the gel, which is connected to function waveform generator shown in Figure 3.1. To characterize the noise, the output was connected to an oscilloscope and the noise data are stored. The stored data then was extracted for further analysis. The minimum interval for the sampling data was 20 ns. The dynamics of electrophoretic separation of the DNA fragments were studied using ImageJ software.

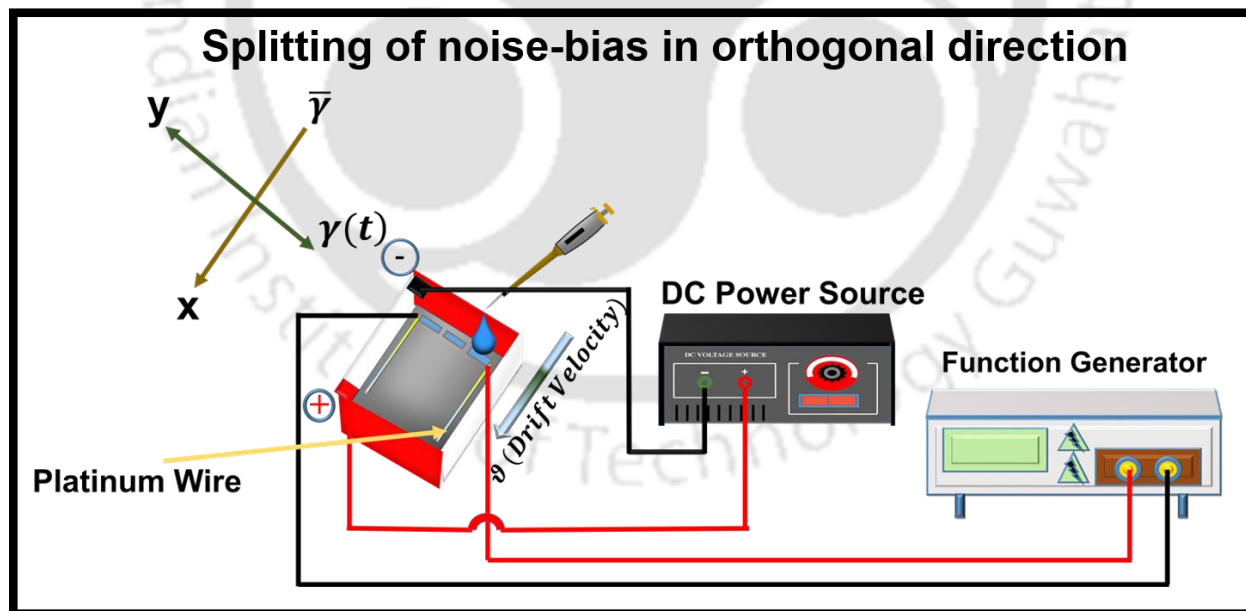


Figure 3.1. Schematic of the experimental setup involving the splitting of noise bias in orthogonal direction. The noise is generated as voltage pulses from the function generator which is fed in such

a way that the bias direction ($\bar{\gamma}$ is the term for bias force along X-direction) and the noise fluctuations ($\gamma(t)$) is the term for external noise fluctuations along Y- direction) are completely orthogonal across the gel interface. The role played by $\bar{\gamma}$ and $\gamma(t)$ are discussed in the subsequent sections and adopted using the modified Langevin equation described in section 3.3.1. The resulting potential is generated due to the presence of TAE buffer and subsequently applied across the two electrodes of the electrophoretic chamber.

3.2.4. Instruments used

The details (Make/Model no.) and use of the following instruments are mentioned below:

Waveform generator (Model: KEYSIGHT 33600A) was used for generating Gaussian white noise in the form of voltage pulses.

Oscilloscope (Model: GW INSTEK MDO-2000A) was used for collecting the noise data generated from the waveform generator.

Electrophoretic chamber (Model: Miniphor UVT System 106888GB) was used to perform the agarose gel electrophoresis to separate the DNA bands.

UV illumination/gel documentation chamber (Make: Chemidoc XRS+ System with Image Lab Software #1708265) was used to visualize the DNA fragments.

3.3. Results and Discussion

3.3.1. Simulation model developed using modified Langevin equation

The basic structure of the numerical simulation used for predicting the drift velocity of the DNA was similar to the previous chapter¹⁹. A linearization of the modified Langevin equation was

performed according to the methodology of Gillepsie²⁰. The DNA molecule was assumed to be point mass at the center of gravity of the molecule at any given time while developing the model. DNA molecule has a complex structure and due to that, at different instants, the molecule gets stuck at the gel matrix while availing different conformations. Because of these conformations, the DNA experiences different frictional forces while undergoing electrophoresis. Burlatsky and Deutch already reported this fact in their seminal work in 1995²¹. However, the objective of this chapter is to capture the dynamics of DNA molecules during electrophoresis and identify the effect of the friction in a much-simplified manner without compromising the essence of the true dynamics. Thus we assumed the point mass of DNA without assuming the complex structure and its conformations but incorporated the effect of the conformations by assuming the random space-dependent friction to the point mass. The random noise used as volt signal was generated using the inbuilt plugin random number generator having Gaussian distribution. The simulation model was devised in a planned manner having an integration time step of $dt = 0.04$ ps such that the ratio of $\frac{\tau L}{dt}$ is of the order of ~ 10 . The purpose of using “Noise” in our study is to reduce the effect of friction to make the DNA drift faster. Using the inbuilt plugin within the Matlab software, random noise was generated. We have considered the inherent presence of thermal noise/fluctuations within the electrophoretic system while developing our simulation model. As, the DNA moves through the gel matrix, the total acceleration of the biomolecule (DNA) along X- direction is the summation of (bias force+ thermal noise). The bias force is related to the biased voltage and also the distance between two electrodes. Along with, the total acceleration of the DNA along Y- direction is the summation of external white noise generated using the random number generator (rand) and thermal noise. The power of the external white noise was adjusted by proper scaling

parameters. Modified Langevin equation was used to predict the DNA molecules' s drifted motion (along X and Y-direction) defined as follows:

$$\frac{d\vartheta_x}{dt} + \frac{\vartheta_x(t)}{\tau_L} + \sigma(\vartheta_x)\Delta(x) = \frac{Eq}{m}, \dots\dots\dots \text{(along X- direction)... (1)}$$

$$\frac{d\vartheta_y}{dt} + \frac{\vartheta_y(t)}{\tau_L} + \sigma(\vartheta_y)\Delta(y) = \gamma(t), \dots\dots\dots \text{(along Y- direction) ... (2)}$$

The power of the noise calculated per base pair of the nucleotide is defined as follows:

Time-dependent random acceleration experienced per base-pair $\gamma(t) = \frac{2CV(t)}{md}$ where

C = Charge of an electron,

d = Distance between two electrodes of the electrophoretic chamber,

m = mass of a base pair,

V(t) = time-dependent voltage generated by function waveform generator,

The mean of the noise input $\langle \gamma \rangle = 0$,

The power of the noise then calculated as $K = \langle \gamma^2 \rangle dt$,

The $\langle \gamma^2 \rangle$ denotes the mean square acceleration and dt is the noise pulse duration (20 ns).

The noise that is used in our developed simulation model is based on time dependent accelerations

$\gamma(t) = \frac{qV(t)}{md}$ experienced by each base pair unit. Here, in this formula m is the average mass of a

unit base pair, q is the total charge of a base pair, d is the distance between the two electrodes, and

$V(t)$ is the delta correlated time-dependent voltage. The distribution of the noise pulses is Gaussian.

Also, in eq. (1) $\bar{\gamma} = \frac{Eq}{m}$ represents the biased force per unit mass acting on the DNA molecule

wherein $E = \frac{V}{d}$, is the electric field pertinent to the applied constant bias voltage V and $\Delta(x)$ is the

space-dependent solid friction associated with a signum function $\sigma(\vartheta) = \frac{\vartheta}{|\vartheta|}$ that defines the

direction of the solid friction opposite to that of the instantaneous velocity, ϑ as used in our model.

Similarly, along Y- direction we have considered the effect of space dependent $\Delta(y)$ in our

developed simulation model. We have adopted the simulation model approach of DNA drift velocity using external applied noise, considering DNA as a point mass without any other specific configuration unlike other research works²² and assumed the translocation of the center of mass in our study. The displacement trajectories traced out from the simulation model verify the fact that net drift of DNA is along the X- direction (bias force) and depicted in figure 3.2.A. The noise pulses generated and acting on the DNA molecule along the Y- direction is depicted in figure 3.2.B. The role played by solid friction is immense in our developed model which is discussed in the next section 3.3.2.

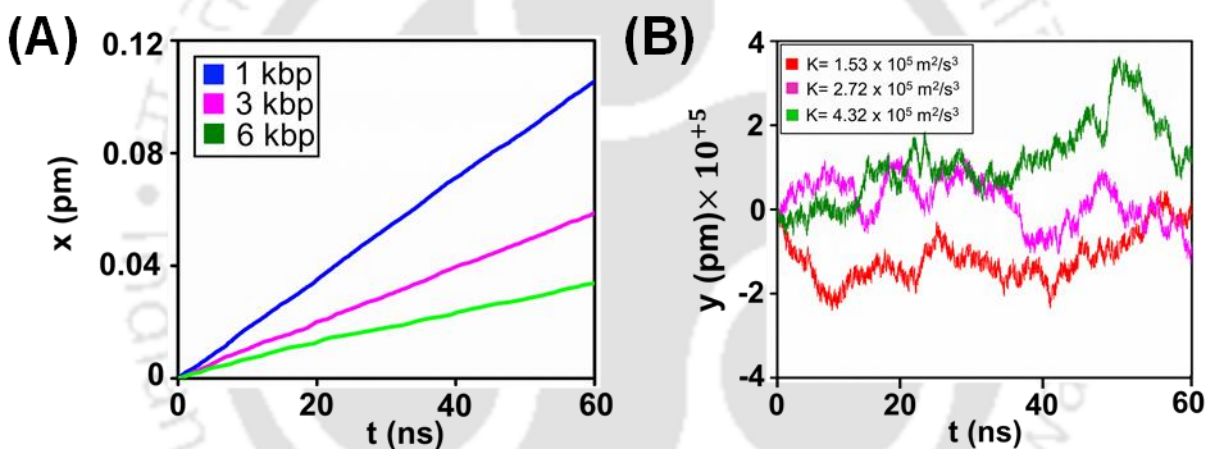


Figure 3.2. (A) Typical simulated trajectories of the DNA fragments (color code is shown in the inset) in gel electrophoretic setting tracked at a particular noise power $K = 4.32 \times 10^5 \text{ m}^2/\text{s}^3$ along X direction. (B) Noise fluctuations along the Y direction in gel electrophoretic setting for $n= 1 \text{ kbp}$ at different noise powers K (shown in inset).

3.3.2. Role of solid friction in gel electrophoresis

Separation of larger molecules based on size and length is typically conducted in a gel medium. Agarose is the chosen medium because it doesn't bind with DNA molecules. Solid friction in gel

electrophoresis can drastically affect the polymer translocation in gel electrophoresis²³. The effect is present when a polymer chain becomes entangled over different gel points distributed over space, leading to a significantly different behavior than predicted by conventional gel electrophoresis theory. Burlatsky et al.²¹ in 1995 acknowledged the influence of solid friction predominating on polymer chain translocation. The authors showcased that the presence of solid friction can drastically change the mobility of the polymer chain dynamics which leads to trapping of long chain molecules with numerous entanglements. Viovy et al.²⁴ contradicted the claims made by Burlatsky and John Deutch regarding the solid friction effects as the polymer chain traverses through the gel matrix.

At the molecular level, the effect of electric field forces polymer segments against the gel fiber's, which dissipates energy by distortion, displacement of solvent and transfer of mechanical energy between local vibrations. We examined the consequences of friction between the moving segments of polymer chain and the gel points distributed over space based on a simulation on modified Langevin model which is discussed already in the section 3.3.1. In a conventional scenario, an extended polymer chain which is assumed to be uniformly charged, is dragged free from its nearby entanglements about a fixed gel point by the action of external field. The non-linear interactions between the DNA molecules and the pores of the gel matrix gives rise to the solid frictional effect which we have considered in our simulation model. Henceforth, the solid friction factor is related to the pore constrictions and distributed throughout the entire space. To introduce the space dependent Δ in our simulation model, we have generated a set of Δ values using the extreme value distribution in both X and Y directions: $P(\Delta) = \frac{1}{s} \exp\left(\frac{\Delta - \Delta_m}{s}\right) \exp\left(-\exp\left(\frac{\Delta - \Delta_m}{s}\right)\right)$. Then each Δ value is assigned to the position, x & y independently, in such a manner so that over a random

length (l) of space, a different Δ value will be experienced in both directions. This length (l) also follows a normal distribution.

So, to prove the presence of solid friction we have considered two specific scenarios: (1) considering the presence of solid friction within the gel matrix, we have approached to develop our simulation model in such a manner that ($\tau_L \sim n^{-0.56}$) and Δ exists throughout space, and consequently adjusted in such a way to match the initial experimental drift velocity without any noise using proper scaling parameters. Here n represents the number of base pairs of DNA in kb unit. Thereafter, with the addition of random white noise the simulated DNA drift velocity profile was computed and matched with the experimental DNA drift velocity (with external noise assisted) as shown in figure 3.3.A. In another scenario: (2) considering the absence of solid friction within the gel matrix, we have adopted a specific approach considering that ($\tau_L \sim n^{-0.45}$) and Δ is not present, such that the simulated DNA velocity profile is computed and matched with the experimental DNA drift velocity (without the presence of noise) using proper scaling parameters. Henceforth, with the addition of random white noise the simulated DNA drift velocity profile is matched with the experimental DNA drift velocity (with external noise) with proper parameters as shown in figure 3.3.B. One inevitable conclusion that can be drawn from our developed model is that when solid friction is present, noise assisted DNA drift velocity shows comparable response (considering both the simulation and experimental approach) to overcome the gel pore barriers and traverse faster whereas when solid friction is not present there is no viable change in the DNA drift velocity even when external noise is applied as shown in figure 3.3.B. Henceforth, the presence of solid friction which is related to constrictions defined by the pore walls, the variation of Δ as function of space is justified accordingly and fits our simulation model. Since, we have proved the influence of solid frictional forces acting on the DNA molecule translocating through the porous

matrix hence, free electrophoresis only in buffer, without the gel, depicts identical mobility towards (+ ve) electrode for larger DNA molecules (having base pairs larger than ~400 bp)²⁵. This gives an idea that only kinematic friction is not able to screen DNA fragments.

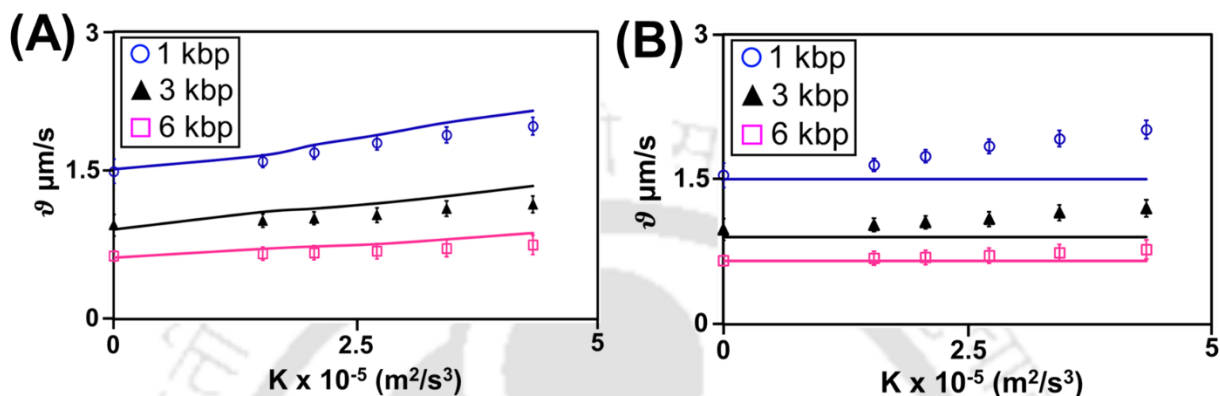


Figure 3.3. Role of solid friction on DNA mobility. (A) Plot of Velocity vs power of noise for $n=1, 3$ and 6 kbp with finite τ and δ (implying presence of solid friction). The symbols represent the experimental drift velocity whereas the solid lines represent the simulation velocity obtained from 30 simulations in each case for different DNA fragments. (B) Plot of Velocity vs power of noise for $n=1, 3$ and 6 kbp with finite τ and $\Delta=0$. The error bars for the experimental data depicts the standard deviation of the results obtained from 9 sets of experiments in each case.

3.3.3. Noise-assisted DNA translocation through the nanoporous matrix

The experimental setup was similar like conventional agarose gel electrophoresis under the influence of bias voltage with the provision of adding Gaussian noise as voltage input. An arbitrary waveform generator was attached providing noise in the form of voltage pulses in the orthogonal direction under the provision of splitting of noise-bias in the orthogonal direction and the resultant potential was applied across a gel in an electrophoretic set-up through a pair of Pt electrodes and Tris Acetate-EDTA (TAE) buffer. Considering this experimental setup, the negatively charged

DNA molecules translocate through the network of tortuous tubes. Keeping the bias voltage fixed at 10V, the intensity of the Gaussian noise was controlled by amplifying the voltage amplitude of the noise. Under the influence of orthogonal splitting of noise-bias, using noise having power $K = 4.32 \times 10^5 \text{ m}^2/\text{s}^3$ almost $\sim 30\%$ enhancement of mobility of 1 kbp DNA over conventional gel electrophoresis was achieved as shown in figure 3.4.B. The gel doc image (figure 3.4.A) also shows that the smallest band 1 kbp has moved the furthest at the same power of noise. There is a concurrent increase in displacement for the 1 kbp DNA band as the noise power K is increased shown in figure 3.4.A. On the other hand, using unidirectional noise-bias approach on DNA translocation, the enhancement of mobility was found $\sim 18\%$ for 1 kbp DNA using same power of noise $K = 4.32 \times 10^5 \text{ m}^2/\text{s}^3$ than conventional gel electrophoresis as shown in figure 3.4.D. A valid justification in regard to enhanced drift velocity of DNA when external noise direction is orthogonal to the net DNA drift direction, although there is no acceleration pulse in the direction of bias. The reason behind such phenomena is once the DNA is dislodged from a stuck state by the acceleration pulse (external noise basically) in the Y-direction, all the contacts with the underlying surface are broken, and hence the molecule is free to move which enhances the mobility faster in such scenarios. In such scenario, bias force along X-direction along with the component of inertial instantaneous velocity in the biased direction provides sufficient impetus to drive the DNA forward. The molecule tries to identify the least energy pathway within the energy landscape and tries to escape through the shortest route. A related study suggests that a soft elastic body might detach sub-critically from a stiff contactor in the presence of mechanical noise, which

showcases diffusive exploration of many states in an energy landscape while incorporating the least-energetic route^{14,26}.

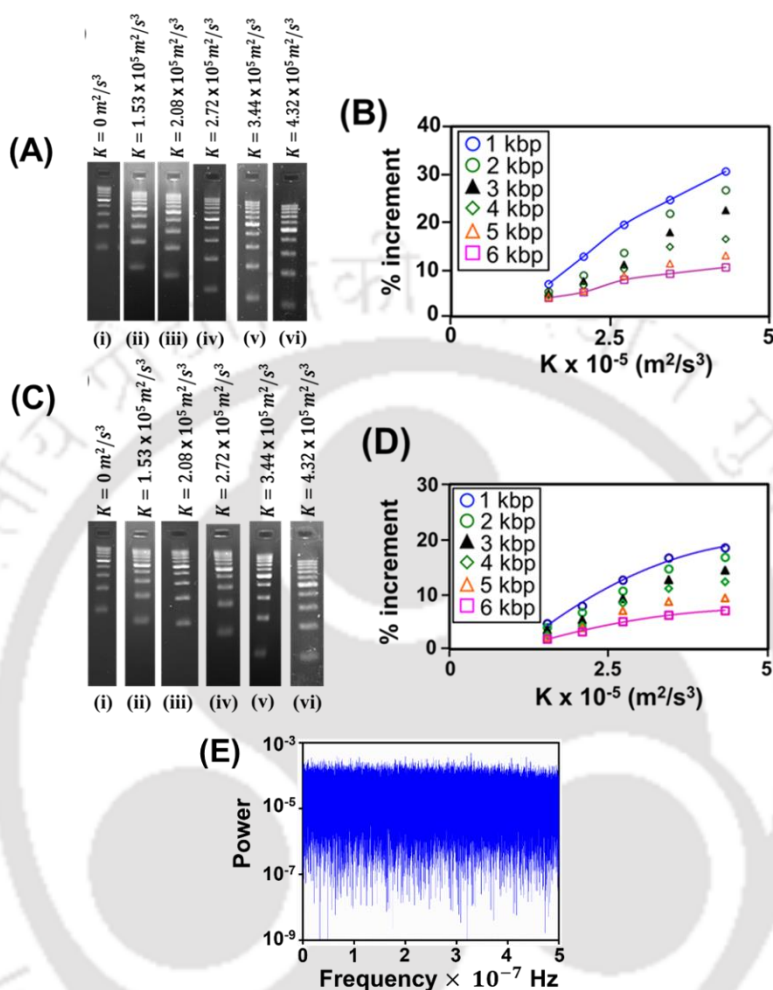


Figure 3.4. Splitting of noise-bias in orthogonal direction. (A) Agarose gel electrophoresis of DNA ladder (1-10 kbp) at 10 V bias for 4 h without any noise (i) and with the splitting of noise-bias in orthogonal direction (ii-vi) with different powers (K) depicted on the image. The DNA fragments in the image start from the well (dark rectangle) and then move downward during electrophoresis. (B) % increment of the displacement was estimated for 1 – 6 kbp at different power of the noise input. The percentage increment in displacement was estimated as % increment = $\frac{(x_n - x_c) \times 100}{x_c}$, here x_n represents displacement for a particular DNA fragment at a particular noise, and x_c is the displacement of the corresponding DNA fragment from the conventional gel

electrophoresis without any noise. To minimize the error while computing, only estimation up to 6 kbp was considered. The noise powers used for calculating are depicted along with the gel doc images mentioned in 3.4.A. **Unidirectional noise-bias induced gel electrophoresis.** (C) Agarose gel electrophoresis of DNA ladder (1-10 kbp) at 10 V bias for 4 h without any noise (i) and with the unidirectional noise-bias (ii-vi) with different powers (K) depicted on the image. The DNA fragments in the image start from the well (dark rectangle) and then move downward during electrophoresis. (D) % Increment of the displacement was estimated for 1 – 6 kbp at different power of the noise input. The percentage increment in displacement was estimated as % increment $= \frac{(x_n - x_c) \times 100}{x_c}$, here x_n represents displacement for a particular DNA fragment at a particular noise, and x_c is the displacement of the corresponding DNA fragment from the conventional gel electrophoresis without any noise. Similar range of noise power was used in this case as in the case of orthogonal noise-bias scenario. (E) A typical power spectrum of the time dependent voltage $V(t)$ as the noise input. The spectrum states that it is reasonably flat up to the frequency $f_c = 5 \times 10^7 \text{ Hz}$. As, this estimation is bounded by the sampling time distribution constraint $dt = 20 \text{ ns}$, so actually we can consider the noise to be white over a larger frequency domain than $5 \times 10^7 \text{ Hz}$.

3.3.4. Modified Langevin Model for predicting DNA mobility

As the DNA molecule traverses through the porous gel network, the random space dependent Δ used in our simulation model takes note of the time dependency of the molecular conformations. FESEM analysis of the porous gel¹⁹ also estimates the fact that there is a random distribution of gel pores throughout the gel matrix which hinders the motion. To overcome such barriers, we proposed this novel strategy to provide noise pulses orthogonal to the DNA drift direction to provide a pathway for faster DNA translocation using conventional gel electrophoresis setup

which has not been studied yet. Granick's group showcased a methodology to map the position of DNA within a porous landscape which eventually leads to a conclusion that there is distribution of pore like constriction (basically gel pores) and hence our assumption that there is a distribution of Δ as a function of position is justified, since we have considered the effect throughout space. We adopted the linear approximation of Eq. 1 (modified Langevin equation) and from the Fokker-Planck solution in the velocity space, we were able to estimate the average drift velocity as:

$$v_d = \frac{\bar{v}\tau_L}{1 + \frac{\Delta^2\tau_L}{K}}, \quad \dots\dots\dots (3)$$

This approximate drift velocity²⁷⁻²⁹ (v_d) agrees well with the experimental drift velocity of the DNA molecules considering proper scaling parameters ($\tau_L \sim n^{-0.56}$). DNA exhibits different types of drift and diffusive responses when subjected to external noise. When $\Delta = 0$, the strong dependence of the drift velocity on the power of noise is a departure from the standard driven Brownian system, where V_{drift} is simply a product of \bar{v} and τ_L . We have computed the drift velocity where both the combination of solid and kinematic friction is operating at the interface when the DNA molecule moves forward. The application of noise in the form of voltage pulses in the direction of net migration substantially improves the migration mobility of the DNA molecules. The approximate equation (3) describes the drift velocity reasonably well, and it fits our developed model shown in figure 3.5. Hence, using the fitting of the drift velocity using eq. (3) the Langevin relaxation time τ_L is found out to be of the order of $\sim 10^{-13}$ s, which is much smaller than the sampling time dt of the external noise input. In ideal scenario, the Langevin relaxation time, τ_L , should be longer than the noise correlation time scale for equation (3) to be applicable. Moreover, the power spectra of the noise reveal that the noise is white till $f_c = 5 \times 10^7$ Hz. Considering this as the corner frequency, the approximate correlation time constant, $\tau_c \sim 3.1$ ns, (from the equation,

$\tau_c = 1/(2\pi f_c)$). The estimation of f_c is however limited by the experimental sampling rate of the noise data collection. Thus, we can expect actual τ_c maybe much smaller than 3.1 ns as the $f_c > 5 \times 10^7$ Hz. The corresponding power spectrum plot of the input noise data is shown in figure 3.4.E.

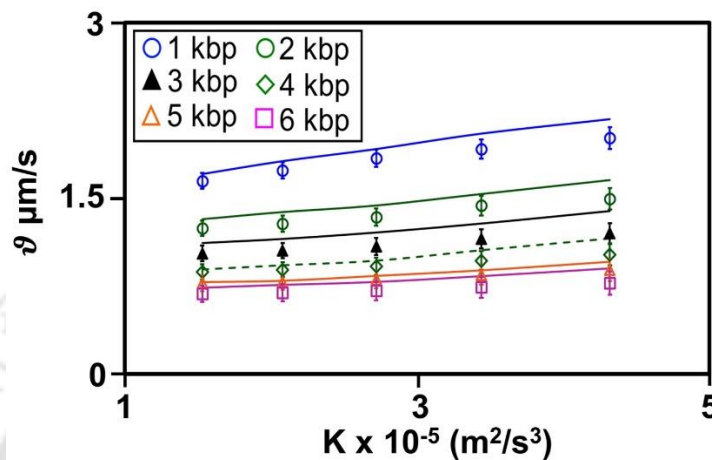
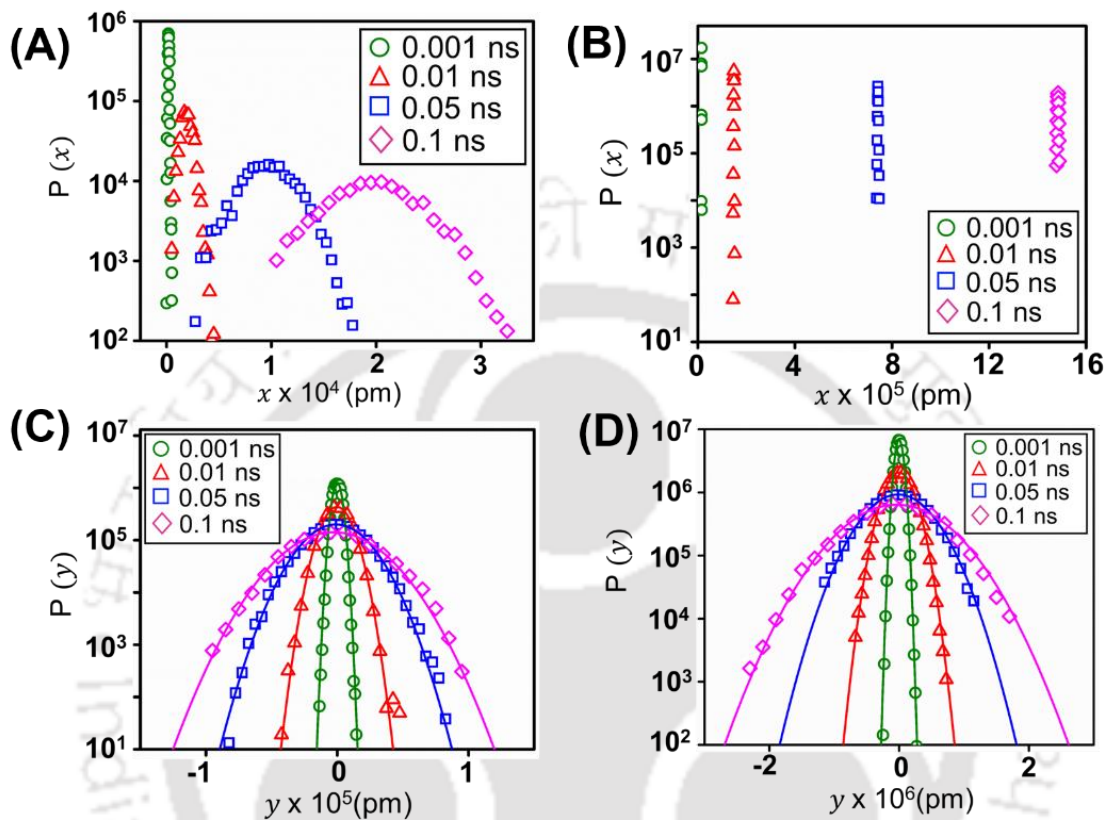


Figure 3.5. Drift velocity of the DNA fragments (splitting of external noise-bias in orthogonal direction). Comparison between the experimental drift velocity (symbols) and the velocity predicted by the equation (3) (line) obtained from 30 simulations in each case for different DNA fragments. The error bar for the experimental data depicts the standard deviation of the results obtained from 9 sets of experiments in each case.

3.3.5. Displacement trajectories tracked using simulation model

In addition to studying the drift velocity of the DNA, we also studied the fluctuations of the displacement distribution related to this system. It has been found that the probability distributions of displacements are non-Gaussian in certain scenarios, which is adequately supported by the numerical simulation of the modified Langevin equation including (Columbic/solid) friction. The asymmetry of the displacement distribution is observed for the bias direction (X-direction) as expected, which increases with the size of the time window as shown in figure 3.6.A in presence of solid friction. The asymmetry ceases to exist when $\Delta = 0$ as shown in figure 3.6.B. On the other

hand no asymmetry is noticed in the PDFs of the displacement in noise direction (Y- direction) as shown in figure 3.6.C and 3.6.D. (both in case of with and without solid friction). One potentially



important, observation in this work is that the displacement PDF is Gaussian at zero delta values, but it exhibits pronounced exponential tails at higher powers of noise having finite delta values. As the power of the noise increases, statistics is improved and the displacement PDF starts exhibiting asymmetry with exponential tails shown in figure 3.7.A & 3.7.B. The Gaussian distribution at a very low power results from the lack of sufficient high energy pulses, thus leading to poor statistics. This transition from a non-Gaussian to a Gaussian PDF might indicate a transition from a state governed by (dry/solid) friction to a state governed by a linear kinematic friction shown in figure 3.7.C. Since, we have used Δ in our simulation as a solid friction term, which is a function of space, which again conforms our justification is true while considering Δ throughout the gel surface.

Figure 3.6. PDF of displacement fluctuations in X and Y direction. The PDF of the displacement fluctuation in semi-log plot at different time windows (0.001, 0.01, 0.05 ns and 0.1 ns) for 1 kbp (A & B) with and without space-dependent Δ . Plot (C) & (D) demonstrates the PDF of the displacement fluctuation along Y- direction for 1 kbp DNA considering finite Δ and with $\Delta = 0$ shows Gaussian distribution and no asymmetric tail distribution. The displacement distributions are generated using the simulation based on modified Langevin equation. The trajectories are traced and plotted at power of noise $K = 4.32 \times 10^5 \text{ m}^2/\text{s}^3$.

The probability density function (PDF) of the displacement \tilde{x} are depicted for 1 kbp and 6 kbp in figure 3.7.A and 3.7.B with a peak shift of $(\tilde{x} = (x - x_p))$. Here x_p denotes the displacement value having a maximum count in the distribution of x . Due to the presence of non-linear friction (finite Δ), the distribution is asymmetric and has a non-Gaussian exponential tail. Considering average solid friction Δ , from the steady-state solution of the Klein-Kramers equation^{30,31} the PDF of the velocity distribution can be adopted as:

$$P(\vartheta) = P_0 \exp\left(-\frac{\vartheta^2}{K\tau_L} - \frac{2|\vartheta|\Delta}{K} + \frac{2\vartheta E q}{Km}\right), \dots \dots \dots (4)$$

The presence of the 2nd term within the argument of the exponential function imparts the asymmetric non-Gaussian tail in the velocity distribution that is evident from the displacement PDF. Simulation with $\Delta=0$ gives rise to symmetric Gaussian distribution according to equation B1, and thus depicted in Figure 3.7.C for 1 kbp DNA.

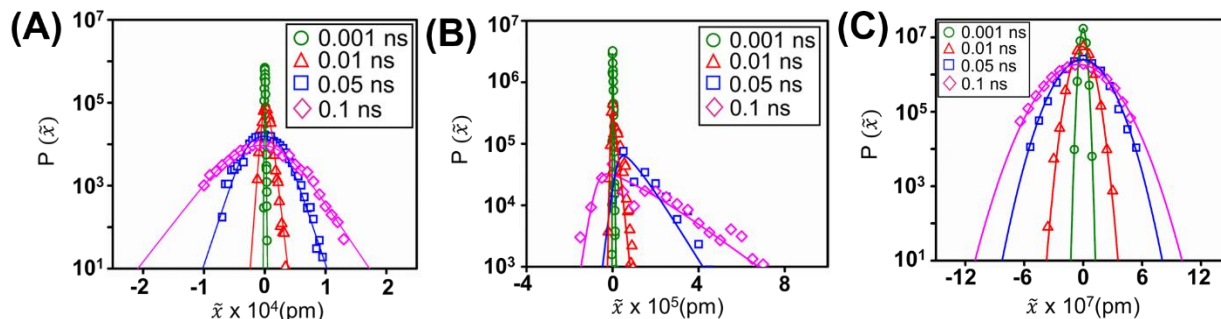


Figure 3.7. The PDF of the displacement distribution in semi-log plot at different time windows (0.001, 0.01, 0.05 ns and 0.1 ns) for 1 kbp (A) and 6 kbp (B) with space-dependent Δ . The peak position of the distribution is shifted to zero by $\tilde{x} = (x - x_p)$. The tails of these distributions are asymmetric and exponential. Plot (C) represent the PDF of the displacement distributions for 1 kbp DNA with $\Delta = 0$ which shows the Gaussian distribution.

Thus, asymmetric distribution could be another signature (in addition to the predominance of the exponential tail type distributions) of a non-equilibrium system where a threshold force namely solid friction is said to be operative, as the DNA traverses through the porous gel network.

3.4. Conclusions

The important outcome of this chapter is that an external noise in one direction can impart sufficient energy to a stuck molecule such that it can become mobile and can be steered in any preferred direction by application of a subcritical biased force. DNA traverse through the tortuous path with the net direction along the opposite (due to negatively charged DNA) to that of the applied electric field and this manifested as the distribution of the drift magnitude and direction. One can imagine at any instant, the segments of a DNA molecule are wrapped around many pinning points (stuck states) following a tortuous pathway with a pull at the two ends of the

molecule in the direction of the biased electric field (say it is horizontal direction). A single instantaneous voltage pulse with an arbitrary (as it is a random pulse) amplitude in the orthogonal direction (vertical direction) may release a few segments from its stuck state if the pulse is strong enough to be able to release them, and a few segments may still remain as stuck state as it was before. In the next instant, the new conformation (due to the release of a few segments of DNA) may change the states of the pinning sites. Along with that, the new orthogonal voltage pulse with a different amplitude (as well as from bottom to up or from up to bottom vertical direction) may release some of the other stuck states. Thus these continuous trains of orthogonal pulses keep on releasing these segmental stuck states and overcoming the frictional barriers posed by those pinning sites. The combined effect of the bias electric field and the electric field due to the orthogonal random voltage pulses keep the DNA moving and enhance mobility. In the simulation, we assumed DNA as a point mass and considered a random space-dependent frictional landscape to account for the effect of conformation. At any instant, the biased electric field (horizontal direction) and the orthogonal (vertical) instantaneous field were considered and their resultant force was on the point mass. Depending on the frictional value at that location, the resultant force may or may not be able to release the point mass (DNA) from its stuck situation. Of course, the assumption of considering the DNA as a point mass was too simplistic, it successfully captured the essence of the DNA dynamics in the simulations. Researchers have studied that noise activated dissociation of an adhered object from a surface suggests that in presence of external vibration two adhered surface can be detached at much lower pulling force than that required for a vibration free system³⁰. It may be possible that the DNA molecule will choose the minimum energy path in the energy landscape when external noise is applied orthogonal to that of the bias direction. Instead of overcoming the apex of the barrier directly it (DNA) may explore the lowest barrier height in the

neighbourhood and take the minimum energy path to bypass the energy loss associated with the apex-crossing. From our previous and present research work, we learned that one can reduce the effect of friction by introducing external noise in the system. Thus, one can expect enhanced mobility of charged particle or DNA molecule through gel matrix when noise in the form of fluctuating voltage is applied in the direction orthogonal to the applied electric field and hence the separation process is enhanced. This model gives useful insight which can be applicable to many practical situations. Other than DNA separation or mobility of charged particle through gel, this may be used in chromatographic separation³² as well.

References

1. Selmeczi, D. *et al.* Cell motility as random motion: A review. *Eur. Phys. J. Spec. Top.* **157**, 1–15 (2008).
2. Luo, K., Ala-Nissila, T., Ying, S. C. & Bhattacharya, A. Dynamics of DNA translocation through an attractive nanopore. *Phys. Rev. E - Stat. Nonlinear, Soft Matter Phys.* **78**, (2008).
3. Fan, R. *et al.* DNA translocation in inorganic nanotubes. *Nano Lett.* **5**, 1633–1637 (2005).
4. Verschueren, D. V. *et al.* Label-Free Optical Detection of DNA Translocations through Plasmonic Nanopores. *ACS Nano* **13**, 61–70 (2019).
5. Slater, G. W., Kenward, M., McCormick, L. C. & Gauthier, M. G. The theory of DNA separation by capillary electrophoresis. *Curr. Opin. Biotechnol.* **14**, 58–64 (2003).
6. A.G. OGSTON. The SPACES IN A UNIFORM RANDOM SUSPENSION OF FIBRES. *Trans. Faraday Soc.* **54**, 1754–1757 (1958).

7. Viovy, J. L. Reptation Theories of Electrophoresis. *Appl. Biochem. Biotechnol. - Part B Mol. Biotechnol.* **6**, 31–46 (1996).
8. Slater, G. W. & Noolandi, J. The biased reptation model of DNA gel electrophoresis: Mobility vs molecular size and gel concentration. *Biopolymers* **28**, 1781–1791 (1989).
9. Slater, G. W. & Noolandi, J. New biased-reptation model for charged polymers. *Phys. Rev. Lett.* **55**, 1579–1582 (1985).
10. Duke, T., Viovy, J. -L & Semenov, A. N. Electrophoretic mobility of DNA in gels. I. New biased reptation theory including fluctuations. *Biopolymers* **34**, 239–247 (1994).
11. Mettu, S. & Chaudhury, M. K. Motion of liquid drops on surfaces induced by asymmetric vibration: Role of contact angle hysteresis. *Langmuir* **27**, 10327–10333 (2011).
12. Buguin, A., Brochard, F. & De Gennes, P. G. Motions induced by asymmetric vibrations: The solid/solid case. *Eur. Phys. J. E* **19**, 31–36 (2006).
13. Subramanian, R. S. Motion of Drops on Gradient Surfaces. *Soft Matter Gradient Surfaces Methods Appl.* 407–429 (2012) doi:10.1002/9781118166086.ch16.
14. Chaudhury, M. K. & Goohpattader, P. S. Noise-activated dissociation of soft elastic contacts. *Eur. Phys. J. E* **35**, 131 (2012).
15. Daniel, S., Chaudhury, M. K. & Chen, J. C. Fast drop movements resulting from the phase change on a gradient surface. *Science (80)*. **291**, 633–636 (2001).
16. Lubensky, D. K. & Nelson, D. R. Driven polymer translocation through a narrow pore. *Biophys. J.* **77**, 1824–1838 (1999).
17. Smith, S. B., Aldridge, P. K. & Callis, J. B. Observation of Individual DNA Molecules

- Undergoing Gel Electrophoresis. *Science (80)*. **243**, 203–206 (1989).
18. Carle, G. F., Frank, M. & Olson, M. V. Electrophoretic separations of large DNA molecules by periodic inversion of the electric field. *Science (80)*. **232**, 65–68 (1986).
 19. Deb, A., Gogoi, P., Singh, S. K. & Gooh Pattader, P. S. Noise-Activated Fast Locomotion of DNA through the Frictional Landscape of Nanoporous Gels. *Langmuir* **38**, 11764–11769 (2022).
 20. Gillespie, D. T. The mathematics of Brownian motion and Johnson noise. *Am. J. Phys.* **64**, 225–240 (1996).
 21. Burlatsky, S. F. & Deutch, J. M. Solid friction in gel electrophoresis. *J. Chem. Phys.* **103**, 8216–8227 (1995).
 22. Duke, T. A. J. & Viovy, J. L. Simulation of megabase DNA undergoing gel electrophoresis. *Phys. Rev. Lett.* **68**, 542–545 (1992).
 23. Burlatsky, S. & Deutch, J. Influence of solid friction on polymer relaxation in gel electrophoresis. *Science (80)*. **260**, 1782–1784 (1993).
 24. Viovy, J. L., Duke, T., Burlatsky, S. & Deutch, J. Solid friction and polymer relaxation in gel electrophoresis. *Science (80)*. **264**, 112–113 (1994).
 25. Heller, C. *et al.* Free-solution electrophoresis of DNA. *J. Chromatogr. A* **806**, 113–121 (1998).
 26. Goohpattader, P. S., Mettu, S. & Chaudhury, M. K. Rolling motion of a rigid sphere on a structured rubber substrate aided by a random noise and an external bias. *arXiv:1108.0915* (2011).

27. De Gennes, P. G. Brownian motion with dry friction. *J. Stat. Phys.* **119**, 953–962 (2005).
28. Touchette, H., Van Der Straeten, E. & Just, W. Brownian motion with dry friction: Fokker-Planck approach. *J. Phys. A Math. Theor.* **43**, 1–18 (2010).
29. Goohpattader, P. S. & Chaudhury, M. K. Random motion with interfacial contact: Driven diffusion vis-à-vis mechanical activation. *Eur. Phys. J. E* **35**, 1–29 (2012).
30. Goohpattader, P. S., Mettu, S. & Chaudhury, M. K. Experimental investigation of the drift and diffusion of small objects on a surface subjected to a bias and an external white noise: Roles of coulombic friction and hysteresis. *Langmuir* **25**, 9969–9979 (2009).
31. Goohpattader, P. S. & Chaudhury, M. K. Diffusive motion with nonlinear friction: Apparently Brownian. *J. Chem. Phys.* **133**, (2010).
32. Viovy, J. L. & Lescq, J. Separation of macromolecules in gels: Permeation chromatography and electrophoresis. *Adv. Polym. Sci.* **114**, (1994).



Chapter 4

Effect of asymmetric wave on the dynamics of the macromolecules through porous gel

Contents

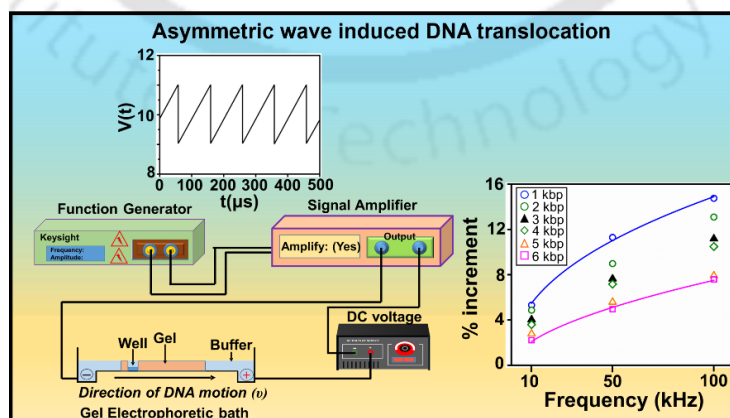
ABSTRACT.....	103
4.1. Introduction	104
4.2. Materials and Methods.....	107
4.2.1. Materials	107
4.2.2. Preparation of gel.....	107
4.2.3. Instruments used.....	108
4.2.4. Experimental Procedure	109
4.3. Results and Discussion	109
4.4. Conclusions and Final remarks	117
References.....	118



ABSTRACT

Numerous biological applications revolve around size-based DNA separation. In recent years, the goal of separating DNA fragments in human genome research has driven attempts to understand the molecular mechanisms driving the electrophoretic separation rate, resulting in the fast development of electrophoretic procedures. The segregation of DNA based on macromolecule size highlights the idea of genome mapping, sorting, and sequencing, which is predicted to play a significant role in healthcare diagnostics and bio-medical imaging. We have designed an experimental set-up wherein the presence of asymmetric periodic ramp vibrations combined with biased voltage, the mobility of 1 kbp DNA increases ~15 % compared to the conventional gel electrophoresis, whereas the increment is around ~7 % for 6 kbp DNA. The pinning barrier of the molecules is overcome by external vibrations in the form of fluctuations, anticipating the symmetry breakdown for the free random motion of macromolecules. Here we address the issue by adding external periodic vibrations, reflecting a synergistic combination of geometry and driving force that can be exploited to predict the enhanced drift mobility of the biomolecule traversing through the nanoporous gel matrix.

Graphical Abstract



Keywords: Asymmetric ramp vibrations, Langevin dynamics, Solid friction.

4.1. Introduction

Caughey and Dienes¹ initially described a random motion with an interfacial resistance in the context of sliding constructions responding to earthquakes nearly fifty years ago. Similar movement with a weak adhesive contact has recently been observed with a colloidal particle on a soft microtubule² and a tiny particle on a solid surface³⁻⁵. Many of these systems exhibit frictional dynamics that are hysteretic or non-linear⁶⁻¹², driven by instabilities^{8,9}. Muser⁸ eloquently said, viscous drag friction originates from the dispersion of impact energy from a Brownian particle's central degree of freedom to the solvent particle's various degrees of freedom. However, fast movements of varying levels of freedom cause "stick-slip" instability and non-linear friction even at an abysmally low velocity of sliding one solid past another. The same instabilities are seen with a mass/spring system and variable noise excitations⁵. They can also be seen as a liquid drop's contact line⁴ relaxes against a solid surface. Long ago, it was postulated¹³ that the collapse of Bloch wall formations and the presence of Barkhausen noise in magnetism both are accompanied by relative instability to that of Coulomb friction. Due to its vast range of micro and nanoscale technology applications¹⁴⁻¹⁶ and for understanding the unidirectional transport found in molecular motors in biophysical systems^{17,18}, rectifying unbiased asymmetric fluctuations to extract meaningful work in non-linear "ratchet-like" systems has attracted enormous interest among researchers. To direct the motion of a macroscopic non-rolling object like a coin, Buguin et al.¹⁹ used dry friction to rectify a spatially asymmetric sinusoidal input and a square pulse. By combining horizontal and vertical oscillations of a horizontal surface, Frei et al.²⁰ could control the sliding friction and regulate motion in a desired direction. The violation of time/space symmetry is invariably linked with directed transport in geometrically symmetric non-equilibrium systems^{21,22}. This may be accomplished by employing general time-periodic signals^{19,23} like

sinusoidal or square pulses, as well as zero mean asymmetric fluctuations in the form of colored or idealized white noise²⁴. As demonstrated by Brunet et al.²⁵ and Noblin et al.²⁶, directed transport may also be accomplished against potential gradients by employing an asymmetry produced by connecting horizontal and vertical vibrations to force a liquid drop to ascend an inclined plane against gravity. Baule and Sollich have explored one-sided and two-sided noisy asymmetric vibrations to demonstrate the effect on object's directed motion²⁷.

Compared to hard (condensed) matter, biological systems defined as soft (condensed) matter at the mesoscopic level exhibit various properties, including complexity, flexibility, and volatility. Multiple processes, including as the movement of tiny biomolecules through nanopores²⁸, the separation of DNA in nanofilters²⁹, and biological ion channels³⁰, all involve the transport of particles and particle-like entities in constrained environments at the micro and nanoscales. These systems establish an energy barrier between two adjacent, more prominent regions accompanied by decreased conformational flexibility. Under these circumstances, transport is characterized by discrete hops over the congested zones, a phenomenon is known as entropic trapping. A weak external driving force may change this free-energy landscape, partially offsetting the entropic cost. Kramers³¹⁻³⁴ took this manner of transportation into account and came up with an equation for the typical hopping frequency (escape rate) in terms of the entropic energy barrier, the driving force, and the thermal energy of the species. However, the wide distribution of the escape rate is naturally prominent, reflecting the underlying random thermal motion that makes successful hops possible. Stochastic resonance³⁵ (SR) may be achieved by accomplishing this, a circumstance where the hopping occurrences and the driving force are synchronized. The synchronization of a system's noise with an external oscillating field to boost the response signal is known as stochastic resonance. Since the initial SR investigations were conducted more than 30 years ago^{35,36}, SR has

been used in numerous academic fields, including physics, chemistry, engineering, biology, and biomedical sciences³⁷⁻⁴³. Hanggi and colleagues first showed that SR may be accomplished in particle transport dominated by entropy and driven by a periodic driving force with a continuous orthogonal component overlaid, leading to increased spectrum amplification in their groundbreaking work^{38,40,42}. From an experimental standpoint, Spagnolo and coworkers showed the dynamics of brief polymer translocation triggered by an oscillating force and the genesis of stochastic resonance behavior in a bistable electrical device, namely the tunnel diode^{44,45}. These investigations uncovered a variety of fascinating phenomena, including the resonant crossing of the energy barrier and increased diffusion through control of the system noise strength⁴⁶⁻⁴⁸. Theory and simulations have both been used to investigate the SR of flexible polymers when their flexible chain crosses a bi-stable potential under an oscillating force field^{47,48}.

Resonance activation (RA)^{39,49} is another phenomenon that has attracted attention and is connected to system noise and particle motion. Resonance activation can reduce crossing time due to the cooperative interaction between the temporally manipulated barrier and noise-induced barrier crossing event. RA has been demonstrated to be a practical phenomenon for stiff particles and short polymers⁵⁰⁻⁵³. Due to the significant impact of thermal fluctuations on biomolecule dynamics, stochastic resonance has garnered particular attention in biological systems. Stochastic resonance presents a potential strategy to harness the stochastic migration of a biomolecule and benefit the signal output.

The crux of our study in this chapter focuses on biomolecule (DNA) transport studies involving asymmetric ramp vibration-induced mobility through a nanoporous gel matrix. We demonstrated how a well-designed experiment could be investigated to showcase the barrier crossing rate using an external periodic vibration⁵⁴. Despite the ubiquitous usage of DNA gel electrophoresis and

considerable theoretical advancement, a crucial subject related to improving migration rate by modifying the conventional system is not explored yet. It is vital to comprehend the molecular processes that separate different types and lengths of nucleic acid chains. This knowledge should help us better understand the electrophoretic transport of polyelectrolytes. Our experiments focused on how a driven drift velocity enhancement experiment compares with an energy exchange process that we are familiar with after being inspired by the optimistic outcomes of earlier experiments of previous chapters.

4.2. Materials and Methods

4.2.1. Materials

From Loba Chemie, agarose powder and ethidium bromide were purchased. The DNA (1 kbp to 10 kbp) molecular weight (MW) ladder and Tris Acetate-EDTA (TAE) buffer were received from Takara Bio Inc. and Himedia respectively. To power the horizontal gel electrophoresis, a DC power supply unit (GeNei Electrophoresis Power Supply, 0-500V, 0-500 mA) was employed together with the electrophoretic gel chamber (Miniphor UVT System (Serial No. 106888 GB)). An arbitrary waveform generator (KEYSIGHT 33600A) and an amplifier (KEYSIGHT TECHNOLOGIES 33502A, 2- Channel 50 Vpp) were used to generate asymmetric ramp vibrations and amplify the signal, respectively.

4.2.2. Preparation of gel

0.8 g of agarose powder was dissolved in 100 ml of 1X Tris Acetate-EDTA (TAE) solution in order to make 0.8% (w/v) agarose. A homogeneous solution was created by first carefully mixing,

and then heating for one minute in a microwave (Power: 900 W) (Make: Samsung Model No: MC28H5023AKTL). The temperature of the solution was less than 100 °C. After cooling the solution to around 30 °C, 3 µL of aqueous Ethidium bromide (EtBr) at a concentration of 0.5 mg/ml was added to the solution. When exposed to UV light, the EtBr makes it easier to recognize DNA bands. The solution's pH was maintained at around 8.0 using TAE buffer. The agarose solution was poured into the gel chamber, and a comb was set up at one end of the gel platform to create the wells into which the DNA would be loaded before electrophoresis. The agarose solution was left to set at room temperature for two hours to finally get the desired agarose gel.

4.2.3. Instruments used

Waveform generator (Make & Model: KEYSIGHT 33600A) was used for generating asymmetric ramp wave vibrations in the form of voltage pulses.

Oscilloscope (Make & Model: GW INSTEK MDO-2000A) was used for collecting the ramp wave data generated from the waveform generator.

Signal Amplifier (Make & Model: KEYSIGHT TECHNOLOGIES 33502A, 2- Channel 50 Vpp) was used to amplify the ramp wave signal generated from the waveform generator.

Gel Electrophoretic chamber (Model: Miniphor UVT System 106888GB) was used for performing the agarose gel electrophoresis for separation of the DNA bands.

UV illumination/gel documentation chamber (Make: Chemidoc XRS+ System with Image Lab Software #1708265) was used for visualization of the DNA fragments.

4.2.4. Experimental Procedure

The gel wells were loaded with a DNA ladder having a molecular weight ranging from (1 kbp to 10 kbp). It was carefully dispensed to avoid any bubbles developing when the DNA was loaded. Between two Pt electrodes, spaced apart by $d = 13$ cm, the gel electrophoresis was operated at 10 V DC at a constant current of 1 mA. The electrophoresis was conducted for 4 hours. The gel and TAE buffer were kept at a constant temperature of 23 ± 1 °C. A Gel Doc (Chemidoc XRS+) device was used to visualize the DNA fragments. The system software uses a variety of magnification modes to collect the images. Using a function waveform generator and a signal amplifier, asymmetric ramp vibrations were produced and amplified. As schematically shown in Figure 4.1., the waveform generator and the amplifier were linked in series with a DC voltage source. An oscilloscope was used to gather the waveform generator's voltage signal output, which was used to quantify the periodic vibrations. After that, the stored data was taken for additional examination. The sample data had a minimum interval of 200 ns. Using the free and open-source ImageJ software, the images of the DNA bands following electrophoretic separation were examined. Displacement of the gel bands are estimated from the distance between the well to the middle point of a particular band using ImageJ software.

4.3. Results and Discussion

The experimental set-up resembled traditional agarose gel electrophoresis under a bias voltage control with a facility for addition of asymmetric ramp wave fluctuations as voltage input. The generated potential was delivered across the gel in an electrophoretic set-up through a pair of Pt

electrodes and Tris Acetate-EDTA (TAE) buffer from a function generator along with an amplifier connected in a series connection with a bias DC voltage source⁵⁵.

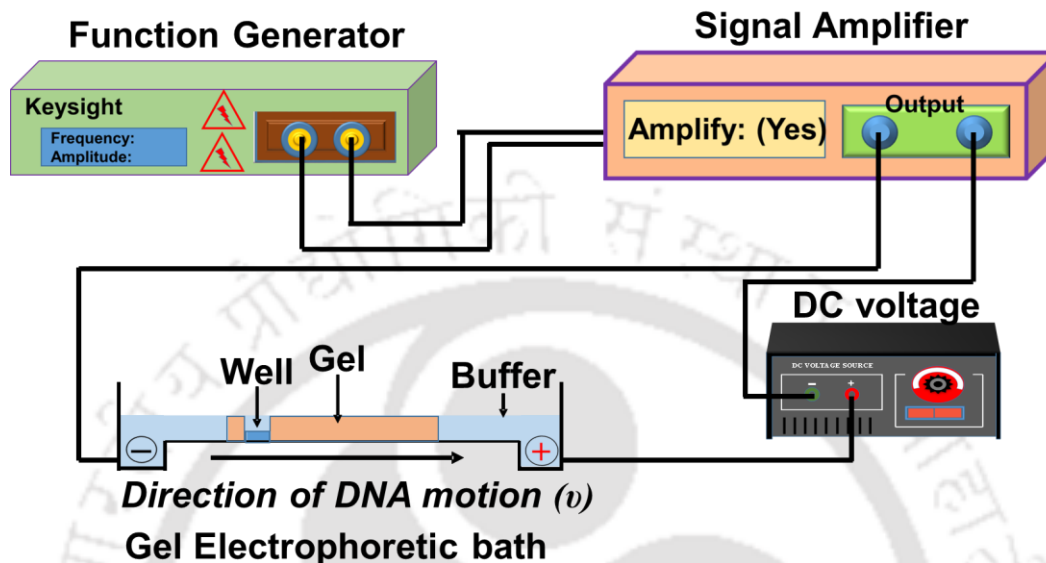


Figure 4.1. Schematic representation of the experimental set-up. The function waveform generator (generating ramp vibrations) is connected with a signal amplifier. The output of the amplifier is linked in series with a source of continuous DC voltage, and the resulting output is applied across the agarose gel in the electrophoretic chamber. The arrow with the symbol denotes the direction of the DNA band motion.

The network of tortuous tubes, can be assumed to be created by the lateral movement of DNA through a gel matrix, under the influence of a bias voltage⁵⁶. The frequency of the ramp wave grew concurrently with the strength of the asymmetric fluctuations while the bias voltage remained fixed at 10 V. Under the influence of asymmetric ramp wave vibrations (Frequency of the wave = 100 kHz), a substantial increase in the drift velocity of the DNA fragments was found, as demonstrated in figure 4.2.B. A justification in regard for this increased drift velocity of DNA molecule can be explained in terms of symmetry breaking of a droplet oscillated with periodic vibration that results

in upward motion of the drop^{25,57–59}. Authors have suggested that hysteresis can be eliminated with a strong vibration^{19,25}. In wake of such literatures highlighting the presence of non-linearity that is responsible for symmetry breaking, our proposed model for enhanced DNA transport through porous gels subjected to ramp vibrations stands justified. Susan Daniel and co-workers^{60,61} also depicted the rectified motion of droplets induced by vibration. Another aspect that deserves attention in this regard, when a biomolecule is subjected to random vibrations the resonance frequency⁶² of the biomolecule undergoes significant change which affects the drift velocity which correlates with the research works of Kelvin⁶³, Chandrasekhar⁶⁴ and Rayleigh⁶⁵. Hence, an inevitable conclusion can be figured out is the presence of ramp vibrations can provide enough energy to a DNA molecule to traverse faster as shown in figure 4.3.A, 4.3.B and 4.3.C.

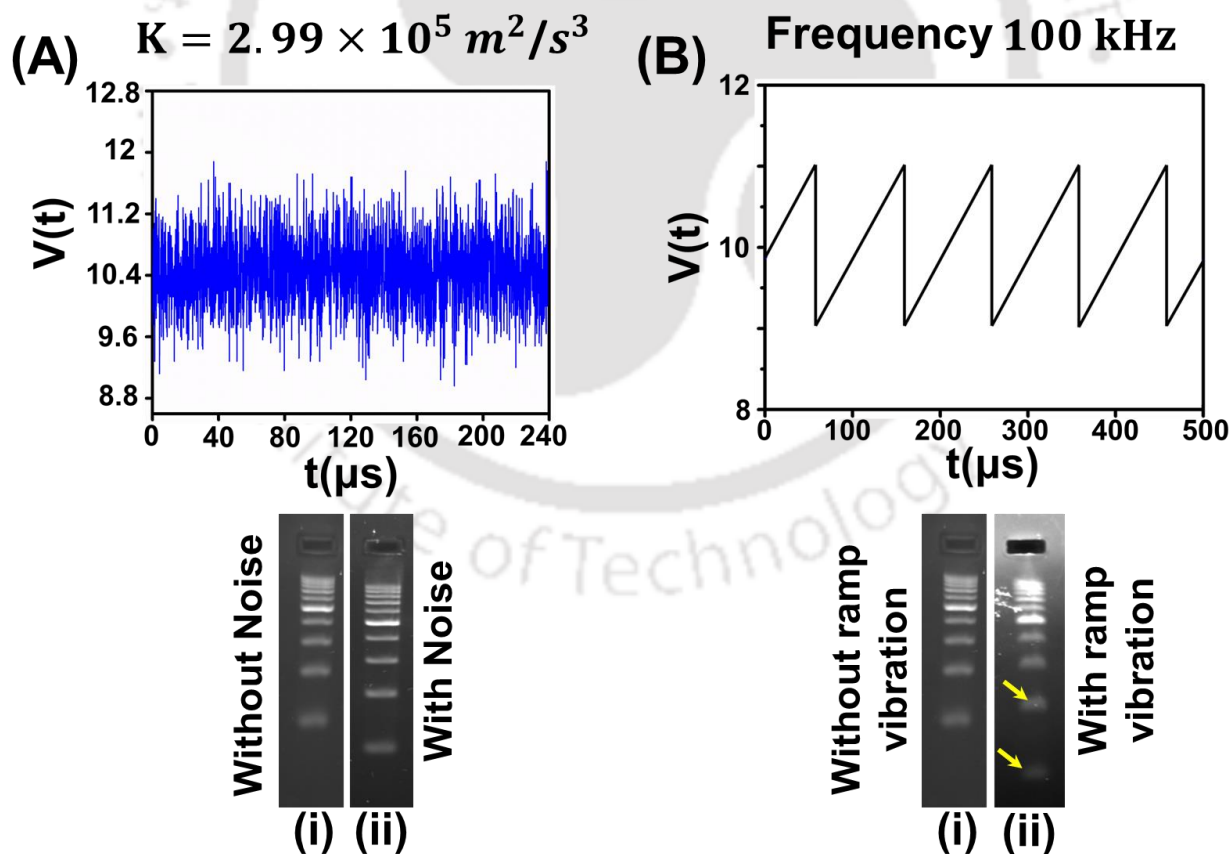


Figure 4.2. (A) A typical example of a time series of noise as voltage input at a particular power of the noise. The corresponding gel doc images represent (i) without noise (conventional gel electrophoresis) and (ii) with noise (external noise-bias induced gel electrophoresis) scenarios. (B) A typical example of a time series of periodic ramp vibrations as voltage input. Here, external ramp vibrations was used along with bias voltage to demonstrate the electrophoretic separation of DNA. The corresponding gel doc images represent (i) without vibration (conventional gel electrophoresis) and (ii) with ramp vibration (ramp vibration induced gel electrophoresis) scenarios. The yellow arrows on the gel doc image (ii) represents the faster mobility of bands. Using ramp vibration of frequency 100 kHz, separation of 1 kbp DNA band was faster by ~ 8% than one with power of noise $K = 2.99 \times 10^5 \text{m}^2/\text{s}^3$. A comparison is made based on the voltage amplitude of noise and the ramp vibrations that were generated using the waveform generator separately.

The Brownian particle has significant conformational variations if not rigid, as in the case of flexible macromolecules. Such a macromolecule experiences a decrease in structural degrees of freedom when it encounters a physical obstacle, creating an entropic barrier⁴⁷. The crossing of the molecule happens across a free energy barrier if there is further energetic interaction between the macromolecule and the physical barrier. Many recent experimental results on single molecule translocations through nonporous materials under a constant external force were extensively interpreted using such a fundamental model⁶⁶. Given the potential implications for macromolecular transport in biological situations, there is growing interest in how an externally imposed oscillatory signal in time connects to the various conformations of the polymer chain and the noise strength as the chain moves through a free energy barrier. Motivated by the encouraging results of the previous studies, the main goal of this work was to discuss the role played by periodic

ramp vibrations that result from the interaction between a biomolecule's translocation over a free energy barrier and an externally imposed periodic signal.

Unlike other research works⁶⁷, in this research work, we have scrutinized the motion of the center of mass of a DNA molecule. During the locomotion through nanoporous gels, DNA frequently becomes trapped inside the constricting pores in loop-like conformations in gels with high agarose concentrations (corresponding to comparatively small pore sizes, thus linked with greater average friction). At a particular time within the nanoporous landscape of the gel matrix, the DNA takes a particular position having a specific configuration and is associated with a particular friction value. The addition of ramp vibrations, along with biased voltage triggers the motion of DNA. The motion of DNA can be compared to an excited Brownian particle which can hop over an entropic barrier in presence of stochastic resonance. Researcher Granick et al.⁶⁸ demonstrated a phenomenology to track DNA shape based on automated single-molecule imaging. They explained that the leading and trailing edges of the DNA molecule remain stuck at a certain point in the porous matrix for some period of time. Henceforth, an inevitable conclusion is the presence of constricting pores within the entire landscape of the agarose gel. DNA molecules of different sizes traverses through the porous matrix and the presence of ramp vibration triggers the scenario to move faster through the constricting pores. The translational entropy caused by containing the particle inside irregular borders leads to the formation of the entropic barrier⁶⁹⁻⁷¹. Such entropic barriers also contribute to SR, popularly known as entropic stochastic resonance (ESR)^{71,72}. Researchers have dwelled on methods that try to investigate the role of stochastic resonance on polymer translocation in a porous matrix regime. The traversal of a flexible chain across an ad-hoc bistable potential barrier under an oscillating force field was investigated using a combination of theory and simulations^{47,73}.

Burlatsky et al. showed that, electrophoretic screening of negatively charged DNA segments is based solely on molecular weight due to the solid friction provided by the porous gel^{56,74}. In case of large DNA molecules (with base pairs greater than 400 bp), free electrophoresis performed in a buffer and without a gel exhibits comparable mobility towards a positive electrode⁷⁵. Since the DNA backbone is phosphate-based, it will carry negative charges under common buffer conditions in the vicinity of pH 7-8. Therefore, DNA will experience an electrostatic force when an external electric field is applied, and its resulting motion in response to the force is quantified by a parameter called the “mobility”. Our study investigated the process by which DNA migrates across gel during electrophoresis more quickly. An inverse correlation between chain length and gel mobility was discovered, i.e., $\frac{\mu}{\mu_0} = \frac{\alpha}{L}$ where μ_0 is the free solution mobility, and μ is the mobility of the reptating chain.

Because the migration rate of dsDNA is inversely correlated with the \log_{10} of DNA strand length, smaller nucleic acid molecules migrate more quickly than bigger ones (Helling et al. 1975)⁷⁶. Larger molecules are more easily entangled in the gel matrix and generate higher frictional drag. As a result, they move through the pore radius less quickly than smaller molecules, which supports our findings because the smaller gel band, 1 kbp in size, has moved the furthest distance in terms of displacement, shown in figure 4.3.A and 4.3.B.

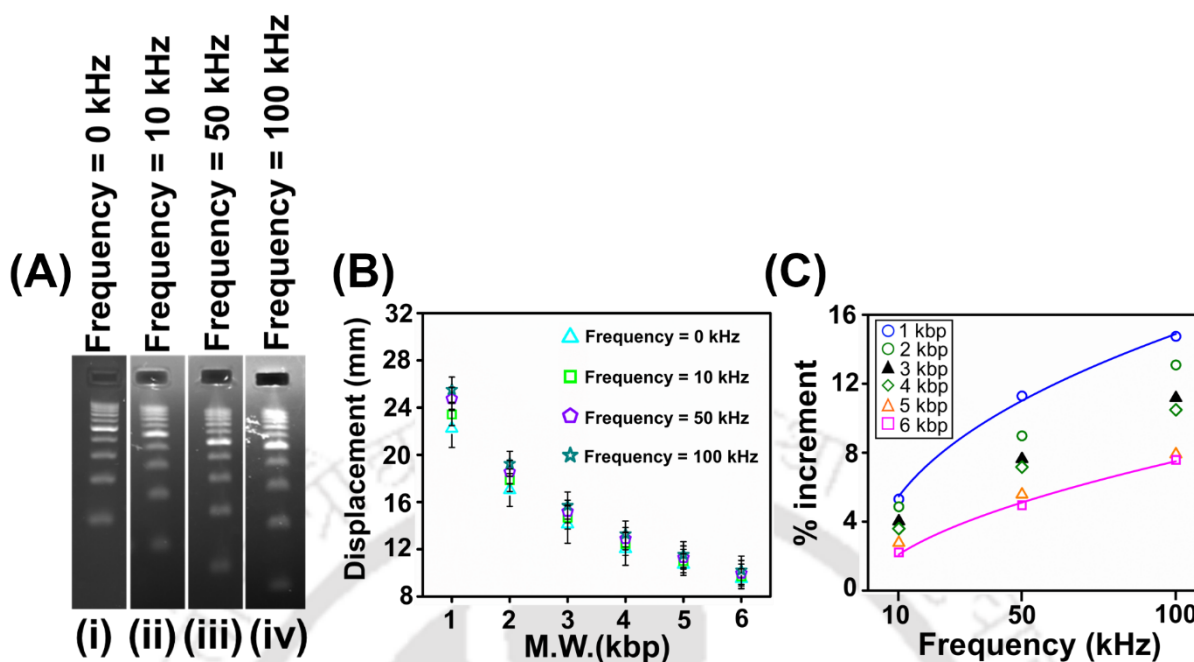


Figure 4.3. Effect of asymmetric ramp vibration on the electrophoretic separation of DNA fragments. (A) Agarose gel electrophoresis of DNA ladder (1-10 kbp) at 10 V bias for 4 h without any ramp vibration (i) and with ramp vibrations of different frequencies depicted on the images (ii-iv). The DNA fragments in the image start from the well (dark rectangle at the top) and then move forward (downward in the image) to the positive electrode during electrophoresis. (B) Displacement of the 1 kbp to 6 kbp after 4 h of gel electrophoresis without ramp vibrations and with ramp vibrations having different frequencies shown in the inset. To reduce the error while calculating, only estimation of the displacement up to 6 kbp was considered. The error bar represents the standard deviation from the results obtained from 9 sets of experiments. (C) % Increment of the displacement was estimated for 1 – 6 kbp. The percentage increment in displacement was estimated as $\% \text{ Increment} = \frac{(x_n - x_c) \times 100}{x_c}$, here x_n represents displacement for a particular DNA fragment (n) at a particular ramp wave frequency, and x_c is the displacement of

the corresponding DNA fragment from the conventional gel electrophoresis without any frequency.

As the frequency of the periodic ramp vibration increases, the overall sieving of the molecules through the gel matrix increases, which is consistent with the sliding dynamics response of the granular systems⁷⁷. The above experimental results also indicated a distinct separation of the DNA fragments with increasing external fluctuations combined with biased voltage as shown in figure 4.3.A.

Despite enormous studies on separation methodologies of nucleic acids, conventional agarose gel electrophoresis remained exclusive in biological sciences research. So, we tried to incorporate a novel strategy by incorporating asymmetric ramp wave vibrations, which have been progressively used in our experiments, along with the simplicity of analyzing the results with straightforward interpretations using the prevalent theories regarding barrier crossing in porous substrates.

Overall, with increase in the voltage amplitude of the ramp vibrations, the strength of the vibrations was regulated while maintaining the bias voltage at 10V. The mobility of the DNA enhances in the presence of ramp vibration induced gel electrophoresis. With the concurrent increase in frequency of ramp vibrations, the mobility of 1 kbp band was found to increase. Using frequency of 100 kHz shown in figure 4.3.C, ~15 % increment of 1 kbp band was found in comparison to the conventional gel electrophoresis. Also, the mobility of 6 kbp band was enhanced by ~7% in comparison to the conventional gel electrophoresis as depicted in figure 4.3.C. This novel strategy harnessed by incorporating asymmetric ramp wave vibrations, helped to analyze the barrier crossing phenomena in porous substrates.

The above observations with increased drift velocities of the DNA fragments are the main reasons behind the justification of modeled experimental set-up, which can be further elaborated using simulation as a future prospect. We discovered that the best coherence between the external signal and the translocation of the DNA macromolecule through the gel pores occurs at the maximum level of external periodic vibrations, indicating the occurrence of the so-called barrier crossing for quicker translocation than conventional gel electrophoresis. According to Jarzynski⁷⁸, the increasing non-linearity that is creeping out due to more significant migration might be attributed to the free energy shift in biological processes from the dissipative work variations.

4.4. Conclusions and Final Remarks

The basic argument of this study is that, in an electrophoretic environment, the contact established by the adhesive interaction of a soft deformable macromolecule with a rigid substrate can be broken sub-critically in the presence of external periodic vibrations. The above research exemplified many interesting phenomenologies under a stochastic setting with increased electrophoretic mobility through the gel matrix. The macroscopic model is interpreted in terms of the mobility, interaction, and dynamics of the DNA molecule. Theoretical interpretation enabled us to develop an insight into the electrophoretic enhancement of the gel bands of DNA molecules by sieving through the gel matrix. The tension across the chain lengths causes stretching of DNA during gel electrophoresis involving steric hydrodynamic long interactions.

Investigations on the DNA migration rate suggest two important points: (a) Firstly, external vibrations alter the relaxation behavior of entangled DNA chains in the molecular/mesoscopic environment, allowing for quicker movement, and (b) Secondly, the analytical experiments

stressed on the entropic fluctuations due to energy dissipation in the non-equilibrium thermodynamic space. Understanding the pinning-depinning kinetics in various bio-inspired adhesives and composites and the (thermal) noise-induced detachments of cells, macromolecules, and soft colloidal matter from surfaces should benefit from the investigations described here. However, additional research is necessary to fully understand DNA "barrier crossing" kinetics within the electrophoretic gel framework that uses external asymmetric ramp fluctuations.

References

1. Caughey, T. K. & Dienes, J. K. Analysis of a nonlinear first-order system with a white noise input. *J. Appl. Phys.* **32**, 2476–2479 (1961).
2. Wang, B., Anthony, S. M., Bae, S. C. & Granick, S. Anomalous yet Brownian. *Proc. Natl. Acad. Sci. U. S. A.* **106**, 15160–4 (2009).
3. Goohpattader, P. S. & Chaudhury, M. K. Diffusive motion with nonlinear friction: Apparently Brownian. *J. Chem. Phys.* **133**, (2010).
4. Mettu, S. & Chaudhury, M. K. Stochastic relaxation of the contact line of a water drop on a solid substrate subjected to white noise vibration: Roles of hysteresis. *Langmuir* **26**, 8131–8140 (2010).
5. Goohpattader, P. S., Mettu, S. & Chaudhury, M. K. Experimental investigation of the drift and diffusion of small objects on a surface subjected to a bias and an external white noise: Roles of coulombic friction and hysteresis. *Langmuir* **25**, 9969–9979 (2009).
6. Prandtl, L. Ein Gedankenmodell zur kinetischen Theorie der festen Körper. *ZAMM - J.*

- Appl. Math. Mech. / Zeitschrift für Angew. Math. und Mech.* **8**, 85–106 (1928).
7. Müser, M. H. First principles-based theory of collective creep. *Proc. Natl. Acad. Sci. U. S. A.* **107**, 1257–1258 (2010).
 8. Müser, M. H. Velocity dependence of kinetic friction in the Prandtl-Tomlinson model. *Phys. Rev. B - Condens. Matter Mater. Phys.* **84**, (2011).
 9. Persson, B. N. J. *Sliding Friction (Physical Principles and Applications)*. (Springer Berlin, 2000).
 10. Müser, M. H., Urbakh, M. & Robbins, M. O. *Statistical mechanics of static and low-velocity kinetic friction. Advances in Chemical Physics* vol. 126 (2003).
 11. Nasuno, S., Kudrolli, A. & Gollub, J. P. Friction in granular layers: Hysteresis and precursors. *Phys. Rev. Lett.* **79**, 949–952 (1997).
 12. Baumberger, T. & Caroli, C. Solid friction from stick-slip down to pinning and aging. *Adv. Phys.* **55**, 279–348 (2006).
 13. Zik, O., Stavans, J. & Rabin, Y. Mobility of a sphere in vibrated granular media. *Europhys. Lett.* **17**, 315–319 (1992).
 14. Tran, S. B. Q., Marmottant, P. & Thibault, P. Fast acoustic tweezers for the two-dimensional manipulation of individual particles in microfluidic channels. *Appl. Phys. Lett.* **101**, (2012).
 15. Reguera, D. *et al.* Entropic splitter for particle separation. *Phys. Rev. Lett.* **108**, 1–5 (2012).
 16. Leff, H. S. *Brownian Ratchets: From Statistical Physics to Bio and Nano-Motors* Brownian Ratchets: From Statistical Physics to Bio and Nano-Motors. CuberoDavid RenzoniFerruccio 198 pp. Cambridge U.P., New York, 2016. Price: \$140 (hardcover).

- ISBN 978-1-107-06352-5. . *Am. J. Phys.* **85**, 557–558 (2017).
17. Astumian, R. D. & Bier, M. Fluctuation driven ratchets: Molecular motors. *Phys. Rev. Lett.* **72**, 1766–1769 (1994).
 18. Astumian, R. D. & Derényi, I. Fluctuation driven transport and models of molecular motors and pumps. *Eur. Biophys. J.* **27**, 474–489 (1998).
 19. Buguin, A., Brochard, F. & De Gennes, P. G. Motions induced by asymmetric vibrations: The solid/solid case. *Eur. Phys. J. E* **19**, 31–36 (2006).
 20. Bohringer, K. F. & Choset, H. *DISTRIBUTED MANIPULATION*. (2000).
 21. Flach, S., Yevtushenko, O. & Zolotaryuk, Y. Directed current due to broken time-space symmetry. *Phys. Rev. Lett.* **84**, 2358–2361 (2000).
 22. Denisov, S., Flach, S. & Hänggi, P. Tunable transport with broken space-time symmetries. *Phys. Rep.* **538**, 77–120 (2014).
 23. Astumian, R. D. & Hänggi, P. Brownian motors. *Phys. Today* **55**, 33–39 (2002).
 24. Dechant, A., Baule, A. & Sasa, S. I. Gaussian white noise as a resource for work extraction. *Phys. Rev. E* **95**, 1–12 (2017).
 25. Brunet, P., Eggers, J. & Deegan, R. D. Vibration-induced climbing of drops. *Phys. Rev. Lett.* **99**, 3–6 (2007).
 26. Noblin, X., Kofman, R. & Celestini, F. Ratchetlike motion of a shaken drop. *Phys. Rev. Lett.* **102**, 1–4 (2009).
 27. Baule, A. & Sollich, P. Singular features in noise-induced transport with dry friction. *Epl*

- 97, (2012).
28. Harms, Z. D., Mogensen, K. B., Nunes, P. S. & Jacobson, S. C. Nanofluidic Devices with Two Pores in Series for Resistive-Pulse Sensing of Single Virus Capsids. *Anal. Chem.* **83**, 9573–9578 (2011).
 29. Fu, J., Yoo, J. & Han, J. Molecular sieving in periodic free-energy landscapes created by patterned nanofilter arrays. *Phys. Rev. Lett.* **97**, 1–4 (2006).
 30. Lee, C. Y., Choi, W., Han, J. H. & Strano, M. S. Coherence resonance in a single-walled carbon nanotube ion channel. *Science (80)*. **329**, 1320–1324 (2010).
 31. Kramers, H. A. Brownian motion in a field of force and the diffusion model. *Phys.* **7** 284–304 (1940).
 32. Hänggi, P., Talkner, P. & Borkovec, M. Reaction-rate theory: Fifty years after Kramers. *Rev. Mod. Phys.* **62**, 251–341 (1990).
 33. Sebastian, K. L. & Paul, A. K. R. Kramers problem for a polymer in a double well. *Phys. Rev. E - Stat. Physics, Plasmas, Fluids, Relat. Interdiscip. Top.* **62**, 927–939 (2000).
 34. Mel'nikov, V. I. The Kramers problem: Fifty years of development. *Phys. Rep.* **209**, 1–71 (1991).
 35. Benzi, R., Sutera, A. & Vulpiani, A. The mechanism of stochastic resonance. *J. Phys. A. Math. Gen.* **14**, (1981).
 36. Neiman, A. & Schimansky-Geier, L. Stochastic resonance in bistable systems driven by harmonic noise. *Phys. Rev. Lett.* **72**, 2988–2991 (1994).
 37. Giacomelli, G., Marin, F. & Rabbiosi, I. Stochastic and bona fide resonance: An

- experimental investigation. *Phys. Rev. Lett.* **82**, 675–678 (1999).
38. Simon, A. & Libchaber, A. Escape and synchronization of a Brownian particle. *Phys. Rev. Lett.* **68**, 3375–3378 (1992).
 39. Doering, C. R. & Gadoua, J. C. Resonant activation over a fluctuating barrier. *Phys. Rev. Lett.* **69**, 2318–2321 (1992).
 40. Pechukas, P. & Hänggi, P. Rates of activated processes with fluctuating barriers. *Phys. Rev. Lett.* **73**, 2772–2775 (1994).
 41. Kawaguchi, M., Mino, H., Momose, K. & Durand, D. M. Stochastic resonance with a mixture of sub-and supra-threshold stimuli in a population of neuron models. *Proc. Annu. Int. Conf. IEEE Eng. Med. Biol. Soc. EMBS* **70**, 7328–7331 (2011).
 42. Hänggi, P. Stochastic resonance in biology: How noise can enhance detection of weak signals and help improve biological information processing. *ChemPhysChem* **3**, 285–290 (2002).
 43. Reimann, P. & Hänggi, P. Surmounting fluctuating barriers: Basic concepts and results. *Stoch. Dyn.* 127–139 (2008) doi:10.1007/bfb0105605.
 44. Mantegna, R. N. & Spagnolo, B. Stochastic resonance in a tunnel diode in the presence of white or coloured noise. *Nuovo Cim. D* **17**, 873–881 (1995).
 45. Mantegna, R. N. & Spagnolo, B. Noise enhanced stability in an unstable system. *Phys. Rev. Lett.* **76**, 563–566 (1996).
 46. Burada, P. S., Schmid, G., Reguera, D., Rubi, J. M. & Hänggi, P. Entropic stochastic resonance: The constructive role of the unevenness. *Eur. Phys. J. B* **69**, 11–18 (2009).

47. Asfaw, M. & Sung, W. Stochastic resonance of a flexible chain crossing over a barrier. *Europhys. Lett.* **90**, (2010).
48. Asfaw, M. Thermally activated barrier crossing and stochastic resonance of a flexible polymer chain in a piecewise linear bistable potential. *Phys. Rev. E - Stat. Nonlinear, Soft Matter Phys.* **82**, 1–6 (2010).
49. Mondal, D., Das, M. & Ray, D. S. Entropic resonant activation. *J. Chem. Phys.* **132**, (2010).
50. Pizzolato, N., Fiasconaro, A. & Spagnolo, B. Noise effects in polymer dynamics. *Int. J. Bifurc. Chaos* **18**, 2871–2876 (2008).
51. Valenti, D. *et al.* Noise Induced Phenomena in the Dynamics of Two Competing Species. *Math. Model. Nat. Phenom.* **11**, 158–174 (2016).
52. Pizzolato, N., Fiasconaro, A., Adorno, D. P. & Spagnolo, B. Resonant activation in polymer translocation: New insights into the escape dynamics of molecules driven by an oscillating field. *Phys. Biol.* **7**, (2010).
53. Ikonen, T., Shin, J., Sung, W. & Ala-Nissila, T. Polymer translocation under time-dependent driving forces: Resonant activation induced by attractive polymer-pore interactions. *J. Chem. Phys.* **136**, (2012).
54. Nath, J., Das, S., Vishwakarma, A. & DasGupta, A. Directed transport of a particle on a horizontal surface under asymmetric vibrations. *Phys. D Nonlinear Phenom.* **440**, 133452 (2022).
55. Deb, A., Gogoi, P., Singh, S. K. & Gooh Pattader, P. S. Noise-Activated Fast Locomotion of DNA through the Frictional Landscape of Nanoporous Gels. *Langmuir* **38**, 11764–11769

- (2022).
56. Burlatsky, S. F. & Deutch, J. M. Solid friction in gel electrophoresis. *J. Chem. Phys.* **103**, 8216 (1995).
 57. Mettu, S. & Chaudhury, M. K. Motion of liquid drops on surfaces induced by asymmetric vibration: Role of contact angle hysteresis. *Langmuir* **27**, 10327–10333 (2011).
 58. John, K., Hänggi, P. & Thiele, U. Ratchet-driven fluid transport in bounded two-layer films of immiscible liquids. *Soft Matter* **4**, 1183–1195 (2008).
 59. Thiele, U. & John, K. Transport of free surface liquid films and drops by external ratchets and self-ratcheting mechanisms. *Chem. Phys.* **375**, 578–586 (2010).
 60. Daniel, S. & Chaudhury, M. K. Rectified Motion of Liquid Drops on Gradient Surfaces Induced by Vibration. *Langmuir* **18**, 3404–3407 (2002).
 61. Daniel, S., Chaudhury, M. K. & De Gennes, P. G. Vibration-actuated drop motion on surfaces for batch microfluidic processes. *Langmuir* **21**, 4240–4248 (2005).
 62. Dorbolo, S., Terwagne, D., Vandewalle, N. & Gilet, T. Resonant and rolling droplet. *New J. Phys.* **10**, (2008).
 63. Kelvin, Lord. *Mathematical and Physical Papers*. vol. I (1882).
 64. Chandrasekhar, S. & Gillis, J. *Hydrodynamic and Hydromagnetic Stability*. *Physics Today* vol. 15 (1962).
 65. Baron Rayleigh, J. W. S. *The Theory of Sound*. *Oxford University* vol. I (1895).
 66. Muthukumar, M. *Polymers under Confinement*. vol. 149 (2012).

67. Duke, T. A. J. & Viovy, J. L. Simulation of megabase DNA undergoing gel electrophoresis. *Phys. Rev. Lett.* **68**, 542–545 (1992).
68. Juan Guan, Bo Wang & Granick, S. Automated single-molecule imaging to track DNA shape. *Langmuir* **27**, 6149–6154 (2011).
69. Zhou, H. X. & Zwanzig, R. A rate process with an entropy barrier. *J. Chem. Phys.* **94**, 6147–6152 (1991).
70. Reguera, D. & Rubí, J. M. Kinetic equations for diffusion in the presence of entropic barriers. *Phys. Rev. E - Stat. Physics, Plasmas, Fluids, Relat. Interdiscip. Top.* **64**, 8 (2001).
71. Mondal, D. & Ray, D. S. Diffusion over an entropic barrier: Non-Arrhenius behavior. *Phys. Rev. E - Stat. Nonlinear, Soft Matter Phys.* **82**, 1–4 (2010).
72. Burada, P. S. *et al.* Entropic stochastic resonance. *Phys. Rev. Lett.* **101**, 1–4 (2008).
73. Asfaw, M. Thermally activated barrier crossing and stochastic resonance of a flexible polymer chain in a piecewise linear bistable potential. *Phys. Rev. E - Stat. Nonlinear, Soft Matter Phys.* **82**, 1–16 (2010).
74. Muthukumar, M. Polymer translocation through a hole. *J. Chem. Phys.* **111**, 10371–10374 (1999).
75. Heller, C. *et al.* Free-solution electrophoresis of DNA. *J. Chromatogr. A* **806**, 113–121 (1998).
76. Helling, R. B., Goodman, H. M. & Boyer, H. W. Analysis of Endonuclease R-EcoRI Fragments of DNA from Lambdoid Bacteriophages and Other Viruses by Agarose-Gel Electrophoresis. *J. Virol.* **14**, 1235–1244 (1974).

77. Kim, A. S. & Kim, H.-J. Dissipative Dynamics of Granular Materials. *Granul. Mater.* (2017) doi:10.5772/intechopen.69196.
78. Hatano, T. Jarzynski equality for the transitions between nonequilibrium steady states. *Phys. Rev. E - Stat. Physics, Plasmas, Fluids, Relat. Interdiscip. Top.* **60**, R5017–R5020 (1999).





CHAPTER 5

Detection of *K.pneumoniae* for UTI diagnosis using gold nanoparticle conjugated aptasensor in gel electrophoretic setting

Contents

ABSTRACT.....	131
5.1. Introduction	132
5.2. Materials & Methods.....	135
5.2.1. Reagents.....	135
5.2.2. Instruments used	135
5.2.3. Phosphate saline buffer.....	136
5.2.4. Gold nanoparticle synthesis	136
5.2.5. Bacterial Culture	136
5.2.6. Aptamer development by Cell-SELEX	137
5.2.7. Preparation of aptamer modified AuNPs.....	140
5.2.8. Optimization of the Apt-AuNP parameters.....	141
5.2.9 Transmission Electron Microscopy study.....	142
5.2.10. Preparation of samples for Raman analysis	142
5.2.11. Specificity assay for target analyte detection.....	143
5.2.12. Development of aptasensor.....	143
5.2.13. Detection of <i>K.pneumoniae</i> in clinical urine samples.....	143
5.2.14. Agarose gel preparation & Experimental Procedure.....	144
5.3. Results & Discussion.....	144

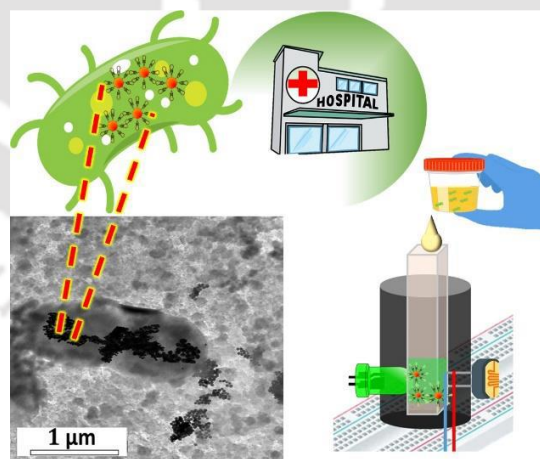
5.3.1. Detection mechanism using gel electrophoretic study.....	144
5.3.2. Detection mechanism.....	146
5.3.3. Characterization.....	152
5.3.4. Specificity study	153
5.3.5. Aptasensor Prototype Fabrication	154
5.3.6. Selection of the LED	155
5.3.7. Specificity of the aptasensor	157
5.3.8. Cost estimation & Description of components.....	159
5.3.9. Calibration & Clinical Trial.....	162
5.3.10. Limit of detection & Stability analysis of aptasensor.....	165
5.3.11. CLED Agar culture of uropathogens.....	167
5.3.12. Summary of the detection mechanism.....	168
5.4. Conclusions.....	169
References.....	170



ABSTRACT

Urinary tract infection (UTI), which can be caused by various pathogens, if not detected at an early stage can be fatal. It is essential to identify the specific pathogen responsible for UTI for appropriate treatment. We have provided a proof-of-concept for specific pathogen detection using external noise induced gel electrophoresis setup. Additionally, this study also describes a generic approach to the fabrication of a prototype for the non-invasive detection of a specific pathogen using a tailor-made plasmonic aptamer-gold nanoparticle (AuNP) assay. The assay is advantageous because the adsorbed specific aptamers passivate the nanoparticle surfaces and reduce and/or eliminate false-positive responses to non-target analytes. Based on the Localized Surface Plasmon Resonance (LSPR) phenomena of AuNP, a point-of-care aptasensor was designed that shows specific changes in the absorbance in the visible spectra in presence of a target pathogen for robust and fast screening of UTI samples. In this study, we demonstrate the specific detection of *Klebsiella pneumoniae* bacteria with LoD as low as 3.4×10^3 CFU/mL.

Graphical Abstract



POC aptasensor for specific instantaneous detection of *K.pneumoniae*

Keywords: Urinary tract Infection, noise induced gel electrophoretic setting, aptasensor.

This chapter is “Under Review” under the title “Specific instantaneous detection of *Klebsiella pneumoniae* for UTI diagnosis with plasmonic gold nanoparticle conjugated aptasensor”.

5.1. Introduction

Over the last decade, investigations related to the properties of gold nanoparticles (AuNPs) have witnessed significant growth owing to the applications of AuNPs in drug delivery¹⁻³, photothermal therapy^{4,5}, diagnostic imaging⁶, biosensors^{7,8}, etc. Apart from being the most stable metallic nanoparticle⁹, AuNP flaunts several other features, including surface plasmon resonance^{8,10} (SPR), high reactivity with specific biomolecules through click chemistry¹¹, high surface area to volume ratios¹², etc. These qualities of AuNP, make it a promising candidate for the development of colorimetric biosensors for disease diagnosis. Literatures have uncovered the DNA conjugation on gold monolayer surfaces by utilizing direct attachment of an aptamer to a gold surface using a thiol-alkane linked to the aptamer sequence¹³. Aptamer immobilization generally operate through chemisorption of thiol onto gold. Henceforth, an aptamer with thiol end group can be used to form a self-assembled monolayer (SAM) on the gold surface^{14,15}. Gold-thiol bonds provide high affinity and are highly stable to complex liquid media containing target biomolecules. An emerging strategy is to exploit the intrinsic surface properties of AuNP¹⁶ and modify the surface by targeting specific pathogens such as bacteria, viruses, or specific biomarkers, etc., which leads to the change in the electrostatic environment of the AuNP and thus the specific color change. ssDNA immobilized on citrate-capped NPs has been used to detect pathogens by color change due to the aggregation of the nanoparticles in the presence of the target analyte¹⁷.

Urinary tract infections¹⁸⁻²⁰ (UTIs) are the most common bacterial infections worldwide and account for the maximum load on hospital's Out Patient Departments (OPDs). UTI is more prevalent in females, especially during pregnancy²¹⁻²³. More than 80% of infection is caused by *Escherichia coli* (*E.coli*) while other major infecting bacteria are *Klebsiella pneumoniae* (*K.pneumoniae*) (~17%), *Staphylococcus aureus* (*S.aureus*) (~30%), *Enterococcus faecalis* (*E. faecalis*) (~2%), etc^{24,25}. UTI diagnosis for bacterial presence is almost exclusively done by

urine culture, which is the gold standard for UTI detection worldwide²⁶. Though urine culture provides precise diagnosis, the method has its limitations including a longer duration for diagnosis and the requirement of trained personnel and sophisticated equipment, which are generally not available in rural settings. In developing countries, UTIs remain almost undetected in rural areas because of the lack of testing facilities²⁷⁻²⁹. A frugal diagnostic kit can be developed which can specifically identify the bacteria causing the UTI without any requirement for laboratory infrastructure. This type of point-of-care (POC) kit may not need any trained personnel to operate³⁰.

Aptamers are a class of small single-stranded DNA or RNA oligonucleotides capable of binding to selected targets, including whole cells, proteins, peptides, and to small molecules with high specificity and affinity, owing to their unique three-dimensional (3D) structures. Aptamers are usually selected from large random nucleic acid libraries by Systematic Evolution of Ligands by Exponential enrichment (SELEX), which involves four significant steps - binding of Aptamer molecules to the target, partitioning of bound aptamers from unbound non-specific aptamers, enrichment of bound aptamers by PCR and regeneration of single-stranded aptamer molecules^{31,32}. Aptamers have been widely used as biosensors to identify bacterial populations in biological fluids, contaminated water, soil, etc.³³ Aptamers bind to the targets by their 3D structures instead of base-pairing. When nucleic acids are used in biosensors for the detection of genomic nucleic acids via hybridization, these biosensors are called genosensors³⁴; on the other hand, if aptamers are applied in biosensors for the recognition of small molecules, proteins, or cells, the biosensors are called aptasensors³⁴. For optical biosensors, the detection methods include fluorescence³⁵, colorimetry^{36,37}, chemiluminescence³⁸, surface plasmon resonance (SPR)¹⁰, Raman spectroscopy³⁹, photoelectrochemical^{40,41} etc. Optical aptasensors have been used for the detection of viruses and foodborne pathogens⁴². Bacteria-binding aptamers interact directly with the cell surface

of the target rather than nucleic acids and thus have the potential for whole bacteria detection⁴³. Whole-cell SELEX is commonly used to generate aptamers against desired bacterial cells. The ease of synthesis, cost-effectiveness, and stability of aptamers along with the high specificity of detection make the aptasensors lucrative for detection, separation, and activity studies⁴¹.

In this study, we developed an aptasensor³⁰ to specifically detect *K.pneumoniae*³⁷ by exploiting the change in surface plasmon resonance of aptamer-modified AuNPs (Apt-AuNP). The tailor-made specific aptamers were immobilized on the gold surface to form Apt-AuNP. For instance, AuNPs show a strong surface plasmon resonance (SPR) absorption peak, which is closely related to the size of NPs^{44,45}. The refractive index close to the nanoparticle surface affects the optical characteristics of gold nanoparticles. The nanoparticle extinction spectrum moves to longer wavelengths as the refractive index changes due to aggregation (known as red-shift or bathochromic shift). While the gold nanoparticles aggregate, the conduction electrons near each particle surface become delocalized and are shared by nearby particles, changing the optical characteristics of the gold nanoparticles. This results in a redshift of the absorption peak (i.e. to longer wavelengths) when the surface plasmon resonance moves to lower energy. The Aptamer used in the present work brings the AuNPs closer to each other and forms a chain-like structure of AuNPs (Apt-AuNPs), associated with a bathochromic shift in the UV-Vis spectroscopy. In presence of a targeted bacteria, these Apt-AuNPs adhere to the surface of the bacteria and enhance the intensity of the UV-Vis signal resulting in a hyperchromic effect. The aptasensor responds almost instantaneously to target analytes with a positive colorimetric signal while remaining insensitive to non-target analytes, ensuring the fast, accurate and reliable detection of *K.pneumoniae*^{37,46,47}. Thus, the best advantages of this assay are its high specificity and rapid detection. The approach is generic and can be modified according to any specific target pathogen causing UTIs. The developed prototype will be an immense help in

choosing the effective antibiotic for the treatment in no time, unlike the conventional clinical method that needs 24 h to identify the UTI-causing pathogen³⁰.

We have targeted *K.pneumoniae* as it is also responsible for various infections, such as lung infection⁴⁸, meningitis⁴⁹, intra-abdominal infection⁵⁰, bacterial pneumoniae, blood-stream infection⁵¹, pyogenic liver abscess,^{52,53} etc. Thus other body fluids such as sputum⁵⁴, blood, or cerebrospinal fluid⁵⁵ (CSF) can also be tested in a similar manner as demonstrated here for the urine samples of suspected UTI patients to quantify the concentration of *K.pneumoniae* in those body fluids and to map the severity of the infections.

5.2. Materials and Methods

5.2.1. Reagents

Purified 5' Thiol modified ssDNA aptamer was procured from Integrated DNA Technologies (IDT, USA). Gold (III) chloride hydrate 99.995 % trace metal basis (HAuCl_4) CAS No. 27988-77-8, tri-Sodium citrate dihydrate, for analysis EMSURE® ($\text{HOC}(\text{COONa})(\text{CH}_2\text{COONa})_2 \cdot 2\text{H}_2\text{O}$) were procured from Sigma-Aldrich. 10X Phosphate Buffered Saline (PBS) was procured from SRL Chemicals. CLED Agar, w/Bromo Thymol Blue Cat No: M792-500 g and Hichrome Chromogenic Coliform Agar (CCA Agar) Cat No: M1997I- 100 gm were procured from HIMEDIA. Agarose powder was procured from Loba Chemie.

5.2.2. Instruments used

An UV-vis spectrophotometer (Shimadzu, UV-2600 230 V EN), Transmission Electron Microscope (JEOL, JEM 2100 at the acceleration voltage of 200 kV), Raman spectrometer (Horiba Scientific, LabRAM HR Evolution), Dynamic light scattering (DLS) (Make: Anton Paar, Litesizer 500) were used to analyze the samples. The Zeta potential of the samples was

also evaluated by DLS, equipped with a semiconductor laser diode (40 mW) having a wavelength of 658 nm. A 3D printer (Make: Ultimaker 3, Netherlands) was used to fabricate the device prototype from polylactic acid (PLA) filament.

5.2.3. Phosphate Buffered Saline (PBS)

10X PBS was stored at 4°C and diluted to 1X using nuclease-free water during experiments.

5.2.4. Gold Nanoparticle synthesis

A stock HAuCl₄ solution of 1 mM was prepared by dissolving 33.9 mg of HAuCl₄ in 100 mL of Molecular biology grade water. A working solution of 0.25 mM was prepared by proper dilution using Molecular biology grade water. The prepared HAuCl₄ solution was then taken in a 50 mL beaker and heated on a magnetic hot plate at 103°C for 20 min. To the rapidly boiling HAuCl₄ solution, 2 mL of 0.38 mM trisodium citrate dihydrate, Na₃C₆H₅O₇ · 2H₂O was added slowly while stirring at 800 rpm. The stirring was continued for 45 min. Trisodium citrate dihydrate reduces the Au (III) and stabilizes the AuNP. In the solution, on the Au surface, adsorbed citrate ions provide negative charges. The negative surface charges induce particle-particle repulsion and thus stabilize the AuNPs. The final color of the solution subsequently turns wine red, indicating the formation of Au NPs. The mean size of the AuNPs was estimated using DLS and was found to be ~26 nm. The AuNP solution thus synthesized was stored at 4 °C in an airtight container for further use.

5.2.5. Bacterial Culture

All bacterial strains were Indian isolates, purchased from MTCC (Microbial Type Culture Collection), Chandigarh, India. The target bacterial strains *Klebsiella pneumoniae* (MTCC-7028) and non-targets *Escherichia coli* (MTCC-42), *Enterococcus faecalis* (MTCC-3159), and *Staphylococcus aureus* (MTCC- 9542) were grown in Luria-Bertani medium (HiMedia) at 37 °C to an OD₆₀₀ of 1.0 (equivalent to ~10⁸ cells/mL). For Cell-SELEX and Aptamer-based

detection assays, cells were centrifuged at 8000rpm for 1 min and washed twice with 1X PBS, and re-suspended in an appropriate buffer.

5.2.6. Aptamer development by Cell-SELEX

The DNA Aptamers development for the target *K. pneumoniae* was performed using Cell-SELEX technology as depicted in Figure 5.1. Briefly, 1.5 μM ssDNA Aptamer library was incubated with 10^8 CFU/ml of target bacterial cells, suspended in binding buffer (1X PBS, 1% BSA, and 0.1mg/ml t-RNA), for 45 min at room temperature with gentle shaking. After aptamer library incubation, cells were centrifuged for 5min at 8000rpm and the unbound ssDNA library molecules were pipetted out and discarded. The cell-bound ssDNA selected aptamers were washed twice with 1X PBS and re-suspended in 250 μl nuclease-free deionized water. Aptamers bound to the cells were recovered by heating the suspension at 95 $^{\circ}\text{C}$ for 10 min followed by centrifugation at 12,000 rpm for 15 min. The selected aptamer pool was transferred to a microcentrifuge tube. This selected aptamer pool was PCR amplified for subsequent rounds of SELEX. PCR amplification was carried out for 10 cycles using 0.15 μM of Forward primer [5'-GGCTGGATGGGGCGTGT-3'] and 0.15 μM 5'-Biotin-labeled reverse primer [5'-CGCTGTCCGCACCGTTG-3'] using 2X DreamTaq PCR master mix (Thermo Scientific). The PCR program used was: pre-denaturation at 95 $^{\circ}\text{C}$, 5min followed by cycling step; 95 $^{\circ}\text{C}$ for 20 s, annealing at 55 $^{\circ}\text{C}$ for 5 s, and extension at 72 $^{\circ}\text{C}$ for 10s. The Amplified dsDNA pool was purified using GeneJET PCR Purification kit (Thermo Scientific) and the concentration of the purified PCR pool was determined by spectrophotometer. 2 μg of biotinylated dsDNA was attached to 100 μl of activated M-280 streptavidin magnetic Dynabeads (Invitrogen) at room temperature in 200 μl of binding buffer (10 mM Tris-HCl pH 8.0, 1 mM EDTA pH 8.0, 2M NaCl). The selected sense DNA strand was separated from the biotinylated strand by 500 μl of 10 mM NaOH. The ssDNA was purified using NAP-5 desalting column (GE Healthcare) in a volume of 1ml water. Before using the ssDNA pool for

the next round, DNA was concentrated using SpeedVac system. The SELEX was carried out for 10 rounds. After SELEX rounds 4, 6, and 8, the negative selection was carried out using non-target species of uropathogens: *E. coli*, *E. faecalis*, *S. aureus*, and *Proteus*. During negative selection rounds, the bound ssDNA aptamer pool was incubated with the non-target bacteria pool for 30 min, and the unbound ssDNA pool was recovered by centrifugation and immediately incubated with target bacteria. The scheme used for bacterial cell-SELEX is detailed in Figure 5.1. After the 10th round of selection, the ssDNA Aptamer pool was PCR amplified using unlabelled forward and reverse primers followed by alcohol precipitation of dsDNA. The purified PCR products were cloned into the TA-cloning vector using pGEM®-T easy vector systems (Promega). 40 positive colonies (white colonies) were inoculated in 5ml of LB media and grown overnight at 37 °C at 220 rpm. Plasmids were isolated and checked on 1.5 % agarose gel. Individual cloned DNA Aptamers were DNA sequenced using Sangers dideoxy chain termination method (1st Base, Axil Scientific, Singapore facility). The 40 selected DNA Aptamers that were sequenced, 5 of them were repeated in 32 of the clones and thus these 5 Aptamers were taken forward for further studies to select finally which one(s) of them will be used for aptasensor development. The five selected DNA Aptamers (KPBA1, KPBA7, KPBA19, KPBA4, and KPBA39) were individually synthesized commercially with FAM label at 5'-end. Flow cytometry was used to assess the binding of the individual aptamer to target *K. pneumoniae* and other non-target bacterial cells. 50pmoles of ssDNA Aptamers were incubated with 10⁷ target *K. pneumoniae* and negative *E. coli*, *S. aureus* and *E. faecalis* cells at 37°C for 45 min. Cells were washed twice with 1X PBS and were re-suspended in 1ml 1X PBS and were analyzed in a flow cytometer. Figure 5.1.1 shows the specificity of selected Aptamers for target *K.pneumoniae* bacteria. The FAM-labeled ssDNA library was used as a control.

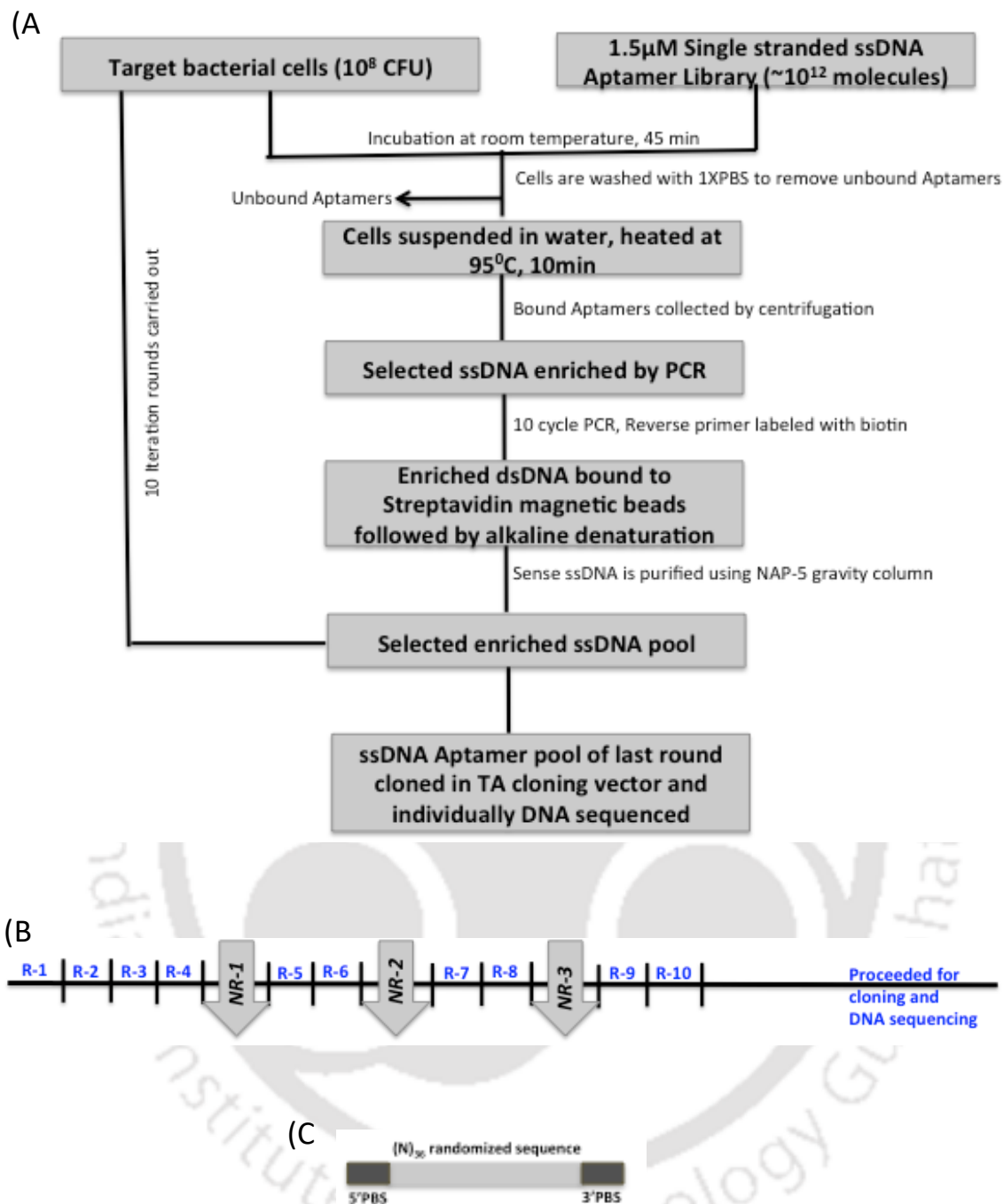


Figure 5.1. Schematics of the Cell-SELEX work flow carried out for DNA Aptamer development for target *K.pneumoniae*. (A) Outline various steps followed in the Cell-SELEX procedure. (B) Depicts the sequence of three Negative Rounds (NR); 1, 2 and 3 during the SELEX. (C) Depicts the ssDNA library construction used in the present SELEX process. PBS is the Primer Binding Site at both 3' and 5' ends which were 17 bases long flanking the randomized sequence of 36 bases.

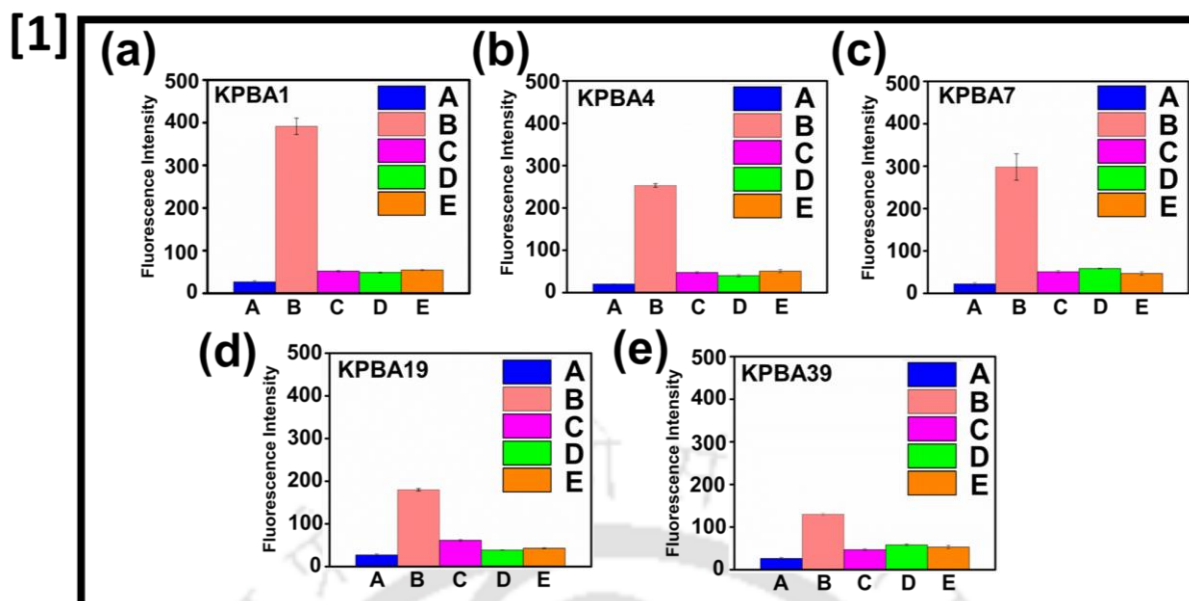


Figure 5.1.1. Specificity of selected Aptamers for target *K.pneumoniae* bacteria. KPBA1 sequence shows the maximum specificity. [The inset shows A- Control, B- *K.pneumoniae*, C- *E.coli*, D- *S.aureus*, E- *E.faecalis*]. The error bars in the diagram indicate the standard deviation of the readings obtained from 3 measurements.

5.2.7. Preparation of aptamer-modified AuNPs

The 5'-thiol modified ssDNA Aptamer, KPBA1 (5'-/5ThioMC6-D/GGC TGG ATG GGG CGT GTG GAG CCC CGT TAG AAT ATC AGA GGT GGT GGC AAC GGT GCG GAC AGC G-3') was immobilized on AuNPs. Briefly, 100 μL of 0.05 μM aptamer was mixed with 100 μL of 1 mM TCEP and incubated at room temperature for 1 h to ensure the cleavage of the disulfide bonds (-S-S-) completely. After that, 300 μL 1X PBS was added to the solution and was heated to 95 $^{\circ}\text{C}$. The solution was then gradually cooled to room temperature. This thermal annealing helps to maintain the structural flexibility of the aptamers to facilitate the binding of the target analyte at the appropriate sites. 250 μL of 0.0024 nM AuNPs was then added and the reaction was incubated at room temperature for 16 h in dark. The free -SH groups of the Aptamer react with the AuNP surface^{56,57}.

5.2.8. Optimization of Aptamer-AuNP coupling parameters

The optimal concentration of Aptamer-AuNP was determined using UV-Vis spectra while reacting different concentrations of aptamer (ranging from 0.001 to 0.5 μM) with the AuNP. The optimal concentration of 0.05 μM was decided by the bathochromic shift of ~ 3 nm shown in the figure below (Figure 5.2). 100 μL of 0.05 μM aptamer was mixed with 100 μL of 1 mM TCEP and incubated at room temperature for 1 h to complete the disulfide cleavage. TCEP being a reducing agent disrupts the disulfide bonds (-S-S-) and frees the (-SH) groups to be bound onto the gold surface⁵⁸. Phosphate Buffer Solution (PBS) having pH=7.4 was added and subsequently thermal annealing was performed to maintain the structural flexibility of the aptamer binding to target detection⁵⁹. AuNPs were finally added to the free aptamer solution. The functionalized nanoparticles were separated from free oligonucleotides via three consecutive centrifugation (13,000 rpm, 20 min) and washing steps. Washing was performed with PBS after each centrifugation. Finally, the particles were re-suspended in PBS buffer.

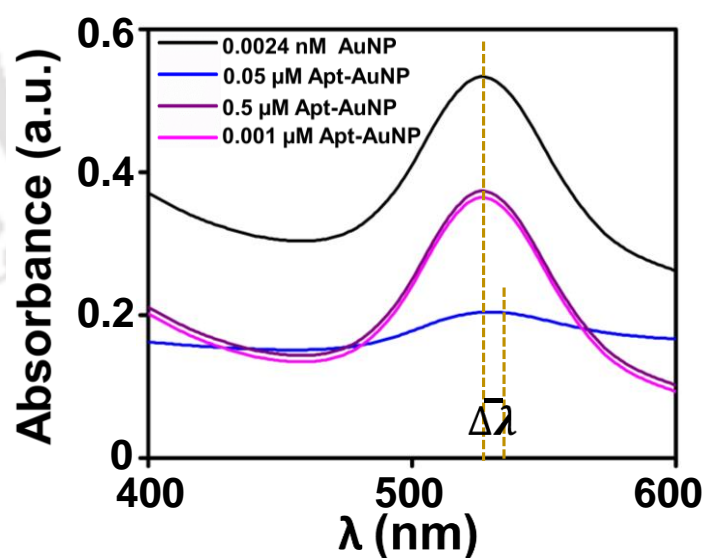


Figure 5.2. UV-Vis spectra demonstrating the optimization concentration of Apt-AuNP conjugation which shows a bathochromic shift of ~ 3 nm using 0.05 μM Apt- 0.0024 nM AuNP.

5.2.9. Transmission Electron Microscopy Study

The TEM images of AuNPs were obtained by using JEOL JEM 2100 transmission electron microscopy with an accelerating voltage of 200 kV. TEM sample was prepared by dispensing 200 μ L AuNP solution onto carbon-coated copper grids and vacuum-dried. A similar protocol was followed for the other samples.

5.2.10. Preparation of samples for Raman Analysis

Raman spectroscopy was used to characterize Au-S interactions due to the adsorption of aptamers onto the AuNP surface (Apt-AuNP). For the characterization, 2 mL of Apt-AuNP matrix was taken in a cuvette. The solution was centrifuged at 13,000 rpm for 20 min and resuspended in the working buffer with the help of sonication. The supernatant solution containing unbound free aptamers was discarded and the volume was adjusted using the working buffer. The above process was repeated thrice to remove unbound aptamers. For a control experiment, the Raman analysis of only the AuNP solution was performed following a similar protocol. To determine the bacterial conjugation with the Apt-AuNP matrix, 600 μ L of target analyte of specific concentrations of *K.pneumoniae* was mixed with 2 mL of the matrix and kept at room temperature for 10 min for binding. The following parameters were used for Raman analysis of all the samples: 532 nm laser wavelength, 25 s accumulation time, 5 s acquisition time, 10 % modulation, grating 600 gr/mm, and 100X optical magnification.

Raman spectra of the samples confirmed the conjugation of *K. pneumoniae* along with the Apt-AuNP matrix as discussed later. A similar protocol was followed when the non-target analytes were mixed with the Apt-AuNP matrix, which showcased non-attachment with the sensing matrix.

5.2.11. Specificity assay for target analyte detection

The specificity of the reaction mechanism was studied to assess the stability of surface plasmon assay-based aptasensor to respond only to the target pathogen *K.pneumoniae*. The assay's specificity was tested against non-targets and common uropathogens such as *E.coli*, *S.aureus*, and *E.faecalis*. The changes in the absorbance were recorded using the developed aptasensor prototype and validated using the UV-Vis spectrophotometer.

5.2.12. Development of aptasensor

A simplistic aptasensor prototype was developed that had a light-emitting diode as an optical source, a light-dependent resistor as a photodetector, a multimeter as the measuring tool, and a cuvette as the sample holding unit. A 3D printer was used to create the device's basic structure. LED and LDR were precisely aligned on the opposite side walls of the 3D printed setup, to ensure that the maximum amount of light from the LED travels through the solution and reaches the LDR. The specific dimensional cuvette ensures the constant optical path length during the entire investigation. Figure 5.4 displays the experimental setup. Additional details about the aptasensor prototype are described in the section 5.3.8.

5.2.13. Detection of *K. pneumoniae* in clinical urine samples

The clinical urine samples from suspected UTI patients were collected from OPD of GNRC Hospital, Guwahati. The ethical committee of both institutes approved the clinical study. Informed consent was obtained from all the participants in the study. Mid-stream urine was collected in a sterile sample cup. For *K.pneumoniae* detection, 600 μ L of urine sample was mixed with already prepared 2 mL of aptamer-gold nanoparticle matrix in the developed aptasensor. Samples were simultaneously cultured by hospital pathology labs which generally takes 24 h to confirm the UTI diagnosis and identification of target bacteria.

5.2.14. Agarose gel preparation & Experimental Procedure

0.8% (w/v) agarose gel was prepared by dissolving 0.8 g of agarose powder in 100 ml of 1X Tris Acetate-EDTA (TAE) buffer. The conventional procedure of gel casting was followed thereafter. 10 μ L of sample was dispensed into each well. The duration of electrophoresis was 4 h. The temperature during electrophoresis was maintained at $23\pm 1^\circ\text{C}$. Waveform generator was used for generating noise and thereafter amplified. Visualization of the fragments was done using a Gel DOC (Model: Chemidoc XRS+) instrument. The connection diagram for performing noise induced gel electrophoresis is depicted in figure 5.3.A. Noise power $K = 3.44 \times 10^5 \text{m}^2/\text{s}^3$ was applied along with biased voltage 10V and the resulting outcome was faster translocation of the Apt-AuNP band depicted in figure 5.3.B.

5.3. Results and Discussion

5.3.1. Detection mechanism based on external noise assisted gel electrophoretic method

The experimental setup was similar to the conventional agarose gel electrophoresis under the influence of a constant bias voltage with a provision for introducing Gaussian noise as time-dependent voltage input. A function generator, along with an amplifier, was attached with a bias DC voltage source in a series connection, and the resultant potential was applied across a gel in an electrophoretic set-up through a pair of Pt electrodes and Tris Acetate-EDTA (TAE) buffer (Figure 5.3. (A)). With the help of external noise induced gel electrophoresis⁶⁰, the DNA aptamer-gold nanoparticle conjugate⁶¹ band moves faster depicted in figure 5.3.(B).

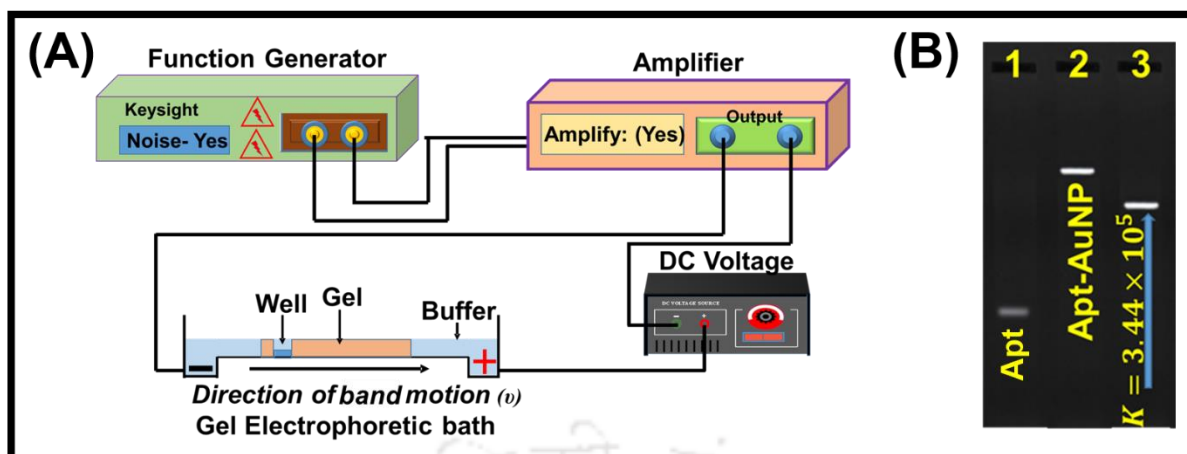


Figure 5.3. Gel doc image depicting the free aptamer (Lane-1), DNA aptamer-gold nanoparticle conjugate band (Lane 2) and external noise exposed DNA Aptamer-AuNP band (Lane 3). Using external noise power $K = 3.44 \times 10^5 \text{m}^2/\text{s}^3$, the mobility of the aptamer-AuNP band increases (Lane 3).

The gel electrophoresis has shown a high potential to separate NP's according to their electrophoretic mobility into several fractions with a higher homogeneity^{61,62}. Since, the electrophoretic mobility is dependent on the plethora of parameters such as particle size, shape, etc along with the gel concentration and applied voltage, whereby differences in the electrophoretic mobilities of two fractions result in different migration velocities and finally in their spatial separation within the gel. Additionally, by literature⁶³, it is possible to adjust the surface of the NP's with various ligands resulting in tailored interactions between the NP's and the gel mesh and buffer solution. All things considered, external noise assisted gel electrophoresis allows quicker, more prominent and useful separation tool for DNA aptamer-NP's conjugate for further purification and detection strategies.

The system developed here provides a proof-of-concept which can be used by biologists and biochemists for detection of the specific pathogen which can be achieved by amplifying the pathogens DNA or RNA using PCR or reverse transcriptase PCR (RT-PCR). Amplified products are then separated by size on agarose or polyacrylamide gel.

Additionally, a pathway to address the issue was to develop a cost-effective non-invasive point-of-care aptasensor to detect specific pathogen on ground level in rural and urban healthcare scenarios. The detection mechanism was sequentially discussed and adopted with proper vision in the next sections.

5.3.2. Detection Mechanism

An overall detection scheme is shown in figure 5.4. As described earlier, the specific detection of the *K.pneumoniae* (KP) bacteria in the urine sample of a patient is based on the hyperchromic effect (increase in the absorbance) of a peak corresponding to the *K.pneumoniae*-Apt-AuNP conjugate at ~ 528 nm. The aptamer, specifically tailored for *K.pneumoniae* bacteria, folds itself in a specific way to favourably bind to the surface of the *K.pneumoniae*. The aptamers anchored with the AuNP thus assist the high accumulation of the AuNPs on the surface of the *K.pneumoniae* bacteria. This accumulation of the AuNPs induces a hyperchromic effect to the peak at ~ 528 nm. This hyperchromic effect is proportional to the concentration of the *K.pneumoniae* present in the urine.

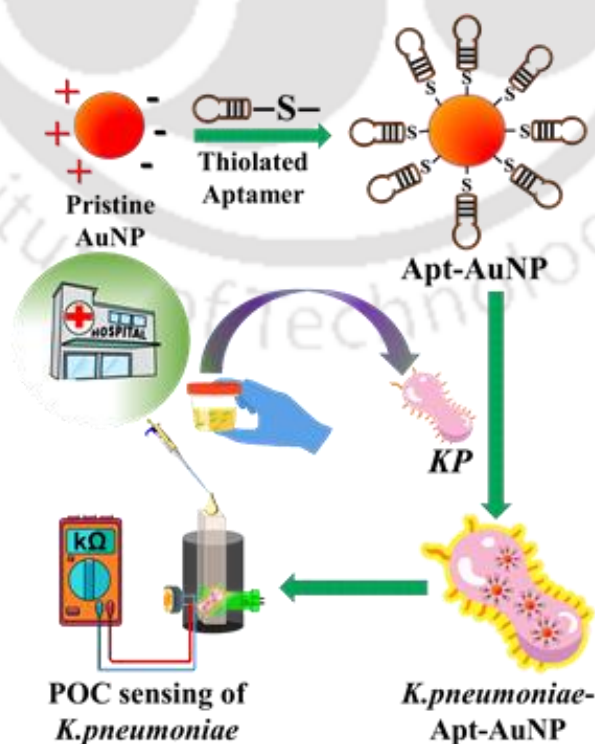


Figure 5.4. A schematic representation of the detection procedure in the developed point-of-care (POC) aptasensor prototype.

The peak absorbance wavelength is sensitive to the interparticle distance between the AuNPs. Due to the presence of citrate, the AuNPs remain stable and dispersed. The TEM image of the same is shown in figure 5.5.A. When photons from incident light interact with the free electrons of the AuNP, the free electrons coherently oscillate together (surface plasmons resonance, SPR). If the surrounding composition of the AuNP changes, the momentum of the surface plasmons changes and thus changes the local surface plasmon resonance (LSPR). After modifying the surface of the AuNP with thiol-terminated aptamers, the Apt-AuNPs form a chain-like structure as shown in figure 5.5.B.

Due to this chain-like Apt-AuNP cluster formation, the LSPR slightly shifts the absorbance peak of unmodified AuNP (~ 525 nm)⁶⁴⁻⁶⁷ towards a higher wavelength of ~ 528 nm. Near field coupling of the AuNPs which occurs due to a change in the interparticle distance between the plasmonic Apt-AuNPs by the formation of chain-like structure (Figure 5.5.B) results in the slight bathochromic shift⁶⁸. This slight bathochromic shift toward 528 nm, along with the peak at ~ 260 nm (Figure 5.5.C) confirms the binding of the aptamer^{69,70}. Also, it must be noted that formation of chain-like structure imparts the heterogeneity and anisotropy (due to variable sized particle oligomers) in the Apt-AuNPs, thus the peak at 528 nm broadens up. Due to LSPR, the coherent oscillation of plasmons on the surface of AuNPs stimulates, and a characteristic peak was observed in UV-Vis spectroscopy. LSPR creates a dipole with separation of charges on the AuNP surface and develops a localized electric field opposing the incident irradiation.

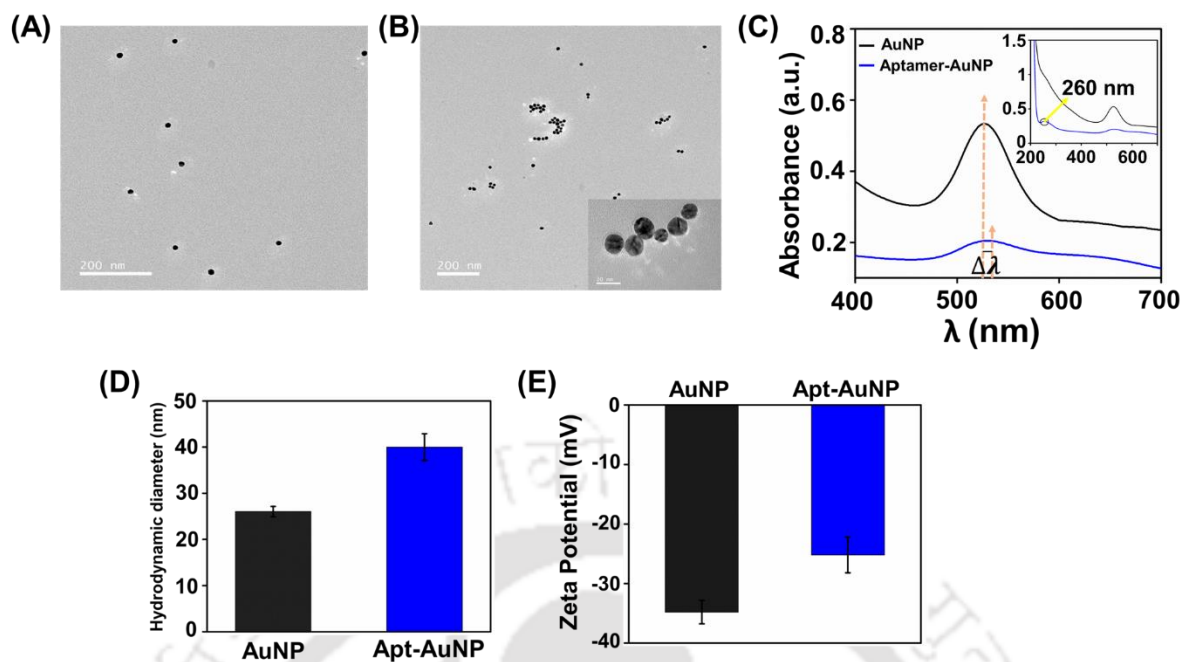


Figure 5.5. (A) TEM image of pristine gold nanoparticles and (B) TEM image of Apt-AuNP conjugate. Plot (C) demonstrates the UV spectra of the pristine AuNP and the Apt-AuNP matrix. The aptamer peak at $\lambda \sim 260$ nm (inset) also confirms the aptamer binding to the nanoparticle surface. Plot (D) shows the average particle size of the synthesized AuNPs and the Apt-AuNP conjugate. Plot (E) shows the zeta potential of the pristine AuNPs and Apt-AuNPs. The error bars in plots (D) and (E) indicate the standard deviation of the particle sizes obtained from 4 separate experimental studies.

The generated electric field can induce charge build-up on the surrounding medium depending on their polarizability⁷¹. Thus, the spectroscopic response of AuNP is sensitive to the surrounding medium. The negative charges on the surface of AuNPs are due to the stabilizing citrate ions. Most of the citrate ions are released after binding of AuNPs with large aptamer molecules through Au-S- covalent bonding. The aptamer conjugation induces mutual polarization that compensates for the accumulation of charges on the surface of AuNPs, eventually reducing the net negative charge on the surface of AuNPs. This is also evident from

the zeta potential of the AuNP and Apt-AuNP (Figure 5.5. (E)). A similar observation was also reported earlier by Wu et al.⁷².

In presence of *K.pneumoniae*, the AuNPs anchor on the *K.pneumoniae* due to the specific folds of the Au-bound aptamers that facilitate the binding to the receptor proteins present on the outer surface of the *K.pneumoniae*. The weakly charged Apt-AuNPs thus aggregated on the surface of the *K.pneumoniae* as shown in the TEM image (Figure 5.6.A). TEM image of the non-targeted bacteria (*E.coli*) (Figure 5.6.B) shows that the Apt-AuNP does not interact with the surface of the bacteria, rather remains indifferent in presence of the non-targeted bacteria and shows the chain-like morphology of the Apt-AuNPs similar to the TEM image shown in Figure 5.5.B.

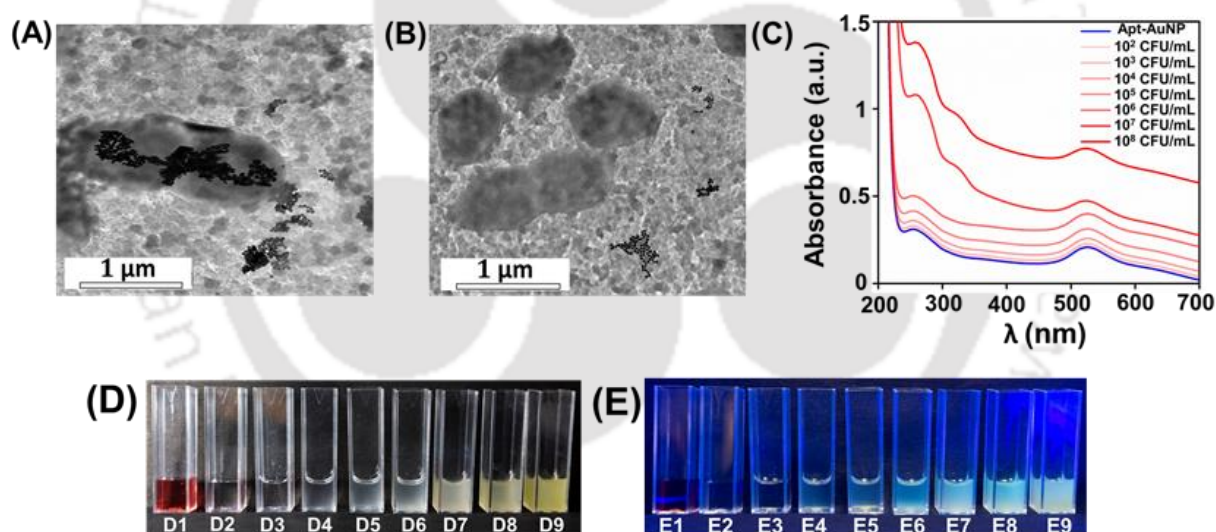


Figure 5.6. (A) TEM image of the Apt-AuNP conjugate attached on the surface of *K.pneumoniae*. (B) TEM image of Apt-AuNP not adhered to the non-target analyte (*E.coli*). Plot (C) shows the UV spectra of *K.pneumoniae* (range: 10^2 - 10^8 CFU/mL). With increasing concentration, the absorbance is also increasing as depicted in the figure. (D) and (E) shows the optical images taken at bright light and UV light (365 nm) respectively. D1, D2 and E1, E2 denote AuNP and Apt-AuNP matrix respectively. D3-D9 and E3-E9 denote the optical images of *K.pneumoniae* solution with increasing concentration ranging from 10^2 - 10^8 CFU/mL in Apt-

AuNP matrix. UV-Vis spectra of *K.pneumoniae* (range: 10^2 - 10^8 CFU/mL) spiked into non-specific aptamer-AuNP conjugate along with the corresponding optical images are shown in the Figure 5.7. Very light pale red as appears in D2 and E2 are illusive, this is due to the reflection from dark red AuNPs in nearby cuvette D1 and E1. (Please refer Figure 5.7.)

Experiments with non-specific aptamer-AuNP (Apt-AuNP) conjugate mixed with different concentrations of *K.pneumoniae* was done to check the specificity. The sequence of the non-specific aptamer used for this study is SABA11 (5'-/5ThioMC6-D/GGC TGG ATG GGG CGT GTT GAT TCG AGT CGG AGA CGG CAT CCT GCA CAA ATG CCA ACG GTG CGG ACA GCG-3'). To examine the developed non-specific Apt-AuNP assay at different concentrations of *K.pneumoniae*, overnight grown cultures of *K.pneumoniae* was diluted sequentially from 10^8 CFU/mL to 10^2 CFU/mL, and then a fixed volume of 600 μ l was dispensed into 2 ml of sensing matrix (non-specific Apt-AuNP) for UV-Vis spectroscopic analysis. The UV-Vis spectra show the intensity of the peak at ~ 528 nm remains constant with the concentrations of *K.pneumoniae* (Figure 5.7.A). The optical images were taken in the bright field and at UV light (~ 365 nm), and are shown in figure 5.7.B and 5.7.C.

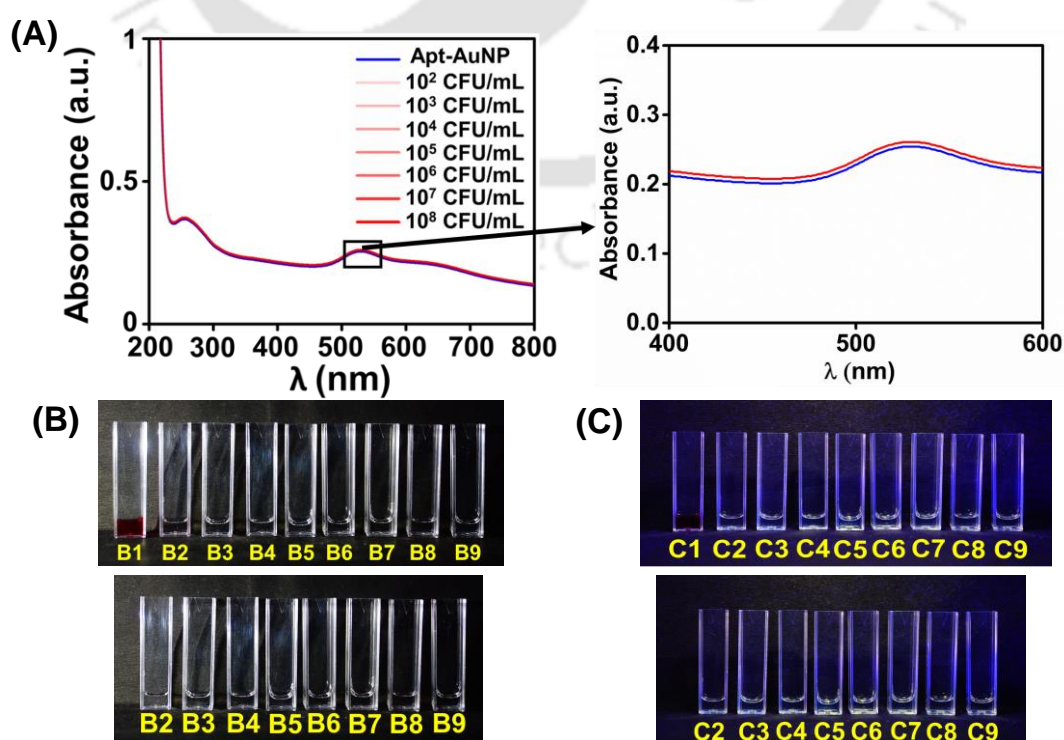


Figure 5.7. Plot (A) shows the UV spectra of *K.pneumoniae* (range: 10^2 - 10^8 CFU/mL) spiked into a non-specific Apt-AuNP. With increasing *K.pneumoniae* concentration, the absorbance change is null as depicted in figure (A). (B) and (C) show the optical images taken at a bright light and UV light (365 nm) respectively. B1, C1 denote AuNP, and B2, C2 show non-specific Apt-AuNP matrix respectively. B3-B9 and C3-C9 denote the optical images of the non-specific Apt-AuNP matrix spiked with *K.pneumoniae* solution of increasing concentration ranging from 10^2 - 10^8 CFU/mL. Lower panels of figure (B) and (C) represent the same cuvettes except the cuvette containing AuNP (B1 and C1). Thus, the B2 (Apt-AuNP) in the lower panel appears almost colorless as the reflection from the nearby B1 cuvette (red in color) is missing. The photograph is illusive (due to vicinity of the dark red AuNP solution), thus UV-Vis spectroscopy is shown in figure (A).

To examine the developed Apt-AuNP assay at different concentrations of *K.pneumoniae*, overnight grown cultures of *K.pneumoniae* was diluted sequentially from 10^8 - 10^2 CFU/mL, and then a fixed volume of 600 μ l was dispensed into 2 ml of sensing matrix (Apt-AuNP) for UV-Vis spectroscopic analysis. The UV-Vis spectra show the intensity of the peak at ~ 528 nm increases with the concentrations of the *K.pneumoniae* (Figure 5.6.C). The aptamer here is acting as a linker between AuNP and the specific targeted bacterial surface. In presence of the targeted bacteria, many AuNPs get attached to the bacterial surface as clusters due to the Aptamer linker. Thus, enhancing the intensity of the absorbance at 528 nm. More targeted bacteria increase the statistics of more such adhered clusters and enhance the intensity of absorbance peak, i.e. hyperchromic response is observed with increased concentration of targeted bacteria. Following the Beer–Lambert law, $A = \epsilon.C.L$ [where A is the absorbance, ϵ is the molar attenuation coefficient (constant), L is the path length (constant), and C is the concentration of the agglomerated Apt-AuNPs on bacteria], as the concentration C increases,

the absorbance increases (hyperchromic effect). The optical images that are shown in Figure 5.6.D and 5.6.E are taken in the bright field and at UV light (~ 365 nm) respectively.

5.3.3. Characterization

Dynamic Light Scattering (DLS) of the AuNP and Apt-AuNP provides the estimate of the particle size and the zeta potential. The average particle size was found to be 26 ± 0.8 nm and $40 \text{ nm} \pm 0.8$ nm (Figure 5.5.D) for the AuNP and Apt-AuNP which was also statistically supported by the TEM images. The PDI (Polydispersity Index) values for AuNP and Apt-AuNP was 0.2 and 0.39 respectively. At the pH of ~ 7.2 , the zeta potential of the AuNP and Apt-AuNP was ~ -35 mV and ~ -26 mV respectively. The relatively high surface charge of the AuNP stabilizes the particles which after binding with aptamer molecules form chain-like structures due to the reduction of surface charges⁷³ as well as the interactions among the anchored aptamers. The thiolated aptamers readily bind with the AuNPs through Au-S bonds. Raman spectra shown in Figure 5.8.A confirm the Au-S bond realized by the peak at 330 cm^{-1} . The peak at 1330 cm^{-1} also corresponds to the Apt- AuNP⁷⁴. The peaks at 898 cm^{-1} and 1078 cm^{-1} confirm the attachment of *K.pneumoniae* with Apt-AuNPs in Figure 5.8.B.

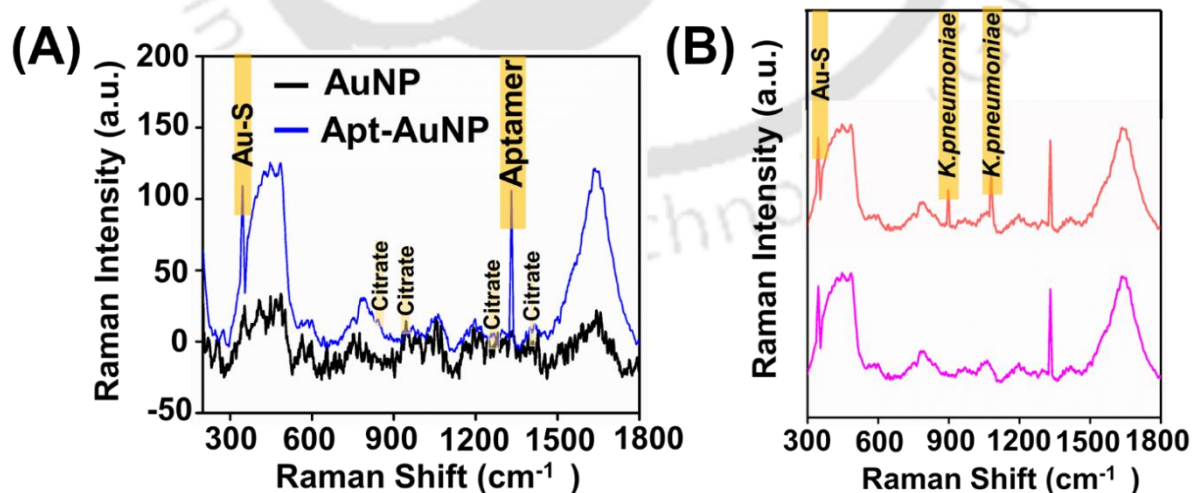


Figure 5.8. Plot (A) shows the Raman spectra of pristine AuNPs and Apt-AuNP conjugation. Since, the particles are stabilized by citrate molecules, the peaks corresponding to the presence

of citrate are mentioned in the plot. The presence of trisodium citrate is depicted by a peak at 830 cm^{-1} signifying $\nu(C - C)$, peak at 943 cm^{-1} signifying $\nu(C - COO)$, peak at $1257\text{-}1282\text{ cm}^{-1}$ signifying $\delta(COO)$ and peak at 1406 cm^{-1} demonstrating $\nu_s(COO)$. Plot (B) denotes the Raman spectra when Apt-AuNP attaches to *K.pneumoniae* (orange). The peaks at 898 cm^{-1} and 1078 cm^{-1} (highlighted in the plot) conform attachment to the target analyte (orange line). The pink line depicts Raman spectra when a non-target analyte (*E.coli*) was dispensed into the Apt-AuNP matrix conforming to no such specific signatures.

5.3.4. Specificity Study

To administer the correct antibiotic to a patient having UTI, it is crucial to identify the exact bacterial species infecting the urinary tract. *K.pneumoniae*, *E.coli*, *S.aureus*, and *E.faecalis* are some of the most common bacteria which may be responsible for UTI. The tailor-made aptamer that is used in this particular work is specific to *K.pneumoniae*, and it is important to make sure that this aptamer is insensitive to the presence of other common bacteria generally responsible for UTI. This will help us to detect the exact bacteria which is responsible for UTI. Similarly, by changing only the aptamer in the Apt-AuNP probe, it is possible to detect any other specific bacteria as well. A series of detection assays were performed using target and non-target bacteria to examine the specificity of the sensing matrix and corresponding UV-Vis spectra are shown in Figure 5.9. (A) and (B). Apart from *K.pneumoniae*, the other common UTI-causing bacteria viz. *E.coli*, *S.aureus*, and *E.faecalis* are also tested with the sensing matrix Apt-AuNP, and it was found that the matrix was responsive only to the targeted *K.pneumoniae* and insensitive to any other bacteria. Two sets of experiments were performed: Firstly, each of the non-targeted bacteria having a concentration of 1×10^5 CFU/mL was tested with the sensing matrix separately (Figure 5.9.A). Secondly, all the targeted and non-targeted bacteria were mixed and then tested using the Apt-AuNP sensing matrix to check if any interference was caused by the presence of the non-targeted bacteria (Fig. 5.9.B). It was found that the in

presence of the non-targeted bacteria, targeted bacteria *K.pneumoniae* shows a positive response to the sensing matrix by increasing the intensity of the absorbance peak at 528 nm (Figure 5.9.B). The TEM images also support that Apt-AuNPs are attached to the surface of the *K.pneumoniae* bacteria (Figure 5.6.A) but remain as a chain-like structure (similar to the case of without any bacteria) in presence of any non-targeted bacteria. A typical TEM image of the Apt-AuNP in presence of non-targeted *E.coli* is presented in Figure 5.6.B.

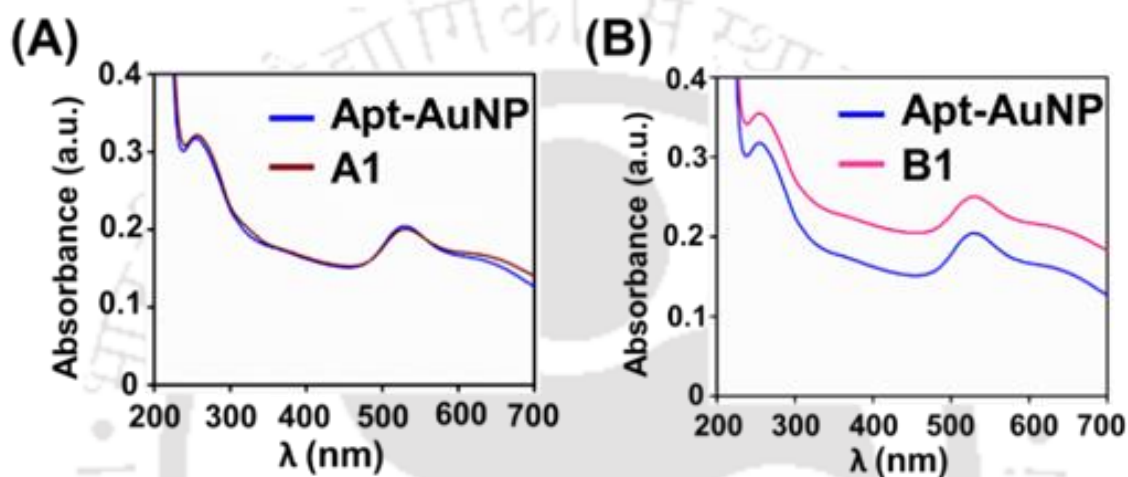


Figure 5.9. Plot (A) shows the UV Vis spectra when a cocktail of non-target analytes (*E.coli*, *S.aureus*, and *E.faecalis*) was mixed and dispensed into the Apt-AuNP matrix denoted by A1. The bacterial concentration of *E.coli*, *S.aureus*, and *E.faecalis* was fixed at 1×10^5 CFU/mL in each case. Plot (B) shows the UV spectra when mixed analytes comprising *K.pneumoniae*, *E.coli*, *S.aureus*, and *E.faecalis* was dispensed into the Apt-AuNP matrix denoted by B1. The bacterial concentration of *K.pneumoniae*, *E.coli*, *S.aureus*, and *E.faecalis* was fixed at 1×10^5 CFU/mL in each case. Due to the attachment of *K.pneumoniae*, a response with an increase in UV absorbance occurs.

5.3.5. Aptasensor Prototype Fabrication

Based on the detection principle and the results discussed in the previous section, a prototype aptasensor is fabricated that consists of an optical source (a light-emitting diode, LED), a

sample holder, a photodetector (a light-dependent resistor), and a measurement unit (a digital multimeter, DMM). The principle of light absorption and transmission (Beer-Lambert Law) through the liquid analyte sample was used for the aptasensor prototype. In the device, as shown in Figure 5.4., in between the LED and the photodetector, a square groove was provided to plug in a standard-sized (1 cm × 1 cm × 10 cm) cuvette cell to accommodate the sample analyte solution. The standard cuvette was used to keep the sample path length constant throughout the quantification process. A 3D printer (model: **Ultimaker 3, Netherlands**) was used to make this arrangement. A LED and a photodetector were perfectly aligned and placed on the opposite wall of the square groove made for the sample. A black PLA filament was used to fabricate the experimental setup to ensure zero external light interference during the experiment. For the 3D printing of the prototype, initially, the CAD model of the 3D printing specimen was created by using Free CAD (an open-source software) and saved as an STL file. Consequently, the STL file was transferred to the software of the 3D printing machine Ultimaker Cura (Ultimaker 3D printer software) to slice the file. The process variables of Ultimaker Cura were adjusted, and the final instructions were exported as a G Cod file. The G Cod file was then transferred to the 3D printer as the last command to print. The 3D printer molded the device structure as the G Cod file instructed by extruding the PLA filament and depositing it layer by layer. Subsequently, the 3D printed mold was removed from the 3D printer, and the brim (if any) was detached mechanically from the device's base.

5.3.6. Selection of the LED

The selection of an LED with a suitable wavelength for the aptasensor device was the most crucial aspect of device optimization. We studied the responses obtained using different LED sources that emit lights in the visible ranges such as red, yellow, blue, green, and white. The light emitted from the LED traverse through the Apt-AuNP matrix mixed with different concentrations of targeted bacterial (*K.pneumoniae*) aqueous solutions to detect the change in

the signal detected by LDR. LDR detected the transmitted light from the sample, and the response was measured in the form of resistance (as shown in Figure 5.10.B). The normalized resistance (N_R) was calculated as $N_R = \frac{R_C - R_{C_0}}{R_{C_0}}$, where $R(C)$ is the resistance at a given concentration (C) of *K.pneumoniae*, and $R(C_0)$ is the resistance of the blank sample (i.e., reading from only Apt-AuNP matrix, without any *K.pneumoniae*). From Figure 5.10.A, it is apparent that the device is more sensitive to the green LED, having a wavelength of 510–555 nm, among all the LED light sources. This is understandable, as the UV-Vis spectra discussed earlier (Figure 5.6.C) for the Apt-AuNPs anchored *K.pneumoniae* shows a strong absorbance peak at ~ 528 nm. Since the aim of the developed prototype aptasensor is for frugal applications, with high specificity and sensitivity for *K.pneumoniae* detection, the inexpensive (cost-effective) LDRs and LEDs are used for the prototype fabrication. All the subsequent experiments were performed using this chosen green LED.

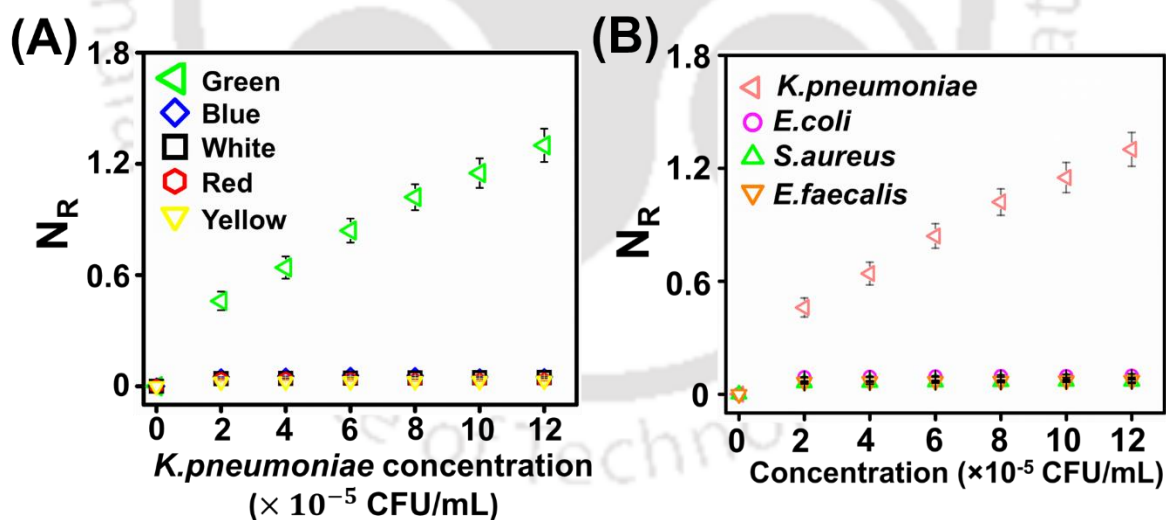


Figure 5.10. Plot (A) shows the response of the device for different types of LEDs, green LED (green inverted triangle), blue LED (blue diamond), white LED (hollow white square), red LED (red polygon), and yellow LED (yellow inverted triangle). Green LED shows the best response for aptasensor detection having wavelength (510-555 nm). Plot (B) shows the specific

response of the aptasensor towards target analyte *K.pneumoniae* detection using green LED. The aptasensor shows negligible response towards *E.coli*, *S.aureus*, and *E.faecalis*.

5.3.7. Specificity of the Aptasensor

To check the specificity of the aptasensor, we first tested with the aqueous solution of targeted (*K.pneumoniae*) and non-targeted (*E.coli*, *S.aureus*, and *E.faecalis*) bacteria having different concentrations ranging from 2×10^5 CFU/mL to 12×10^5 CFU/mL. The result shown in Figure 5.10.B clearly shows that the developed aptasensor can successfully detect the targeted *K.pneumoniae* bacteria.

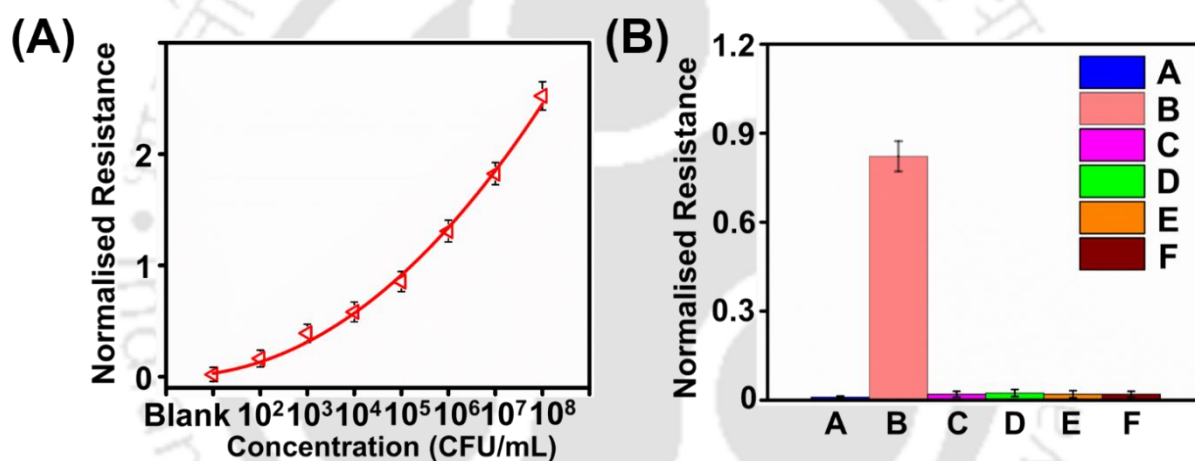


Figure 5.11. Plot (A) shows the aptasensor response when healthy fresh urine is spiked with increasing concentrations of *K.pneumoniae* (10^2 - 10^8 CFU/mL) using identical volume. (Red color inverted triangle) is fitted with allometric regression of the form, Normalised Resistance \sim Concentration^{2.1} which represents the power law relation. Plot (B) shows the aptasensor response when *K.pneumoniae*, *E.coli*, *S.aureus*, and *E.faecalis* were spiked into fresh healthy urine. The readings were taken within laboratory premises. [A-Blank, B-*K.pneumoniae*, C-*E.coli*, D-*S.aureus*, E- *E.faecalis*, F- *E.coli*, *S.aureus* & *E.faecalis* mixed together]. The concentration of the respective bacteria was 1×10^5 CFU/mL in each case. The error bars in the

diagram indicate the standard deviation of the readings obtained from 4 measurements with the aptasensor.

As a next step, we were interested to know if there is any interference that can be caused by the components present in the human urine sample. To examine this, urine samples from healthy volunteers are collected and spiked with a known amount of *K.pneumoniae* ranging from 10^2 - 10^8 CFU/mL. For this, a stock bacterial suspension of *K.pneumoniae* was cultured in LB media and incubated at 37 °C overnight. The cultures were then diluted with 1X PBS (pH=7.4) sequentially to prepare the desired concentrations of *K.pneumoniae* (10^2 , 10^3 , 10^4 , 10^5 , 10^6 , and 10^7 CFU/mL). 600 μ L of *K.pneumoniae* bacteria was then spiked into 1 mL of a urine sample from a healthy volunteer in a small vial. This sample was tested using the fabricated aptasensor. The result, shown in Figure 5.11.A, depicts a monotonic increase in the responses with the *K.pneumoniae* concentrations and thus confirms that there is no significant interference when urine samples are used. The experiments for each concentration were performed with 4 different urine samples.

Next, the urine samples from a healthy volunteer were also spiked with the same concentration (1×10^5 CFU/mL) of *K.pneumoniae* as well as non-targeted bacteria such as *E.coli*, *S.aureus*, *E.faecalis*, and the mixture of non-targeted bacteria. The result shown in Figure 5.11.B confirms that the developed aptasensor is specific to only *K.pneumoniae* and insensitive to non-targeted bacteria. Another non-specific aptamer sequence SABA11(5'-/5ThioMC6-D/GGC TGG ATG GGG CGT GTT GAT TCG AGT CGG AGA CGG CAT CCT GCA CAA ATG CCA ACG GTG CGG ACA GCG-3') was used as a negative control. This aptamer sequence is specific for another non-target bacterial species (*S. aureus*) and does not bind to target *K.pneumoniae*.

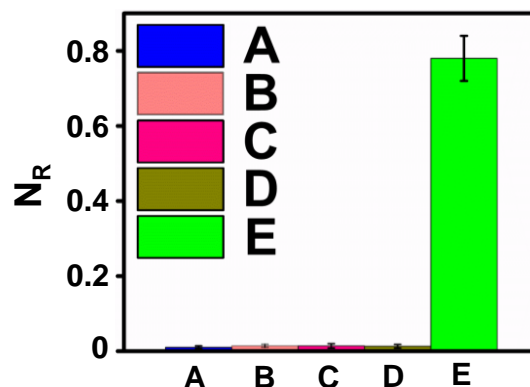


Figure 5.12. Plot shows the POC aptasensor response using a non-specific aptamer sequence SABA11 (5'-/5ThioMC6-D/GGC TGG ATG GGG CGT GTT GAT TCG AGT CGG AGA CGG CAT CCT GCA CAA ATG CCA ACG GTG CGG ACA GCG-3'). The aptamer used is non-specific for *K.pneumoniae* but specific to *S.aureus*. *K.pneumoniae*, *E.coli*, *S.aureus*, and *E.faecalis* were spiked into fresh healthy urine. The readings were taken within laboratory premises. [A-Blank, B-*K.pneumoniae*, C-*K.pneumoniae* and *E.coli* mixed, D-*K.pneumoniae*, *E.coli*, and *E.faecalis* mixed, E- *S.aureus*]. The concentration of the respective bacteria was 1×10^5 CFU/mL in each case. The error bars in the diagram indicate the standard deviation of the readings obtained from 4 measurements with the developed aptasensor prototype.

5.3.8. Cost Estimation & Description of the components used

A detailed description of the components used for the fabrication of the aptasensor mentioning its cost is presented below:

Sl. No.	Component	Approx Cost in (Rs)
1	LED	~ 0.80
2	LDR	~ 4.50
3	Digital Multimeter	~ 300.00
4	9V Battery	~ 20.00

5	3D Printed Cuvette holder (Black)	~ 40.00
6	Breadboard	~ 230.00
7	Cuvette	~ 12.00
		Total = 607.30 ~ 608.00

The reagent cost of the sensing matrix is ~ Rs 8.00 (\$ 0.10)

In USD, the price of the aptasensor will be ~ \$ 7.47. (Considering 1USD = 81.36 INR).

The components used and the manufacturer's name is mentioned in detail below for the fabrication of the aptasensor:

Component	Specification	Remark
Breadboard, MB102 830 Points Solderless Prototype PCB Breadboard Make: Robo India Model: MB-102	630-tie point terminal strip, 2 distribution strips 200 points, both sides have slots, support joining. A solderless breadboard is easy to use for creating temporary prototypes and experimenting with circuit design. Referencing letters are printed on the side for easy reference of individual holes. Double-side adhesive tape back is easier and more convenient to use.	A breadboard (also called a plug block) is used for building circuits. A breadboard consists of a plastic block holding a matrix of electrical sockets of a size suitable for gripping thin connecting wire, component wires or the pins of transistors and integrated circuits (ICs). The sockets are connected inside the board, usually in rows of five sockets.
Green LED Make: Sharvi Electronics Model: 2001SM0327	The LED used in this work is very vital since the aptasensor works on the principle of incident light captured by the LDR. Micro 10 mm diameter, Wide viewing angle=120-130 degrees, Super bright Power: 0.5 Watt Input (DC): 3-3.2 V/ 80 mA High luminous intensity, high brightness chip on board. Working Life span: 40000 hours	The use of a high-intensity green-colored LED with a specific wavelength eliminates the interference of other wavelengths of light to allow a noise-free signal display. Green LED with a narrow wavelength range ~ 510-550 nm is used as the optical source.

<p>LDR</p> <p>Make: Diode House</p> <p>Model: Generic</p>	<p>Light resistance 50-100 kΩ, Rated power 200 W, Diameter 5 mm, LDR is QC tested.</p>	<p>An LDR (light-dependent resistor) is one type of resistor whose resistance varies depending on the amount of light falling on the surface. When the light falls on the resistor, then the resistance changes. This resistor works on the principle of photoconductivity.</p>
<p>Digital Multimeter (DMM)</p> <p>Make: Mastech</p> <p>Model: M92AH</p>	<p>DC Voltage Range (Volts): 200mV-1000V; DC Voltage Accuracy: \pm (0.5 percent +3)</p> <p>AC Voltage Range (Volts): 200mV to 700V; AC Voltage Accuracy: \pm(0.8 percent +5)</p> <p>DC current range (Amp) 20uA - 10A; DC current accuracy \pm (1.0 percent +5);</p> <p>AC current range (Amp) 20uA - 10A; AC current accuracy \pm (1.8 percent +5)</p> <p>Resistance range (Ohm) 200Ω - 200MΩ; Resistance accuracy \pm (0.8 percent +3) - \pm5 percent</p> <p>Battery Powered</p>	<p>A digital multimeter measure and verifies multiple electrical stimuli including resistance, voltage, and current. It is the most common diagnostic tool which involves the features of a voltmeter, ammeter, and ohmmeter.</p>
<p>Portable battery 9V</p> <p>Make: Hi- Watt</p> <p>Model: Sha-186</p>	<p>Battery cell composition- Zinc carbon</p> <p>Battery weight – 36 g</p> <p>Voltage- 9V</p> <p>Dimension: 26.5mm x 48.5mm x 17.5mm</p> <p>Operating temperature range (deg. C): -20 to +85</p> <p>Discharge resistance (ohms): 620</p>	<p>Hi-Watt 9W battery is used for charge storage. It is non-rechargeable and has high capacity and is a low-cost solution for electronic devices.</p>
<p>3D printed cuvette holder</p> <p>Make: eSun</p> <p>Model: 315610</p>	<p>3D printer (Make: Ultimaker 3, Netherlands) was used to fabricate the device prototype from polylactic acid (PLA) filament.</p> <ul style="list-style-type: none"> • Filament diameter- 1.75 mm • Melt Flow Index (g/10 min)- 2(190⁰C/2.16 kg) • Roundness Accuracy- \pm 0.5 mm <ul style="list-style-type: none"> • Color: Black 	<p>The 3D printed model of the prototype was developed using Free CAD (open source software). 3D printed box is used to minimize stray light and ensure the fixed optical distance between the source and the detector</p>

Cuvette	Rectangular macro cell, disposable, polystyrene, open top, 10 mm path length, Cell Volume 3.5mL, 500/pk.	Cuvette of specific dimension was used to maintain a constant path length so that changes in the response from the device due to target analyte detection are accurately measured.
Make: Agilent	For use over a wavelength range from 340-800 nm.	
Part No.		
6610018800		

5.3.9. Calibration and Clinical Trial

As discussed earlier, the UV-Vis spectra confirm that the Apt-AuNP sensing matrix can detect the target analyte *K.pneumoniae* to a concentration as low as 10^3 CFU/mL.

However, usually, the UTI is triggered by a single organism with a high concentration of $> 10^5$ CFU/mL²⁵.

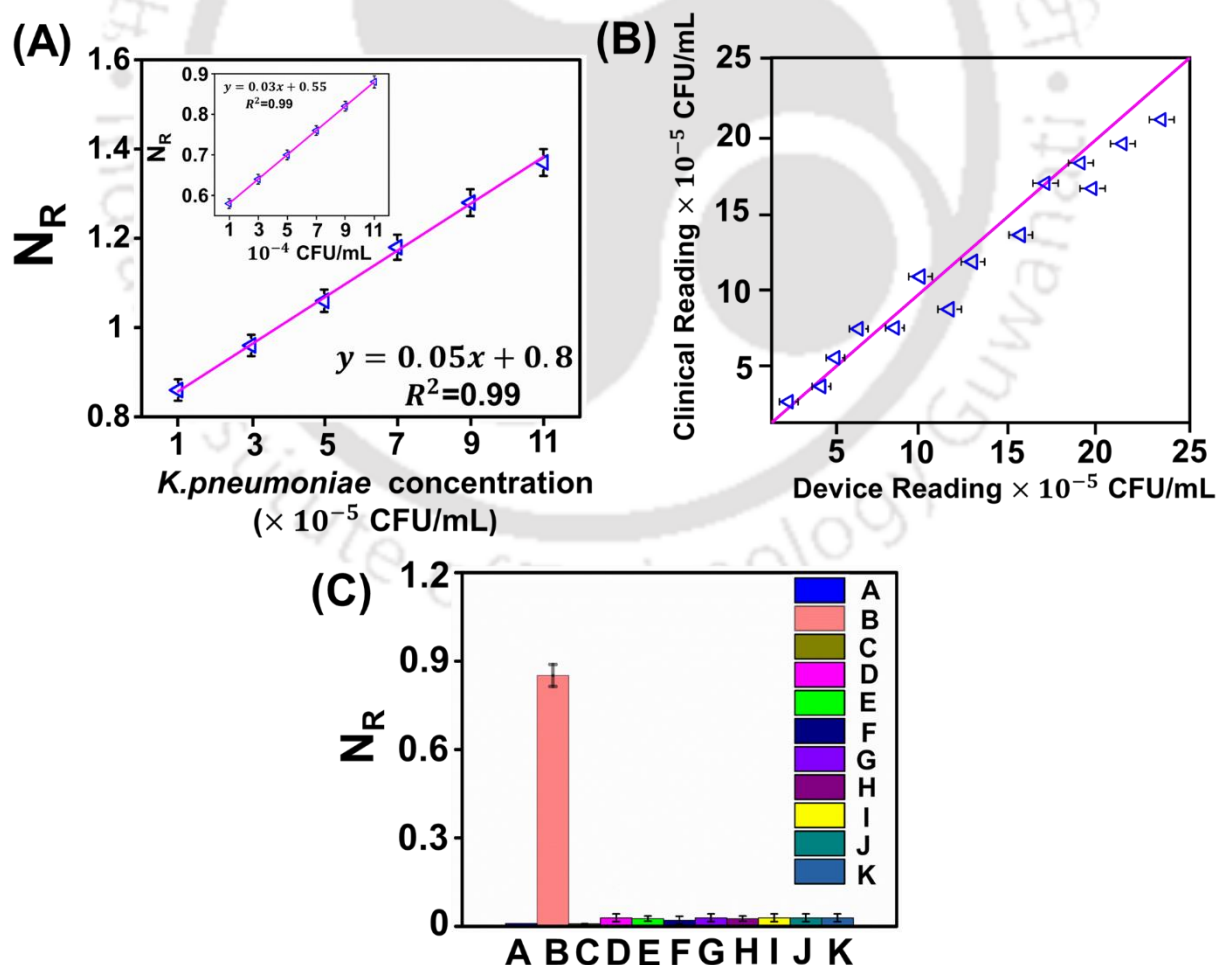


Figure 5.13. Plot (A) shows the calibration curve for the *K.pneumoniae* concentration $((1-11)\times 10^5$ CFU/mL as a function of normalized resistance. The inset shows the calibration curve for the *K.pneumoniae* concentration $((1-11)\times 10^4$ CFU/mL as a function of normalized resistance. Plot (B) shows the comparison of clinical results (obtained from a GNRC hospital) from UTI patients with the results obtained from the optical device developed in this work using the calibration curve. Plot (C) shows the aptasensor results taken from the clinical UTI patient samples (OPD) within GNRC hospital premises. The signal change was found only in the case of a positive *K.pneumoniae* infected urine sample which was also confirmed by the hospital reports. [A- Blank, B- *K.pneumoniae*, C- Sterile, D- *E.coli*, E- *S.aureus*, F- *P.aeruginosa*, G- *C.freundii*, H- *C.koseri*, I- *P.vulgaris*, J- *Enterococcus species*, K- *Candila species*]. The error bars in the diagram indicate the standard deviation of the readings obtained from 4 measurements with the help of the aptasensor.

Thus, to quantify the organism, a calibration chart for the relevant range of concentrations of bacteria is essential. For this purpose, urine samples from healthy volunteers, that do not contain any *K.pneumoniae*, are spiked with the same to have *K.pneumoniae* concentration ranging from $(10)^4$ - $(10)^6$ CFU/mL. 600 μ L of the sample was then mixed with 2 mL of the Apt-AuNP matrix for each concentration. The intensity of the transmitted light was recorded by LDR. The LDR resistance was measured using a digital multimeter (DMM). The change in resistance with the change in the concentration of the *K.pneumoniae* was systematically recorded with the help of DMM. For a lower concentration of *K.pneumoniae* in the solution, LDR recorded lower resistance due to the higher intensity of transmitted light from the samples placed in the cuvette. For the higher concentration of *K.pneumoniae* in the sensing solution, LDR showed higher resistance because of the lower intensity of transmitted light from the samples placed in the cuvette, and therefore DMM recorded higher resistance. From these recorded resistances, the normalized resistance as defined earlier was calculated. The

calibration curve, thus prepared and shown in Figure 5.13.A, was used to find the unknown *K.pneumoniae* concentration of an infected sample.

The reliability of this aptasensor was verified using OPD UTI patient samples procured from a nearby hospital **GNRC, North Guwahati**, Assam, INDIA. The normalized resistances obtained from different UTI-suspected human patient samples were checked with our aptasensor prototype. The readings obtained from the hospital's clinical samples were compared with our prototype results for the samples which were *K.pneumoniae* positive. The results, shown in Figure 5.13.B, reasonably agree with the clinical result. The slight variation can be caused by human errors that can be imbibed from both the hospital and our laboratory test ends. Apart from this, it is undeniable that some components in the urine may influence the test results, and based on the health conditions of the patients such as co-morbidity, and age variations, the components of the urine samples may vary and may affect the test results.

(A)	Age Group	No. of male	No. of female
	18-30	25	90
	30-50	55	157
	50-70	10	45

(B)	No. of days with symptoms	No. of male	No. of female
	Symptoms for > 5 days	25	90
	Symptoms for < 5 days	55	157

(C)	CLED Agar Culture (+ve)	CLED Agar Culture (-ve)	Total
Aptasensor +ve	38	11	49
Aptasensor -ve	8	270	278
Total	46	281	327
Chi-square	192.15 (when p<0.00001)		

(D)	Statistics	Value	95% CI
	Sensitivity	82.61%	68.58-92.18%
	Specificity	96.09%	93.10-98.03%
	Positive Likelihood ratio	21.1	11.65-38.23
	Negative Likelihood Ratio	0.18	0.10-0.34
	Disease Prevalence (*)	14.07%	10.49-18.31%
	Positive Predicted Value (*)	77.55%	65.60-86.22%
	Negative Predicted value (*)	97.12%	94.73-98.45%

Figure 5.14. Demographic data corresponding to validation of aptasensor prototype. Table (A) and (B) shows the statistical variations (age, sex, symptoms) of the suspected UTI patients from which the urine samples were collected. Table (C) and (D) shows the statistical confidence level⁷⁵⁻⁷⁸ analysis from the collected UTI patient samples from GNRC hospital.

Thus, testing a large number of samples and feeding the output results along with the different variable information such as health conditions, age variations, etc. to the AI-ML platform may open up the possibility of a robust and accurate UTI detection device. Here in this device, we tested a large volume of sample size (327 UTI suspected patients' samples) to study the robustness of our developed prototype and simultaneously to test whether there is any interference caused by any component of the human patient samples. The demographic data of the test samples are shown in Figure 5.14. The UTI caused by other pathogens showed insignificant resistance as depicted in Figure 5.13.C. In practice, culture growth in urine for 24 h is performed in clinics on a CLED agar plate which is assumed to be the gold standard for UTI detection. However, the reliability of the results is questionable for pathogen concentration $<10^4$ CFU/mL⁷⁹. In this process, after streaking with urine samples, the CLED agar plates were incubated overnight. The multiplication of the bacterial colony occurs with distinct patterns having specific signatures of the types of pathogens. Distinct patterns formed on the CLED agar plate by different pathogens are shown in figure 5.17. Contrary to the current detection method that takes 24 h to culture, our developed aptasensor can identify the specific pathogen within 5 minutes. The limit of the detection (LoD) (3.4×10^3 CFU/mL) is also much lower than the current pathological practice (See Figure 5.15. for the LoD calculation).

5.3.10. Limit of detection test & Stability, Storage conditions of the aptasensor

The limit of detection (LOD) of the *K.pneumoniae* based on the aptasensor was calculated to be (3.4×10^3) CFU/mL. Moreover, as this device does not require any expensive materials or complicated probe preparation, unlike other methods, simple and easy quantification of *K.pneumoniae* makes this inexpensive device a potential candidate for specific detection.

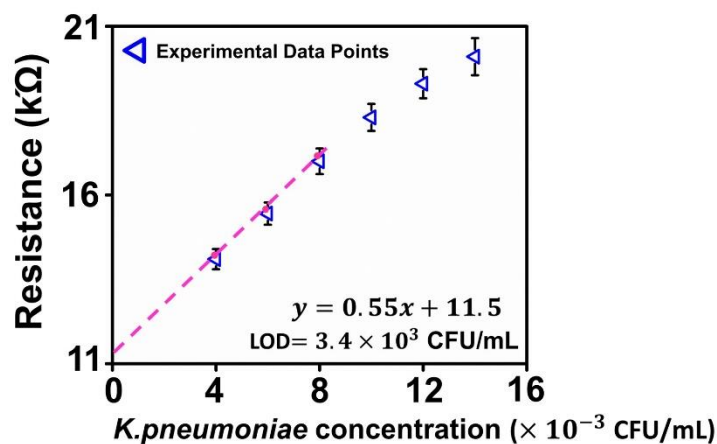


Figure 5.15. Absolute resistance ($k\Omega$) as a function of *K.pneumoniae* concentration (CFU/mL).

In order to calculate the limit of detection (LOD) of the device, a plot of measured absolute resistance ($R(C)$) values against different concentrations of *K.pneumoniae* mixed in Apt-AuNP matrix was prepared. Here $R(C)$ is the resistance at a given concentration (C) of *K.pneumoniae*. A blank test was also performed with only the aptamer-AuNP matrix without any *K.pneumoniae*. To estimate the LOD, a tangent to the developed resistance vs C curve at a low concentration regime was drawn with equation $R(C) = 0.55 C + 11.5$. The LOD was then estimated using the following equation given below⁸⁰:

$$\text{LOD} = \frac{\text{Mean}_{\text{blank}} + 1.645(\text{SD}_{\text{blank}}) + 1.645(\text{SD}_{\text{low concentration sample}}) - \text{Intercept}}{\text{Slope of the curve}}$$

Where SD_{blank} is the standard deviation from the blank samples and $\text{SD}_{\text{low concentration samples}}$ is the standard deviation at low *K.pneumoniae* concentration. Using the above equation, the calculated LoD is 3.4×10^3 CFU/mL.

The aptamer-AuNP matrix was stored in a refrigerator at 4°C after preparation. Subsequently, the effective resistances were measured weekly using the aptasensor for a fixed concentration of (1×10^5) CFU/mL. The result shows that the Apt-AuNP sensing matrix is reasonably stable over two months.

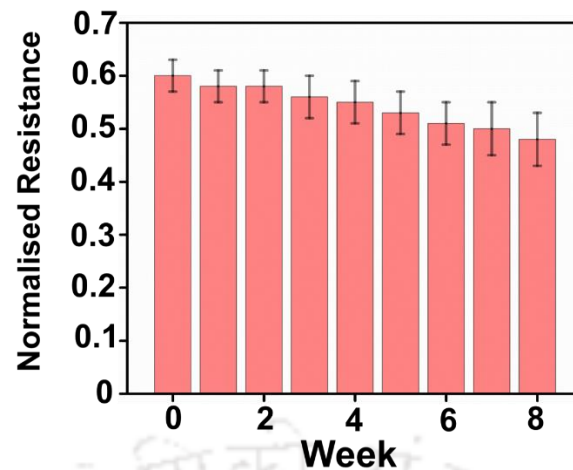


Figure 5.16. Stability of the aptamer-AuNP matrix response of the device for a particular concentration of *K.pneumoniae* (1×10^5) CFU/mL over the period of 8 weeks. The error bars in the figure indicate the standard deviation of readings obtained during the measurement of the same sample three times with our aptasensor.

5.3.11. CLED Agar culture of the Uropathogens

CLED agar (Cystine Lactose Electrolyte Deficient) is differential, non-selective culture medium used for the isolation, enumeration and differentiation of urinary microorganisms. It promotes the growth of microorganisms and this prevalent technique is used in the hospital premises for uropathogen identification. Distinct patterns of uropathogens were traced while clinical urine sampling testing within GNRC Hospital, INDIA premises as shown in figure 5.17. below:

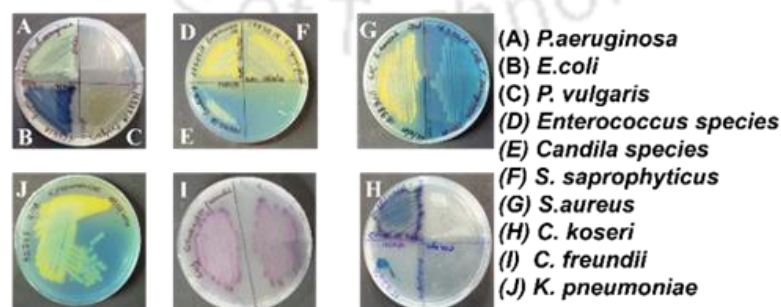


Figure 5.17. Streaked CLED agar plates of different pathogenic bacteria causing UTI. The streaking was done within GNRC hospital laboratory premises.

5.3.12. Summary of the detection methodology

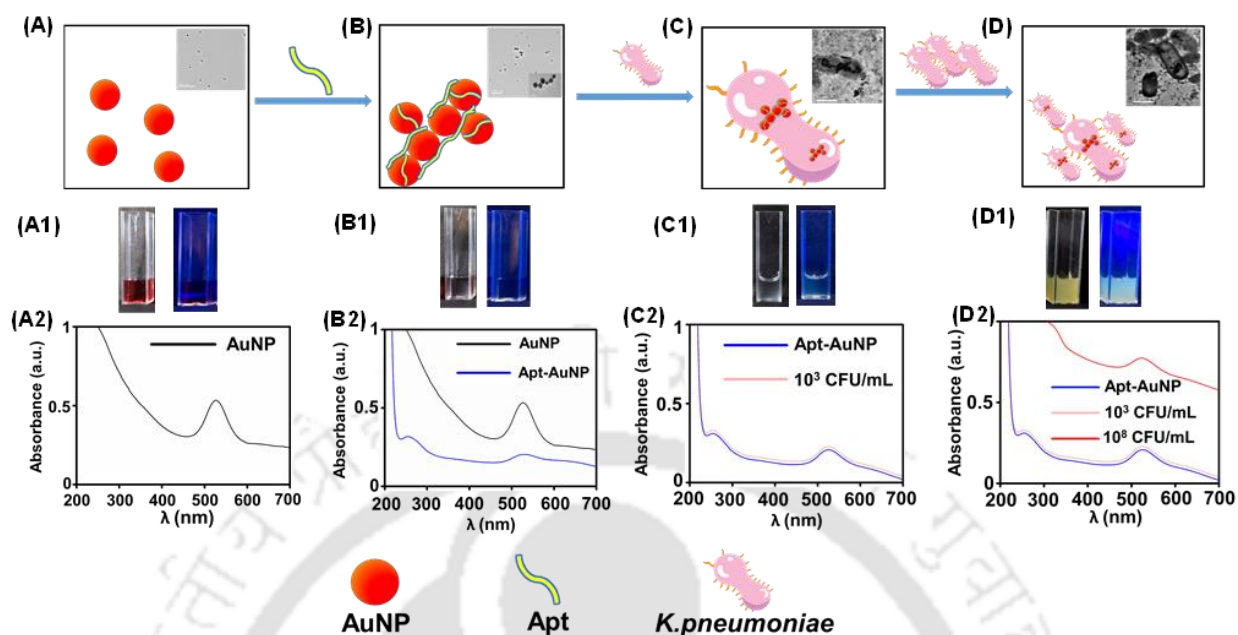


Figure 5.18. Schematic representation of the detection procedure of the target analyte (*K. pneumoniae*) using the developed Apt-AuNP assay. (A), (B), (C) and (D) represents the AuNPs, Apt-AuNP assay, *K. pneumoniae* (10^3 CFU/mL) binding with Apt-AuNP and high concentration of *K. pneumoniae* (10^8 CFU/mL) binding with Apt-AuNP respectively. Inset shows the respective sequence of TEM images. A1, B1, C1 and D1 demonstrates the bright field and UV light (~ 365 nm) exposed images of AuNP, Apt-AuNP assay, *K. pneumoniae* (10^3 CFU/mL) bound Apt-AuNP assay and *K. pneumoniae* (10^8 CFU/mL) bound Apt-AuNP assay respectively. A2, B2, C2 and D2 demonstrates the respective UV-Vis spectroscopy of the above-mentioned sequence.

5.4. Conclusions

This study shows the detection of specific pathogen using external noise induced gel electrophoretic setup along with the development of a POC aptasensor prototype for the quantification of the pathogen present in the UTI suspected patient along with the identification of a specific pathogen within 5 min. A generic methodology is developed that can confirm a specific bacterial presence in the clinical sample which can aid the doctor if the antibiotics should be administered. This particular work shows the quantification of *K.pneumoniae* in human urine samples. Not only that, the developed prototype may help to identify the specific drug that can be effective or ineffective due to mutations in pathogens that cause antimicrobial resistance (AMR).

The developed aptasensor prototype for *K.pneumoniae* was tested against the gold standard clinical practice from a nearby Hospital (GNRC Hospital Guwahati) and the results were found promising for frugal application as the costs of the aptasensor prototype and that of a single test are ~ \$ 7.47 and ~ \$ 0.1 (See section 5.3.8 for the cost estimation) respectively.

The developed aptasensor prototype shows the pathway of detecting and quantifying pathogens in body fluids. Pathogens such as *K.pneumoniae* causes infections-related health issues worldwide, and pose significant treatment challenges due to the extensive use of antibiotics. Our developed aptasensor has the potential to be the frugal point of care device for the detection of such pathogens and contribute significantly to primary healthcare.

References

1. Boisselier, E. & Astruc, D. Gold nanoparticles in nanomedicine: preparations, imaging, diagnostics, therapies and toxicity. *Chem. Soc. Rev.* **38**, 1759–1782 (2009).
2. Ghosh, P., Han, G., De, M., Kim, C. K. & Rotello, V. M. Gold nanoparticles in delivery applications. *Adv. Drug Deliv. Rev.* **60**, 1307–1315 (2008).
3. Paciotti, G. F. *et al.* Colloidal gold: A novel nanoparticle vector for tumor directed drug delivery. *Drug Deliv. J. Deliv. Target. Ther. Agents* **11**, 169–183 (2004).
4. Gobin, A. M. *et al.* Near-infrared resonant nanoshells for combined optical imaging and photothermal cancer therapy. *Nano Lett.* **7**, 1929–1934 (2007).
5. Huang, X., El-Sayed, I. H., Qian, W. & El-Sayed, M. A. Cancer cell imaging and photothermal therapy in the near-infrared region by using gold nanorods. *J. Am. Chem. Soc.* **128**, 2115–2120 (2006).
6. Eghtedari, M. *et al.* High sensitivity of in vivo detection of gold nanorods using a laser optoacoustic imaging system. *Nano Lett.* **7**, 1914–1918 (2007).
7. Mayer, K. M. & Hafner, J. H. Localized surface plasmon resonance sensors. *Chem. Rev.* **111**, 3828–3857 (2011).
8. Anker, J. N. *et al.* Biosensing with plasmonic nanosensors. *Nanosci. Technol. A Collect. Rev. from Nat. Journals* **7**, 308–319 (2009).
9. Daniel, M. C. & Astruc, D. Gold Nanoparticles: Assembly, Supramolecular Chemistry, Quantum-Size-Related Properties, and Applications Toward Biology, Catalysis, and Nanotechnology. *Chem. Rev.* **104**, 293–346 (2004).
10. Willets, K. A. & Van Duyne, R. P. Localized surface plasmon resonance spectroscopy

- and sensing. *Annu. Rev. Phys. Chem.* **58**, 267–297 (2007).
11. Van Der Meer, S. B. *et al.* Click Chemistry on the Surface of Ultrasmall Gold Nanoparticles (2 nm) for Covalent Ligand Attachment Followed by NMR Spectroscopy. *Langmuir* **35**, 7191–7204 (2019).
 12. Nehl, C. L. & Hafner, J. H. Shape-dependent plasmon resonances of gold nanoparticles. *J. Mater. Chem.* **18**, 2415–2419 (2008).
 13. Herne, T. M. & Tarlov, M. J. Characterization of DNA probes immobilized on gold surfaces. *J. Am. Chem. Soc.* **119**, 8916–8920 (1997).
 14. Love, J. C., Estroff, L. A., Kriebel, J. K., Nuzzo, R. G. & Whitesides, G. M. *Self-assembled monolayers of thiolates on metals as a form of nanotechnology. Chemical Reviews* vol. 105 (2005).
 15. Mahato, K. *et al.* Gold nanoparticle surface engineering strategies and their applications in biomedicine and diagnostics. *3 Biotech* **9**, 1–19 (2019).
 16. Dreaden, E. C., Alkilany, A. M., Huang, X., Murphy, C. J. & El-Sayed, M. A. The golden age: Gold nanoparticles for biomedicine. *Chem. Soc. Rev.* **41**, 2740–2779 (2012).
 17. Agasti, S. S. *et al.* Nanoparticles for Detection and Diagnosis. *Adv. Drug Deliv. Rev.* **62**, 316–328 (2010).
 18. Sheerin, N. S. Urinary tract infection. *Medicine (Baltimore)*. **39**, 384–389 (2011).
 19. Vasudevan, R. Urinary Tract Infection: An Overview of the Infection and the Associated Risk Factors. *J. Microbiol. Exp.* **1**, 42–54 (2014).
 20. Foxman, B., Barlow, R., D’Arcy, H., Gillespie, B. & Sobel, J. D. Urinary tract infection: Self-reported incidence and associated costs. *Ann. Epidemiol.* **10**, 509–515 (2000).

21. Galate, L. B. & Bangde, S. Urinary Tract Infection: Study of Microbiological Profile and its Antibiotic Susceptibility Pattern. *Int.J.Curr.Microbiol.App.Sci* **4**, 592–597 (2015).
22. Yadav, K., Prakash, S., Serayi, R., Shilpkar, T. & Shrestha, S. Antimicrobial susceptibility test of pathogens isolated from urinary tract infection suspected cases. *Janaki Med. Coll. J. Med. Sci.* **2**, 28–34 (2014).
23. Lawrentschuk, N., Ooi, J., Pang, A., Naidu, K. S. & Bolton, D. M. Cystoscopy in women with recurrent urinary tract infection. *Int. J. Urol.* **13**, 350–353 (2006).
24. Blondeau, J. M. Current issues in the management of urinary tract infections: Extended-release ciprofloxacin as a novel treatment option. *Drugs* **64**, 611–628 (2004).
25. Flores-Mireles, A. L., Walker, J. N., Caparon, M. & Hultgren, S. J. Urinary tract infections: Epidemiology, mechanisms of infection and treatment options. *Nat. Rev. Microbiol.* **13**, 269–284 (2015).
26. Bartlett, J. G. Laboratory diagnosis of urinary tract infections in adult patients. *Infect. Dis. Clin. Pract.* **12**, 360–361 (2004).
27. Goldstein, I. Recognizing and treating urogenital atrophy in postmenopausal women. *J. Women's Heal.* **19**, 425–432 (2010).
28. National Centre for Disease Control; Directorate General of Health Services. National Guidelines for Infection Prevention in Health and Control in healthcare Facilities. *MoHFW, Gov. India* 139–140 (2020).
29. Pai, N. P., Vadnais, C., Denkinger, C., Engel, N. & Pai, M. Point-of-Care Testing for Infectious Diseases: Diversity, Complexity, and Barriers in Low- And Middle-Income Countries. *PLoS Med.* **9**, (2012).

30. Mach, K. E., Wong, P. K. & Liao, J. C. Biosensor diagnosis of urinary tract infections: A path to better treatment? *Trends Pharmacol. Sci.* **32**, 330–336 (2011).
31. Nooranian, S., Mohammadinejad, A., Mohajeri, T., Aleyaghoob, G. & Kazemi Oskuee, R. Biosensors based on aptamer-conjugated gold nanoparticles: A review. *Biotechnol. Appl. Biochem.* **69**, 1517–1534 (2022).
32. Dykman, L. & Khlebtsov, N. Gold nanoparticles in biomedical applications: Recent advances and perspectives. *Chem. Soc. Rev.* **41**, 2256–2282 (2012).
33. Zhang, Y. *et al.* Magnetic-assisted aptamer-based fluorescent assay for allergen detection in food matrix. *Sensors Actuators, B Chem.* **263**, 43–49 (2018).
34. Paniel, N., Baudart, J., Hayat, A. & Barthelmebs, L. Aptasensor and genosensor methods for detection of microbes in real world samples. *Methods* **64**, 229–240 (2013).
35. Zuber, A. *et al.* Detection of gold nanoparticles with different sizes using absorption and fluorescence based method. *Sensors Actuators, B Chem.* **227**, 117–127 (2016).
36. Singh, S. K., Srinivasan, A., Mitra, S. & Gooh Pattader, P. S. Carbon dots and Methylene blue facilitated photometric quantification of Hemoglobin. *Spectrochim. Acta - Part A Mol. Biomol. Spectrosc.* **271**, 120906 (2022).
37. Ahmadi, S., Kamaladini, H., Haddadi, F. & Sharifmoghadam, M. R. Thiol-Capped Gold Nanoparticle Biosensors for Rapid and Sensitive Visual Colorimetric Detection of *Klebsiella pneumoniae*. *J. Fluoresc.* **28**, 987–998 (2018).
38. Liu, Z., Zhao, F., Gao, S., Shao, J. & Chang, H. The Applications of Gold Nanoparticle-Initiated Chemiluminescence in Biomedical Detection. *Nanoscale Res. Lett.* **11**, 1–8 (2016).
39. Kastanos, E., Kyriakides, A., Hadjigeorgiou, K. & Pitris, C. A Novel Method for

- Bacterial UTI Diagnosis Using Raman Spectroscopy. *Int. J. Spectrosc.* **2012**, 1–13 (2012).
40. Zhu, J. H. *et al.* Ultrasensitive photoelectrochemical aptasensor for detecting telomerase activity based on Ag₂S/Ag decorated ZnIn₂S₄/C₃N₄ 3D/2D Z-scheme heterostructures and amplified by Au/Cu²⁺-boron-nitride nanozyme. *Biosens. Bioelectron.* **203**, 114048 (2022).
41. Zhu, J. H. *et al.* Nanosheets-assembled hollow CdIn₂S₄ microspheres-based photoelectrochemical and fluorescent dual-mode aptasensor for highly sensitive assay of 17β-estradiol based on magnetic separation and enzyme catalytic amplification. *Sensors Actuators B Chem.* **347**, 130553 (2021).
42. Du, H., Li, Z., Wang, Y., Yang, Q. & Wu, W. Nanomaterial-based Optical Biosensors for the Detection of Foodborne Bacteria. *Food Rev. Int.* **38**, 655–684 (2022).
43. Duan, N. *et al.* Advances in aptasensors for the detection of food contaminants. *Analyst* **141**, 3942–3961 (2016).
44. Halas, N. J., Lal, S., Chang, W. S., Link, S. & Nordlander, P. Plasmons in strongly coupled metallic nanostructures. *Chem. Rev.* **111**, 3913–3961 (2011).
45. Wu, Y., Ali, M. R. K., Chen, K., Fang, N. & El-Sayed, M. A. Gold nanoparticles in biological optical imaging. *Nano Today* **24**, 120–140 (2019).
46. Cristea, O. M. *et al.* Urinary tract infection with *Klebsiella pneumoniae* in Patients with Chronic Kidney Disease. *Curr. Heal. Sci. J.* **43**, 137–148 (2017).
47. Paczosa, M. K. & Mecsas, J. *Klebsiella pneumoniae*: Going on the Offense with a Strong Defense. *Microbiol. Mol. Biol. Rev.* **80**, 629–661 (2016).
48. Vieira, A. T. *et al.* Control of *Klebsiella pneumoniae* pulmonary infection and

- immunomodulation by oral treatment with the commensal probiotic *Bifidobacterium longum* 51A. *Microbes Infect.* **18**, 180–189 (2016).
49. Jingru Zhao, MD, Tiantian Huo, MD, Xintong Luo, MM, Fan Lu, BS, Shuo Hui, BS, Baoming Yang, M. *Klebsiella pneumoniae*-related brain abscess and meningitis in adults. *Medicine (Baltimore)*. **101**, (2022).
50. Zhang, H. *et al.* Update of incidence and antimicrobial susceptibility trends of *Escherichia coli* and *Klebsiella pneumoniae* isolates from Chinese intra-abdominal infection patients. *BMC Infect. Dis.* **17**, 1–9 (2017).
51. Anderson, D. J. *et al.* Bloodstream infections in community hospitals in the 21st century: A multicenter cohort study. *PLoS One* **9**, 1–10 (2014).
52. Yinnon, A. M., Butnaru, A., Raveh, D., Jerassy, Z. & Rudensky, B. *Klebsiella* bacteraemia: Community versus nosocomial infection. *QJM - Mon. J. Assoc. Physicians* **89**, 933–941 (1996).
53. Wang, J. H. *et al.* Primary liver abscess due to *Klebsiella pneumoniae* in Taiwan. *Clin. Infect. Dis.* **26**, 1434–1438 (1998).
54. Hao, Y. *et al.* Molecular Characterization of *Klebsiella pneumoniae* Isolated from Sputum in a Tertiary Hospital in Xinxiang, China. *Infect. Drug Resist.* **15**, 3829–3839 (2022).
55. Denoya, C. D., Trevisan, A. R. & Zorzopulos, J. Adherence of multiresistant strains of *Klebsiella pneumoniae* to cerebrospinal fluid shunts: Correlation with plasmid content. *J. Med. Microbiol.* **21**, 225–231 (1986).
56. Strong, L. & Whitesides, G. M. Structures of Self-Assembled Monolayer Films of Organosulfur Compounds Adsorbed on Gold Single Crystals: Electron Diffraction

- Studies. *Langmuir* **4**, 546–558 (1988).
57. Ralph G. Nuzzo and David L. Allara. Adsorption of Bifunctional Organic Disulfides on Gold Surfaces. *J. Am. Chem. Soc.* **105**, 4481–4483 (1983).
58. Burns, J. A., Butler, J. C., Moran, J. & Whitesides, G. M. Selective Reduction of Disulfides by Tris(2-carboxyethyl)phosphine. *J. Org. Chem.* **56**, 2648–2650 (1991).
59. Tan, L. *et al.* Colorimetric Detection of Hg²⁺ Based on the Growth of Aptamer-Coated AuNPs: The Effect of Prolonging Aptamer Strands. *Small* **13**, 1–8 (2017).
60. Deb, A., Gogoi, P., Singh, S. K. & Gooch Pattader, P. S. Noise-Activated Fast Locomotion of DNA through the Frictional Landscape of Nanoporous Gels. *Langmuir* **38**, 11764–11769 (2022).
61. Pellegrino, T., Sperling, R. A., Alivisatos, A. P. & Parak, W. J. Gel Electrophoresis of Gold-DNA Nanoconjugates. *J. Biomed. Biotechnol.* **9** (2007) doi:10.1155/2007/26796.
62. Hanauer, M., Pierrat, S., Zins, I., Lotz, A. & Sönnichsen, C. Separation of nanoparticles by gel electrophoresis according to size and shape. *Nano Lett.* **7**, 2881–2885 (2007).
63. Barasinski, M. & Garnweitner, G. Restricted and Unrestricted Migration Mechanisms of Silica Nanoparticles in Agarose Gels and Their Utilization for the Separation of Binary Mixtures. *J. Phys. Chem. C* **124**, 5157–5166 (2020).
64. He, Y. Q., Liu, S. P., Kong, L. & Liu, Z. F. A study on the sizes and concentrations of gold nanoparticles by spectra of absorption, resonance Rayleigh scattering and resonance non-linear scattering. *Spectrochim. Acta - Part A Mol. Biomol. Spectrosc.* **61**, 2861–2866 (2005).
65. Yeom, S. H. *et al.* Enhancement of the sensitivity of LSPR-based CRP immunosensors by Au nanoparticle antibody conjugation. *Sensors Actuators, B Chem.* **177**, 376–383

- (2013).
66. Noh, S. *et al.* Recent advances in crp biosensor based on electrical, electrochemical and optical methods. *Sensors* **21**, (2021).
 67. Wang, Y., Zhou, J. & Li, J. Construction of Plasmonic Nano-Biosensor-Based Devices for Point-of-Care Testing. *Small Methods* **1**, 1–13 (2017).
 68. Rechberger, W. *et al.* Optical properties of two interacting gold nanoparticles. *Opt. Commun.* **220**, 137–141 (2003).
 69. Nelson, E. M. & Rothberg, L. J. Kinetics and mechanism of single-stranded DNA adsorption onto citrate-stabilized gold nanoparticles in colloidal solution. *Langmuir* **27**, 1770–1777 (2011).
 70. Li, H. & Rothberg, L. Colorimetric detection of DNA sequences based on electrostatic interactions with unmodified gold nanoparticles. *Proc. Natl. Acad. Sci. U. S. A.* **101**, 14036–14039 (2004).
 71. K. Lance Kelly, Eduardo Coronado, Lin Lin Zhao, and G. C. S. The Optical Properties of Metal Nanoparticles: The Influence of Size, Shape, and Dielectric Environment. *J. Phys. Chem. B* **107**, 668–677 (2003).
 72. Wu, W. H. *et al.* Aptasensors for rapid detection of Escherichia coli O157: H7 and Salmonella typhimurium. *Nanoscale Res. Lett.* **7**, 1–7 (2012).
 73. Liu, J. Adsorption of DNA onto gold nanoparticles and graphene oxide: Surface science and applications. *Phys. Chem. Chem. Phys.* **14**, 10485–10496 (2012).
 74. Pang, S., Labuza, T. P. & He, L. Development of a single aptamer-based surface enhanced Raman scattering method for rapid detection of multiple pesticides. *Analyst* **139**, 1895–1901 (2014).

75. Douglas G Altman et al. Statistics with Confidence. *BMJ Books* 1–254 (2000).
76. Nathaniel D. Mercaldo, K. F. L. and X. H. Z. Confidence intervals for predictive values with an emphasis to case-control studies. *Stat. Med.* **26**, 2170–2183 (2007).
77. Xiao-HUA ZHOU, Nancy A. Obuchowski. Statistical Methods in Diagnostic Medicine. *Wiley_Interscience* 1–592 (2002).
78. Holm, A. *et al.* Effect of point-of-care susceptibility testing in general practice on appropriate prescription of antibiotics for patients with uncomplicated urinary tract infection: A diagnostic randomised controlled trial. *BMJ Open* **7**, 1–8 (2017).
79. Guido Schmiemann, Eberhardt Kniewl, Klaus Gebhardt, Martha M. Matejczyk, E. H.-P. The Diagnosis of Urinary Tract Infection - A Systematic Review. *Medicine (Baltimore)*. **107**, 361–367 (2010).
80. Armbruster, D. A. & Pry, T. Limit of blank, limit of detection and limit of quantitation. *Clin. Biochem. Rev.* **29 Suppl 1**, S49-52 (2008).

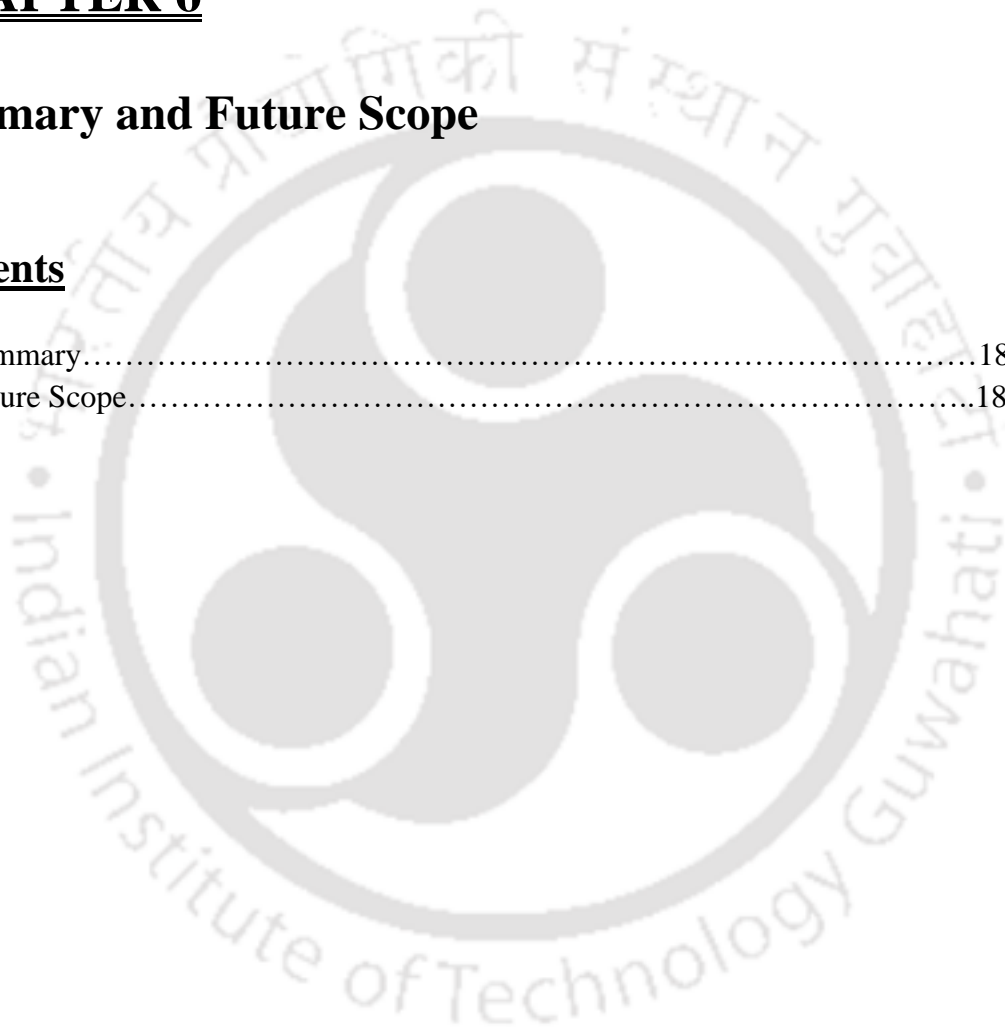


CHAPTER 6

Summary and Future Scope

Contents

6.1. Summary.....	182
6.2. Future Scope.....	185





6.1. Summary

The main goal of my doctoral research has been to elucidate the role played by the external gaussian noise/ periodic ramp vibrations affecting the macromolecular dynamics within the gel electrophoretic framework. Despite increasing interest in DNA separations using microdevices, practical application of these systems is only possible after solving several critical issues. As a conclusion, the research work mentioned in this thesis presented a methodology for biological physics on mesoscopic scales based on the theories of stochastic processes and soft matter physics. One problem is to ensure sufficiently high separation performance in limited length scales, which requires understanding of the interplay between gel structure, applied electric field, and separation resolution. Initial attempts to explain the physical origin of noise described that the phenomena which at first glance appears chaotic, is really controlled by fundamental physical principles and predicted statistically. Research in the past decades, have demonstrated a sharp increase in interest in noise and emphasis on how noise impacts design across a variety of scientific and engineering fields. Higher sensitivity detectors using the presence of noise are needed to investigate the physical world more accurately. Scientifically, our work is an extensive study on noise induced stochastic dynamics which has led to deeper understanding of external fluctuations providing greater impetus on biomolecule translocation through nanoporous gels. We used two powerful mathematical tools for the analysis of external noise induced phenomenon: Langevin equation and Fokker-Planck equation for the development of the simulation model. Additionally, our studies have illuminated the mechanism of external noise induced gel electrophoretic system for the diagnosis of specific bacteria. The phenomenon of macromolecule transport plays an important role in numerous biological processes such as the passage of DNA and RNA through nuclear pore complex, viral transfection of eukaryotic cells and protein transport across membrane channels. The crucial findings are described in chapter wise as follows:

Chapter 2 demonstrated that through the use of external Gaussian noise, our investigations showed that the mobility of DNA molecules in gel electrophoretic settings can be substantially faster (by 100% or more) than that of conventional gel electrophoresis. Another important aspect of this work highlights the fact that at high energy of the external noise, the DNA drift velocity generated by activated "noise-lubricity" follows the Arrhenius-Eyring-like escape rate. While at low energy, the DNA molecule's cooperative dynamics induce super Arrhenius-like behavior. Incorporating space-dependent nonlinear solid friction resulting from the wide range of gel pore size, a modified Langevin simulation correctly predicts the drift velocity for an applied bias and noise. Contrary to common belief, this study shows that a tremendous amount of solid friction (10^7 m/s²) is present at the DNA-gel matrix interface.

Chapter 3 demonstrated a key argument that an external noise coming from one specific direction can provide a stuck object/biomolecule enough energy to become mobile in any desired direction. The experimental results explained the phenomenon that noise applied in a direction that is orthogonal to the bias direction, it is feasible that the object/biomolecule will select the path that uses least amount of energy in the energy landscape. Instead of directly crossing the barrier's apex, the molecule might look for the neighbourhood's lowest barrier height and follow the least energy-consuming route to avoid the energy loss caused by the apex-crossing.

Henceforth, by the application of splitting of noise-biased voltage in orthogonal direction, the possible expected outcome is greater mobility of charged particles (DNA molecules) across gel matrix and as a result the separation efficiency enhances.

Chapter 4 showcased that in an electrophoretic environment, due to the presence of asymmetric vibration, the adhesive engagement of a soft deformable macromolecule with a

rigid substrate results in the sub-critical rupture of the contact. The overwhelming effects of Brownian motion on molecular motion, point to modifications in the dynamics of motion inside the gel matrix. Studies on the DNA migration rate points out an important scenario: In the molecular/mesoscopic environment, external vibrations change the relaxation behavior of entangled DNA chains allowing for faster movement. The analytical experiments discussed the entropic fluctuations originating due to the external asymmetric ramp vibrations within the electrophoretic framework.

Chapter 5 demonstrated that using external noise induced gel electrophoretic platform, how Aptamer-AuNP band mobility can be enhanced enabling rapid detection of specific pathogen by biologists for proper antibiotic medication and further guidance. The additional goal of this research was to create an aptasensor based on the surface plasmon resonance (SPR) of gold nanoparticles that produces a straightforward colorimetric output. Optical effects of surface plasmon resonance have been implemented for pathogen detection by inducing particle aggregation. Nanoparticle functionalization and competing binding sites control these effects. This research project also exploits the unique tools provided by nanotechnology to produce a simple colorimetric aptasensor using the intrinsic properties of gold nanoparticles, aptamer and bacteria and the interactions between them. The colorimetric response can be controlled through nanoparticle size and shape, giving the biosensor flexibility. The findings in the disciplines of nanotechnology, microbiology, and materials science connecting with the fundamentals of chemical engineering are presented in this chapter. Improved sensitivity, detection in complicated media, and in-depth knowledge of the elements of bacteria generating the colorimetric response are some of the directions that will be pursued in future investigations.

Along with the scientific findings elaborated above, the thesis also discloses various aspects of research works, which could be extended for future study.

6.2. Future Scopes

The proposed methodology for biological physics on mesoscopic scales that we described in this dissertation is based on the theories of noise-induced stochastic processes and soft matter physics. In the past two decades, a number of microfluidic devices have been developed for the separation of DNA molecules according to their size. These devices take advantage of the enhanced knowledge and control of the physics of fluids at the micro and nano-scales. These devices aim to challenge the dominance of gels as a separation medium and address the limitations of conventional gel electrophoresis. In our dissertation, we proposed a novel strategy for enhanced DNA separation based on the physics of external applied fluctuations. While our proposed methodology in the above-mentioned chapters outperform conventional gel electrophoresis in daily use, some important decisive outlook needs to be taken into consideration for future prospects mentioned below:

- The presence of external Gaussian noise facilitated the enhancement of mobility of DNA molecules in gel electrophoretic setting in comparison to conventional gel electrophoresis. Gaussian noise is just an ideal scenario for fluctuations in physical systems. In fact, particular scenarios were found where external noise can be described by distribution of impulses following heavy-tail stable law statistics of infinite variance. Lévy noise, as an important non-Gaussian noise, has heavy-tails, jumps and infinite divisibility. One important feature of Lévy noise is that the distribution of Lévy noise exhibits the asymptotic power-law decay, while Gaussian distribution decays exponentially. Lévy noise has been observed in physical, natural, social and complex systems. Recent study in the fields of finance, science, and engineering has

focused on dynamical systems energized by Lévy noise. So, it is worth studying the stochastic resonance (SR) phenomenon induced by non-Gaussian Lévy noise in gel electrophoretic system to inspect the mobility of DNA locomotion through nanoporous gels in comparison to conventional gel electrophoresis.

- The effect of external gaussian noise induced electrophoresis can be extended to the field of protein separation. Polyacrylamide gel electrophoresis is the preferred methodology for protein separation. In contrast to agarose, polyacrylamide forms smaller pores that enables the separation of relatively small proteins and makes the procedure more favourable for separation of proteins than long polynucleotides DNA or RNA. The presence of external gaussian noise will aid faster separation which will eventually enhance protein purification. The readily available need for purified proteins is important for many bio-medical applications like therapeutics and diagnostics and in regenerative medicine and biosensing.
- We investigated the translocation dynamics of biomolecule (DNA) driven by external periodic ramp vibrations across a potential barrier facilitated by gel pores in an electrophoretic setting. The mean translocation time as a function of frequency of the driving field characterizes the drift velocity regime for rapid separation efficiency. The research can be further extended as a future prospect, where the driving frequency can act as a tuning mechanism to sort out a particular molecular weight band (kbp) for further purification using restriction enzymes. Moreover, in continuation the driving frequency can activate the resonant regime of the biomolecule translocation and further reduce the mean time of translocation. This prospect can truly benefit the biochemistry and nano-biotechnology domain and of fundamental importance regarding experiments relating to the cell metabolism, DNA-RNA sequencing and drug delivery mechanism in anti-cancer therapy.

➤ The experiments in Chapter 3 showcased the effect of splitting of external Gaussian noise and bias in orthogonal direction on the drift velocity of the DNA molecules. Our proposed methodology can be further extended forward as a future prospect by exerting external pressure on the casted gel to modulate the gel pores. As a result, possible wide variety of pore size range can be achieved which can enable to ascertain the DNA sequencing probability. In general, nanopore based DNA sequencing technology has become one of the most attractive and promising modern-generation sequencing technologies because of its outstanding characteristics of label-free, amplification-free, great read length, and high throughput, which offer possibilities of high-quality gene sequencing applications, such as *de novo* sequencing, high-resolution analysis of chromosomal structure variation, and long-range haplotype mapping. However, several other factors that demand research is the geometry of biological nanopore required for high efficiency DNA sequencing and how to take control of DNA translocation behavior and velocity through the nanopore.

To sum up, the research covered in this thesis is merely the beginning of a prolonged journey toward understanding how external fluctuations function in biological settings. Our simulation models may be improved upon or modified to fit a variety of research needs, not just biomolecule translocation. We are expecting that this thesis will serve as a foundation and provide fresh concepts for further research.



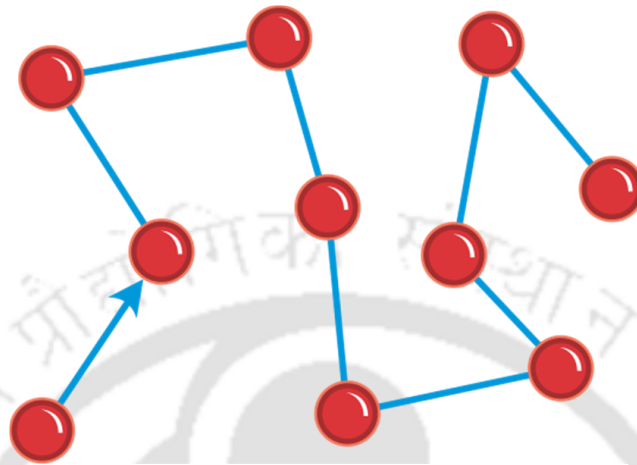
APPENDIX-A

The macroscopic characteristics of an equilibrium system, including its temperature, pressure, volume, energy, and entropy, as well as their relationships, are the focus of classical thermodynamics. A well-defined gel electrophoretic system was systematically exposed to external fluctuations and the output was recorded as enhanced mobility in the form of drift velocity. In this thesis, we have methodically addressed these challenges and explored the stochastic dynamics regime. We shall explore various definitions of statistical words and their properties in this annexure.

A.1. Brownian Motion

Initial attempts to explain Brownian motion resulted in the emergence of the idea of thermal fluctuation. Robert Brown¹, a British botanist, made the initial discovery of this persistent random movement of pollen particles floating in liquid in 1827. Robert Brown, a botanist, felt compelled to explain the discovery by imbuing pollen grains with a life force. Brown himself later disproved this biologically inspired theory by pointing out that small particles of inorganic substances were also prone to the same erratic motion. As a result, the idea of Brownian motion shifted from biology to physics², where Einstein and Smoluchowski^{2,3} laid the first significant theoretical basis on the dynamic phenomena around the turn of the 20th century in their key works. Another series of groundbreaking investigations on Brownian motion by Langevin, Fokker, and Planck⁴⁻⁶, who gave further profound insights and potent mathematical tools, extended the theoretical discovery by Einstein and Smoluchowski. Brownian motion has been at the center of the study of stochastic process and thermal fluctuations ever since the important theoretical discoveries in the early 20th

century. The discipline has thrived, providing a vast reservoir of techniques to investigate a variety of dynamic systems affected by noise⁷⁻⁹.



Brownian Movement of a Particle

Figure A.1. A typical Model of Brownian motion.

A.2. Fluctuation- Dissipation theorem

During fluctuation and dissipation, the Brownian particle transfers energy with the thermal bath. While dissipation is an energy transfer from the particle to the thermal bath, fluctuation tends to enhance the energy of the particles. These two energy fluxes cancel one other out in thermal equilibrium, maintaining the particle's mean energy at $k_B T/2$, which is dictated by energy partition. A crucial statistical physics theory known as the fluctuation-dissipation theorem describes this delicate equilibrium between fluctuation and dissipation¹⁰⁻¹⁴.

A.3. Markov Process

The definition of a Markov process¹⁵ in a stochastic setting is "memory-less," meaning that the next state of the system depends solely on the current state and is unrelated to any of the past states it had before the current state. The Markov process should have zero autocorrelation time according to its specification. An illustration of a Markov process is a ship in a stormy sea, a kite in the sky, a moving vehicle, the motion of a colloidal particle in thermal fluid, etc. A colloid particle's Brownian motion results from the random collisions of nearby fluid molecules with the colloid particle. Consequently, the magnitude and direction of the colloid particle's velocity randomly vary. If the particle has velocity V at time t , it will collide with more fluid molecules up front. Any change in the particle's velocity during the following brief time interval, dt , will only depend on its current velocity, V , and not on its past behaviour. Consequently, the colloid particle's velocity serves as an illustration of the Markov process.

A.4. Skewness

The criterion for a distribution's asymmetry is called skewness (S). When the values of the random variables are equally spaced from the mean and the frequencies are symmetrically dispersed about the mean, the distribution is said to be symmetrical. The distribution's skewness is shown by:

$$S = \frac{m_3}{m_2^{3/2}}$$

Where m_2 and m_3 are the second and third cumulants.

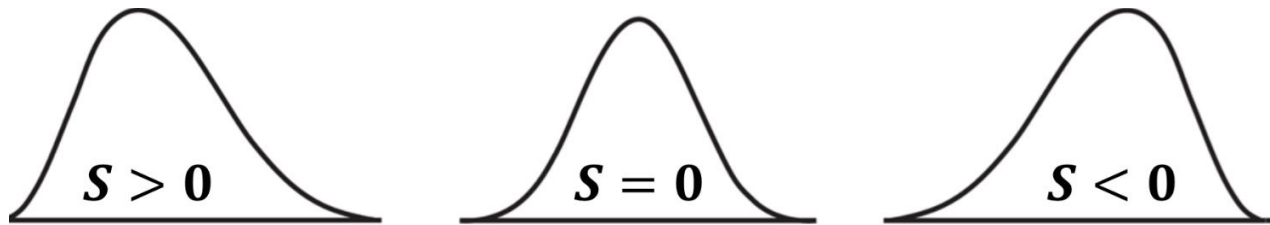


Figure A.2. Schematic representing the skewness of a distribution.

In the case of a symmetric distribution, $S=0$; otherwise, it takes on a positive or negative value depending on whether the distribution is skewed toward values greater or lower than the mean.

A.5. Gaussian Noise

The gaussian distribution may be used to explain the Brownian motion of colloid particles and the thermal fluctuation of atoms in conductors. The mean and variance of the Gaussian distribution are finite. The dynamics of a macromolecule affected by a bias force and external white noise was the major topic of our research, which has been elaborately discussed. Unless otherwise mentioned, we utilized Gaussian noise as an external white noise throughout the most of the portion. In our dissertation, we have used time-dependent random acceleration pulses ($\gamma(t)$) with constant temporal pulse width τ_c to introduce external Gaussian noise into the system. A typical distribution of the acceleration is represented in figure A.3. below:

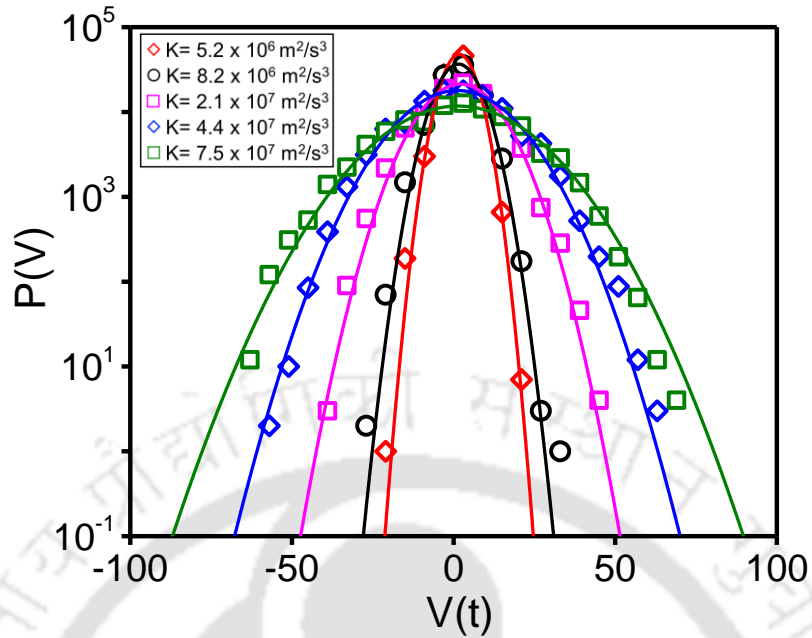


Figure A.3. Semi-Log plot of input noise in the form of voltage pulses.

The pulses of a real white noise should be delta correlated. Consequently, the defined autocorrelation time shows a tendency towards zero, and the noise's power spectra will be flat over the whole frequency range. The input gaussian noise generated via the function generator has the following properties:

$$\langle \gamma(t_1)\gamma(t_2) \rangle = \Gamma^2 \text{ for } |t_1 - t_2| < \tau_c$$

$$\langle \gamma(t_1)\gamma(t_2) \rangle = 0 \text{ for } |t_1 - t_2| > \tau_c$$

Where Γ is defined as the root mean square acceleration. The power of noise K is defined as $\Gamma^2\tau_c$ (m^2/s^3).

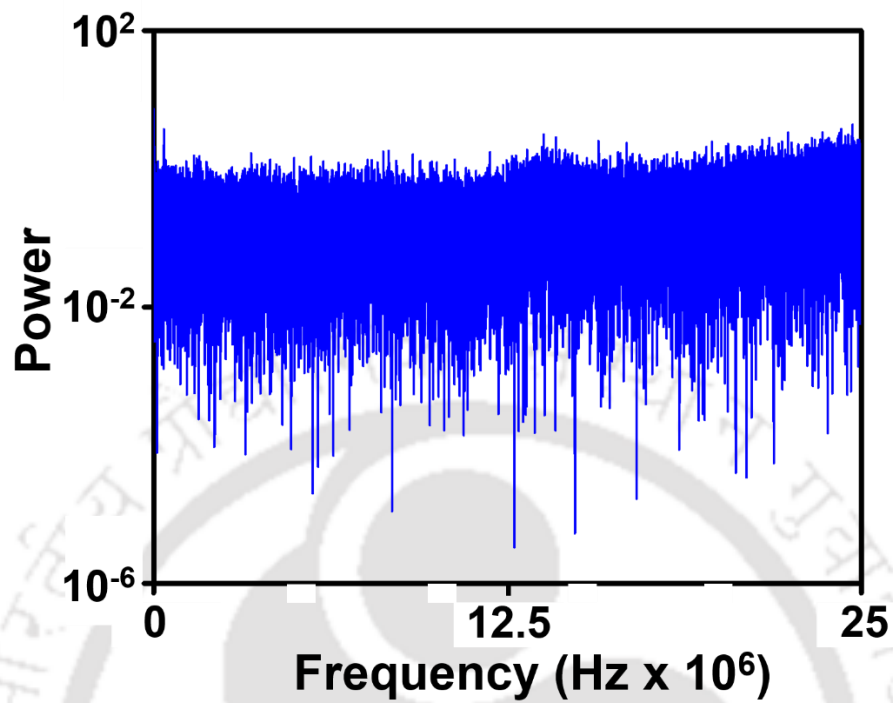


Figure A.4. Power spectrum of input white noise.

References

1. Robert Brown. *Brownian Motion*. (1827). doi:10.1007/978-3-642-58244-8_1
2. Einstein, A. INVESTIGATIONS ON THE THEORY OF THE BROWNIAN MOVEMENT. *DOVER Publ. INC* **17**, 549–560 (1905).
3. M.von Smoluchowski. *Zur kinetischen Theorie der Brown'schen Molekularbewegungen und der Suspensionen*. *Annalen der Physik (Leipzig)* **1**, (1906).
4. Lemons, D. S. & Gythiel, A. Paul Langevin 's 1908 paper ““ On the Theory of Brownian Motion ”” & On the Theory of Brownian Motion, A note from M . P . Langevin, presented

- by M. . Mascart . *Am. J. Phys.* **65**, 1079–1081 (1997).
5. Fokker, A. D. Die mittlere Energie rotierender elektrischer Dipole im Strahlungsfeld. *Ann. Phys.* **348**, 810–820 (1914).
 6. Planck, M. *Treatise on Thermodynamics*. (1903).
 7. D.R.Cox & Miller, H. D. The Theory of Stochastic Processes. *Ann. Math. Stat.* **37**, 1848–1851 (1966).
 8. Wax, N. & Cohen, M. H. Selected Papers on Noise and Stochastic Processes. *Phys. Today* **8**, 19–19 (1955).
 9. Van Kampen, N. G. *Stochastic Process in Physics and Chemistry*. (2003).
 10. Bernard, W. & Callen, H. B. Irreversible thermodynamics of nonlinear processes and noise in driven systems. *Rev. Mod. Phys.* **31**, 1017–1044 (1959).
 11. Callen, H. B. & Welton, T. A. Irreversibility and Generalized Noise. *Phys. Rev.* **83**, 34–40 (1952).
 12. Callen, H. B. & Greene, R. F. On a theorem of irreversible thermodynamics. *Phys. Rev.* **86**, 702–710 (1952).
 13. Jackson, J. L. A Note On ‘ Irreversibility and Generalized Noise’. *Phys. Rev.* **87**, 471–473 (1952).
 14. F.Reif. *Fundamentals of statical and thermal physics*. McGraw-Hill INC (1965).
 15. Lagzi, F. & Rotter, S. A Markov model for the temporal dynamics of balanced random networks of finite size. *Front. Comput. Neurosci.* **8**, 1–23 (2014).



APPENDIX-B

Curriculum Vitae

Mr. Aniruddha Deb

Education

PhD

2017-2023

Department of Chemical Engineering

Indian Institute of Technology, Guwahati

Thesis Supervisor: Dr. Partho S.G. Pattader

Project Title: *Noise-activated dynamics of DNA through nanoporous gel.*

M.Tech

2015-2017

Department of Chemical Engineering

Indian Institute of Technology, Guwahati

Thesis Supervisor: Dr. Partho S.G. Pattader

Project Title: *Micro Patterning of thin polymer (Polystyrene, Block Co-Polymer) films on silicon substrates.*

B. Tech

2009-2013

Department of Chemical Engineering

Heritage Institute of Technology, Kolkata

Project Supervisor: Dr. Sulagna Chatterjee

Project Title: *Study on micro droplet behaviour for a piezoelectric inkjet printing device.*

Professional Experience

- Summer training at Haldia Petrochemicals Limited (HPL), West Bengal, India
- Graduate engineer trainee, Gujarat Fluorochemicals Limited, GFL, Vadodara, Period – July 2013 to June 2014

Teaching Assistantship Experience

Teaching assistant in Analytical Lab, Department of Chemical Engineering, IIT Guwahati

Role: My role was to help the undergraduate and postgraduate students and ensuring smooth operation & functioning of the instruments listed below:

- ✓ UV/Visible Spectrophotometer
- ✓ Tensiometer
- ✓ Delsa Nano (Particle Size analyser)
- ✓ Rheometer
- ✓ Optical Microscope
- ✓ TGA (Thermogravimetric Analyzer)
- ✓ DSC (Differential scanning calorimetry)

Teaching assistant in Process & Instrumentation lab, Department of Chemical Engineering, IIT Guwahati (July 2016- Dec 2016)

Skills

Computer

MATLAB (R2022b)
 AutoCAD
 Free CAD
 Microsoft Word
 Microsoft Excel

Key Courses

Fluid mechanics
Heat Transfer
Colloid & Interfacial Science
Chemical Reaction engineering
Microfluidics & Bio-sensing techniques

Language

English- Speak & Write
Bengali- Speak & Write
Hindi- Speak & Write

Fellowship and Honour's**2009**

Recipient of "CENTRAL SECTOR SCHOLARSHIP SCHEME, MHRD" for excellent performance in Higher Secondary Examination.

2015

Received MHRD scholarship for qualifying GATE for pursuing M. Tech at IIT GUWAHATI (Chemical Engineering with specialization in Material Science & Technology).

2017

Received MHRD scholarship for pursuing PhD in Chemical engineering. (July 2017- July 2022).

Current Position:

- ✓ Working as a Post-Doctoral Research Associate under the mentorship of Prof. Arnab Atta, Associate Professor, **Chemical Engineering, IIT Kharagpur** starting from 3rd May 2023 till date.

